Single Nanoparticle Magnetism: Hysteresis of Monomers, Dimers and Many-Particle Ensembles

Von der Fakultät für Physik
der Universität Duisburg-Essen
zur Erlangung des akademischen Grades
Doktor der Naturwissenschaften

genehmigte Dissertation

von
Nina Friedenberger
aus Heiligenhaus

Referent: Prof. Dr. Michael Farle

Korreferent: Prof. Dr. Thomas Brückel

Tag der mündlichen Prüfung: 25. November 2011

meinen Eltern

Abstract

In this thesis, structural and magnetic properties of single Fe and Fe_xPt_{1-x} self-assembled nanoparticles are investigated and correlated.

- First, surface properties of cuboctahedral Fe_xPt_{1-x} nanoparticles are investigated using high resolution transmission electron microscopy (HRTEM). A novel oscillatory surface layer relaxation of the order of several percent is observed. The large outward relaxation of the outermost surface layer is attributed to carbon traces present in the experiment.

- Second, the bulk magnetic properties of these nanoparticles are investigated. Using the high resolution achievable by photoemission electron microscopy with circularly polarized x-rays, the magnetic hysteresis loops of *individual Fe nanoparticles* with side length smaller than 20 nm are measured for the first time. In addition, the hysteresis loops of nanoparticle configurations consisting of a few nanocubes are recorded at room temperature and 110 K in differently oriented magnetic fields (up to 100 mT). The coercivity of individual ~ 18 nm Fe nanocubes is determined to be about 2.5 mT at room temperature.
  The measurements, using the XMCD effect [x-ray magnetic circular dichroism], yield a reduced magnetization for the Fe nanocubes corresponding to 50 % of that of bulk Fe. This is attributed to thermal fluctuations of the magnetization over the time scale of the measurement.
  Moreover, a shift of the hysteresis loop reminiscent of a positive exchange bias is observed in most configurations consisting of multiple Fe nanocubes. The origin of this shift, however, cannot be fully explained by either the presence of an exchange bias or by the magnetostatic interaction between nanocubes.

- Third, the relationship between the structural and magnetic properties of the nanoparticles is investigated. To this effect, the three-dimensional morphology experimentally measured by TEM is introduced in micromagnetic simulations, revealing a strong dependence of the coercive field on particle morphology. For example, a 10 % elongation increases the coercivity by one order of magnitude.

The measurements carried out in this thesis on different nanoparticle systems demonstrate the possibility of characterizing the magnetization down to a scale of a few nanometers by means of x-ray microscopies: x-ray photoemission electron microscopy (XPEEM) and magnetic transmission x-ray microscopy (MTXM).

Kurzfassung

In dieser Arbeit werden die strukturellen und magnetischen Eigenschaften einzelner selbstorganisierter Fe- und Fe_xPt_{1-x}-Nanopartikel untersucht und korreliert.

- Die strukturelle Oberflächenrelaxation von kuboktaedrischen Fe_xPt_{1-x}-Nanopartikeln wurde lagenaufgelöst mittels hochauflösender Transmissionselektronenmikroskopie (HRTEM) untersucht. Eine oszillatorische Relaxation von mehreren Prozent wurde erstmalig beobachtet und die starke Aufweitung der äußersten Lage einem experimentell bedingten Kohlenstoff-Einfluss zugeordnet.

- Die magnetischen Eigenschaften kubischer Nanopartikel kleiner 20 nm wurden mittels Photoemissionselektronen-Mikroskopie unter der Verwendung von zirkular polarisierter Röntgenstrahlung untersucht. Hysteresekurven individueller und aus wenigen Partikeln bestehender Konfigurationen wurden erstmalig bei Raumtemperatur und 110 K sowie in verschiedenen Orientierungen des Magnetfeldes (bis zu 100 mT) aufgenommen. Das Koerzitivfeld eines einzelnen ~ 18 nm Fe Nanowürfels bei Raumtemperatur konnte bestimmt werden (~ 2.5 mT). Mittels des XMCD-Effekts wurde eine im Vergleich zum Volumenmaterial um 50 % reduzierte Magnetisierung in den Fe Nanowürfeln gemessen und durch thermische Magnetisierungsfluktuationen über den Zeitraum der Messungen erklärt. Desweiteren wurde eine an einen positiven Exchange Bias erinnernde Verschiebung der Hystersekurve in Fe Nanowürfel-Konfigurationen beobachtet. Dabei bieten weder die gängigen Exchange Bias Modelle noch die magnetostatische Wechselwirkung zwischen den Nanowürfeln eine hinreichende Erklärung dieses Effekts.

- Das komplexe Zusammenspiel von Struktur und Magnetismus der Nanopartikel wurde mittels mikromagnetischer Simulationen untersucht. Hierbei wurde die durch TEM ermittelte drei-dimensionale Morphologie in den Rechnungen berücksichtigt und eine starke Abhängigkeit gefunden. Beispielsweise resultieren 10 % Elongation in einer Vergrößerung des Koerzitivfeldes um eine Größenordnung.

Die in dieser Arbeit durchgeführten Messungen an verschiedensten Nanopartikelsystemen verdeutlichen die Möglichkeit, den Magnetismus auf der Skala weniger Nanometer mittels verschiedener röntgenmikroskopischer Methoden (Röntgen-Photoemissionselektronen-Mikroskopie (XPEEM) und Magnetischer Röntgen-Transmissions-Mikroskopie (MTXM)) vollständig zu charakterisieren.

List of Abbreviations

ALS	Advanced Light Source
BESSY	Berliner Elektronenspeichering für Synchrotronstrahlung mbH
EB	exchange bias
H_c	coercive field (coercivity)
(HR)TEM	(high resolution) transmission electron microscope/microscopy
LT	low temperature
M_s	saturation magnetization
(M)TXM	(magnetic) transmission x-ray microscope/microscopy
RT	room temperature
SEM	scanning electron microscope/microscopy
SPM	superparamagnetism
SQUID	superconducting quantum interference device
T_b	blocking temperature
XAS	x-ray absorption spectroscopy
XMCD	x-ray magnetic circular dichroism
XPEEM	x-ray photoemission electron microscope/microscopy

Contents

Introduction

Over the last decades magnetic nanoparticles [1] have attracted great interest in science because of their manifold applications in biomedicine, magnetic sensors and high density data storage devices [2–10]. Since pioneering work on the synthesis of monodisperse magnetic FePt-nanoparticles superlattices by Sun et al. [11], many research groups turned their focus towards the FePt-system [12, 13]. Due to its extreme magnetic hardness in the chemically ordered fct $L1_0$-phase - the effective anisotropy can be as large as $1000\,\mathrm{kJ/m^3}$ (bcc Fe bulk: $48\,\mathrm{kJ/m^3}$) - FePt-nanoparticles seemed to be the perfect candidates serving as individual bits in high magnetic data storage media [11]. The obstacle for their application in storage devices up to present, is the synthesis of perfectly monodisperse particles and their controlled self-organization in larger arrays. The chemically disordered fcc $A1$-phase of FePt has also received attention in connection with its possible use as a room temperature superparamagnet for biomedical applications, such as magnetic hyperthermia and biosensors (see [14] and references therein). FePt-nanoparticles can also be used for catalytic applications. Other popular magnetic materials for in vivo applications in general are Fe-oxide nanoparticles due to their bio-compatibility. The desired structural and magnetic nanoparticle properties depend on their application. For instance, the thermal stability of the magnetization (blocking temperature, p. 13 ff.) at room temperature needs to be high for data storage devices (more than 10 years).
For most biomedical applications, however, the nanoparticles need to be in the superparamagnetic state, i.e. the time scale for thermally driven magnetization fluctuations (superparamagnetic limit, p. 13 ff.) has to be smaller than milliseconds. By controlling the magnetocrystalline anisotropy energy (MAE) and/or the volume of the material, the superparamagnetic limit can be tuned: For increased anisotropy, the size of the particles which have a stable magnetization at room temperature decreases. Decreasing the particle size, however, changes not only the magnetic properties, but also enhances the fraction of atoms in the interfacial or surface regions increases, e.g. 37 % (49 %) for 10 nm (5 nm) particles[1], whereas the fraction for 100 nm clusters only amounts to 3 %. This means that for fine magnetic particles the effect of surface and interface electronic structure on the magnetic properties becomes more and more important, and detailed knowledge about the correlation of particle structure/morphology and its magnetic properties is crucial.

[1] Assumption: Spherical nanoparticles with 1 nm thick surface shell

This thesis deals with both aspects and is divided into two parts:

(1) Structural Analysis of Individual Nanomagnets

(2) Magnetic Analysis of Individual and Small Ensembles of Nanomagnets

The main motivation of the **structural part** was to investigate if oscillatory surface layer relaxations occur in metallic (magnetic) nanoparticles. This phenomenon is known at bulk metal surfaces and has been intensively studied experimentally and theoretically (see e.g. Table 1.1, p. 3). However, it has never been addressed in (magnetic) nanoparticles which exhibit a large surface area formed by different facets. This task was successfully addressed in this work by high resolution transmission electron microscopy (HRTEM) in combination with the method of exit wave reconstruction (EWR) on Fe_xPt_{1-x} nanoparticles. Furthermore, the questions whether the observed relaxations are

- size dependent,
- direction dependent,
- facet size dependent,
- material dependent, or if they are
- intrinsic or extrinsic properties

are addressed. The Fe_xPt_{1-x} particle system was chosen since it can be synthesized by different approaches, such as gas phase condensation and organometallic synthesis. The latter technique uses organic ligands attached to the particles' surface for their stabilization in solution. Comparing the surface relaxation of these differently synthesized nanoparticles allows to investigate the influence of surface adsorbates on the relaxation behavior. Furthermore, Fe_xPt_{1-x} is a good model system for bimetallic compounds, and many works focussing on its magnetic properties have been published, e.g. [15].
Since structural relaxations, i.e. local changes of the lattice parameter in the range of several percent result in dramatic changes of orbital and spin contributions to the total magnetic moment [16, 17], these investigations are of fundamental interest for the understanding of nanoparticle magnetism which is addressed in the "magnetic" part of this thesis.
The **magnetic part** was motivated by the following questions and challenges:

- What are the orbital μ_l and spin μ_s contributions to the total magnetic moment in a single nanomagnet?

- How does the hysteresis loop of an individual nanoparticle - measured along different crystallographic directions - look like? In other words: what is the MAE of an individual particle?
- How does the coercive field depend on size, temperature, shape and morphology?
- What is the magnetization reversal mechanism?
- What is the blocking temperature of the individual particle?
- To what extent does non-collinear spin-alignment at the surface influence the magnetic properties, e.g., in core-shell or bi-metallic particles?

Whereas the structural properties of individual nanoparticles can be routinely studied by HRTEM, most of the magnetic characterization techniques probe the collective response in nanoparticle systems consisting of millions of particles. Common techniques are e.g. superconducting quantum interference device (SQUID)-magnetometry, ferromagnetic resonance (FMR), and synchrotron studies employing the x-ray magnetic circular dichroism (XMCD) effect.

All of these techniques average over the size distribution of the particles, the distribution of magnetocrystalline anisotropy axes and dipolar interactions, and consequently the magnetic information on the individual particle is lost.

In the beginning of this study, few methods existed which could address single nanoparticle magnetic properties: Jamet et al. reported switching field (not hysteresis) measurements of specially prepared individual nanomagnets (20 nm Co) at low temperatures ($35\,\mathrm{mK} < \mathrm{T} < 30\,\mathrm{K}$) using a micro-SQUID technique [18]. Cleuziou et al. discussed the possibility that the sensitivity of this technique could be improved to detect the switching field of single magnetic molecules when using carbon nanotubes (CNTs) as Josephson junctions [19]. For particles in the range between 20 nm - 1 μm, magnetic hysteresis and domain configurations have been determined by ballistic hall micro-magnetometry [20], differential phase contrast microscopy [21], and more recently, by holography [22] in transmission electron microscopy (TEM). High-resolution crystallographic and compositional information combined with magnetic contrast have been obtained by Electron Magnetic Chiral Dichroism (EMCD) in the TEM as well [23]. This technique holds the promise for the investigation of magnetic properties with a magnetic resolution as small as 2 nm in special sample geometries [24]. Nevertheless, these techniques require highly specialized or complicated sample preparation. Furthermore, they are usually limited to a small temperature range. The main drawback is that only few particles can be analyzed in a reasonable amount of time, resulting in poor statistics. Long-range dipolar interactions in nanoparticle ensembles cannot be addressed at all. Due to these reasons, the desired in-situ correlation of composition, crystal structure and morphology on the one hand and the magnetic and electronic structure of one individual particle on the other hand cannot be provided.

Recent developments in magnetic imaging by soft x-ray microscopies [25–29] offered new possibilities with a claimed lateral resolution of about 25 nm. In this thesis, x-ray photoemission electron microscopy (XPEEM) in combination with scanning electron microscopy (SEM)[29] was employed since it offers the following advantages/possibilities:

- Element-specific magnetic imaging based on the XMCD effect with a lateral resolution in the range of the particle size (~ 25 nm)
- Determination of the chemical (electronic) state of the system by x-ray absorption measurements
- Temperature-dependent measurements
- Relative orientation of particle (sample) with respect to the in-plane external magnetic field (magnitude up to 33 mT [30][2]) can be adjusted
- Simultaneous sampling of up to several hundreds of individual particles and small particle configurations due to a several μm^2 field of view

The approach of hundreds of particles allows to investigate dipolar interactions and their impact on the following issues:

- Do neighboring particles influence the individual magnetic response? If yes:
- What is the interaction radius?
- What is the magnetic response in small dipolar coupled ensembles?
- Does the magnetic response depend on the relative orientation of the particles with respect to each other?
- How do small changes in morphology affect the magnetic response in a dipolar coupled configuration?
- What is the effect of dipolar coupling on the blocking temperature?

The latter is of special interest since experiments on macroscopic ensembles have shown that different particle configurations and compositions display opposite shifts of T_b [31] and a clear theoretical understanding [32] has not been reached so far. Experiments for identifying the dominating magnetic interactions on the nanoscale have been called for. In this work, it is demonstrated that XPEEM simultaneously provides quantitative information on the chemical state, coercive field and magnetic moment of hundreds of sub 20 nm individual nanomagnets (Fe nanocubes) in different configurations and in magnetic fields of up to almost 100 mT in a single experimental run. In combination with

[2] During this work, the magnitude of the external field was increased to almost 100 mT.

SEM and TEM, to identify shape, crystal structure, geometry and topological distribution, the challenge of "in-situ" correlation of morphology, electronic structure, surface composition and magnetic properties of individual nanoparticles could be met. This will contribute to the understanding of how small changes on the nanoscale can affect the macroscopic response.

The thesis is structured as follows:

Subsequent to the *Introduction* in **Chapter 1** the relevant *physical fundamentals* in the context of this work are summarized: *surface relaxation in metals*, p. 1 ff., and the *magnetic behavior of monodisperse nanomagnets* with a focus on the required quantities studied in this thesis (*MAE, interactions, magnetization reversal, coercivity, blocking temperature, dipolar interactions, etc.*), p. 7 ff. **Chapter 1** also includes a discussion on the physical background of the *magnetic contrast mechanism (XMCD) of the magnetic measurement techniques* (p. 35 ff.). The experimental techniques which were utilized for structural (*HRTEM & EWR*) and magnetic (*XPEEM/MTXM* complemented by *micromagnetic simulations*) characterization are presented in **Chapter 2** (p. 33 ff.). In **Chapter 3** the different *synthesis* routes *of* the *nanoparticles* and *sample preparation* based on electron beam lithography and plasma reduction treatment are presented. The *results* are discussed in **Chapters 4** (*structural part*, p. 53 ff.) and **5 - 7** (*magnetic part*, p. 68 ff.). **Chapter 5** starts with a section in which details of the *XPEEM measurements and the data treatment* are illustrated. The first XPEEM *hysteresis measurements on individual 18 nm Fe nanocubes* are presented. For a better understanding of the individual switching behavior, micromagnetic simulations have been performed, and the *influence of morphology* is discussed. In **Chapter 6** *ensemble* measurements are discussed: *T-dependent magnetic hysteresis and XMCD measurements* on different nanoparticle configurations are presented. It is demonstrated how the remanent magnetization direction and strength can be determined in a well-dispersed sample. Furthermore, volume sensitive *Magnetic Transmission X-ray Microscopy (MTXM) measurements* on Fe polyhedra and nanocubes are shown. Additionally, first *MTXM heating measurements* on Fe polyhedra particles are presented. *Preliminary results* by x-ray microscopy measurements on *Co-nanorods* are shown in **Chapter 7**. **Chapter 8** provides the *conclusion*.
The **Appendix** contains *additional information and data*.

1. Fundamentals

1.1. Surface Relaxation

1.1.1. Oscillatory Surface Relaxation in Semi-Infinite Models

Experimental studies with low energy electron diffraction (LEED) and medium energy ion scattering have confirmed [33] (see also Table 1.1, p.3) theoretical studies [34, 35] proposing that the magnitude of the structural relaxation at a metal's surface is quasi-linearly related to the "openness", i.e. the reciprocal packing density, of the surface. The more open (rough)[1] the surface, the more significant the surface relaxation. Different theoretical models have been derived to explain the various features of the observed relaxations. The different aspects of these models are:
(a) the general tendency of sp electrons to spread smoothly at the surface,
(b) the different roles of localized d and delocalized sp electrons,
(c) the termination of the crystal and its influence on the electronic structure [37].
The lower coordination at the surface leads to a change of the charge density distribution in a simplified model. The local charge density for simple metals can be described by the jellium model [38] in which the density variation reveals two features: a) spill out and b) oscillations as it approaches an asymptotic value that exactly compensates the uniform (bulk)background charge. These Friedel oscillations are of wavelength π/k_F [39].

In the effective medium approach, which is a special formulation of the jellium model, oscillatory surface relaxations are explained in a very simple picture [38]: The surface atoms are embedded in a medium with lower average electron density than those in the bulk. Therefore the surface atoms will move towards a position with higher density that brings them nearer to the immersion curve minimum resulting in an inward relaxation of the outer layer. As a consequence, the second layer atoms "sense" additional charge in their surrounding and "push" away the third layer. The net result is, the spacing of the first pair of atomic planes is contracted and the spacing of the second pair is expanded with respect to the bulk spacing. The spacing of the third pair of planes is contracted again and so on resulting in a damped oscillatory relaxation into the bulk[2].

[1] Surface Roughness: The inverse of the fraction of the area in one plane occupied by atoms of radii equal to one half of the bulk nearest-neighbor distance [36].

[2] Note that the jellium model does not take into account the particular 3d-character of the electrons. It can not be applied directly to the surfaces of transition metals, as Fe, Co and Ni with their localized d-electrons. Nevertheless it gives some insight and may describe the s-electrons of transition metals. It has been suggested that is applies to rare earth metals such as Gd [40].

A more detailed understanding, especially of the typical contraction of the surface layer spacing, is given by the following descriptions [41–46]. (a) If a perfect crystal is cut along the Wigner-Seitz cells to create a surface (Fig. 1.1 b), the electronic charge density becomes smoother to reduce its kinetic energy (fig. 1.1 a) [42, 43]. This (Smoluchowski) smoothing is equivalent to moving charge from the regions directly above the surface atoms to the areas between them. The net result is an inward electrostatic force [41, 42].

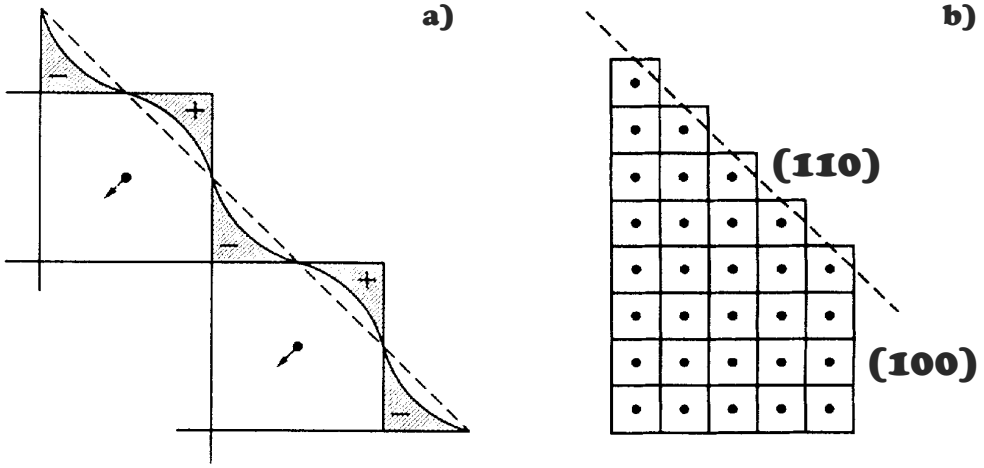

Figure 1.1.: Smoluchowski smoothing from refs. [37, 43]. (a) Charge redistribution at surface. (b) Dependence of the smoothing effect on the surface roughness.

This contraction can also be explained in a model based on Pauling's work on the chemical correlation of the bond-order-bond-length and thus on the saturation of valency [46]. Finnis and Heine explain the relationship between surface relaxation - which is a contraction for most transition metal surfaces - and the roughness. Their description fails for the surface relaxation of noble metals though. The suggested model by Heine and Marks focusses on the contributions of d electrons to the surface relaxation and predicts outward relaxation for noble metal surfaces [47, 48]. Furthermore tight-binding approaches have been employed to investigate the way in which the wave function of the infinite crystal is modified when a surface is introduced [37, and references therein]. In an extension of the tight-binding approaches Allan and Lannoo derived explicit expressions for the total energy of a semi-infinite crystal explaining the existence of oscillatory multilayer relaxations [49]. These and other models on surface relaxation are described e.g. in [37, 50, and references therein].

system	$d_{1/2}$(%)	$d_{2/3}$(%)	$d_{3/4}$(%)	$d_{4/5}$(%)	$d_{5/6}$(%)	method[reference]
Pt (001)	-> +2.5					X-ray reflectivity(e)[51]
Pt (100)	+0.8					RBS[52][A]
Pt (111)	+1.5					MEIS(e), T = 420 K[53]
Pt (111)	+1.0					LEED(t) to (e)[54]
Pt (111)	+0.6	-0.9	+0.4			DFT(t)[55]
$Pt_3Fe(111)^*$	-2.9	-0.1	-2.1			DFT(t)[55]
$Pt_3Fe(111)^{**}$	+3.3	-1.9	-0.5			DFT(t)[55]
$Pt_{80}Fe_{20}(111)^*$	+0.9	-1.6	-1.7			DFT(t)[55]
$Pt_{80}Fe_{20}(111)^+$	+1.7	-0.2	-0.8			DFT(t)[55]
Ag (110)	-9.5	+4.3				RBS(e)[56]
Ag (110)	-7.8	+4.3				Ion Scattering(e)[57]
Al (110)	-7	+4	-3	+1		OF-AIMD(DFT)(e)[58][B]
Cu (117)	-13	-2	-10	7	-1	LEED(e)[59]

Notes: $d_{i/j}$: interlayer spacing of layer i and j (i = 1: surface layer) with respect to the bulk value

(e): experiment, (t): theory; **LEED:** low energy electron diffraction, **FLAPW:** full-potential linearized augmented plane wave, **GGA:** generalized gradient approximation, **MEAM:** modified embedded atom method, **DFT:** density functional theory, **RBS:** Rutherford back scattering, **MEIS:** medium energy ion scattering, **OF-AIMD:** orbital free - ab initio molecular dynamics

[A] and nuclear microanalysis, LEED(e), T = 175K

[B] T-dependent lattice spacing simulated, here the data obtained for 70 K is presented

[*] FM (ferromagnetic) configuration

[**] NM (non-magnetic) configuration

[+] AF (antiferromagnetic) configuration

Table 1.1.: Literature overview of theoretical and experimental works on surface multilayer relaxation of Pt, Pt_xFe_{1-x}, Ag, Cu, Al metal surfaces.

system	$d_{1/2}$(%)	$d_{2/3}$(%)	$d_{3/4}$(%)	$d_{4/5}$(%)	$d_{5/6}$(%)	method[reference]
Fe (211)	−10.5	+5.1	−1.7			LEED(e)[36] [A]
Fe (310)	-16.1	+12.6	-4.0			LEED(e)[36] [A]
Fe (210)	-22	-9.5	+10.8	-3.3		LEED(e)[36] [A]
Fe (111)	-15.4					LEED(e)[60]
Fe (110)	+0.5					LEED(e)[61]
Fe (100)	-1.4					LEED(e)[62]
Fe (310)	-13.3	+2.2				FLAPW/GGA(t)[63]
Fe (211)	-10.4	+5.4	-1.3			LEED(e)[64, 65]
Fe (310)	-16.1	+12.6	-4.0			LEED(e)[66]
Fe (210)	-22.0	-11.1	+17	-4.8		LEED(e)[67]
Fe (111)	-16.9	-9.8	+4.2	-2.2		LEED(e)[68]
Fe (111)	-10.5	-16.5	+12.2	+0.5	-6.0	MEAM(t)[69]
Fe (110)	-1.5	+0.1				MEAM(t)[69]
Fe (100)	-1.1	+1.1				MEAM(t)[69]
Fe (110)	-10.5	-16.5	+12.2	+0.5	-6	MEAM(t)[69]
Fe (110)	-0.1	+0.3	-0.5	-0.2	+0.04	DFT(t)[70]
Fe (100)	-3.6	+2.3	+0.4	-0.4	-0.01	DFT(t)[70]
Fe (211)	-9.1	+3.7	-0.5	+0.2	-0.8	DFT(t)[70]
Fe (310)	-15.2	+5.5	-2.9	+2	-3.2	DFT(t)[70]
Fe (111)	-17.7	-8.4	+11	-1	-0.5	DFT(t)[70]
Fe (321)	-18.7	-1.37	+5.41	-3.3	+1.1	DFT(t)[70]
Fe (210)	-23	-5.6	+15.3	-8.2	-2.4	DFT(t)[70]

Notes: $d_{i/j}$: interlayer spacing of layer i and j (i = 1: surface layer) with respect to the bulk value
(e): experiment, (t): theory; **LEED:** low energy electron diffraction, **FLAPW:** full-potential linearized augmented plane wave, **GGA:** generalized gradient approximation, **MEAM:** modified embedded atom method, **DFT:** density functional theory, **RBS:** Rutherford back scattering, **MEIS:** medium energy ion scattering, **OF-AIMD:** orbital free - ab initio molecular dynamics
[A] comparison with theoretical data for $d_{1/2}$ in [35]

Table 1.2.: Literature overview of theoretical and experimental works on surface multilayer relaxation of Fe surfaces.

The theoretically predicted oscillatory behavior has experimentally been proven for many systems over the last decades, see e.g. Table 1 in [71, and references therein]. Experimental and theoretical works especially focusing on Fe, Pt and FePt-alloys are summarized in tables 1.1 and 1.2 (only Fe). Outward relaxation of the surface of up to 3 % is found for Pt and Pt_3Fe(111). For Ag, Cu, Al and Fe surfaces, the first layer relaxes inward and the first layer spacing is contracted with respect to the bulk. These contractions can have enormous magnitudes of up to -22 % in Fe(210) [36, 36]. Oscillatory multilayer relaxations typically in the range of several percents and with different periodicity are observed in all metals. For some Fe surfaces, however, the oscillations of the first three layers show magnitudes which vary by more than ± 10 %. One example is the previously mentioned Fe(210) surface. The large magnitudes are found in both, experiment and theory and consequently cannot be explained by errors but seem to be an intrinsic property of that surface. Besides, it is in good accordance with calculations which predict larger relaxation magnitudes for open surfaces [34, 35].

1.1.2. Surface Relaxation in Magnetic Nanoparticles

Nanoparticles in general are characterized by their large surface to volume ratio. For a sphere or cube of about 2 nm size, 50% of all atoms are surface atoms. Nanoparticles exhibit a surface area composed of different crystalline facets, i.e., surfaces with different "roughness". Thus the question arises, if oscillatory surface layer relaxation can also be observed in metallic (magnetic) nanoparticles. Due to their limited dimensions resulting in interfaces with different facets, missing rows, etc., the surface electronic structure of nanoparticles is different from the bulk. This may result in different surface relaxation behavior which has been investigated theoretically [72] as well as experimentally [73]. Whereas relaxation effects at metallic bulk surfaces can be studied by low energy electron diffraction (LEED) and ion beam scattering, for nanoparticles these methods are not suitable.

Recent developments in High Resolution Transmission Electron Microscopy like the reconstruction of the electron exit wave from focal series of lattice images allow for aberration corrected imaging (see chapter 2.1, p. 33). Atomic column resolved analysis of nanoparticle structures and the study of surface relaxation in small particles became possible. Very few work, however, has focussed on that subject so far. Wang et al. found a 9 % outward surface layer relaxation for FePt icosahedral nanoparticles [74, 75]. Furthermore, a lattice expansion in Fe_xPt_{1-x} nanoparticles has been confirmed by others [16, 76]. Outward relaxation of the first layer and a general lattice expansion has also been observed for Pt-nanoparticles [77]. Whereas Wang et al. [74] attribute the origin of the large outward relaxation to Pt segregation at the surface as also predicted by DFT [78, 79] it is attributed to an amorphous oxide or an dissolution of oxide into the particle by Du et. al [77]. Apart from chemical inhomogeneity in the particle [80], structural properties are also influenced by adsorption of, e.g., H or CO [55]. The latter is important for colloidal nanoparticles, which are stabilized by organic ligands.

Any structural variation from the ideal crystal struture, e.g., due to surface layer relaxation, chemical ordering or chemical inhomogeneities goes along with changes in the magnetic properties [80, 81]. For example, in cubic structures any anisotropic lattice distortion will result in an enhanced orbital contribution to the magnetic moment [81]. In conclusion, the investigation of surface layer relaxation in nanoparticles is mandatory for the understanding of their individual magnetic properties.

1.2. Magnetism

1.2.1. Magnetic Anisotropy

For magnetic materials the magnetic anisotropy energy (MAE) is the energy difference associated with rotating the magnetization from an easy axis (direction of minimum ground state energy) to an hard axis (direction of maximum ground state energy) in a ferromagnet. The only two microscopic sources of MAE, which couple the spin to the lattice [82, 83], are:

- spin-orbit coupling
- dipole-dipole interaction

The exchange interaction $\hat{H} = \sum_{i \neq j} J_{ij} \mathbf{S_i S_j}$ does not contribute to MAE, since it depends only on the relative orientation of the spins to each other and not on their orientation with respect to the lattice. The easy axis is determined by the minimum of the anisotropic part of the free energy density, which in an external magnetic field can be written as the sum:

$$F = F_{Zee} + F_{ex} + F_{an} + F_{el} + F_{mag.el} + F_{\sigma} + F_{d} \tag{1.1}$$

with the following contributions: Zeeman energy $-\vec{M}\vec{B}$ (F_{Zee}), exchange interaction energy (F_{ex}), crystallographic magnetic anisotropy energy (F_{an}), internal elastic energy of the crystal (F_{el}), energy of magnetoelastic interaction ($F_{mag.el}$), energy of external stress - magnetostriction - (F_{σ}) and energy of demagnetizing field - magnetostatic energy - (F_{d}). The magnetic anisotropic contributions to the free energy density depend on different sample characteristics:

1. crystal symmetry (magnetocrystalline anisotropy, Chapter 1.2.1.1)
2. shape (magnetostatic or shape anisotropy, Chapter 1.2.1.2)
3. surface (surface and step anisotropy, Chapter 1.2.1.3)
4. stress (stress/induced anisotropy - by annealing, deformation or irradiation)[3]
5. exchange anisotropy [84] (Chapter 1.2.4)

[3] Induced anisotropy is not discussed explicitly here, since the physical origin is the same as of magnetocrystalline anisotropy - only the atomic positions are slightly different from the ideal crystal.

1.2.1.1. Magnetocrystalline Anisotropy

Magnetocrystalline anisotropy is due to the spin-orbit coupling which is in the range $1.4\,\mu$eV/atom (bcc - Fe) - $65\,\mu$eV/atom (hcp - Co) for the four elemental ferromagnets [85]. When an external field is applied trying to rotate the spin, the orbital momentum also tends to be turned. The orbital momentum itself, however, is strongly coupled to the lattice. Consequently, the spins are coupled to the crystal only via spin-orbit interaction.
P. Bruno [86] showed in a perturbation theory approach, that magnetic anisotropy energy is related to the anisotropy of the orbital moment $\mu_l^{\parallel} - \mu_l^{\perp} = \Delta\mu_l$ and can be written as:

$$\Delta E = \frac{G}{H}\frac{\lambda}{4\mu_B}\Delta\mu_l \tag{1.2}$$

where λ is the spin-orbit-coupling constant and the factor $\frac{G}{H}$ depends on details of the electronic band structure. The magnetocrystalline contribution to magnetic anisotropy usually is phenomenologically expressed as a power series. For uniaxial symmetry, as in case of hexagonal crystal structures, e.g. Co, F_{uni} is calculated as follows:

$$F_{uni} = K_0 + K_2 \sin^2\theta + K_4 \sin^4\theta + ... \tag{1.3}$$

where θ is the angle between the easy axis and the magnetization, see Figure 1.2. For most purposes it is sufficient to keep only the first three terms, where K_0 has no meaning for anisotropy [82]. For cubic crystals, the free energy density can be expanded in powers of the direction cosines $\alpha_{\mathrm{i}} = \frac{\mathrm{M_i}}{\mathrm{M_s}}$ (i = x,y,z). By applying symmetry operations only those terms which leave the energy invariant are kept and the cubic anisotropy is written as[4]:

$$F_{cubic} = K_0 + K_4(\alpha_1^2\alpha_2^2 + \alpha_2^2\alpha_3^2 + \alpha_3^2\alpha_1^2) + K_6(\alpha_1^2\alpha_2^2\alpha_3^2) + ... \tag{1.4}$$

1.2.1.2. Shape Anisotropy

Due to the shape of a magnetic body, there are free poles at the surfaces and in conjunction with that the magnetic strayfield. Inside, this strayfield is compensated by the demagnetization field. The energy associated with the demagnetizing field of the sample is also called magnetostatic energy:

$$E_{ms} = \frac{\mu_0}{2}\int \vec{M}\vec{H}_d dV \qquad (SI), \qquad F_d = \frac{E_{ms}}{V} \tag{1.5}$$

[4] The coefficients of the anisotropy constants are chosen so that they correspond to the order of angular dependence as suggested in [83]. In literature, careful consideration of the K_i is necessary, because different nomenclatures are used, e.g. in cubic systems K_1 and K_2(here: K_4 and K_6, respectively).

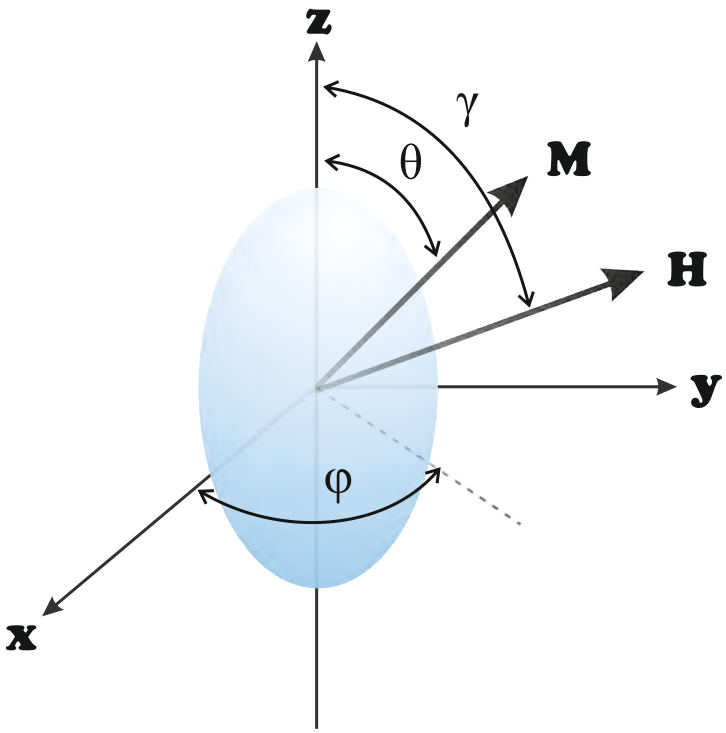

Figure 1.2.: Standard x, y, z coordinate system used to define the orientation of the magnetization with respect to the sample geometry. For ellipsoidal sample shape, the long axis is commonly chosen along the z-direction. θ is the polar angle and φ the azimuth of the magnetization inclined with the sample coordinate system. γ is the inclination of the external magnetic field vector with the z-axis. For thin film systems, the coordinate system is commonly chosen that way, that the x-y-plane is the film plane and the z-direction parallel to the normal vector.

$$\vec{H}_d = \underline{\underline{N}}\vec{M} \tag{1.6}$$

$\underline{\underline{N}}$ is the demagnetization tensor and H_d the demagnetization field, which is anisotropic if the sample is not a sphere. The magnetostatic energy can be straightforwardly written

for samples of ellipsoidal shape since in this case $\vec{H}_d$ is homogeneous inside the body. Its contribution to the magnetic anisotropy density is given by [83, 87]

$$F_d = \frac{E_{ms}}{V} = \frac{\mu_0}{2}(N_x M_x^2 + N_y M_y^2 + N_z M_z^2) \tag{1.7}$$

For the demagnetization factors N_x, N_y, N_z the following relation is fulfilled:

$$N_x + N_y + N_z = 1 \tag{1.8}$$

Due to the rotational invariance, $F_d = 0$ for a sphere ($N_i = 1/3$). Of more practical interest are the ellipsoids of revolution (spheroids). For a prolate spheroid (see Fig. 1.2) the shape anisotropy F_d can be calculated as follows:

$$F_d = \frac{1}{2}[(M\cos\theta)^2 N_z + (M\sin\theta)^2 N_x] = \frac{1}{2}M^2 N_z + \frac{1}{2}(N_x - N_z)M^2\sin^2\theta \tag{1.9}$$

Consequently the shape anisotropy constant K_d is given by $\frac{1}{2}(N_x - N_z)M^2$ or $\frac{1}{2}(\Delta N)M^2$. Considering an infinite thin film (in x-y plane), only the z-component of the demagetization tensor is non-zero and according to equation 1.8 $N_z = 1$. Using equation 1.7, the shape anisotropy of a thin film is:

$$F_d = \frac{E_{ms}}{V} = \frac{\mu_0}{2}M_z^2 \tag{1.10}$$

If the "infinitely" thin film consists of close-packed magnetic nanoparticles the formula is modified by a filling factor f, which considers the volume of single separate nanoparticles with respect to the volume of a continuous layer [88]:

$$F_d = \frac{E_{ms}}{V} = \frac{\mu_0}{2}fM_z^2 \tag{1.11}$$

1.2.1.3. Surface Effects and Effective Anisotropy

When decreasing the particle size, the fraction of the surface with respect to the whole volume increases. Due to the lower coordination number, atomic step or terrace structures or different lattice spacing at the surface (as will be discussed later in Chapter 4, p. 53 ff.) the electronic structure and magnetic interactions at the surface might differ significantly from the volume. Consequently, there will be additional contributions to the magnetic anisotropy[5]. Although, the shape of a nanoparticle in first order is often approximated by a sphere, the surface is built up by different facets as it is illustrated in Figure 1.3 for a typical truncated octahedral shape. According to Wulff's theorem this is the equilibrium shape of fcc clusters and the surface of those particles is build up by six (100)- and eight (111)-facets[6]. Consequently, the local coordination number of

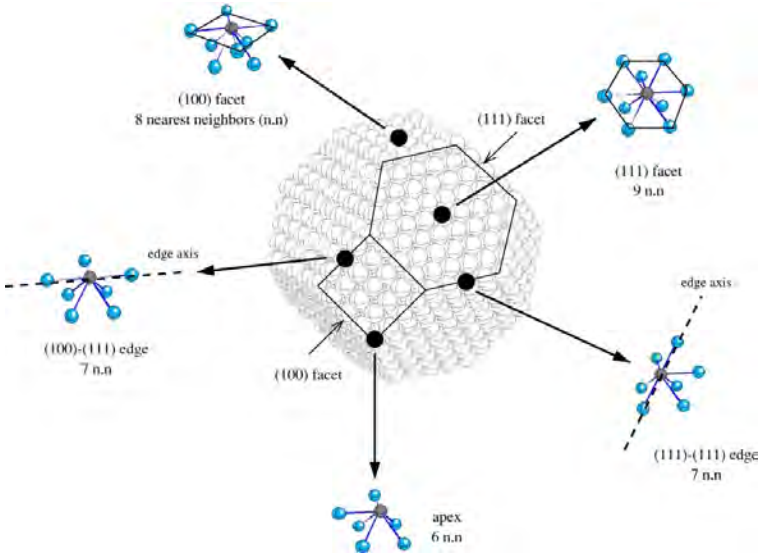

Figure 1.3.: Surface atomic positions on a perfectly truncated octahedral nanoparticle consisting of 1289 atoms [89]. Depending on the position, the number of next neighbors varies from 6(apex) - 9((111)-facet).

[5] In case of a thin film, there are also contributions from the interface of film and substrate which cannot be discriminated by most measurements. Therefore an effective anisotropy constant expressing the average over both surfaces by $2K_{si}$ is used and for a thin film of thickness d [83]:

$$K = K_v + \frac{2K_{si}}{d} \tag{1.12}$$

[6] As will be shown in chapter 4, in nature the nanoparticles often exhibit also (110)-surfaces, although they are not energetically favorable.

the atoms at the edges, corners or within the facets varies strongly resulting in different local surface anisotropies. Furthermore, the facets are not necessarily smooth and may contribute to the total magnetic anisotropy by step anisotropies. In a phenomenological model based on Néel's anisotropy model [90] - which is also widely used for magnetic thin films - magnetic anisotropy at a given surface atom can be calculated by summing up all the next neighbors pair interactions $L(\vec{m}\cdot\vec{r}_{ij})^2$[89, 91][7] and the surface anisotropy energy for the whole particle is given by:

$$E_{surf} = \frac{L}{2}\frac{\sum_{i,j}(\vec{m}\cdot\vec{r}_{ij})^2}{\|\vec{r}_{ij}\|^2} \tag{1.14}$$

All volume and surface anisotropy contributions sum up to an effective anisotropy, which in first order is assumed to be uniaxial, and is expressed by the effective anisotropy constant K_{eff}[8]. In the case of a sphere with diameter d [92]:

$$K_{eff} = K_v + \frac{6}{d}K_{surf} \tag{1.15}$$

The equation clearly shows the increasing importance of surface anisotropy with decreasing particle diameter.

Experimental Determination of Anisotropy Constants

Anisotropy constants can experimentally be determined by different methods, e.g. by torque curve measurements, Torsion pendulum, magnetometry or by magnetic resonance techniques [87]. In this work magnetometry, i.e. the recording of hysteresis loops, in form of XPEEM employing the XMCD effect and and SQUID magnetometry, was utilized.

[7] L is the Néel constant and depends on the interatomic distance r according to:

$$L(r) = L(r_0) + \left(\frac{dL}{dr}\right)_{r_0} r_0\eta \tag{1.13}$$

r_0 and η are the unstrained bond length in the bulk and the bond strain, respectively. $L(r_0)$ and $\left(\frac{dL}{dr}\right)_{r_0} r_0$ for free metal surfaces can be expressed dependent on magnetostriction and elastic constants - for fcc and bcc crystals see e.g. [91]. Due to this dependence of L on the interatomic distance also effects of surface strains are included in the model which can be applied for the study of nanoparticles consisting of a few thousand atoms.

[8] In a macroscopic treatment of particles (many particle system) also dipolar interactions between the particles may be included.

1.2.2. Magnetic Nanoparticles Related Phenomena

1.2.2.1. Superparamagnetism and Blocking Temperature

Magnetic Anisotropy induces an energy barrier in the free energy landscape which is given by the product of K_{eff} and the volume V of the particle:

$$\Delta E = K_{eff} V \tag{1.16}$$

In Figure 1.4 this is schematically illustrated for a particle with uniaxial anisotropy and

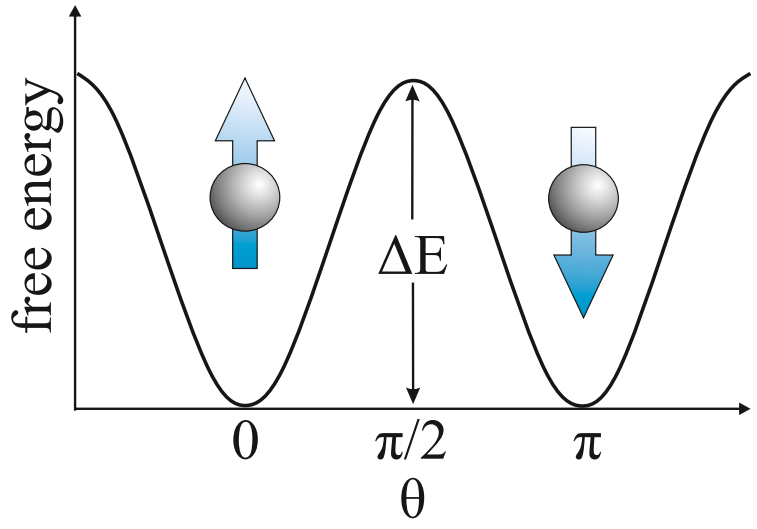

Figure 1.4.: Free energy of a magnetic nanoparticle with uniaxial anisotropy in zero external field as a function of the angle θ between magnetization and the easy axis of magnetization.

the easy axes along the z-direction. Without any external magnetic field, the magnetization points along an easy axis, either up or down. If the thermal energy $k_B T$ is of the same magnitude or larger than the energy barrier ΔE, the magnetization within the particle is no longer stabilized but fluctuates. Néel [93] performed calculations for the relaxation time τ. Assuming uniaxial anisotropy and a uniform rotation of coupled spins he calculated for $k_B T >> K_{eff} V$ (isotropic superparamagnetic limit):

$$\tau = \tau_0 \exp\left[\frac{\Delta E}{k_B T}\right] = \tau_0 \exp\left[\frac{K_{eff} V}{k_B T}\right] \tag{1.17}$$

where the characteristic time τ_0 depends on the relaxation path[9]. Typical values are in the range $10^{-12} - 10^{-9}s$. In the isotropic superparamagnetic limit the field and temperature dependent magnetization behavior of an ensemble of *single-domain* particles can be treated in the same way as an ensemble of magnetic moments by Langevin paramagnetism[10]:

$$\frac{M}{M_s} = \coth x - \frac{1}{x} = \mathrm{L}(x) \quad , \quad x = \frac{M_s V B}{k_B T} \tag{1.18}$$

The only difference is, that not atomic spins but "macro-spins" with magnetization M consisting of up to $\sim 10^5$ atoms[11] are considered. That has lead to the expression *superparamagnetism* (SPM) [96]. In the limit of small fields ($x \leq 1$) $\coth x$ can be expanded in a Taylor-series. In this approximation and for ($x \leq 0.5$) $L(x)$ is a straight line with slope of $\frac{1}{3}$ and thus:

$$\frac{M}{M_s} = \frac{x}{3} \tag{1.19}$$

When the particle system is cooled down, the fluctuations slow down and thus τ increases. The systems exhibits a quasi static behavior when the probing time of the measurement τ_m is in the range of τ or shorter. It seems to be blocked and according to equation 1.17 a blocking temperature T_b can be defined, which is characteristic for the time scale of the measurement:

$$T_b = \frac{K_{eff} V}{k_B \ln \frac{\tau_0}{\tau}} \tag{1.20}$$

The shorter the probing time, the higher T_b, i.e. depending on the measurement technique different blocking temperatures are determined for the same systems. This is schematically illustrated in Figure 1.5 which shows simulated ZFC-magnetization curves for SQUID ($\tau = 100\,\mathrm{s}$) and FMR ($\tau = 10^{-9}\,\mathrm{s}$) measurements. If there was no volume distribution $D(V)$ within a particle ensemble, the magnetization would drop to zero at T_b. $D(V)$ however, leads to an outsmearing of this edge and the peak of maximum magnetization is shifted to higher temperatures. In literature, however, this effect is often neglected, and the blocking temperature is determined by the maximum magnetization and is thus too high.

[9] and other parameters like the longitudinal magnetostriction constant and Young's modulus. The spin system was treated in a gyroscopic approach; verifying that approach Brown's model [94] allows the determination of τ for any anisotropy energy [95].

[10] Note that the particle ensemble is treated as paramagnetic although the system is still below its Curie-Temperature.

[11] The maximum number of atomic spins in a macro-spin is given by the monodomain limit.

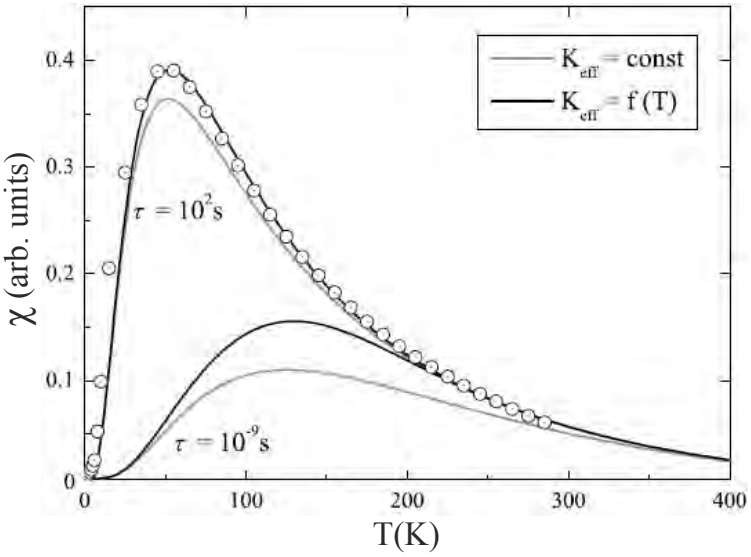

Figure 1.5.: Experimental (circles) and simulated zero field curves of low field susceptibility χ as obtained by different measurement techniques (τ is the time window of the measurement) assuming both temperature dependent and independent effective anisotropy [97].

1.2.2.2. Single Domain Limits

The single domain limit for a spherical particle with uniaxial anisotropy energy density K_u is for 90° and 180° domain walls with energy σ_w given by the critical radius [98]:

$$r < \frac{9\sigma_w}{\mu_0 M(T)^2} \tag{1.21}$$

And for the stability of 1 year ($\tau = 31.536 \times 10^6 s$) the critical parameter for superparamagnetic behavior is calculated as [82]:

$$r_c \approx \left(\frac{9k_B T}{K_u(T)}\right)^{1/3} \tag{1.22}$$

Kittel calculated the critical diameter of a cube using the demagnetization factors of a sphere, which are identic to those of a cube along the main axis, as a rough assumption [99]: Considering a single cube of length L having only one domain, i.e. all atomic

magnetic moments pointing into one direction. This configuration has large stray field components at the edges of the cube and the magnetic energy is given by

$$F \cong (2\pi/3)M_s^2 L^3 \quad (CGS) \tag{1.23}$$

where the effective demagnetization factor has been taken as $4\pi/3$ (CGS), the value for a sphere [99]. In case of an internal flux closure the magnetic energy is zero. According to Kittel the domain wall energy σ_w and the anisotropy energy density K_{eff}, which is relatively small, can be expressed as follows:

$$F_w = \sigma_w 2\sqrt{2}L^2 \quad and \quad F_a = \frac{K_{eff}}{L^3/2} \quad (CGS) \tag{1.24}$$

If the exchange stiffness constant A and the uniaxial magnetic anisotropy energy coefficient K_u are known σ_w can be calculated for Bloch/Néel walls according to the following two equations [82]:

$$\sigma_w^{Bl} = 4(AK_u)^{1/2} \tag{1.25}$$

$$\sigma_w^{N} = 2\pi(AK_u)^{1/2} \tag{1.26}$$

$A = (1-2) \times 10^{-11}\,\mathrm{J/m}$ (SI)[12] are typical exchange stiffness values for ferromagnetic materials. Often only experimental values for the spin-wave exchange stiffness constant D can be found in literature. In case of exclusive next neighbor interactions, that is for sc, bcc, fcc and hcp lattices, A and D are related by

$$A = \frac{D\rho_a\mu_a}{2g\mu_B} \tag{1.27}$$

with ρ_a and μ_a being the atomic density and the atomic magnetic moment, respectively, and $\rho_a\mu_a = M_s$ [100]. g is the g-factor.
The flux closure configuration becomes energetically favorable, if the magnetic energy of the single domain state exceeds the sum of wall and anisotropy energy which are due to formation of the domain walls. A few simple mathematical transformations lead to the critical length L_c:

$$L_c = \frac{2\sqrt{2}\sigma_w}{(2\pi/\sqrt{3})M_s^2 - K_{eff}/2} \tag{1.28}$$

K_4 (used for K_{eff} here) of bcc Fe at room temperature is $4.8 \times 10^4\,\mathrm{J/m^3}$ (SI)[13] [82]. Assuming a Bloch wall and $A = 10^{-6}\,\mathrm{erg/cm}$, σ_{dw} is $1.6\sqrt{3}\,\mathrm{erg/cm^2}$ (eqn. 1.25). The resulting critical length is $1.348 \times 10^{-6}\,\mathrm{cm} = 13.48\,\mathrm{nm}$. For ferrimagnetic materials

[12] $(1-2) \times 10^{-6}\,\mathrm{erg/cm}$ (CGS)
[13] $4.8 \times 10^5\,\mathrm{erg/cm^3}$ (CGS)

no standard values for A are known. For magnetite it can be calculated to $8.648 \times 10^{-12}\,\mathrm{J/m\,(SI)}$[14] using $g = 2.20$ [101], $D = 71 \times 10^{-41} Jm^2$ [102, and references therein]. With $\mathrm{M_s} = 497 \times 10^3\,\mathrm{A/m\,(SI)}$[15] and $\mathrm{K_{eff}} = 5 \times 10^4\,\mathrm{J/m^3\,(SI)}$[16], the critical length is $2.783 \times 10^{-5}\,\mathrm{cm} = 278.3\,\mathrm{nm}$. For this calculation mean values of M_s and K_{eff} were used [$\mathrm{M_s} = (476.76 - 518) \times 10^3\,\mathrm{A/m}$ and $\mathrm{K_{eff}} = (10^4 - 10^5)\,\mathrm{J/m^3}$, cf. table D.1]. Using smaller and larger values, respectively, the critical length for magnetite can be in the range from below 100 nm to more than 1 μm.

1.2.2.3. Size Dependence of Coercive Field

Decreasing the size modifies the characteristic properties of materials (size effects). The size dependence of the coercive field H_c is illustrated in Figure 1.6 for a fixed temperature. H_c increases with decreasing particle diameter d, until it reaches a maximum at a diameter d_{sd} and then it further decreases to zero. This maximum in coercivity is related to the transition from the multi-domain to the single-domain state. The latter becomes energetically favorable, if the magnetostatic energy of the single domain state is lower than the sum of domain wall and anisotropy energy. Depending on material and shape of the particles critical diameters for single domain particles have a large variety. Typical values for critical radii r_{sd} (see chapter 1.2.2.2) are for example 15 nm (Fe), 35 nm (Co) and 750 nm ($SmCo_5$) [95]. When the particle diameter decreases further, the coercivity decreases as well due to thermal fluctuations. Until the second critical diameter d_{SPM} the magnetization in the particle is stable. Reaching d_{SPM} the thermal effects are now strong enough to spontaneously demagnetize the particles and thus coercivity vanishes completely for smaller particle diameters. The particles are now in the SPM state. For lower T, d_{SPM} also decreases.

1.2.2.4. Magnetic Dipolar Coupling

Whenever specific magnetic particle configurations (ensembles) or samples with high particle density are probed, magnetic dipolar coupling has to be considered. The interaction energy for magnetic moments (dipoles) $\vec{\mu}_{i,j}$ at distance $\vec{r}_{ij}$ with $r_{ij} = |\vec{r}_{ij}|$ is:

$$E_{dip} = \frac{\mu_0}{4\pi r_{ij}^3}\left[\vec{\mu}_i \cdot \vec{\mu}_j - \frac{3(\vec{r}_{ij} \cdot \vec{\mu}_i)(\vec{r}_{ij} \cdot \vec{\mu}_j)}{r_{ij}^2}\right] \tag{1.29}$$

Assuming a magnetic moment of $|\vec{\mathrm{m}}| = 1\mu_\mathrm{B}$ and a distance of r = 0.1 nm yields a dipolar potential energy in the order of 10^{-23} J or 1 K in temperature and can safely be neglected for magnetic ordering. However, for particles with a diameter of several nm, the magnetic moments can be in the order of $10^5 \mu_B$ and thus the dipole energy in

[14] $8.648 \times 10^{-7}\,\mathrm{erg/cm(CGS)}$
[15] $497\,\mathrm{emu/cm^3}$ (CGS)
[16] $5 \times 10^5\,\mathrm{erg/cm^3}$ (CGS)

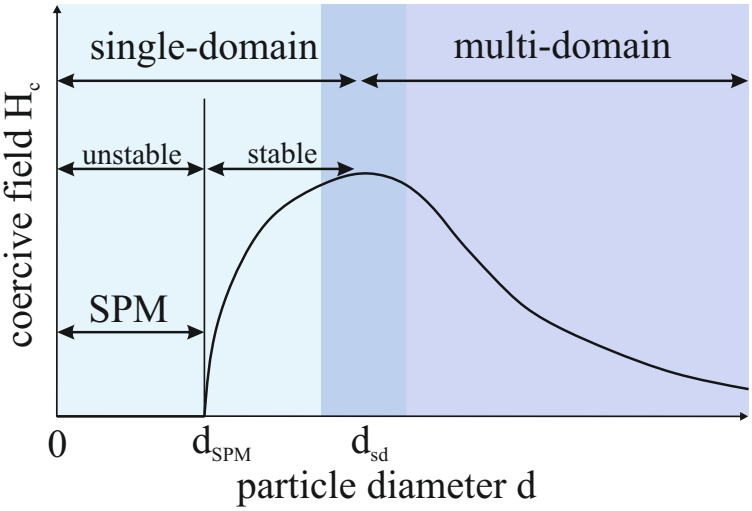

Figure 1.6.: Coercive field dependence on the particle diameter according to [87]. Particles with diameter $d > d_{sd}$ are in a multi domain state. They reverse their magnetization via domain wall motion (section 1.2.3.3, p. 24) [103]. Around the critical diameter d_{sd} the domain configuration within a particle changes from the multi- to the single-domain state. In the latter, magnetization reversal occurs via different mechanisms of spin rotation [87] (sections 1.2.3.1 and 1.2.3.2, p. 19 ff.). The coercivity reaches its maximum in this range. For smaller d the magnetization in the particle is stable and shows hysteresis, however, the coercivity is continuously decreasing until it vanishes at the second critical diameter d_{SPM}, at which M is not stable any longer, and it exhibits superparamagnetic (SPM) behavior.

the range of several tens of Kelvins [104]. Consequently, magnetic dipolar interactions influence the blocking temperature. Experiments on macroscopic ensembles have shown, that different particle configurations and compositions display opposite shifts of T_b [31] and a clear theoretical understanding has not been reached so far [32].

1.2.3. Magnetization Reversal

Typically, one talks about the "switching" of the magnetization when reversing the magnetization in a sample from one direction into the opposite. But this terminology is misleading since it suggests a direct reversal, which is generally not the case. Whenever a magnetic field is applied to a magnetized sample a torque is induced forcing the magne-

tization to precess towards the new equilibrium position. This time dependent variation of the magnetization is mathematically described by the Landau-Lifshitz equation:

$$\frac{d\vec{M}}{dt} = -\gamma \left[\vec{M} \times \vec{B}_{eff}\right] + \alpha \frac{\gamma}{M_s} \left[\vec{M} \times \left(\vec{M} \times \vec{B_{eff}}\right)\right] \tag{1.30}$$

where B_{eff} is the sum of all acting fields, like external, internal and possible rf-fields, α the damping parameter and the gyromagnetic ratio $\gamma = g\frac{\mu_B}{\hbar}$ (g is the g-factor). More details on magnetic relaxation can be found for example in [105, 106, and references therein].

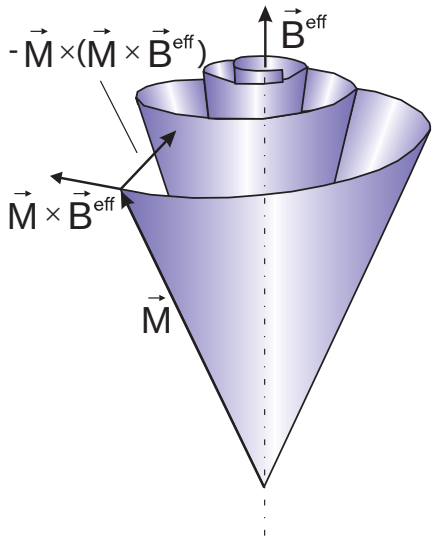

Figure 1.7: Precession of magnetization including damping according to eqn. 1.30 [105, 107]

In the next sections different modes of magnetization reversal are discussed according to [87, 108]. Small single domain particles (see single domain limit, chapter 1.2.2.2) are expected to switch magnetization via uniform rotation, whereas for larger ones other reversal mechanisms as curling, fanning or domain wall motion occur.

1.2.3.1. Uniform Rotation - Stoner Wohlfarth Model

Magnetization reversal in a single domain particle has been treated in the simplest classical model by Stoner & Wohlfarth and Néel [109, 110]. In this model, all magnetic moments are collinear due to the exchange energy forming a so called "macro-spin". The energy balance is given by the anisotropy energy K_2V, which in this model is assumed to be purely uniaxial and the Zeeman energy due to the applied field H:

$$E = K_2 V \sin^2(\theta) - \mu_0 M_s V H \cos(\gamma - \theta) \tag{1.31}$$

where γ and θ are the angles of applied field and magnetization with respect to the easy axis of magnetization (see also Fig. 1.2), K is the anisotropy energy density and V the volume of the particle. The potential energy has two minima at $\theta = 0$ and $\theta = \pi$ separated by an energy barrier for H = 0 (Fig. 1.4). A change of H and γ changes the energy landscape, the magnetization will rotate towards the angle θ which locally minimizes the energy E, according to θ, i.e. $\frac{\partial E}{\partial \theta} = 0$. The minimum field at which the energy barrier vanishes defines the reversal field, i.e. $\frac{\partial E}{\partial \theta} = \frac{\partial^2 E}{\partial \theta^2} = 0$. Its angular dependence is:

$$h_{sw}^0 = \frac{H_{sw}^0}{H_a} = \frac{1}{\left(\sin^{2/3}\gamma + \cos^{2/3}\gamma\right)^{3/2}} \tag{1.32}$$

where H_{sw}^0 is the switching field, or in dimensionless units: $\mathrm{h_{sw}^0} = \frac{\mathbf{H_{sw}^0}}{\mathbf{H_a}}$. $\mathrm{H_a}$ is the anisotropy or nucleation field $\frac{2\mathrm{K_2}}{\mu_0 \mathrm{M_s}}$. The corresponding plot is shown in Fig. 1.8 a. Due to the specific shape these curves are also called *Stoner-Wohlfarth astroids*. The corresponding hysteresis loops (Fig. 1.8 b) are extracted by determining the component of magnetization projected along the field direction, i.e. $M_H = M_s \cos(\gamma - \theta)$.

As mentioned above, this is a very simple model and is very limited in application. Real systems are more complex, including additional non-uniform magnetocrystalline, magnetoelastic and surface anisotropies. Thiaville [111, 112] generalized the Stoner-Wohlfarth model including higher-order effective anisotropies. The magnetic anisotropy energy within this macro-spin ($\mathbf{m}$) model is given by:

$$E_0(\mathbf{m}) = E_d(\mathbf{m}) + E_{an}(\mathbf{m}) + E_{surf}(\mathbf{m}) + E_{mag.el}(\mathbf{m}) \tag{1.33}$$

where the different contributions can be expanded into power series: Shape anisotropy (E_d) as biaxial anisotropy (2 second order terms), magnetocrystalline (E_{an}) as either uniaxial (second order term) or cubic (second and forth order terms) and the magneto elastic ($E_{mag.el}$) and surface (E_{surf}) anisotropy as second order terms. Thiavilles model also predicts the energy barrier height ΔE close to the switching field, i.e. $\epsilon = 1 - \left(\frac{\mathbf{H}}{\mathbf{H_{sw}^0}}\right) << 1$ which is important for temperature dependent measurements [108]. For the cases (1), (2) and (3) as indicated in Fig. 1.8 a ΔE is:

(1)	(2)	(3)
$\Delta E = E_0 \epsilon^{3/2}$	$\Delta E = E_0 \epsilon^3$	$\Delta E = E_0 \epsilon^2$

Table 1.3.: Energy barrier hight close to the switching field for γ at positions (1), (2) and (3) as marked in Fig. 1.8 a. E_0: Magnetic anisotropy energy.

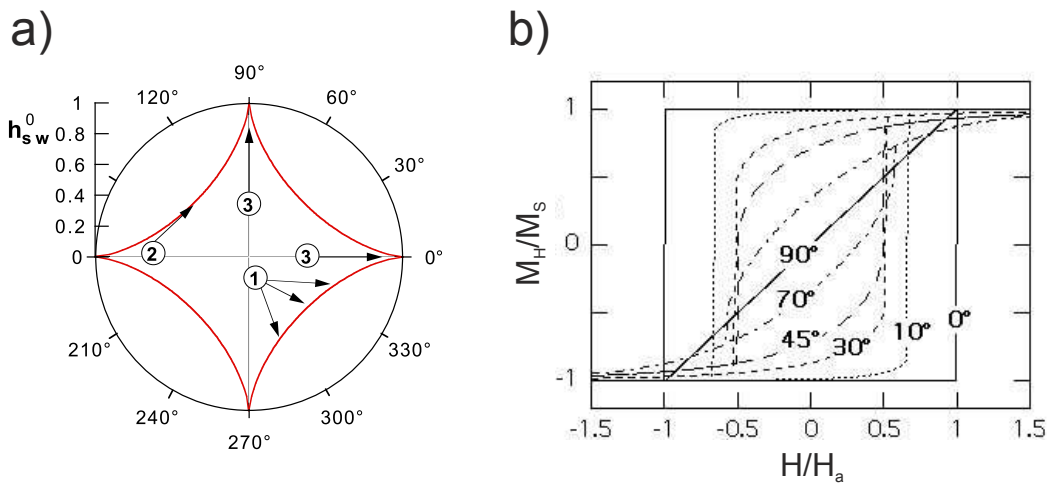

Figure 1.8.: (a) Stoner Wohlfarth Astroid: Angular dependence of the Stoner Wohlfarth switching field h^0_{sw} . (1) - (3) mark special points on the critical curve of the switching field (red line) and are discussed in detail in [108, 111, 112]. (2) indicates a point, at which the field direction is vertical to the critical surface of the switching field (e.g. for $\gamma = 135°$ as marked here), (3) corresponds to the cusp points (for the astroid shown here: the magnetic field is aligned either parallel or perpendicular to the easy axis). Eqns. 1.34 and 1.35 and those in table 1.3 give the energy barrier barrier hight close to the switching field for cubic and uniaxial anisotropy, respectively, for cases (1) - (3). (b) Stoner Wohlfarth hysteresis loops for different values of γ. The M-component along the field direction is plotted [projection of M onto field axis: $M_H = M_s \cos(\gamma - \theta)$]. Adapted from [108].

In the case of the 2D Stoner-Wohlfarth model with uniaxial anisotropy the equation for cases (1) and (3) become:

$$\Delta E = 4K_u V \left(\frac{2}{3}\right)^{3/2} \frac{|\cos\gamma|^{1/3}}{1+|\cos\gamma|^{2/3}} \epsilon^{3/2} \qquad (1) \tag{1.34}$$

$$\Delta E = K_u V \left(1 - \frac{H}{H_a}\right)^2 \quad , \qquad 0 \le H \le H_a \qquad (3) \tag{1.35}$$

Cubic Anisotropy

In the 2D approach and cubic anisotropy eqn. 1.31 can be rewritten:

$$E = E_0 - \mu_0 V M_s (H_x \cos\theta + H_y \sin\theta) \tag{1.36}$$

where

$$E_0 = V K_2 \sin^2(\theta + \theta_0) + V K_4 \sin^2\theta \cos^2\theta \tag{1.37}$$

and V are the volume, M_s the saturation magnetization and K_2 and K_4 anisotropy constants, e.g. shape and cubic crystalline anisotropy. θ_0 is a constant allowing for turning one anisotropy contribution with respect to the other one. The locus of the critical switching fields can be parameterized as:

$$H_x = -\frac{1}{2\mu_0 V M_s}\left(\sin\theta\frac{\partial E}{\partial\theta} + \cos\theta\frac{\partial^2 E}{\partial\theta^2}\right) \tag{1.38}$$

$$H_x = +\frac{1}{2\mu_0 V M_s}\left(\cos\theta\frac{\partial E}{\partial\theta} - \sin\theta\frac{\partial^2 E}{\partial\theta^2}\right) \tag{1.39}$$

In contrast to the Stoner-Wohlfarth astroid for uniaxial anisotropy (Fig. 1.8 a), this curve can cross itself several times and the the switching field depends on the path of the applied field [108].

1.2.3.2. Fanning and Curling

Magnetic measurements for elongated Fe particles yielded intrinsic coercive fields H_{ci} which were too large to be explained by magnetocrystalline anisotropy $[\frac{2K}{M_s}]$ and too small for shape anisotropy $[(N_a - N_c)M_s$, where N_a is the demagnetizing factor along the short and N_c along the long axis] [113]. Since coherent rotation could not explain the observed reversal [87] incoherent reversal modes like *fanning* and *curling* had to be introduced.

Fanning

Two incoherent reversal processes of the magnetization have been discussed by Jacobs and Bean in the *chain of spheres* model [114]. Each sphere is assumed to have no anisotropy on its own and all spins, i.e. the magnetization, rotate coherently. Two reversal mechanism were considered: (A) symmetric fanning, i.e. magnetization vectors of successive spheres fan out in a plane by rotating in alternate directions and (B) coherent rotation, i.e. magnetization vectors in all spheres are always parallel (Fig. 1.9). The magnetostatic energy between two dipoles $E_{ms} = \frac{\mu_1\mu_2}{r^3}[\cos(\theta_1 - \theta_2) - 3\cos\theta_1\cos\theta_2]$ (Fig. 1.9 D) and the resulting intrinsic coercive fields calculated for scenarios A and B

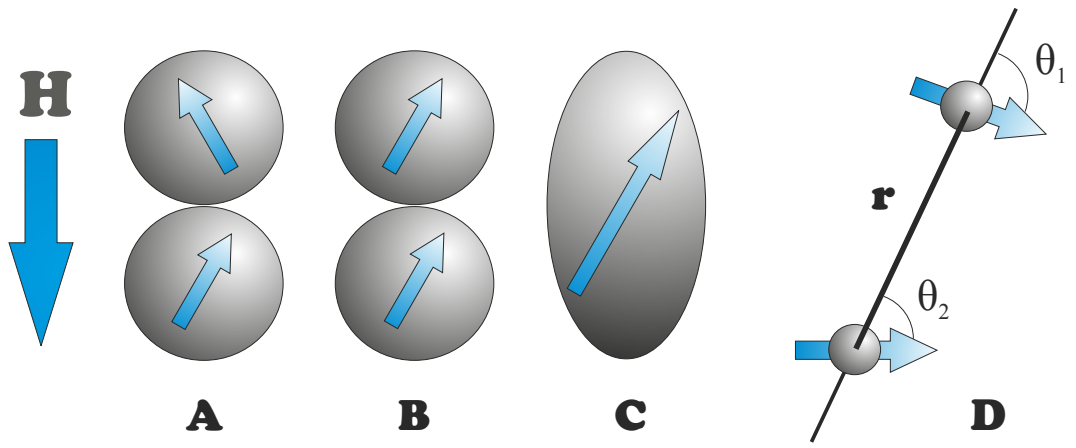

Figure 1.9.: Two-sphere chains with fanning (A) and coherent rotation mode (B) in accordance to [87, 114]. (C): Prolate spheroid with same c/a-ratio as the two-particle chains. H is the direction of the applied magnetic field for particle configurations in (A) - (C). (D): Sketch of two dipoles at distance r. For scenario A $\theta_1 = \theta, \theta_2 = -\theta$ and $\theta_1 = \theta_2 = \theta$ for scenario B.

are shown in Table 1.9. H_{ci} for scenario C (coherent rotation) is $2\pi M_s$ for $c/a = \infty$. The fanning mode yields 12 times smaller values.

mode	E_{ms}	H_{ci}
A	$\frac{\mu^2}{d^3}(1+\cos\theta^2)$	$\frac{\mu}{d^3} = \frac{\pi M_s}{6}$
B	$\frac{\mu^2}{d^3}(1-3\cos^2\theta)$	$\frac{3\mu}{d^3} = \frac{\pi M_s}{2}$
C	-	$\leq 2\pi \mathrm{M_s}$*

d: sphere diameter, $\mu = \mathrm{M_s}\left(\frac{4\pi}{3}\right)\left(\frac{\mathrm{d}}{2}\right)^3$, * $0.5\,\mathrm{M_s}$ (SI)

Table 1.4.: Mutual potential (magnetostatic) energy E_{ms} and coercive field H_{ci} for magnetization reversal modes as indicated in Fig. 1.9.

Curling

Another mode of non-uniform reversal is the curling mode. For a prolate spheroid (Fig. 1.2) with an initial magnetization along the + z-axis is and an applied magnetic field along the - z-axis the spins are forced to rotate about the radius in the x-y-plane. In the middle of the reversal process all spins lie in that plane and form a circular flux closure pattern to reduce the magnetostatic energy. $\mathrm{E_{ms}}$ vanishes completely at this

point if the axial ratio of the spheroid approaches infinity, approximated by an infinite cylinder. Here, the spins are alway parallel to the surface, i.e. no free poles at the surface and thus no contribution of magnetostatic energy. And, the energy difference between the coherent and the curling reversal mode is given only by the exchange energy. For smaller axial ratios c/a the magnetostatic energy will also play a role, since the spins are no longer always parallel to the surface. A critical parameter is the exchange length $\lambda = \sqrt{\mathrm{A}}/\mathrm{M_s}$ (A: exchange constant). When for example the radius r of a cylinder is larger than λ, magnetization reversal via curling is more favorable. An analytic result for an ellipsoid of rotation which can be approximately applied to most nanoparticles and nanowires is reviewed in [108]. According to [87] the reduced intrinsic coercivities h_{ci} for an infinite cylinder, a prolate spheroid and a sphere are given by:

$$h_{ci} = \frac{H_{ci}}{2\pi M_s} = \left(\frac{1.08}{r/\lambda}\right)^2 \quad \text{(infinite cylinder)} \tag{1.40}$$

$$h_{ci} \geq \frac{N_c}{2\pi} - \left(\frac{k}{r/\lambda}\right)^2 \quad \text{(prolate sheroid, r = a)} \tag{1.41}$$

$$h_{ci} \geq \frac{2}{3} - \left(\frac{1.39}{r/\lambda}\right)^2 \quad \text{(sphere)} \tag{1.42}$$

where k depends on the axial ratio and can have values $1.08 < k < 1.39$. The latter equation is only valid for $r/\lambda > 1.44$ defining a critical radius of $1.44\,\lambda$. Since the intrinsic coercivity for the curling mode is strongly size dependent (decreases with increasing size) and for coherent rotation and fanning it is not, larger particles will reverse by curling.

1.2.3.3. Domain Wall Motion

For particles exceeding the critical single domain size, i.e. diameter (compare also section 1.2.2.2) the magnetization reversal can occur via nucleation and annihilation of domain walls within the particle. The condition for the nucleation of a domain wall in a single particle is, that the sum of applied field H_a and the demagnetizing field H_d is larger than $2K_c/M_s$. If H_d, M_s are larger or K_c smaller than expected for a perfect crystal, H_a can be quite small. M_s may be different in the vincinity of e.g. interstitials and vacancies and the local anisotropy is determined by the local symmetry of the crystal field that is dependent on the arrangement and type of neighboring atoms. Local variations of H_d, however, are usually assumed as domain wall nucleators [87]: For example, at sharp corners, as in cubes, H_d can exceed M_s, the maximum value for a spheroid (SI). Detailed discussion about domain walls and magnetization loops correlated with domain wall nucleation and annihilation has been given by Hubert and Schäfer [103].

1.2.4. Exchange Bias

In this chapter the phenomenon of exchange bias (EB) in ferro/antiferromagnetic (FM/AFM) systems is discussed for the case that the Néel temperature $T_N <$ the Curie temperature T_C. EB was discovered in 1956 by Meiklejohn and Bean on oxide-coated Co-nanoparticles [115, 116]: The hysteresis measured after field cooling below T_N of the AFM was shifted opposite to the cooling field direction. A new type of magnetic anisotropy was suggested as the origin of this effect, called *exchange anisotropy*. It is unidirectional, as manifested by torque curves being proportional to $\sin\theta$ and not to $\sin 2\theta$ as for uniaxial material like pure Co [17][115]. This unidirectional anisotropy (K_{ud}) acts as an effective field which shifts the hysteresis by the exchange bias field $H_e = \frac{K_{ud}}{M_s}$ along the field axis:

$$H_{eff} = H - \frac{K_{ud}}{M_s} = H - H_e \tag{1.44}$$

Since its discovery, the effect has been intensively studied and has also been found in in both ferri-ferromagnetic and ferri-antiferromagnetic systems. Several models to explain this effect (see e.g. Fig. 1.10) have been discussed in literature.

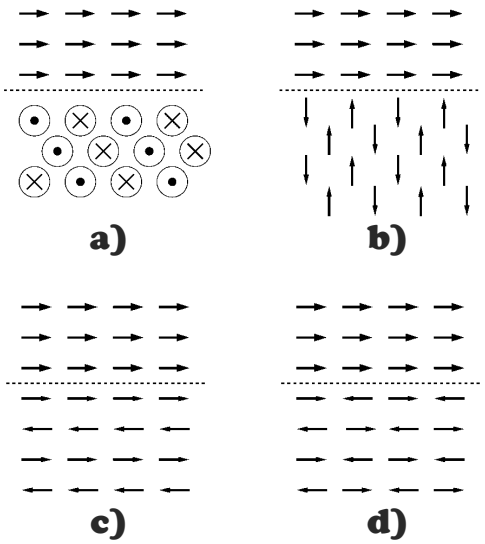

Figure 1.10: Different magnetic FM/AFM interface alignments. (a), (b) noncollinear spin alignment, (c), (d) trivial collinear magnetic structure. Adapted from [117].

[17] In addition, non-vanishing rotational hysteresis

$$W_{rot} = \frac{1}{2}\int_0^{2\pi} R\mathrm{d}\theta \quad , \quad [W_{rot}] = \frac{(\mathrm{ergs/cycle})}{\mathrm{cm}^3} \tag{1.43}$$

was found for high fields larger than $\frac{2K}{M_s}$ for the ferromagnetic component. The rotational torque R is determined by fitting the difference of clockwise and counterclockwise measured torque curves.

General reviews can be found in [84, 117–119], reviews focusing on nanostructures can be found in [120, 121]. Applications based on the EB effect are: hard magnets in recording media, flux amplifiers for magnetic resonance settings and recently also spin valves and magnetic tunnel junctions based on the GMR[18].

Figure 1.11 shows a FM/AFM bilayer system at a temperature below T_C of the FM but above T_N, i.e. the spins of the FM align parallel to H, whereas the spin orientations in the AFM are random.

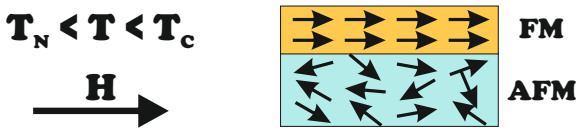

Figure 1.11.: FM-AFM bilayer sample structure at $T_N < T < T_C$. The spins of the FM are aligned into the field direction, whereas the spin configuration in the AFM is still random, i.e. paramagnetic.

In the following EB is described in a very simple intuitive picture according to [120]. For ferromagnetic coupling at the FM/AFM interface all spins of the AFM-bilayer align parallel to the magnetization direction of the FM when the sample is field-cooled through T_N as shown in Fig. 1.12 (1).

Reversing the field leads to a rotation of the spins in the FM whereas those of the AFM are fixed, if the AFM anisotropy K_{AFM} is strong enough. As indicated in Fig. 1.12 (2) they exert a torque on the spins of the FM trying to keep them in their original orientation due to the ferromagnetic coupling. Therefore, the field to reverse the magnetization of the FM is higher than for a non-coupled system. This additional energy needed to overcome the torque leads to a higher coercive field in the opposite cooling direction [Fig. 1.12 (3)].

When the field is reversed again the interaction of the spins with the AFM will favor the magnetization reversal towards the cooling field direction [Fig. 1.12 (4)]. Consequently, the coercive field will be smaller compared to the uncoupled case. The net effect is a shift of the hysteresis opposite to the cooling field direction.

[18] EB could be also used to stabilize the magnetization of nanostructures against thermal fluctuations, see [119, 120, and references therein]. Further applications are magnetoresistive devices as read heads and magnetic force microscopy tips [120]. If the loops are significantly shifted, the squareness $\frac{M_r}{M_s} = 1$ and the nanostructures are single domain at remanence. Therefore magnetization reduction or noise effects due to the presence of domains are minimized.

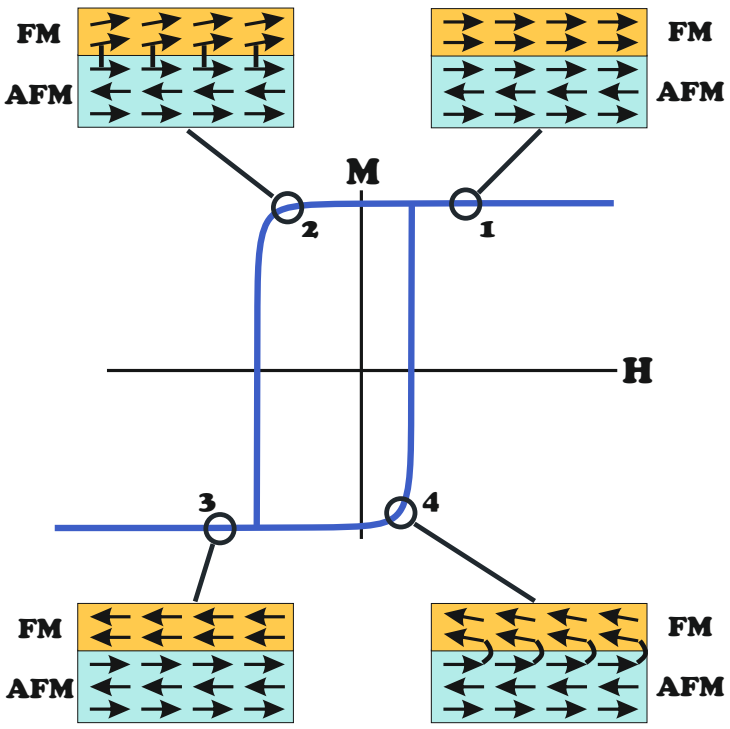

Figure 1.12.: Spin configurations as found at different stages of a hysteresis loop for a sample with large K_{AFM} according to [120]. For details see text.

The effect is different for low anisotropy of the AFM (K_{AFM}) as sketched in Fig. 1.13. The starting situation [Fig. 1.13 (1)] is the same in both cases, the spins of the FM at the interface are aligned parallel to the positive cooling field. But in case of low K_{AFM} the interfacial coupling can be stronger than K_{AFM} and the spins of both FM and AFM start to rotate. This results in an irreversible twist in the AFM which again induces increased coercivity with respect to the uncoupled case. After saturation in negative fields [Fig. 1.13 (3)] an analogous behavior is observed resulting in a net broadening of the hysteresis loop and no shift.

1.2.4.1. Positive Exchange Bias

Exchange bias can also have a positive sign, i.e. the loop is shifted towards the cooling field direction, or of oscillatory type and e.g. in [122] it depends on the thickness of the underlayer and the number of multilayers. Positive EB was first reported in 1996 by Nogues et al. in $FeFe_2 - Fe -$ bilayers for field-cooling through T_N in large fields [123]. The effect was attributed to a mixture of antiferromagnetic exchange at the interface and

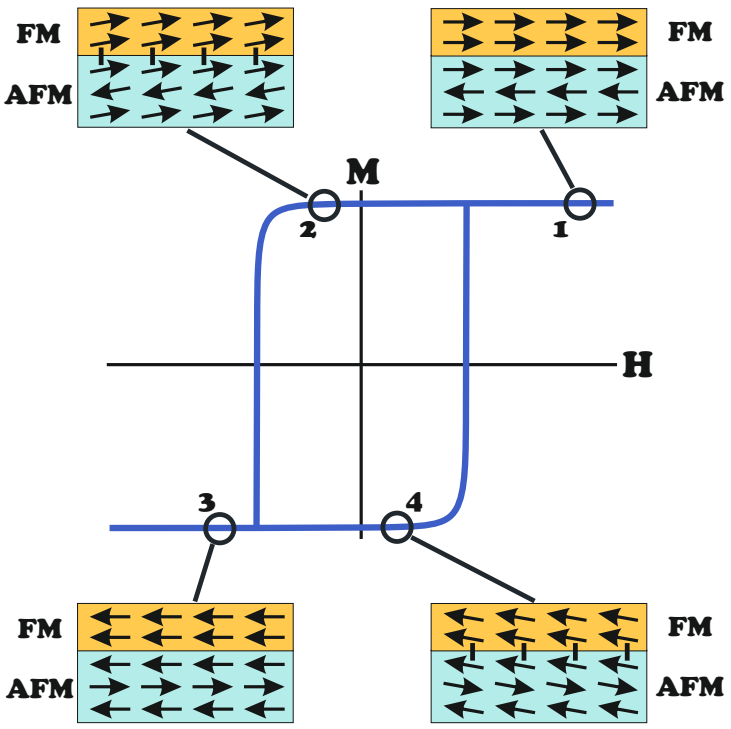

Figure 1.13.: Spin configurations as found at different stages of a hysteresis loop for a sample with small K_{AFM} according to [120]. For details see text.

a ferromagnetic coupling of the AFM surface spins to the cooling field above T_N. In a recent work such a coupling mechanism was also supported by the observation of training induced positive exchange bias in NiFe/IrMn-bilayers [124]. Positive exchange bias was also found in ferromagnetic/ferrimagnetic bilayers [125] and several other works. However, all results confirm that the interface coupling favors antiferromagnetic alignment [119, 122, 124, 125, and references therein].

1.2.4.2. Thickness Dependence of Exchange Bias

In the first theoretical model Meiklejohn and Bean [115, 118] proposed in the limit of infinite anisotropy of the AFM:

$$H_e = \frac{JS_{FM}S_{AFM}}{M_{FM}t_{FM}} \tag{1.45}$$

which includes the dependence of H_e on the layer thickness of the FM t_{FM} only. J is the coupling constant, S_{FM} and S_{AFM} are the interface spin moment of the FM and AFM, respectively, and M_{FM} is the magnetization of the FM. Note that H_e is expected to vanish when the anisotropy energy in the AFM is smaller than the exchange interaction between the interfacial spins, i.e. $K_{AF}t_{AF}^{cr} = JS_{FM}S_{AFM}$ [126]. $\mathrm{K_{AF}t_{AF}^{cr}}$ is the product of the antiferromagnetic anisotropy constant and the critical thickness of the antiferromagnetic layer below which no loop shift occurs. The general drawback of the model is an overestimation of H_e compared to experimental results. Binek et al. extended that model including the AFM layer thickness t_{AF} [127]:

$$H_e = H_E^{\infty}\left(1 - \frac{(\Delta E)^2}{8K_{AF}^2 t_{AF}^2}\right) \tag{1.46}$$

$\mathrm{\Delta E = JS_{FM}S_{AFM}}$ and $\mathrm{H^{\infty}} = \frac{\Delta E}{M_{FM}t_{FM}}$ the EB saturation value at large t_{AF}. Another model by Malozemoff also includes roughness of uncompensated and compensated interfaces [128]:

$$H_e = \frac{2}{M_{FM}t_{FM}}\sqrt{\frac{J_{AF}K_{AF}}{a}} \tag{1.47}$$

where a is the lattice parameter and $\mathrm{J_{AF}}$ the exchange constant. Experimentally the inverse proportionality of the exchange bias on the ferromagnetic layer thickness has been observed in all systems whereas the correlation of $\mathrm{H_e}$ and the antiferromagnetic layer thickness is rather complex [119, and references therein].

In conclusion, an EB effect can be manifested by a horizontal shift of the hysteresis loop after field cooling through $\mathrm{T_N}$. Typically this shift is opposite to the direction of the cooling field (negative). Depending on the sample system and layer thicknesses, however, the shift can also be in the opposite (positive) direction in seldom cases. A further remarkable feature in this context is the training effect[19] which constitutes a hint that the interface actually is in a metastable equilibrium [117]. Above a critical thickness of the AFM, most models give an $1/\mathrm{t_{FM}}$-dependence for $\mathrm{H_e}$.

[19] Training effect: the dependence of $\mathrm{H_e}$ on the number of measurements with the value of $\mathrm{H_e}$ decreasing as n increases [117].

1.3. X-ray Absorption Spectroscopy (XAS)

In the following a short overview of the x-ray absorption process is presented. In general, the attenuation of an electromagnetic wave propagating through a continuous homogeneous medium with thickness t is given by Lambert-Beer's Law:

$$I(E,t) = I_0 \cdot e^{-\mu(E)\cdot t} \tag{1.48}$$

where I_0 is the incident intensity and μ the attenuation coefficient. The attenuation coefficient is given by the photoabsorption coefficient[20] and therefore proportional to the photoabsorption cross-section σ_{abs} defined as follows:

$$\sigma_{abs} = \frac{T_{if}}{\Phi_0} \tag{1.49}$$

where T_{if} is the transition probability per unit time and Φ_0 the photon flux [25]. The transition probability from an initial to a final state can be calculated according to Fermi's Golden Rule in the one electron approximation:

$$T_{if} \propto \sum_f \left|\langle \Psi_f | \, H_{int} \, | \Psi_i \rangle\right|^2 \delta(E_f - E_i - \hbar\omega) \tag{1.50}$$

$\langle \Psi_f |$ and $| \Psi_i \rangle$ are the final and initial states, respectively, E_f and E_i the corresponding energies and the interaction Hamiltonian H_{int}. With the momentum operator $\mathbf{p}$ and the vector potential $\mathbf{A}$ of the incident wave field, the transition matrix element $\left|\langle \Psi_f | \, \frac{e}{m_e}\mathbf{p}\cdot\mathbf{A}(\mathbf{r}) \, | \Psi_i \rangle\right|^2$ can be written as follows in dipole approximation: $\left|\langle \Psi_f | \, \mathbf{p}\cdot\epsilon \, | \Psi_i \rangle\right|^2$ which includes the photon polarization vector ϵ. Within that approximation the allowed dipole transitions are:

$$\Delta m_s = 0, \quad \Delta m_l = \pm 1 \tag{1.51}$$

The dipole approximation properly describes most of the absorption processes. However, for some $L_{2,3}$-edge rare earth XMCD spectra and for metal K-edges quadrupolar transitions need to be considered as well [129].
In x-ray absorption spectroscopy (XAS) measurements, core level electrons are excited by photon excitation into unoccupied electronic states. XAS is an elemental sensitive probe, since the binding energies of the electrons are element specific. The empty core level states will be re-occupied by electrons from higher energy levels, either by photon or Auger electron emission[25].

In this thesis the following two XAS methods were used:

[20] Elastic Rayleigh and inelastic Compton scattering can be neglected for the range of X-rays utilized here [129] where the photo effect is the driving interaction

- X-ray absorption near-edge structure (XANES) ⇒ electronic structure
- X-ray magnetic circular dichroism (XMCD) ⇒ orbital and spin magnetic moments

1.3.1. X-ray Absorption Near Edge Structure (XANES)

The XANES or also NEXAFS (near-edge x-ray absorption fine structure) region extends from the absorption edge till about 50 eV above followed by the up to several hundred eV wide EXAFS[21] region. Since XANES probes the density of unoccupied states its spectral shape (fine structure) allows to determine the electronic structure providing chemical information of the absorbing material [130]. This is exemplarily shown for Fe and different Fe-Oxides in Fig. 1.14 at the $L_{2/3}$-edges, where core level electrons from the spin-orbit split $2p_{1/2}$ (L_2-edge) and $2p_{3/2}$ (L_3-edge) states are excited into unoccupied d-states. For oxidized Fe the L_3-edge shifts to higher photon energies, both L_2- and L_3-peaks show distinct multiplet features.
XANES measurements are typically performed with linearly polarized light.

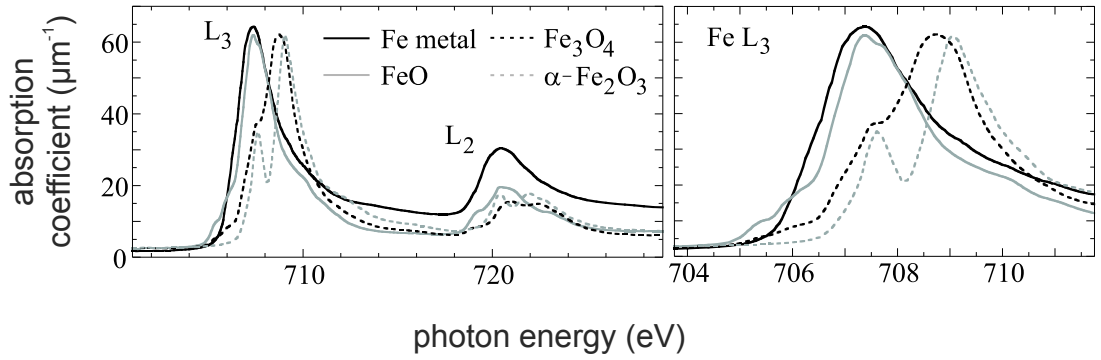

Figure 1.14.: XANES of the Fe $L_{2,3}$-edges of Fe and Fe-oxides [wustite (FeO), hematite (α-Fe_2O_3) and magnetite (Fe_3O_4)] [131].

1.3.2. X-ray Magnetic Circular Dichroism (XMCD)

Using circulary polarized photons, the density of unoccupied spin-up and spin-down states can be probed allowing for magnetization measurements. The XMCD effect was theoretically predicted by Erskine and Stern in 1975 [132] and was first experimentally reported by Schütz et al. in 1987 [133]. It can be explained in a two-step model, in the

[21] EXAFS (extended x-ray absorption fine structure) probes bond lengths and correlation but will not be discussed in this thesis. For further information please see the respective literature.

case of the $L_{2,3}$-edges. In the first step angular momentum from the incident photons is transferred to the excited photoelectrons. In the second step of the model, these spin polarized electrons probe the spin polarization of the final unoccupied 3d-states, i.e. the magnetization (direction). The XMCD signal is the difference between two XANES spectra for parallel and anti parallel sample magnetization with respect to the incident photon spin (equivalent: different photon spin for identic sample magnetization) and is directly proportional to the atomic magnetic moment at the L-edges (Fig. 1.15) [25]. As discussed in [25] the XMCD allows for the determination of the element specific magnetic moment (μ) and its orbital and spin contribution [134–136]. The signal intensity is a measure of the temperature dependent Magnetization $|\mathbf{M}|$, projected onto the propagation vector $\mathbf{k}$ of the incident photons (Fig. 1.15).

The combination of element-specific magnetization sensitivity by XMCD measurements with the electronic structure and chemical sample information obtained by XANES measurements makes XAS one of the most powerful techniques in magnetic materials' charaterization. Exploiting the large magnetic contrast at the L_3-edge x-ray microscopies (Chapter 2.2) also allow for magnetic imaging on the 25 nm scale.

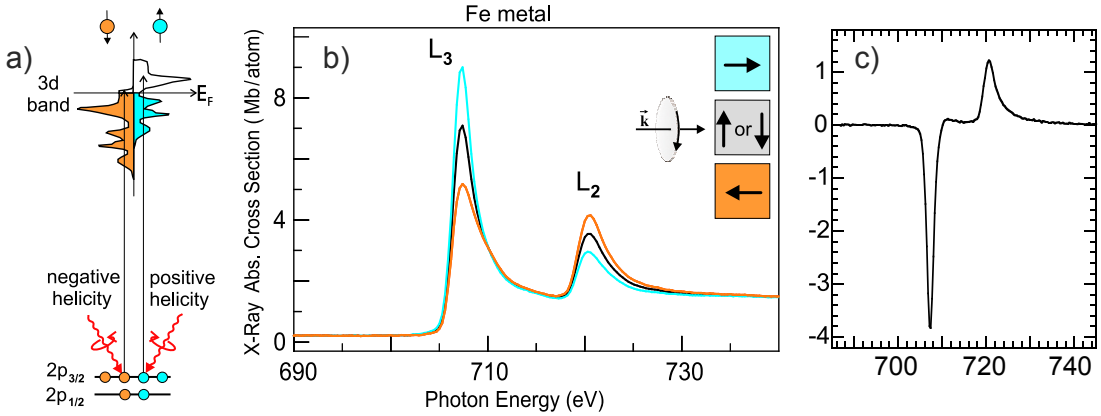

Figure 1.15.: XMCD effect - schematic, adapted from [25]. The XMCD effect is displayed for the Fe L-edge absorption of circulary polarized X-rays with positive helicity. The color codes correspond to the magnetization directions in the sample (insets in b). If the helicity was negative, the colors of the spectra would invert. The corresponding XMCD signal, which is typically negative at the L_3-edge, is plotted in (c). Note that the the XMCD signal at the L_3-edge is almost of the same size as the chemical contrast. In (a), the density of spin-up and spin-down states for Fe metal is sketched and the photoelectron excitation from the 2p into the unoccupied 3d states. The magnetization points upwards.

2. Experimental

2.1. High Resolution Transmission Electron Microscopy

High resolution transmission electron microscopy (HRTEM) is an essential characterization technique in materials science [137, 138]. Two basic fields of application can be distinguished: a) structural analysis (conventional TEM) and b) chemical analysis (analytical TEM). The latter employs energy dispersive x-ray spectroscopy (EDS) energy loss spectroscopy (EELS). In the structural analysis, either the imaging or the diffraction mode of the TEM are used. Lattice images with Å-resolution allow the determination of lattice spacings from the observed lattice fringes. The interpretation of HRTEM images, however, is often complicated, since they are generally not a direct representation of the structure of the sample, especially for complex crystal structures. Complementary simulations are useful.

For the structural analysis of nanoparticles, the imaging of separated atomic columns is desired. But the exact identification of the surface structure is hindered by delocalization effects due to a non-zero spherical aberration coefficient C_S of the optical system of the microscope. C_S can be corrected either by hardware[1], i.e. correctors, or software solutions as exit wave reconstruction (EWR) which was employed here.

Even if a C_S-corrected microscope is used, it is still essential to do EWR, since it reconstructs amplitude and phase information from the electron exit wave. In standard TEM images only the intensity is detected, i.e. the square of the electron wave function, and therefore, phase and amplitude information are lost. Phase images are of special interest because they yield information on the chemical composition within individual atomic columns.

2.1.1. Exit Wave Reconstruction (EWR)

Exit Wave Reconstruction (EWR) is a computational method which reconstructs the full electron wave function from a focal series[2] of HRTEM images. The method was developed by Kirkland, Thust and Coene [139–141]. The main purpose of EWR is the reconstruction of the image directly below the sample plane and therefore removing all

[1] Recent technical improvements correcting for the spherical aberration even pushed the resolution below 0.5 Å in the TEAM (Transmission Electron Aberration-Corrected Microscope) microscope.

[2] A focal series is a series of HRTEM images acquired at slightly different defoci Δf. Depending on the microscope Δf is typically in the range of 2 nm - 4 nm.

disturbances, i.e. aberrations, due to the electron optics of the microscope. Furthermore, based on the focal series acquisition around the Lichte defocus [142], it allows to exploit the full range of the contrast transfer function (CTF)[3] [137] up to the information limit of the microscope. For a more detailed description of this technique see [16, 143] and the works by Thust and Coene [140, 141].

In summary, EWR allows for artifact free imaging on the atomic scale due to the removal of delocalization and other aberrations. Furthermore, full phase and amplitude information of the electron exit wave are recovered.

2.1.2. Microscopes

For the TEM investigations, two different microscopes were used: The TecnaiF20 ST in Duisburg for overview images and determining the size distribution of the particles and the tomography[4] studies. Focal series were acquired at the OÅM, a modified Philips CM300FEG/UT, at the National Center for Electron Microscopy in Berkeley. Both microscopes are shown in Fig. 2.1 [16]. See appendix section A.1 for technical information.

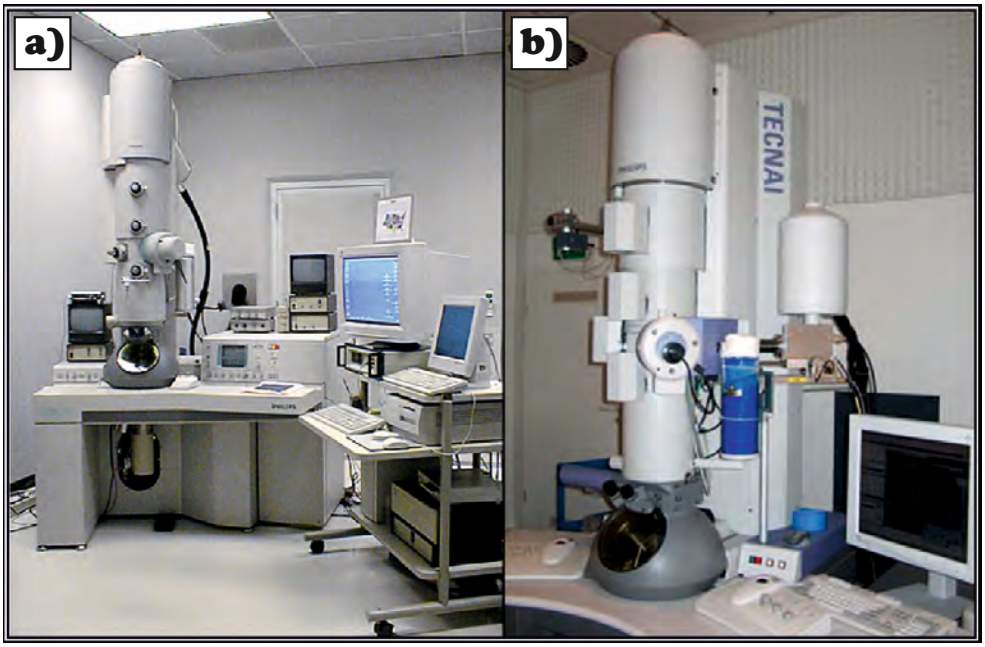

Figure 2.1.: Transmission Electron Microscopes: (a) CM300 - (NCEM, Berkeley, CA) (b)Tecnai - (University of Duisburg-Essen, Duisburg)

[3]The CTF describes how the information of each point of the specimen is transferred into the final image by the electron optics of the microscope.

[4]Diploma thesis by C. Möller [144]

2.2. Synchrotron Radiation & Magnetic Imaging with X-rays

X-ray microscopy measurements in this thesis were carried out at two different synchrotron facilities: X-ray photoemission electron microscopy (XPEEM) studies at the Berliner Elektronenspeicherring Gesellschaft für Synchrotronstrahlung m.b.H (BESSYII) in Berlin and magnetic transmission electron microscopy (MTXM) measurements at the Advanced Light Source (ALS) in Berkeley, CA, USA. Apart from its broad energy range, from infrared to hard x-rays [26], synchrotron radiation [25, 145, 146, and references therein][5] is characterized by its large intensity, coherence, brilliance[6] and its high degree of polarization which all make it very powerful for materials characterization.

Magnetic imaging with polarized x-rays yields the advantage of elemental specificity in addition to the magnetization sensitivity via the XMCD effect for ferromagnetic or the x-ray magnetic linear dichroism (XMLD) for antiferromagnetic systems [148, 149]. The combination of element-specific and magnetic imaging with lateral resolution is also referred to by the term spectro-microscopy [150, 151]. In this work, magnetic imaging was realized in photoemission (XPEEM) and transmission (MTXM) experiments with respective sampling depths of several nanometers and of up to 100 nm. For a more detailed overview of magnetic imaging techniques utilizing x-rays see for example [25] or the chapters by W. Kuch in [145] and F. Nolting in [146]. Here, the basic principles of XPEEM and MTXM (Fig. 2.2) and their respective setups at BESSYII and the ALS are described.

2.2.1. X-ray Photoemission Electron Microscopy - XPEEM

In (x-ray) photoemission electron microscopy ((X)PEEM)[7], a sample is illuminated by photons (either x-rays, e.g. at synchrotron sources, or UV) under grazing incidence of 16 ° - 30 ° (with respect to the surface plane), and electrons - high energetic Auger, lower energetic secondary and photo electrons - are emitted (Fig. 2.2 b). The secondary electron tail (0 - 20 eV) determines the XPEEM intensity and resolution. By using an aperture in the back focal plane of the microscope the resolution can be improved due to the suppression of chromatic aberrations [151]. Additional reduction of chromatic aberration is achieved by the implementation of an energy analyzer, which acts as an band pass filter. The low energy electrons emitted from the sample are accelerated by a strong electrostatic field (10 - 30 keV) in the objective lens, of which the specimen is an integral part [153]. These fast electrons are imaged after passing the electron optics (consisting of an assembly of electrostatic and magnetic lenses), which magnifies the image and

[5] see [106, 147] for BESSYII specifications

[6] Brilliance is defined as the number of photons per area, solid angle and time with respect to a band with of 0.1% in energy.

[7] Note that PEEM is also referred to as photoexcitation electron emission microscopy [152] or photoelectron emission microscopy [150], it means the same technique though. Here I use the definition according to [25]. Also note, that the expression refers to both method and instrument.

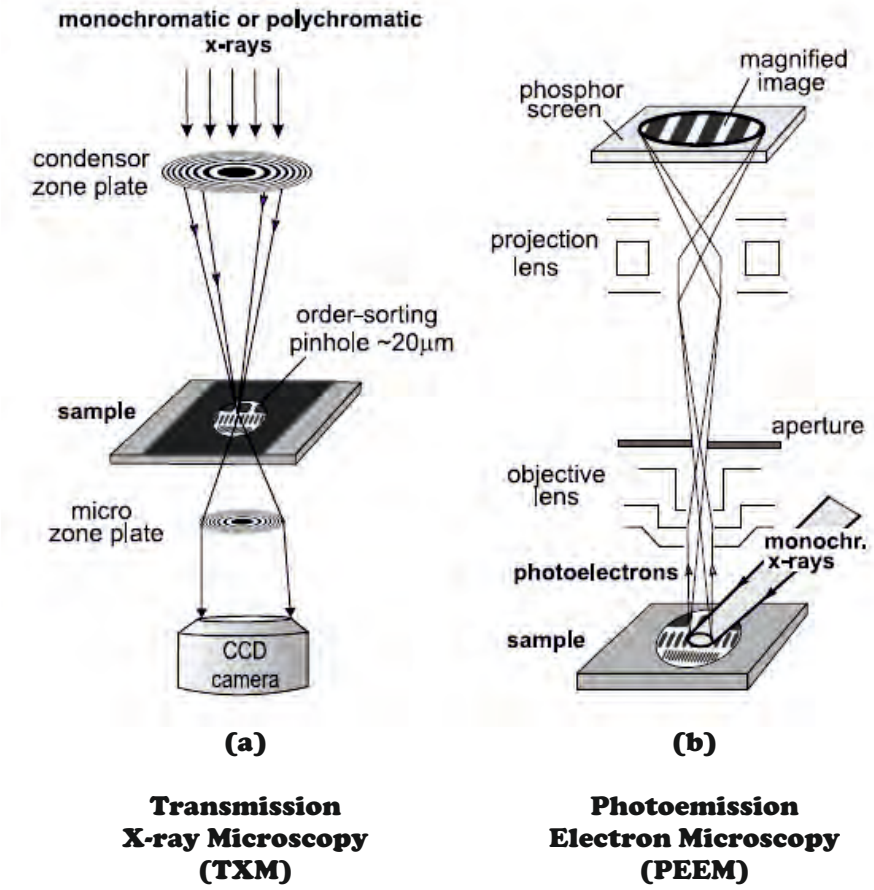

Figure 2.2.: Schematic representation of two x-ray microscopy techniques, TXM (a) and PEEM (b) [25]. For details see text.

corrects for image distortions. Micro channel plates (MCPs)[8] and a fluorescence screen typically detect the electrons and an image is recorded at a subsequent CCD camera. The basic contrast mechanisms in XPEEM are [151]:

- chemical (spectroscopic) contrast
- local work function

[8] A micro channel plate (MCP) is a secondary electron multiplier consisting of one plate with microscopic channels typically separated by 10 μm. Between both sides of the plate a voltage is applied creating a cascade of electrons once one electron hits a channel wall.

- topology
- magnetic contrast (XMCD, XMLD)

Currently, a lateral resolution of about 25 nm is obtainable in x-ray imaging. Recent designs employing energy filters and aberration correcting optics hold the promise to image at 1 nm lateral resolution [154]. More about the XPEEM technique and its applications in nanoscience has been reported in [152, 153, 155, 156].

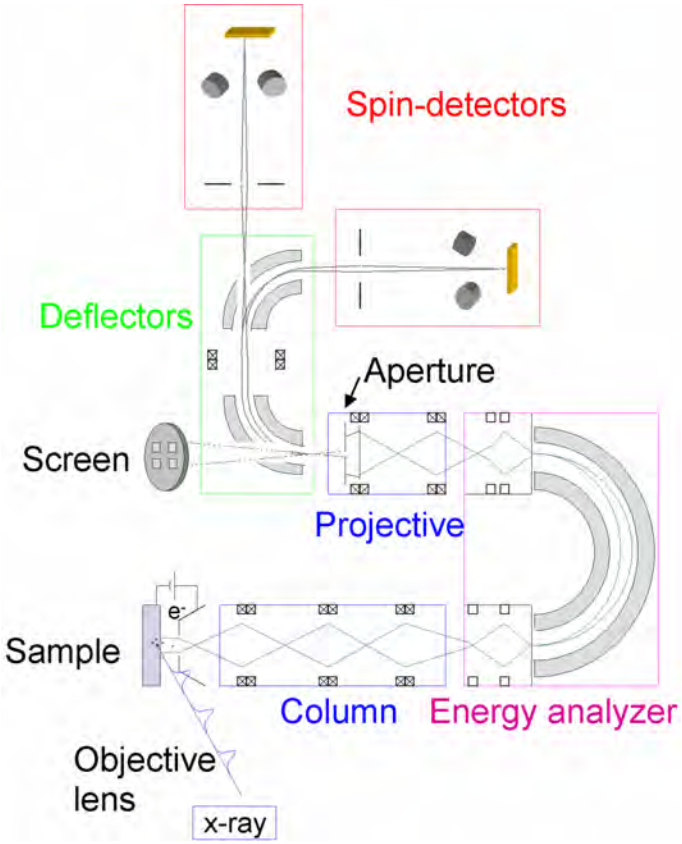

Figure 2.3.: Schematic setup of the SPEEM instrument (based on commercial Elmitec PEEM III with energy analyzer) [30]. The basic imaging elements of this instrument are the column and the objective lens, the energy analyzer, the projective lenses and the screen. With two 90° deflectors and two Mott detectors this setup allows also for spin-resolved imaging. For details see text.

2.2.1.1. SPEEM Instrument at Beamline UE49-PGM - BESSYII

The XPEEM instrument used in this thesis, which is also referred to as SPEEM (spin-polarized photoemission electron microcsope), is located at beamline UE49-PGM at BESSYII in Berlin[9]. The accessible energy range is 100 - 1800 eV with an spectral resolution $E/\Delta E = 10000$ at 700 eV and a flux of 10^{11}-10^{13} photons per second and 100 mA ring current. This microfocus beam line has a spot size of $8\,\mu m \times 34\,\mu m$ (FWHM) at the sample position. The horizontal width is due to the grazing incidence of 16° of the photons which is conditional upon the setup of the instrument. Fig. 2.3 shows the setup of the instrument which is based on a commercial Elmitec PEEM III instrument with energy analyzer[10]. The sample is typically at a potential of - 20 kV which accelerates the electrons emitted due to x-ray illumination into the electron optics of the microscope (objective lens, projective lenses, MCP, fluorescence screen, CCD). Using the deflectors it is also possible to direct the electrons onto one of the two (Mott) spin detectors for spatial analysis of the spin distribution (not employed in this thesis). 2 stigmators and 4 deflectors inside the electron optics columns allow for the distortion correction and shifting of the image. To reduce aberrations and to obtain a better lateral resolution a contrast aperture located in the objective column (not shown here) is used.

2.2.1.2. Sample Holder for Magnetic Measurements

Due to the Lorentz force the application of magnetic fields in low energy electron imaging is challenging. A sample holder with a magnetic yoke[11] below the sample allows for the application of fields of up to 33 mT in plane without significant reduction in resolution. Remaining photoelectron deflections due to the stray field can be compensated [30]. The sample holder is illustrated in the inset of Fig. 2.4 which shows the simulated stray field at distance d above the sample plane for three different gap values. The calculations demonstrate the minimization of the magnetic stray field components with decreasing gap size. For our experiments a gap size of 80 μm (500 μm) were utilized, i.e. the magnetic field is confined to the 80 μm (500 μm) gap. For more information on the holder and implementation into the setup see [147].

2.2.2. (Magnetic) Transmission X-ray Microscopy - (M)TXM

Transmission x-ray microscopy is an photon-in/photon-out technique and therefore not sensitive to the presence of magnetic fields during imaging. This is a big advantage with respect to XPEEM which is a photon-in/electron-out technique and very sensitive to in situ applied magnetic fields. Both techniques work with the spectroscopic contrast.

[9] For technical information on the beam line setup and illustration of the undulator working principle see Appendix figs. B.1 and B.2.
[10] Elmitec: "SPEPEEM"
[11] monolithic and of soft magnetic Fe

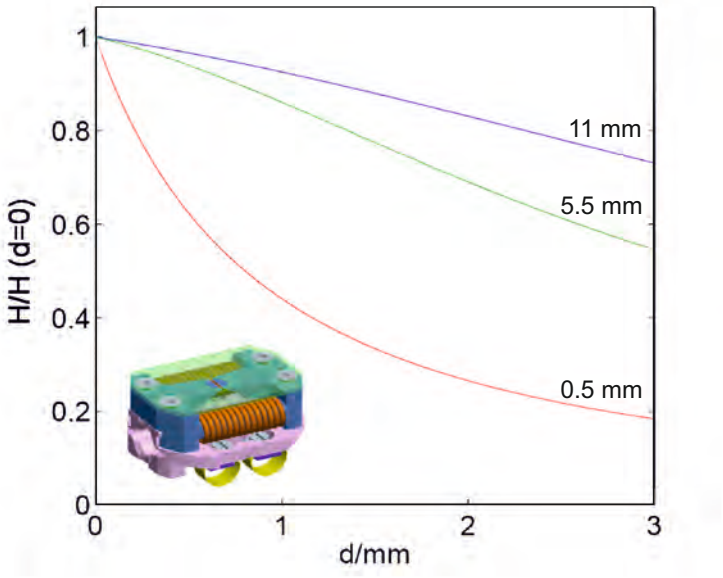

Figure 2.4.: Calculated magnetic field distribution (relative units) for PEEM sample holder with magnetic yoke. The magnetic field is calculated at the position d above the center of the gap for gap values of 11 mm (blue), 5.5 mm (green) and 0.5 mm (red) [30, 147]. For the latter the sample thickness becomes a critical parameter.

Additional contrast in TXM arises from differences in the x-ray absorption cross section at non-resonant photon energies either due to differences in thickness or chemical composition [25]. The basic setup of a TXM, also referred to as MTXM if it is used for magnetic imaging, is sketched in Fig. 2.2 a. The functional principle of a full field TXM is explained in more detail for the XM-1 set up at the ALS in Berkeley which was used in this thesis. The state of the art spatial resolution, which is provided by the width Δr of the outermost zone width of the micro zone plate (MZP) [157], is about 25 nm in MTXM imaging and values below 15 nm have been demonstrated [158, 159] .

2.2.2.1. XM-1 at Beamline 6.1.2 - ALS

The optical setup of the XM-1, which is a full-field soft x-ray microscope end station, is shown in Fig. 2.5. At beamline 6.1.2 synchrotron light is emitted by a bending magnet. Circularly polarized light radiated above or below the horizontal plane of the storage

ring. An aperture upstream of the condenser zone plate (CZP) yields circular polarized x-rays with a polarization degree of 60 %-70 %. The x-rays impinge on the CZP which is a Fresnel zone plate (FZP)[12]. Providing a hollow cone illumination on the sample the CZP acts as a linear monochromator, i.e. the focal length determines the wavelength, in combination with a pinhole close to the sample. For an CZP with an outermost zone width of 40 nm, one has an 1 eV spectral resolution in the energy range of 500 - 1000 eV (corresponding to 20 - 30 cm focal length). Here the energy resolution is $E/\Delta E = 500 - 700$ and the flux is 1000 photons per 3 s at 0.2% band width at 517 eV [160]. After transmitting through the sample the photons pass another Fresnel zone plate, the MZP. It generates a magnified image of the transmitted photons which is detected by the x-ray sensitive CCD (charge coupled device) camera. The field of view is about 10 μm. Apart from technical parameters, the illumination time depends on the optical thickness of the sample and is typically in the range of seconds. For magnetic imaging fields up to 2 - 3 kOe in out of plane geometry and about 1 - 2 kOe in in plane geometry of the sample can be applied. For the latter, the sample is typically tilted by $\alpha = 60°$ angle with respect to the optical axis resulting in magnetic contrast reduced by 50% ($\cos\alpha$) and an increased effective thickness by a factor $1/\sin\alpha$. The XM-1 end station is also equipped with an optical microscope allowing for aligning the sample prior to x-ray exposition. For more information on the XM-1 and TXM see [25, 28, 146, 157, and references therein].

In summary, both techniques XPEEM and MTXM provide magnetic imaging at about 25 nm spatial resolution using the XMCD-effect. Whereas XPEEM is rather surface sensitive (probing several nm), MTXM probes the volume properties up to about 100 nm. For the latter, the application of high magnetic fields in plane and out of plane during imaging is possible. The obtainable field values are only limited by the geometrical restrictions, i.e. the distance between the zone plates and the sample is well below 1 mm. The available in plane magnetic field is in the same order as for the XPEEM, namely about 100 mT. XPEEM offers the advantage of additional spectroscopy measurements which are rather difficult in MTXM due to the limited energy resolution and the correlation of focal length and wavelength. For MTXM, the samples have to be prepared on electron transparent membranes such as Si_3N_4-membranes which demand careful handling. Standard Si-substrates can be used for XPEEM measurements. Combining both techniques offers complementary magnetic characterization of nanostructures on both the static as on the dynamic scale. In this work, only the static case is addressed.

[12] Fresnel zone plates (FZPs) are circular gratings with radially increasing line density [157]. FZPs for x-ray microscopy are typically fabricated by e-beam lithography [158].

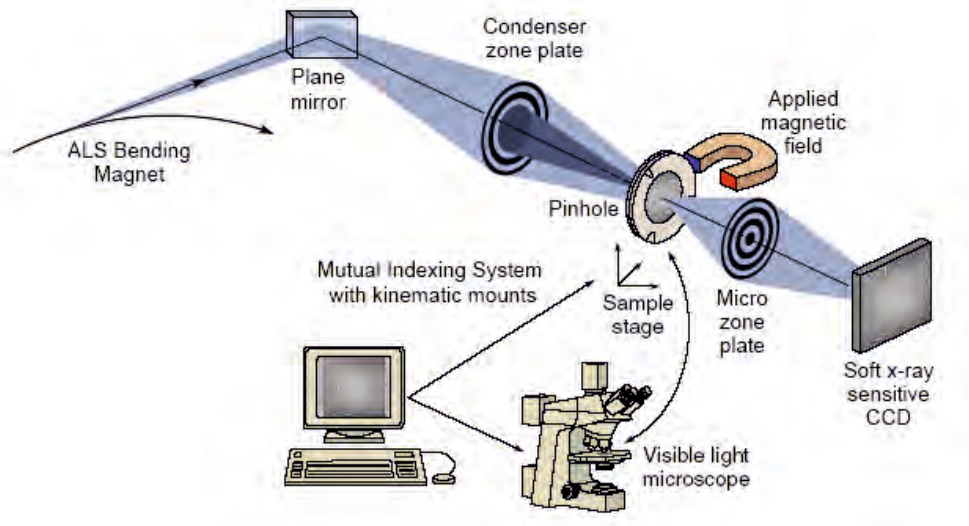

Figure 2.5.: Schematic optical setup of the XM-1 instrument at the ALS, Berkeley, CA [157, 161].

2.3. Other Experimental Techniques

2.3.1. Scanning Electron Microscopy (SEM) & E-Beam Lithography (EBL)

The local particle coordination on the synchrotron samples was investigated by scanning electron microscopy (SEM). The SEM instrument (LEO 1530) with an accelerating voltage range of 3 - 30 kV and a max. lateral resolution of 2 nm was also used for e-beam lithography. For the latter, the writing unit "ELPHY Plus Advanced SEM/FIB Nanolithography System" by Raith company was used. In the Appendix, an exemplary standard electron beam lithography process is sketched in Fig. A.1, p. 160 and described in the figure caption. The SEM instrument is also equipped with an EDS-unit allowing for chemical analysis. SEM overview images were also acquired utilizing an FEI Inspect F instrument.

2.3.2. SQUID Magnetometry

Magnetic characterization was performed using a SQUID (superconducting quantum interference device) magnetometer by Quantum Design company (model MPMS-XL5). Magnetic hysteresis and ZFC/FC (zero field cooled/field cooled) magnetization measurements were performed in a temperature range 4 K - 300 K. In a ZFC measurement,

the sample is cooled down in 0 field, then a small field is applied (here 100 Oe) and the magnetization is detected with increasing temperature. In an FC measurement the sample is cooled in high fields (here 40 kOe) and measured in low fields with increasing temperature again.

2.4. Micromagnetic Simulations

Two different kinds of micromagnetic simulations solving the Landau-Lifshitz-Gilbert (LLG) equation in three dimensions were performed: (a) using a finite-element code[13] [162] and (b) using the object oriented micromagnetic framework (OOMMF) program[14] [163]. For both methods, the sample needs to be divided into discrete sub-cells [tetrahedal (a), cuboid (b)] so that a multiple of the cell dimension matches the sample dimension. The magnetization direction in all the sub-cells is calculated for any field step taking into account exchange and dipolar interactions with neigboring cells. In the hysteresis loops the overall magnetization is plotted. In (a), the external field is varied linearly in time. This suppresses fast magnetic precession processes and other artifacts that may occur otherwise from a stepwise change of the field. Hysteresis loops were determined in the quasi-static limit assuming a large damping constant of $\alpha = 0.25$. Dipolar interactions are included by using a hybrid finite-element/boundary element method [164]. For the OOMMF hysteresis simulations, either time[15] (1) or minimization[16] (2) evolvers were used [165]. The first one is based on solving the LLG dynamics and describes the temporal development of the magnetization with time. The field is varied once a stable condition of the magnetization is reached (defined by stopping criteria). The second evolver only takes the energy surface into account and locates local minima through minimization. Once a minimum is found the magnetization for the next field step is calculated. Especially for quasi-static hysteresis simulations, the energy minimization is the faster route. OOMMF offers also the possibility of an indirect temperature implementation based on the Euler-evolver[17] by adding a highly irregular fluctuating field to the effective magnetic field. Thereby the Landau Lifshitz (LL) differential equation is altered to a stochastic type [167].

[13] performed by Sebastian Gliga
[14] performed by Christoph Hassel and Sven Stienen
[15] Oxs_EulerEvolve
[16] Oxs_CGEvolve
[17] thetaevolve[166]

3. Sample Preparation

In the following, the synthesis of Fe_xPt_{1-x}, Fe/Fe-oxide nanoparticles, Co nanorods and the sample preparation for the synchrotron studies are described. Fe_xPt_{1-x} nanoparticles were obtained by two different approaches: Gas phase condensation and organometallic synthesis. FePt particles from the gas phase were synthesized by O. Dmitrieva [168] and colloidal Fe_xPt_{1-x} particles by O. Margeat [169]. Organometallic synthesis routes were also carried out for the preparation of Fe/Fe-oxide nanocubes and polyhedra by A. Shavel [170, 171] and Co nanorods by M. Comesaña-Hermo [172].

3.1. Synthesis of Fe_xPt_{1-x} Nanoparticles

3.1.1. Gas Phase Condensation

Detailed information on the preparation of FePt-nanoparticles by the gas phase condensation technique is given in [173–175]. The preparation setup (consisting of a nucleation chamber, sintering furnace and deposition chamber) allows for gas phase condensation of nanoparticles and thermal sintering in vacuum before thermophoretical deposition onto a cooled substrate. Particles investigated in this thesis were prepared by adding nitrogen in the sputtering process yielding single crystalline, mostly $L1_0$-ordered particles [176, 177]. Within ± 5 at. % the chemical composition is FePt and the size distribution yielded a mean diameter of 5.75 ± 0.4 nm [16].

3.1.2. Organometallic Synthesis

Colloidal Fe_xPt_{1-x}-nanoparticles were prepared as described by Sun et al. [11]: simultaneous decomposition and reduction of the two precursors iron pentacarbonyl ($Fe(CO)_5$) and platinum acetylacetonate ($Pt(acac)_2$), while $2-bromooctanoic\ acid$ was used as ligand. *Dioctyl ether* served as solvent and the solution was heated at 280°C for one hour. Afterwards, it was washed by adding ethanol, centrifugated and redispersed prior to deposition onto the sample substrate. To remove the excess of ligands, the sample was exposed to an acetone bath. TEM investigations yielded a shape and size inhomogeneity in the range of several nanometers diameter. Furthermore, chemical composition determination utilizing energy dispersive spectroscopy (EDS) was quite difficult due to strong charging effects and yielded compositions with a tendency to Pt-excess [16].

3.2. Synthesis of Co nanorods

The nanorods used for the XPEEM measurements (chapter 7, p. 147) were prepared as described for Sample 3-1 (p. 183) in reference [172]. In Fig. 3.1, TEM images of the product, i.e. nanorods with a diameter of about 4 nm and length of 100 nm - 300 nm and small spherical nanoparticles of 3 nm diameter are shown. There is strong agglomeration of the nanorods, most likely due to magnetic interactions and sticking ligands. To obtain individual Co nanorods for the synchrotron studies, the toluene-solution was diluted and sonificated prior to deposition onto the substrate. For MTXM and further XPEEM experiments different nanorods with lengths up to the micron range were synthesized as described in the following: 2 mmols of oleic acid (633 μL) and 1 mmol of oleylamine (328 μL) were mixed in 20 mL of distilled anisole. The resultant solution was added to 276 mg (1 mmol) of $Co(\eta^3 - C_8H_{13})(\eta^4 - C_8H_{12})$ inside a Fisher-Porter bottle forming a violet solution that was stirred for 15 minutes. Afterwards, the solution was hydrogenated under 3 bars of H_2 for 15 minutes, and the bottle was introduced in an oil bath at 150°C for 48 hours. At the end of the reaction, a brown solution containing spherical NPs was removed and the black solid deposited on the stirring bar was stored inside the glovebox.

For TEM sample preparation, a small amount of this powder was solubilized in toluene. The resulting sample was composed of bunches of Co nanowires with lengths of several micrometers and a diameter of about 7 nm. A few spherical nanoparticles with 3 nm diameter are also observed. The solution is not stable for long periods of time, and after several days, a black precipitate is observed at the bottom of the flask due to the precipitation of the big Co nanowire bunches. Shorter Co nanorods of ranging in length between 200 nm and 500 nm were kept in solution. The x-ray imaging samples were prepared by deposition of one drop of the solution onto the respective substrate and drying under Ar-atmosphere.

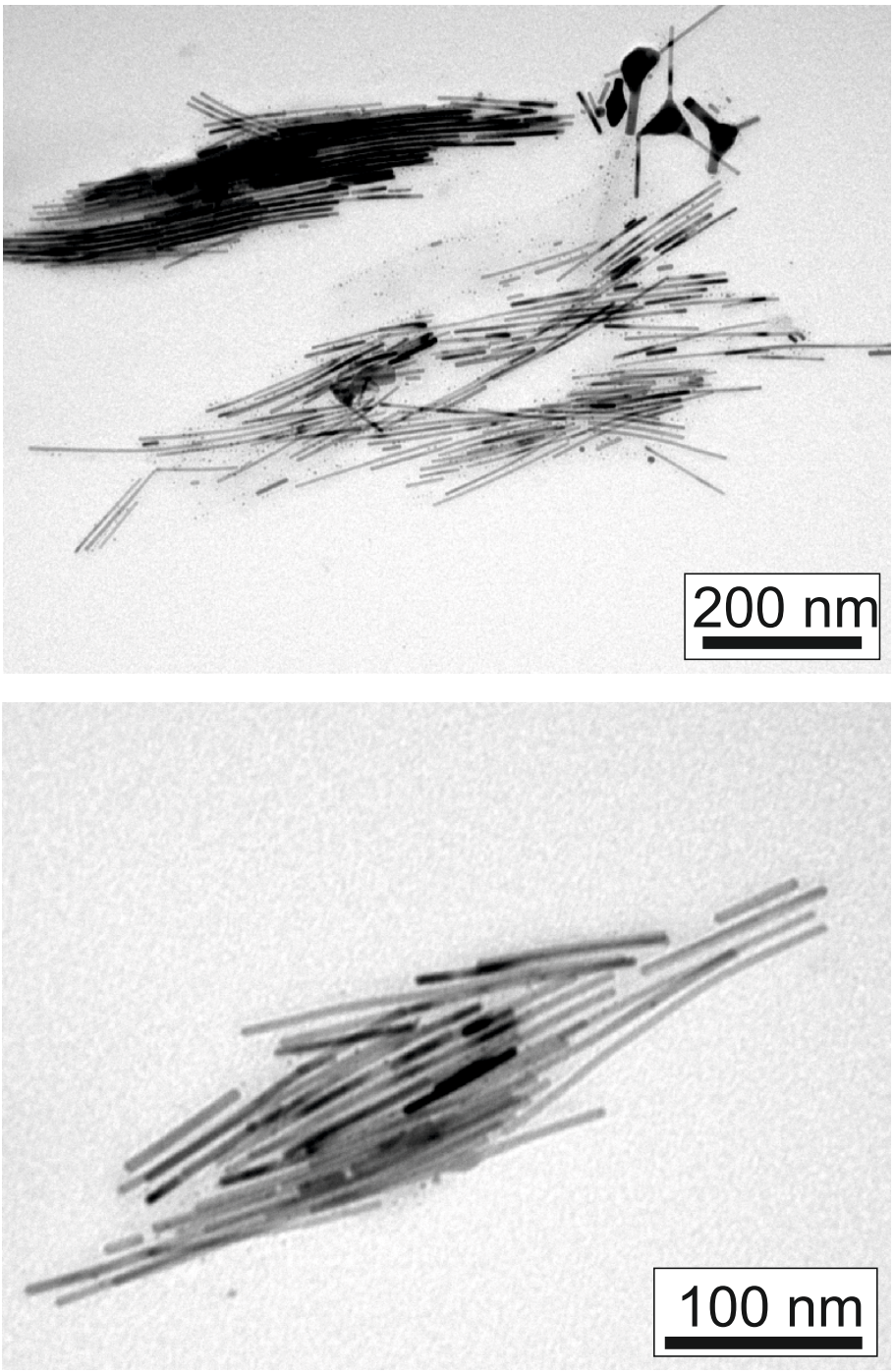

Figure 3.1.: TEM overview images of the Co nanorods used for the XPEEM investigation discussed in chapter 7 (p. 147). For details on the synthesis, please see [172].

3.3. Synthesis of Fe-oxide Nanocubes and Polyhedra

For the nanocube synthesis, the decomposition of iron oleate in octyl ether in the presence of oleic acid yielding monodisperse iron oxide nanocrystals was used. This route is based on the work by Park et al. who also proposed different morphologies [170]. Here, however, a different solvent (squalene) was used and a small amount of sodium oleate was present in case of the nanocubes [170]. It was also found that these particles have a pseudocubic shape with small {110} and large {100}-facets, and most of them exhibit a core/shell-structure with a typical oxide-shell thickness of about 3 nm. The nanocubes used in this thesis were dissolved in squalene/tetracosane 50/50 wt% and further diluted in hexane. A small amount of THF was also added to the solution. For all samples, a 10μL drop of the solution was deposited onto the substrate. The mean diameter of the particles was 18.1 ± 0.8 nm with a center-to-center distance of 20.1 ± 1.8 nm, i.e. the particles are separated by about 2 nm.

Octahedric Fe/Fe-oxide nanoparticles were synthesized as described in [171] and dissolved in toluene. Shavel et al. found also metallic Fe-rich areas by XPS and determined the structure of the oxide shell as Fe_2O_3(maghemite). Due to their large size of about 50 nm, the octahedra have a blocking temperature of about 370 K and an open hysteresis at room temperature. Deposition of single - non-agglomerated - particles onto the substrate was not possible due to the strong magnetic dipolar interactions resulting in agglomerations. A mixture of the particle solution and THF, however, seemed to improve separation. Representative TEM images and magnetic measurements of both sample systems are shown in Fig. 3.2.

3.4. Sample Design

The two x-ray magnetic imaging techniques (XPEEM, MTXM) required different sample preparation [(50 μm) Si-substrates (XPEEM) or Si_3N_4-membranes of 100 - 200 nm thickness (MTXM and XFTH[1])]. The samples were marked by Au crosses to find the same sample position in the x-ray microscope and SEM. The fabrication of the Au-marker is described in section 3.4.1, while section 3.4.2 deals with the preparation of a heating device on a Si_3N_4-membrane. For SEM and SQUID measurements, the particles were deposited on conventional Si-substrates and on standard carbon-coated (thickness about 100 nm) Cu-grids for HRTEM investigations.

[1] X-ray fourier transform holography (XFTH). Not followed up in this thesis. For more details see [178, 179]

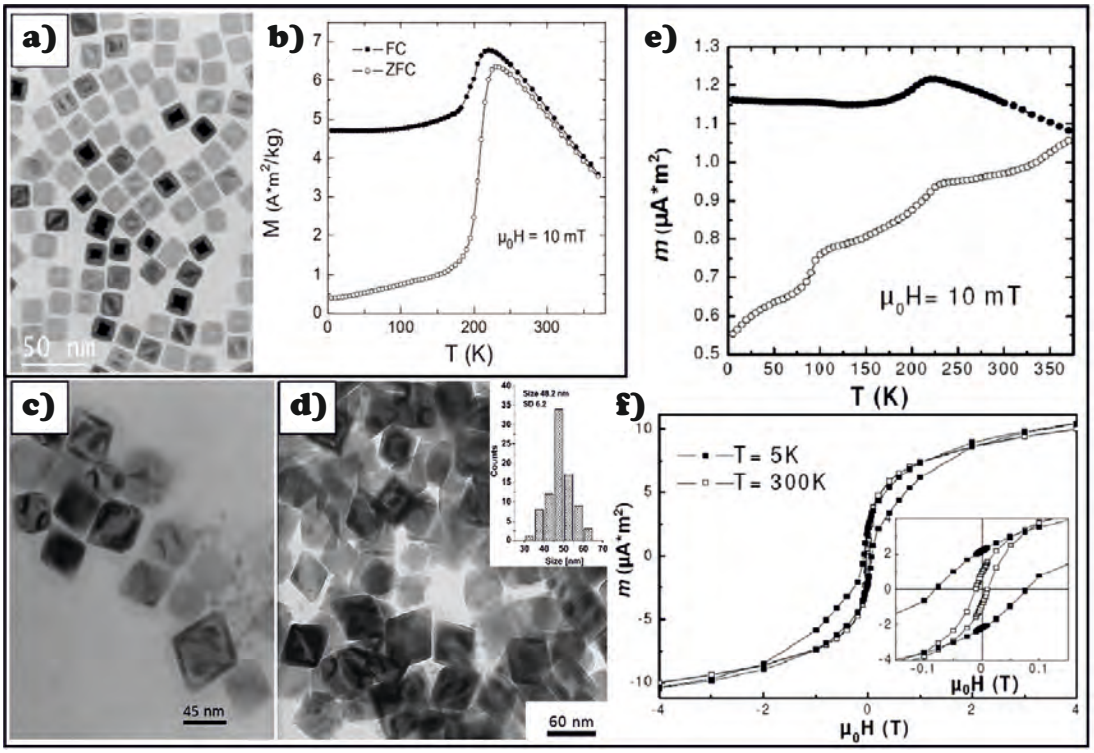

Figure 3.2.: [170, 171]. TEM micrographs of colloidal Fe/Fe-oxide nanocubes (a) and of colloidal Fe/Fe-oxide nanooctahedra (c), (d). The nanocubes are monodisperse with a mean diameter of 18 nm and for the nanooctahedra the size distribution yields a mean diameter of 48 nm (d). ZFC/FC SQUID measurements for the surface-oxidized cubes of (a) are shown in (b) and for the octahedra in (e). Hysteresis loops for the octahedra measured at 5 K and 300 K are presented in (f). For 300K the coercive and the irreversibility field are 100 Oe and 1 kOe, respectively.

3.4.1. Au-Markers for XPEEM and MTXM studies

A numbered array of crosses was fabricated which could also be used for focusing and alignment (correct for astigmatism) in XPEEM and MTXM studies. The fabrication was standard e-beam lithography on Si-substrates or Si_3N_4-membranes as schematically shown in Fig. A.1. For more details, see figure caption. In case of the membrane e-beam process, a thin (5 nm) Au-film was evaporated onto the resist before exposure to the e-beam to avoid charging effects due to the isolating substrate. Exemplary SEM pictures of Au-markers on an XPEEM sample are shown in Fig. 3.3.

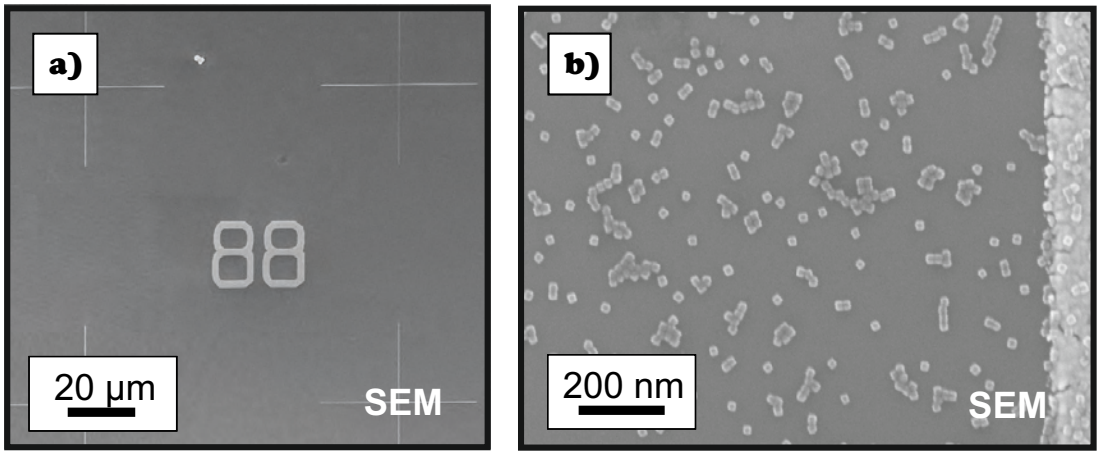

Figure 3.3.: Representative SEM images of XPEEM samples with lithographically prepared Au-makers after deposition of Fe nanocubes as described in chapter 3.3, p. 46. (a) shows an Au-marker array consisting of crosses and a number. (b) is a zoom next to a bar of a cross (right).

3.4.2. Heater Samples for MTXM studies

One purpose of MTXM experiments was to locally heat the particles above their blocking temperature. Heating the whole sample stage and holder induces too large drift effects which limit or even impede high resolution x-ray imaging [159]. Due to this fact and the beam line setup with narrow space at the probing position, a new sample holder was developed. An ohmic heating should be implemented in the sample itself so that very confined heating becomes possible. A similar idea was proposed by the Hellman group aiming at heat capacity measurements using an e-beam lithographically fabricated nanocalorimeter on the Si_3N_4-membrane during x-ray imaging [180]. In our case, local ohmic heating was achieved by driving an electrical current through a lithographically prepared heating structure (Fig. 3.4) on a Si_3N_4-membrane.

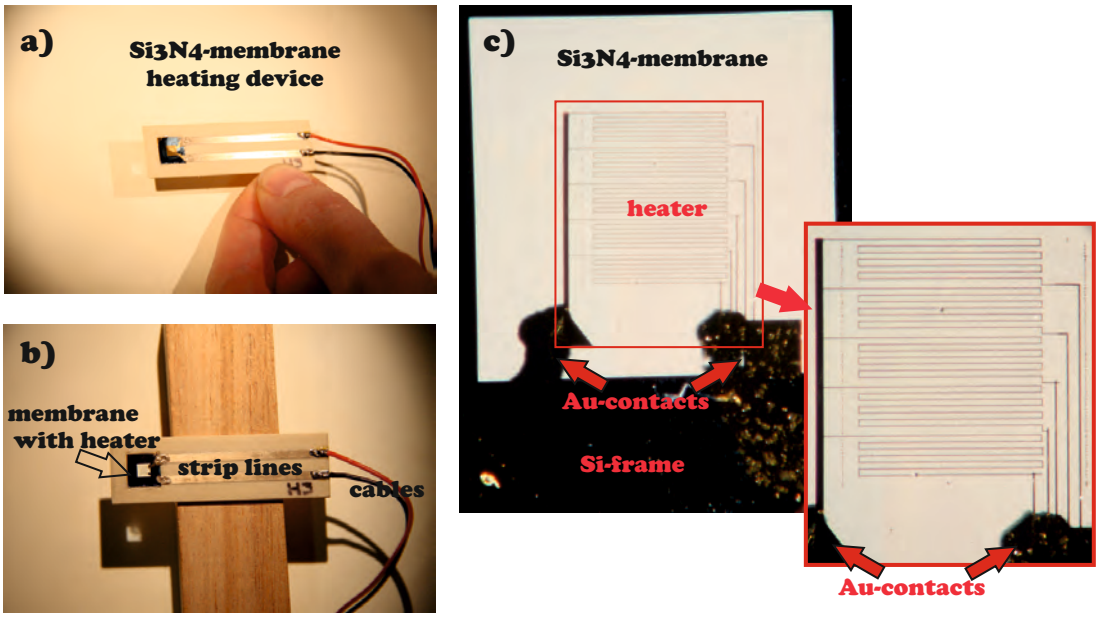

Figure 3.4.: Optical micrographs of a Si_3N_4-membrane heating device. (a), (b) Overview images showing the membrane heating device with the strip lines and the membrane heater sample. Electric input lines are realized by soldered cables at the end of the strip lines. The dimension of the whole sample holder is 50 mm × 15 mm × 0.81 mm. The side length of the membrane is 3 mm with a thickness of 100 nm and the Si-frame size $75 \times 75\,\mathrm{mm}^2$. The membrane with the heater device is shown in (c) and the enlarged device itself is shown in the cutout. The heater consists of five parallel heaters made from Au-strip lines of 80 nm thickness. The triangles at the bottom are contact patches. The Au-contacts over the Si-frame (can weakly be seen on the bottom right in (c)) are evaporated through a mask. Electrical contact to the strip lines on the ceramic was realized by silver conductive paint. Note, that on the membrane a drop of nanoparticle solution was already deposited. This drop dried mostly in the top right corner of the membrane which can be seen in (a) and in the shade in (b).

The membrane was fixed by nail polish in a ceramic (RO4003C by Rogers)[2] sample holder with two strip lines, which were fabricated by optical lithography, consequent etching and gold-coating. Input lines are soldered to the end of the strip lines so that it can be connected to a power supply (e.g. Keithley 2400). This sample holder design is based on a standard microwave guide sample holder at XM-1.

The e-beam and lift-off process for the heating device is very delicate (80% loss). Apart from the large, thin membranes, which are strain sensitive, the heater strip lines are small and narrow and also the Au-adhesion on silicon nitride is rather bad. Therefore, 5 nm Ti was evaporated as an adhesive layer before the evaporation of 80 nm Au (Fig. A.1 d). Furthermore, the heater was optimized by a design of 5 parallel heaters with 6 loops each. The advantage of 5 parallel heaters instead of a single one with many loops is that if there were any short circuit in one or several of the 5 heating structures due to a non-optimal lift off, the other ones would retain their functionality.

3.5. Low-Energetic Plasma Treatment & Al-capping

Nanoparticles synthesized by wet chemical approaches are stabilized by surrounding ligands in solution; in our case typically carboxylic acids (COOH) and amines (NH_2) with long (1 - 2 nm) aliphatic chains. These ligands remain adsorbed at the surface of the nanoparticles after deposition onto a sample substrate impeding a direct contact. Furthermore, they also act as a natural spacer when the nanoparticles are deposited. This becomes important when considering the strength of dipolar interactions (s. Chapter 1.2.2.4) between several particles. Once the particles are exposed to air, natural oxidation starts. In this work, the magnetic properties of as prepared and "pure" (reduced and ligand-free) Fe particles are investigated. Thus, the ligands had to be removed and Fe-oxide had to be reduced to Fe. Both can be addressed by applying an oxygen and/or hydrogen plasma [181, 182]. The carbon molecular chains react with the oxygen plasma resulting in volatile CO/CO_2-gas. The use of reactive oxygen, however, also leads to unavoidable further oxidation of the particles. Subsequent hydrogen plasma is applied to counteract this process. The hydrogen reacts with the superficial oxygen resulting in the formation of H_2O-molecules which can be pumped out. Recent investigations have shown that hydrogen plasma alone is sufficient, and the use of oxygen plasma is avoidable [81]. To avoid any sample damage, the plasma needs to be low-energetic (soft). Detailed investigations on the plasma influence on the sample structure have been performed by A. Trunova [107]. No change of position and particle shape was observed by TEM and SEM.

[2] Polymer resin with glass fibre and ceramic powder, Cu capped from both sides (35 μm)- micro wave guide material

The plasma setup has also been modified in this work from a capacitive to an inductive generator. This modification was necessary due to possible Cu contamination caused by sputtering of the inner electrode (Cu cylinder) of the UHV coaxial capacitor during the plasma process. In the modified setup, the Cu coaxial capacitor is replaced by a glass cylinder enclosed with a Cu coil, which also proved to be more effective. More detailed technical information can be found in [107]. Typical plasma parameters used for samples investigated here are:

Capacitive Plasma

- ignition of O_2 plasma at 0.5 mbar, then reduction to 0.05 mbar with a power of 30 W, 20 min
- ignition of H_2 plasma at 0.7 mbar, then reduction to $0.07 - 0.075$ mbar with a power of 30 W, 2.5 h

Inductive Plasma

- ignition of O_2 plasma at 0.05 mbar, then reduction to 0.025 mbar with a power of 20 W, $15 - 20$ min
- ignition of H_2 plasma at 0.15 mbar, then reduction to 0.05 mbar with a power of 20 W, < 2 h

Subsequent to the plasma treatment, the ligand- and oxide-free nanoparticles were in-situ capped by an evaporated Al-film (~ 4 nm) to prevent them from re-oxidation. Al was chosen, since it has no absorption edges in the vincinity of the Fe-edges which would disturb the XMCD measurements at the synchrotron sources. Furthermore, for XPEEM and x-ray transmission studies, the capping material has to be as electron transparent as possible. This is why Ag capping with subsequent Pt[3] capping was excluded. Earlier samples were Al-capped in a different chamber. The sample transfer from the plasma to this preparation chamber took approximately 10 minutes and was performed under Ar atmosphere to limit the re-oxidation. In this chamber, the Al was magnetron sputtered after additional hydrogen plasma treatment (0.002 mbar, 40 mA) for about 1.5h with an ECR plasma source (Tectra GenII).

For XPEEM-studies of different oxidation states in the nanoparticles, the plasma setup, which is usually adapted to the transfer chamber of an UHV preparation and analysis chamber in Duisburg [183], was transferred to BESSY. At the Beamline UE49-PGM-a-SPEEM, it was connected to the load lock of the preparation chamber of the SPEEM end station (see Fig. 3.5). Thus, an in situ transfer of the plasma treated sample into the PEEM was achieved.

[3] Ag/Pt is commonly used for capping of Fe. The Ag lattice fits well to the Fe lattice and forms no alloys. But since oxygen diffuses through Ag, an additional passivating capping like Pt is needed.

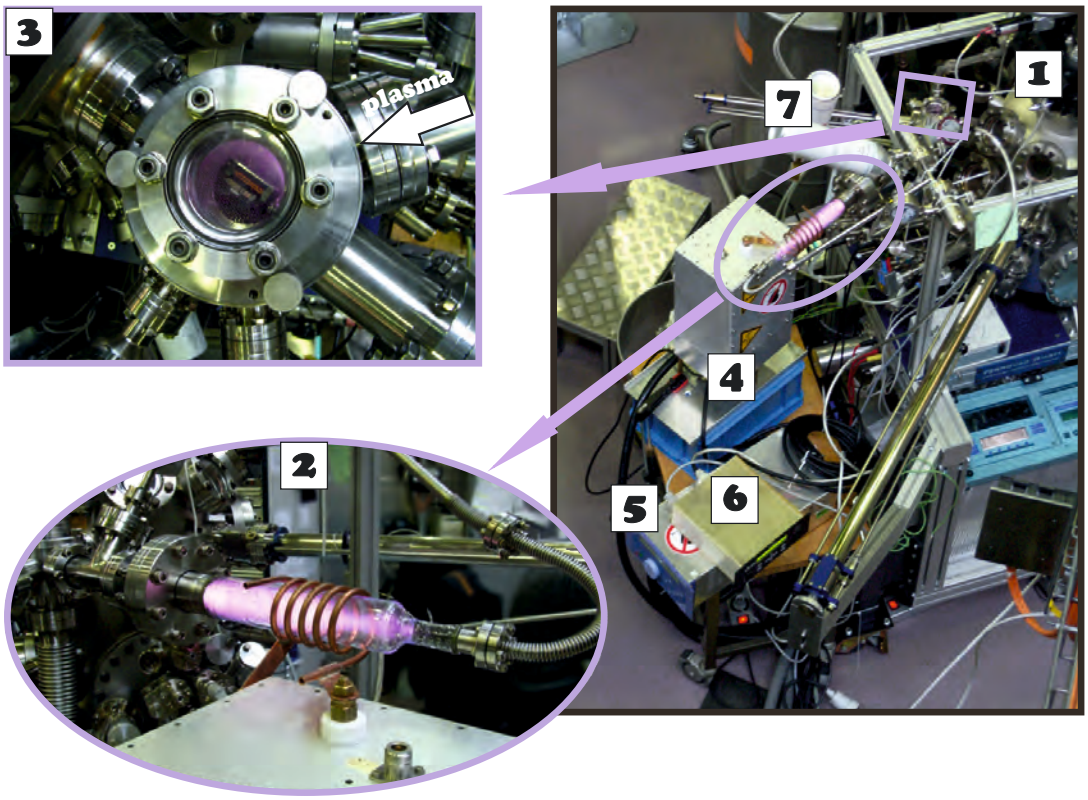

Figure 3.5.: Photographs of the plasma setup at BESSY, Berlin. The plasma equipment is connected to the standard preparation chamber (1) of the SPEEM end station setup. The glass finger, in which the plasma is inductively enlightened (copper coil) is shown in more detail in a cutout (2). The sample itself is positioned in the load lock (3) of the preparation chamber, facing the plasma under $\sim 35°$ incidence angle. (4) rf-generator and power supply (5), baratron (6) and standard laboratory gas bottles - H_2, O_2(7).

4. Oscillatory Surface Relaxation in Fe_xPt_{1-x} Nanoparticles

In this chapter the layer-resolved lattice spacings for two differently synthesized Fe_xPt_{1-x} nanoparticles are presented. Phase images retrieved by focal-series acquisition in the TEM with subsequent exit wave reconstruction (Chapter 2.1.1, p. 33) were used. Aberration corrected, reconstructed phase images were obtained with a lateral resolution of 0.8 Å and due to their large signal-to-noise ratio, they allow for direct pinpointing of atomic column positions with a precision of several pm [184]. Layer spacings were determined by the acquisition of phase intensity line-scans perpendicular to the facets utilizing the DigitalMicrograph software (by Gatan) and measuring the distance between successive peaks. The data represent a refined analysis of a preliminary determination of lattice spacings in my diploma thesis [16].

4.1. FePt Nanoparticle from the Gas Phase

In Fig. 4.1, the HRTEM data of a gas phase synthesized, chemically disordered, twinned FePt nanoparticle of about 6 nm diameter [16], which is typical for the preparation conditions and this size, is presented. The lattice image obtained by conventional HRTEM is depicted in (Fig. 4.1 a). Delocalization effects are apparent and obscure the identification of atomic columns and the surface. The twin boundary can only be identified in the reconstructed phase image (Fig. 4.1 b) and the fast Fourier transformation (FFT) image (Fig. 4.1 c). The results of the lattice spacing analysis are displayed in Figs. 4.2 and 4.3. All diagrams are built up as follows: Left y-axis gives the spacing as a function of layer number which is measured from the surface to the core. That is, the lattice spacing 1 corresponds to the distance (d) between surface and subsurface layer, lattice spacing 2 to the distance between subsurface and subsequent layer and so on. In the discussion, the nomenclature $d_{x/x+1}$ (x = 1: surface layer) will be used. The right y-axis gives the relative deviation from the bulk lattice spacing. Error bars for the individual line scans are 5 pm. For the average of several scans, the standard deviation is the error bar.

In Fig. 4.2, layer-resolved lattice spacings for three {111}-facets of the bottom twin area of the particle are presented. Left, bottom and right indicate the position of the surface layer which served as the starting point of the scan. Additionally, the average of all scans acquired along all <111>-directions in the particle (also in the upper twin) is shown. For the latter, the two {111}-facets exhibit a step-like surface structure, and

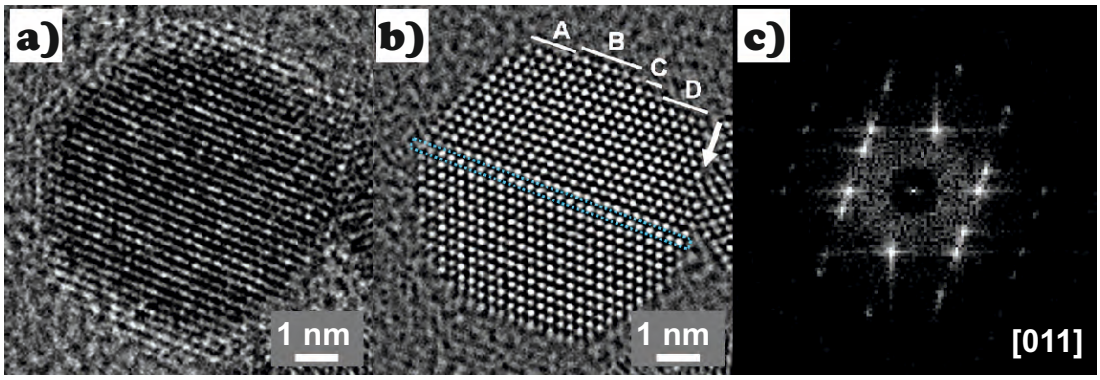

Figure 4.1.: Gas phase synthesized cuboctahedron FePt nanoparticle. (a) Conventional HRTEM lattice image at Scherzer defocus. (b) Reconstructed phase image of the same particle. The corresponding FFT is shown in (c). Note that the twinned structure of the particle is only revealed in the phase image and by the double reflexes in the FFT, i.e. after exit wave reconstruction. The common (111)-plane defining the twin boundary is marked by a dashed box. The arrow in (b) indicates the direction of the surface terraces (A - D) resolved line profiles presented in Fig. 4.3 c.

the scans were taken along the width of each terrace. For the upper facet, the terrace resolved layer spacings are plotted separately in Fig. 4.3 c, where A, B, C and D mark the corresponding step. The arrow marks the scan direction of the intensity profiles for this facet. In the following, the results for the <111>-directions in the bottom twin (Fig. 4.2) are discussed.

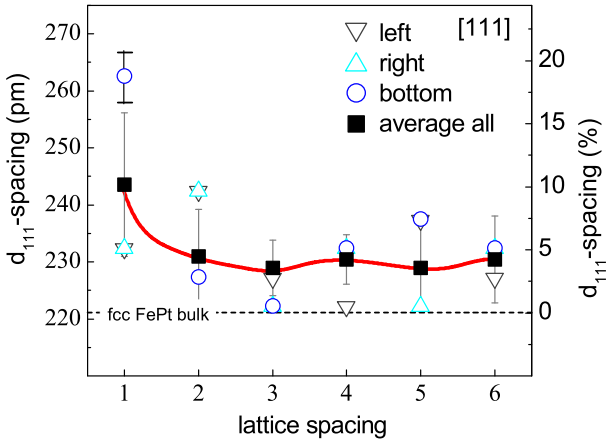

Figure 4.2: Lattice spacings measured from the three {111}-facets of the bottom twin of the FePt nanoparticle shown in Fig. 4.3 b. The red line is drawn as guide to the eye.

Note that a general expansion of the lattice spacing of approximately 5 % with respect to the bulk parameter is observed, as also reported in previous work, e.g., [16, 76, 185]. This expansion is immense (about +18%) for the bottom surface layer whereas right and left facets only show an expansion in the order of +5%. In case of the bottom layer, the lattice spacing decreases constantly until it reaches almost the bulk value for the $d_{3/4}$-spacing. For the $d_{4/5}$- and $d_{5/6}$-spacings, a continuous increase of up to +7.5% with respect to the bulk is found. It then drops again. The net result is an apparent oscillatory lattice layer relaxation starting with a huge expansion followed by an oscillation with 2-layer periodicity and relative amplitude in the order of ±3%.

For the two opposite side scans, the behavior is completely different. $d_{1/2}$ is compressed by almost 5 % with respect to $d_{2/3}$ and has even smaller values for $d_{3/4}$. From there on, an oscillatory spacing with an amplitude of about 2 % and one layer periodicity is observed from the right side. There are also d-spacing oscillations for the left side scan, however, with no distinct periodicity. The total <111> average (10 individual scans) relaxation behavior shows an outward relaxation of the surface layer of about 10 % followed by a damping over a two layer distance down to a value of +3% expansion with respect to the bulk. There is also evidence for subsequent oscillations with a relative amplitude of ±1%. However, the amplitude of the d-spacing oscillations is smeared out in the average as there are different periodicities of the individual directions.

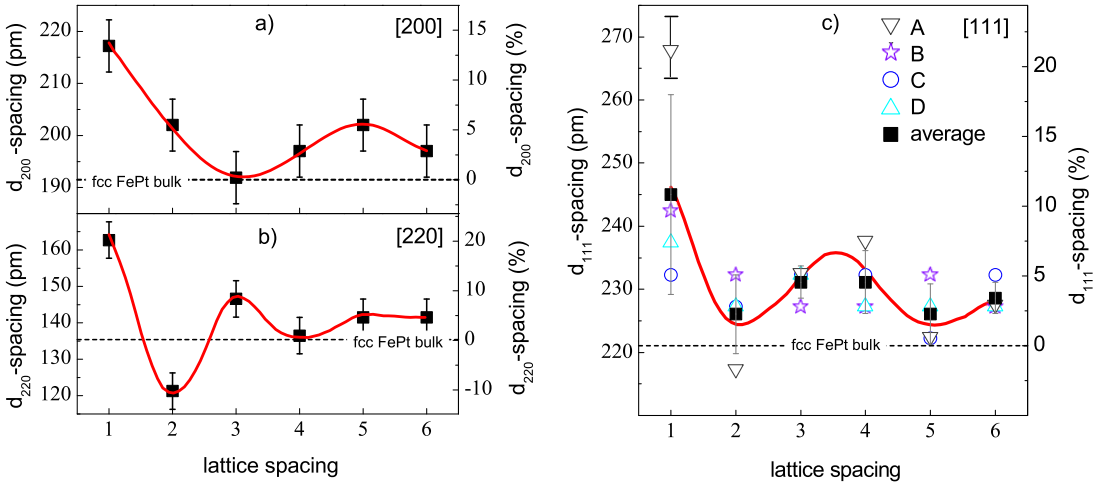

Figure 4.3.: Layer-resolved lattice spacing of the gas phase synthesized nanoparticle as shown and indicated in Fig. 4.1. Additional data of the <111>-directions are presented in Fig. 4.2.

In a next step, the spacings perpendicular to the different terraces of the upper {111}-facet were analyzed. The results are shown in Fig. 4.3 c (labelling according to Fig. 4.1 b). The averaged line-scans yield again a large outward relaxation of 10 % with respect to the bulk for the outermost surface layer in good agreement with the results for the lower twin. In case of the surface layer of terrace (A) an expansion in the order of 20 % was determined, similar to the outermost 'bottom' surface layer. This huge d-spacing is based on the large outward movement of the left most two atom columns. The positions at the borders of several facets are often not occupied (missing row structures) [74, 75] as they are less favorable from the energetic point of view due to their reduced coordination. Here, however, the rows are occupied but moved further away from the particle core resulting in bent surface layers and enhanced outward relaxation. Also, the A-facet spacings show a pronounced ocillatory behavior with non-constant periodicity and relative amplitude of more than 3 %. Note that $d_{2/3}$ is even smaller by - 2 % when compared to the bulk. Apart from this value, all other spacings are expanded.

The general trend of an outward relaxation of the outermost layer can also be confirmed for facet steps B - D (+ 5 -10 % with respect to bulk FePt). The inner d-spacings oscillate at no constant periodicity. Only for facet step D a strongly damped (relaxed at $d_{4/5}$) oscillatory behavior with one-layer periodicity can be assumed. The C-terrace exibits larger relative amplitudes within the inner part of the particle. Due to the partly opposed relaxation behavior perpendicular to steps A - D, the average gives also varying lattice spacing, but a pronounced oscillatory relaxation (as suggested by the red line) cannot be confirmed. Most probably, the reason for the very different behavior is the different size of the terraces. Smaller facets like C (3 atomic columns in surface) will be more strongly influenced by the surrounding configuration than larger and especially outermost ones. For a perfect symmetric particle, the same relaxation behavior for opposite facets can also be expected by neglecting the effect of the substrate carbon layer. Indeed the relaxation along the common <111>-direction of the twin, i.e. in the B-direction and perpendicular to the bottom {111}-facet, is very similar to that with a 2-layer periodicity.

As a first conclusion for the <111>-directions, there is evidence for an oscillatory surface relaxation and a large outward relaxation of the surface layer. Two exceptions were found: a) very small facets (3 surface atomic columns) and b) atom columns which are part of a twin boundary. For b), no additional strain due to the boundary is expected from bulk material. Note also that there is a connection to the particle on the right side, possibly leading to additional strain. In this projection of the particle, one sees only one {100}- and one {110}-facet, i.e., {200} and {220} surfaces, in the bottom twin. The results are shown in Fig. 4.2 a, b. d_{200}- and d_{220}-spacings are determined. Furthermore, oscillatory relaxation with two (a) and one (b) layer periodicity is found, and its magnitude is larger for the more open {220}-surface as expected from theory [36]. The latter additionally shows a strongly damped relaxation which seems to vanish at the 5th subsurface layer. In both directions, a huge outward relaxation of the surface layer of up to 20 % for the {110}-planes is observed.

4.2. $FePt_3$ Nanoparticle from Organometallic Synthesis

Due to the organometallic synthesis of the nanoparticles, organic ligands cover the surfaces of the particles. The chemical bond influences the electronic properties at the surfaces and leads to structural relaxation [55, 186]. Furthermore, open surfaces as the {220}-surface may allow easier carbon diffusion into the particle which will also significantly alter the electronic structure and a more complex relaxation behavior is expected with respect to the 'clean' particles from the gas phase. Note, that for pure Pt bulk systems carbon has a very low solubility and Pt-carbides have only recently reported at high pressures and high temperatures (P≈ 60 GPa, T≈ 2000 K) [187]. For an Pt-rich Fe_xPt_{1-x} nanoparticle, the Pt atoms are likely to diffuse towards the surface and the carbon not likely to dissolute into the particle based on the bulk findings. Nevertheless, in nanoparticles, which exhibit a huge surface area and a different electronic structure in comparison to the bulk, a different solubilizing behavior of the carbon may occur.

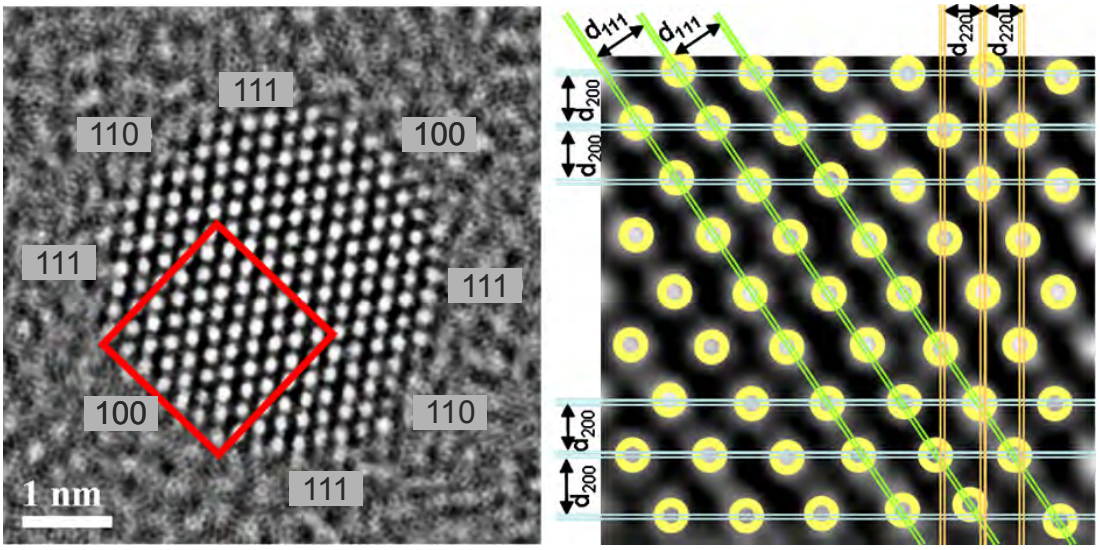

Figure 4.4.: Left: Reconstructed phase image of wet chemical synthesized $FePt_3$ nanoparticle. Right: Zoom into left phase image as marked by the red square frame. The bottom layer is the (100)-surface layer. Yellow circles mark the position of atomic columns and some lattice layer spacings are exemplarily drawn.

Fig. 4.4 shows the reconstructed phase image of an $FePt_3$ truncated cuboctahedral nanoparticle prepared by organometallic synthesis. The different facets are indicated. The particle has a diameter of about 4 nm and is almost symmetric: Though energetically very unstable there is a (110)-facet on the left. A small (110)-facet may also be present on the right side of the particle. The lower right particle edge is rather built up of two {111}-facets with some missing or incomplete atomic columns in the right (111)-surface plane. Note also that three of four atomic columns at the edges of the {111}- and {100}-facets are missing.

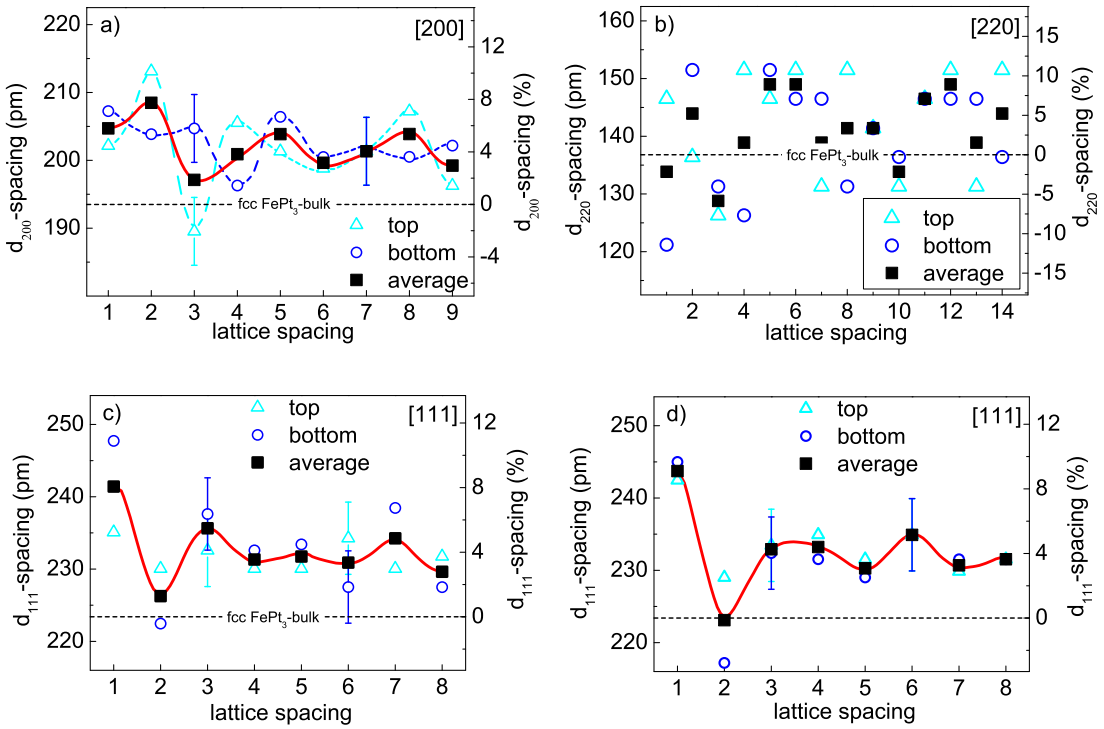

Figure 4.5.: Layer-resolved lattice spacings for organometallic synthesized $FePt_3$ nanoparticle in three directions throughout the whole particle. Spacings are determined perpendicular to: {100}-facets (a), {110}-facets (b), and {111}-facets (c) and (d). In (d) "top" refers to an intensity line scan from left to right and "bottom" to a scan from right to left perpendicular to the correponding {111}-facets. Red lines are guides-to-the-eye for average values.

The right part of the figure shows an enlargement of the atomic columns from the area marked by the red box. The position of the columns (center of intensity) is indicated by the yellow circles. The bottom layer is the lower (100)-surface layer. There are also two single atomic columns on top of this layer (below the frame) which were not included in the analysis of the layer spacings. The right graph also depicts some paradigmatic layer spacings in three different directions. The (100)-surface layer is strongly corrugated. Additionally, the intensity distribution around the columns is also blurry indicating an irregular lattice in this part of the particle.

The lattice layer relaxation from the bottom (100)-surface layer towards the core is given by the circles in Fig. 4.5 a. The triangles indicate the relaxation from the opposite facet. Both show oscillating lattice spacings, but with no special periodicity and partly also with opposed trends. In the bottom case, the surface layer is complete, and $d_{1/2}$ is slightly expanded with respect to $d_{2/3}$.

For the relaxation from the top of the particle, where one atomic column in the surface layer seems to be missing or incomplete, the trend is opposite. $d_{1/2}$ is slightly contracted by about - 5 % with respect to $d_{2/3}$. $d_{3/4}$ is also contracted by about - 12 % with respect to $d_{2/3}$ and thus also slightly smaller than the bulk value for $FePt_3$. Apart from this value, all other spacings are expanded when compared to the volume of the materials. Panel (b) of the same figure shows the spacings perpendicular to the {110}-facets. As described previously, these facets are quite open and on the right side of the particle not well-defined ("bottom" in the diagram). Values in both directions show no regular relaxation behavior and vary around the bulk value in a range of ± 10 % within a tendency to enlarged spacings when compared to the bulk. Along the <111>-directions (c), (d) the behavior is more regular. The average for both directions shows a $d_{1/2}$ enlargement (+ 8 %) with respect to $d_{2/3}$. $d_{3/2}$ is expanded again in all 4 cases. Deeper layers are equally spaced within ± 2 %.

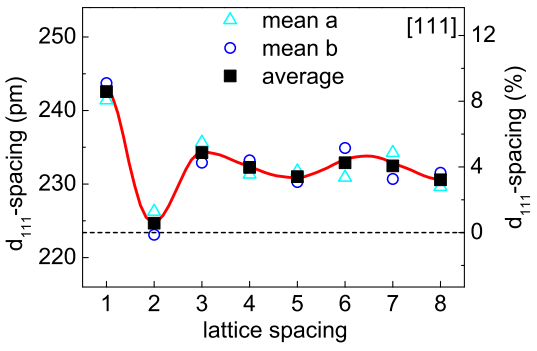

Figure 4.6: Comparison of average <111> surface relaxation results in $FePt_3$ nanoparticle. Here, the scans a b are the average scans along the two <111>-directions as shown in Fig. 4.5 c (mean a) and d (mean b), i.e. they show the averaged surface relaxation from two opposite facets. Averaging these two directions results in the data represented by the black squares.

Interestingly, the horizontal spacings (d) are very symmetric apart from the second spacing (about 6 % difference). The lattice spacings determined from the left and from the right side differ by about 2 pm maximum.

Comparing the averages of both <111>-directions (Fig. 4.6) also reveals a rather regular relaxation behavior. The trend is the same in both directions, and the maximum deviation of the two averages is smaller than 2 %. As found for all other directions, {111}-lattice spacings are also enlarged with respect to the corresponding $FePt_3$ bulk value.

4.3. Discussion & Conclusion

In summary, the layer-resolved analysis for two differently synthesized nanoparticles revealed:

1. a general lattice expansion of several percent with respect to the corresponding bulk value.

2. damped oscillatory relaxation behavior from the surface to the core, which is more evident in the 'clean' gas phase particle than in the particle prepared by organometallic synthesis (the magnitude of these oscillations is in the range of several percent).

3. complex, direction dependent relaxation behavior and a scaling with the openness of the surface.

4. a huge outward relaxation of up to 20 % of the outermost surface layer.

(1.) is in good agreement with other experimental findings for FePt nanoparticles by x-ray absorption measurements and TEM studies [16, 76, 185]. XAS revealed a 1-2 % lattice expansion for oxide-free FePt nanoparticles [76], i.e., it is an intrinsic property and not related to the presence of oxides.
(2.) confirms what theoretical models [188, 189] predict for the bulk, except for the experimentally observed outward relaxation which is contrary to theoretical predictions [34].
Theory for bulk transition metals [35, 36] also predicts that the magnitude of the oscillations increases with the openness of the surfaces. This is confirmed here (3.). The more open {200} and especially the {220} surfaces show huge outward relaxations (+ 15 - 20 %), whereas the smoother {111}-surface shows a smaller outward relaxation (+ 10 %). The latter is also in good agreement with previous observations in FePt icosahedral gas phase nanoparticles, where indications for oscillatory layerwise relaxation can also be seen but were not discussed [74].
The oscillations in the <111>-directions of the chemically synthesized particle are found

to be more complex than the gas phase one, although both agree well in magnitude. One reason for the different relaxation behavior in both particle types is certainly the different chemical composition. The colloidal particle is Pt-rich and covered with organic ligands. Generally, adsorbates change the LDOS at the surface [186], and consequently, the lattice distortion is expected to be larger in the presence of ligands. Nevertheless, observation of oscillatory-like layer relaxation in both clean and colloidal nanoparticles supports the assumption that this effect is an intrinsic property of the Fe_xPt_{1-x}-system. The models used to explain oscillatory layer relaxation in the bulk do not provide an explanation for the magnitude of the general outward relaxation of the first surface layer observed by HRTEM (4.).

Du et al. also found an outward relaxation of the surface planes in Pt-nanoparticles, which was related to an amorphous oxide and or to dissolution of oxygen on subsurface sites [77]. Wang et al. showed by controlled removal of the surface layers that the large surface layer relaxation in icosahedral FePt-nanoparticles is not due to oxidation but possibly due to a Pt segregation to the surface [74, 75]. In our studies, a first qualitative analysis of the phase information did not reveal conclusive prove of Pt segregation but rather a non-uniform distribution of Fe and Pt atoms within the particles. Furthermore, only an outward relaxation of about 1 % is expected from experiments for both clean and H_2/CO-covered Pt bulk surfaces [52, 54]. Therefore, oxygen and Pt segregation as the only origin can be ruled out.

This leads to the possibility that the effect might be related to the presence of small carbon traces unavoidable in HRTEM studies, since standard HR sample grids have an amourphous carbon coating. To address the questions of the influence of carbon towards the structure of FePt nanoparticles DFT calculations using the Vienna Ab Initio Simulation Package were carried out by M. Gruner. The chemically disordered cuboctahedral FePt test particle consisted of 309 atoms and a shell of 252 carbon atoms was placed around that particle. Fig. 4.7 shows the model of the particle prior (top) and after (bottom) structural relaxation. On the left hand side, simulated TEM contrast images of the particle are shown in projection onto a (110) plane. Every atomic columns is represented by a Gaussian function, where its integral is proportional to the $Z^{2/3}$-dependence of the intensity in HRTEM imaging, and its width is proportional to the atomic diameter.

The carbon has a huge influence on the structure of the particle as it diffuses into the particle's surface shells and dramatically modifies the surfaces. Strong modification especially of the more open {200} surfaces becomes obvious. Outside the particle, the carbon forms chains. Corrugations of the atomic columns in the planes and also a general outward relaxation of the surface layer is evident, and also 'blurry' atomic columns in the approximated TEM image as found in the experimental data can be explained by carbon. As described previously, this result is in contrast to reported bulk behavior for Pt-rich alloys [187]. A high mobility of surface atoms and the huge surface, which is very open for some facets, are possible explanations. Therefore, the large outward expansion of the surface found here might be attributed to the presence of carbon.

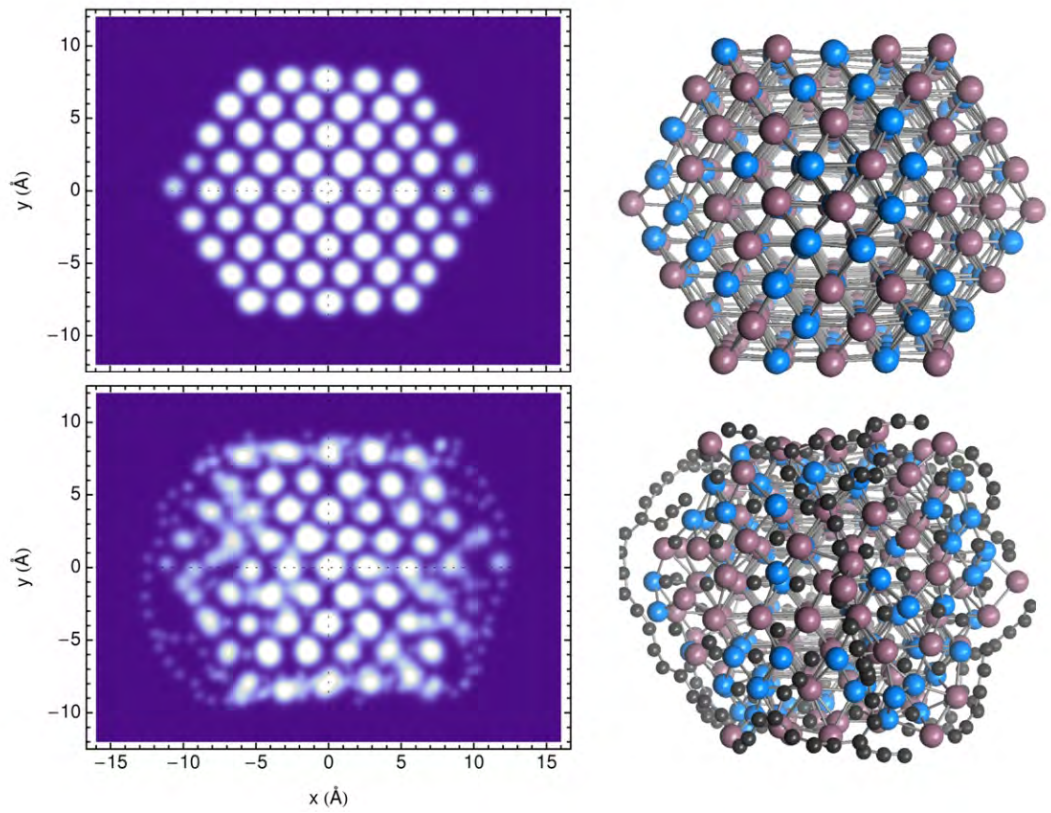

Figure 4.7.: Simulated FePt-nanoparticle consisting of 309 atoms (chemically disordered). Fe atoms are represented by blue, Pt by brown spheres. The cluster was surrounded by a shell of 252 carbon atoms (black spheres) which are allowed to diffuse into the particle causing a structural deformation. The left shows approximated TEM contrast images based on atom positions of the models on the right. The atom positions are projected onto a (110) plane. [Courtesy of M. Gruner]

Other possible origins could be charging of the particle by the interaction with the electron beam. Positive and negative structural relaxation in Au_{309} clusters were calculated for negative and positive charging [190]. DFT calculations to investigate the charging aspect were also performed by M. Gruner. These calculated results did not find large outward relaxation. Since FePt is a magnetic system, the magnetic field of the objective lens (which can be more than 1 T) might also induce magnetostriction in the particle. Literature, however, only gives a value as small as 0.8 % for Invar Fe_3Pt [191], so this

effect can be ruled out as well. In this context, it is worth mentioning, that for magnetic materials the surface relaxation behavior is also determined by the magnetic configuration as found in the work by Hirschl et al. [55]. Here, for $FePt_3$ in a non-magnetic configuration the outward relaxation can be as large as 3.3 %.

In conclusion, strong evidence for oscillatory lattice layer relaxation in Fe_xPt_{1-x} nanoparticles is found. The magnitude of these oscillations can be related to the "openness", that is the reciprocal packing density, of the surface as predicted by theory [35, 36] for metal single crystals. The well accepted bulk phenomenon of oscillatory surface multilayer relaxation apparently may be transferred to bimetallic nanoparticles. It is, however, more complex in this case due to the three dimensional lateral limitation which can also be highly asymmetric. The presence of organic ligands at the surface further complicates the matter. This has to be considered in further theoretical calculations and may lead to a deeper understanding of single nanoparticle magnetism. Large outward relaxations of the surface layer which are often observed in HRTEM imaging could be attributed to structural modifications of the particle's surface layers by carbon. Since traces of the latter are always present in the TEM (especially if the standard Cu-grids with amorphous C film are used) this result is crucial for the analysis and interpretation of HRTEM nanoparticle images. Although the carbon has a dramatic influence on the particles' morphology, especially in case of the ligand enclosed metal organic synthesized ones, the oscillatory relaxation behavior itself can be not attributed to the carbon 'contamination'. Final confirmation that oscillatory relaxation is an intrinsic property of this or even other nanoparticle systems[1] can only be obtained by investigations in the absence of carbon or other contaminations.

[1] Recent studies of pure Pt nanoparticles by metallorganic synthesis also revealed oscillatory lattice layer relaxation [private communication Zi-An Li, in preparation].

5. Single Nanocube Hysteresis

5.1. Measurement and Data Treatment

This section describes the treatment of the raw XPEEM data and the extraction of the hysteresis loops or x-ray absorption data. Figs. 5.1 and 5.2 schematically display the experimental setup (a) and the way in which x-ray absorption spectra (b,c) and hysteresis loops (d,e) were obtained from the XPEEM images. Both, XAS and hysteresis data were extracted from the local intensities (several pixels) as a function of photon energy and magnetic field, respectively. For good statistics it was necessary to average up to several hundred of images at each field step of the hysteresis cycle or energy step in a XAS measurement. These image series yielding different information are called "scans" in the following:

XAS scan: The photon energy was varied in small steps (typically 0.2 eV) around the absorption edges and an image was acquired at each energy (acquisition time: 1 - 2 seconds). At the Fe $L_{2/3}$-absorption edges the scans were taken in the energy interval 700 - 740 eV. Linearly polarized light was used for probing the chemical state of the sample. XMCD XAS scans were acquired with circularly polarized light (σ^+ or σ^-). Up to 20 scans with alternating helicity ($\sigma^+/\sigma^-/\sigma^-/\sigma^+/...$) were acquired for good statistics .

Hysteresis Scan: The hysteresis data was recorded with circularly polarized light at the L_3 resonance. A typical number of field steps for a hysteresis loop was 24 and at each field of a the cycle up to four scans were recorded. Each scan typically contained about 120 - 240 images depending on the acquisition time (1 - 2 seconds) and thus on the stability of the system. To average out possible artifacts due to intensity fluctuations, the polarization was changed in regular intervals within a single scan. For example, a scan containing 240 images with 1 s integration time per image could have the following sequence:

$$20(\sigma^+)/40(\sigma^-)/40(\sigma^+)/40(\sigma^-)/40(\sigma^+)/40(\sigma^-)/20(\sigma^+).$$

The data was further evaluated using an IGOR Pro routine [192] allowing for element-specific quantitative analysis: several scans can be loaded at once, after normalization[1]

[1] Prior to each experiment a fully defocussed image is acquired for normalization. Before any further treatment each image was normalized to that reference to remove illumination artifacts resulting from

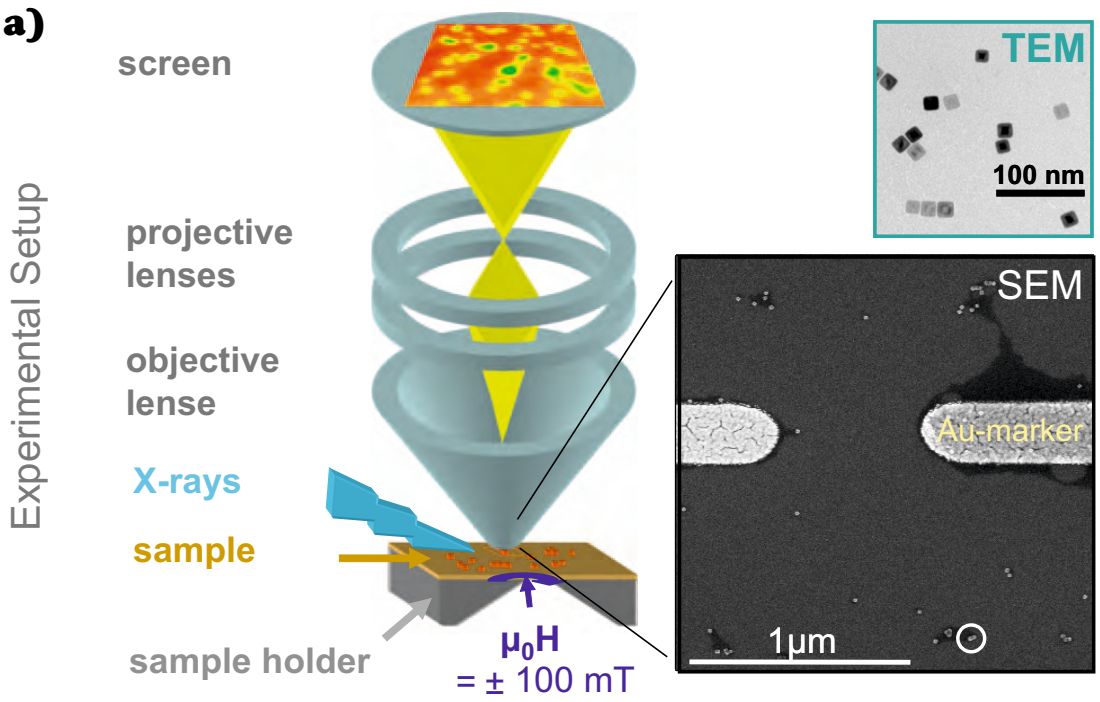

Figure 5.1.: Schematic representation of the experimental measurement setup used for magnetic imaging and spectro-microscopy (Figure 5.2) of individual nanoparticles in an applied magnetic field of up to ±100 mT. a) left: Schematic of the x-ray photoemission electron microscope with a magnetic yoke integrated into the sample holder; right: transmission electron microscopy image showing typical nanocube configurations and representative SEM image of a sample with Au-markers and Fe nanocubes.

and drift correction the images are averaged for each polarization (hysteresis[2]) and photon energy (XAS). These average images were collected in so-called image stacks either as function of photon energy (XAS –> spectroscopy) or magnetic field (XMCD –> hysteresis) as indicated in Fig. 5.2 b,d. From a particular region of interest containing an individual nanoparticle or nanoparticle configuration the intensity was integrated to obtain the XAS (Fig. 5.2 c,) or XMCD (Fig. 5.2 e) signal. The background was subtracted using a neighboring particle-free region. Additionally, the background was checked for

an inhomogeneous amplification of the channel plates or defects of the electronic imaging unit (wave guides, MCP, Screen, CCD).

[2]Thus, several thousands of images recorded within one hysteresis cycle were reduced to about fifty for the final evaluation.

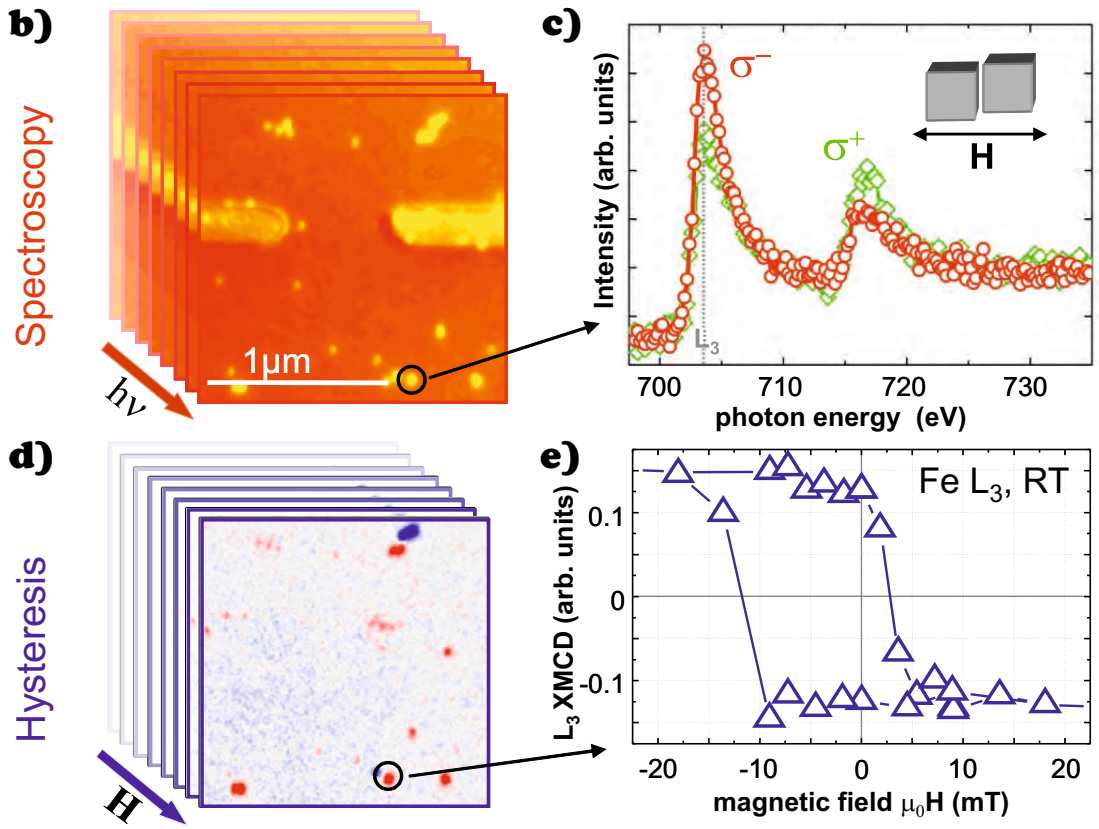

Figure 5.2.: b) XPEEM image stacks of the same area as shown in the SEM image in Fig. 5.2 a at different photon energies hν and d) magnetic contrast at the Fe L_3-edge as a function of external magnetic field H applied along the indicated direction. In the latter the blue and red colors indicate opposite magnetization directions in the particles. c) X-ray absorption spectrum of one dimer (two Fe cubes aligned parallel to H as indicated in the inset) marked by the circles in images b, d and Fig. 5.1 a. Green diamonds correspond to a positive, red circles to a negative helicity of the photons. e) A hysteresis loop for a dimer aligned with its easy axis parallel to the applied field recorded at the Fe L_3-edge (indicated by the dotted line in c).

intensity differences of the helicities which were corrected in the further analysis. In the hysteresis data the XMCD signal (see for example Fig. 5.2 e) is displayed as the difference of Fe L_3-intensities for two opposite helicities divided by their sum (asymmetry). Plotting of the asymmetry yields the advantage, that the amplitude of the magnetic signal

is not related to the visibility (intensity[3]) of the nanoparticle configuration but only to the magnetization vector of the element. The XMCD is sensitive to the component of the magnetization **M** parallel or antiparallel to the propagation vector **k** of the incident x-ray beam. Due to the experimental setup the latter differs by 16° grazing incidence from the direction of the applied magnetic field. Thus the signal is reduced by about 4 % with respect to ideal parallel conditions.

5.2. Experimental Results

Room temperature hysteresis measurements of Fe nanocubes have been performed on sample 4b, which was prepared as described in Chapter 3.5 (capacitive plasma setup and ∼4 nm Al capping by magnetron sputtering). In Fig. 5.3 3 different images acquired at the same position are shown: (a) SEM, (b) XPEEM chemical contrast ($\sigma^- + \sigma^+$) and (c) magnetic/dichroic contrast ($\sigma^- - \sigma^+$) image . Opposite magnetization directions (either parallel or antiparallel to photon spin/magnetic field) in the particles correspond to black and white contrast in (c). The circles mark three individual particles.

Fig. 5.4 shows a XAS spectrum acquired prior to the hysteresis measurement. The L_3

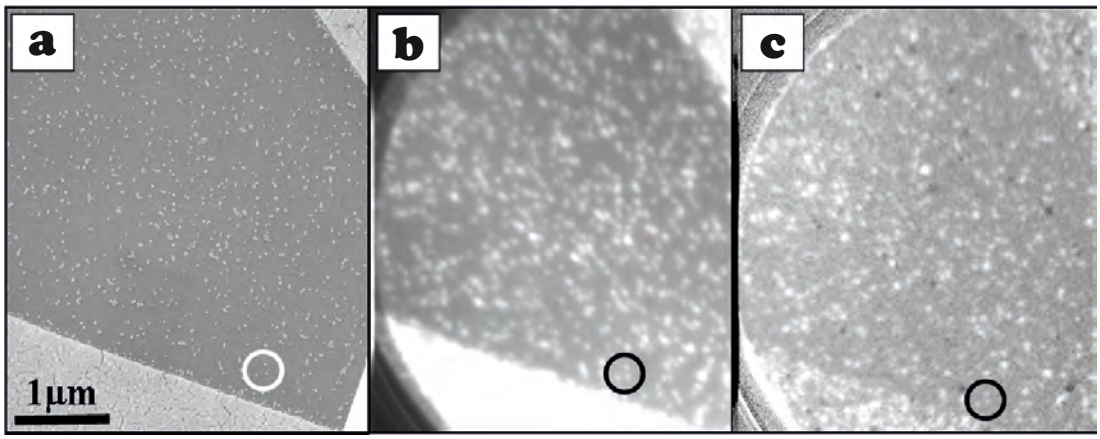

Figure 5.3.: SEM (a), PEEM chemical contrast (b) and XMCD magnetic contrast image (c) of the same sample position. The circles mark three individual nanocubes. In (c) black and white colors indicate opposite magnetization directions.

peak position at 707 eV and its shape indicate that there is no or very little oxidation.

[3]Note that the intensity can locally change due to uneven thickness of the capping layer or contamination.

Due to the limited probing depth of the PEEM ($< 10\,\mathrm{nm}$), the oxidation state at the interface of the particle (thickness 18 nm) and the substrate can not be determined.
The hysteresis loops of almost 300 different nanocubes and nanocube configurations were analyzed. On the following pages a selection of magnetic hysteresis loops of individual nanocubes is shown to point out the diversity of the shapes of the loops for different particles (Figs. 5.6 - 5.9). The numbering refers to the SEM overview image shown in Fig. 5.5, p. 70.

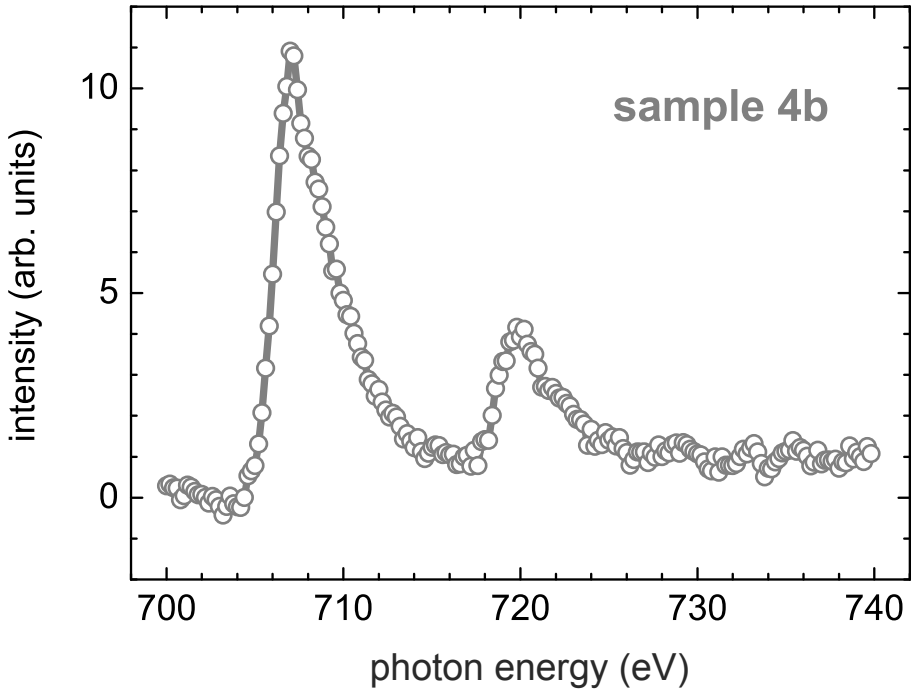

Figure 5.4.: XAS data of a cluster configuration of Fe nanocubes.

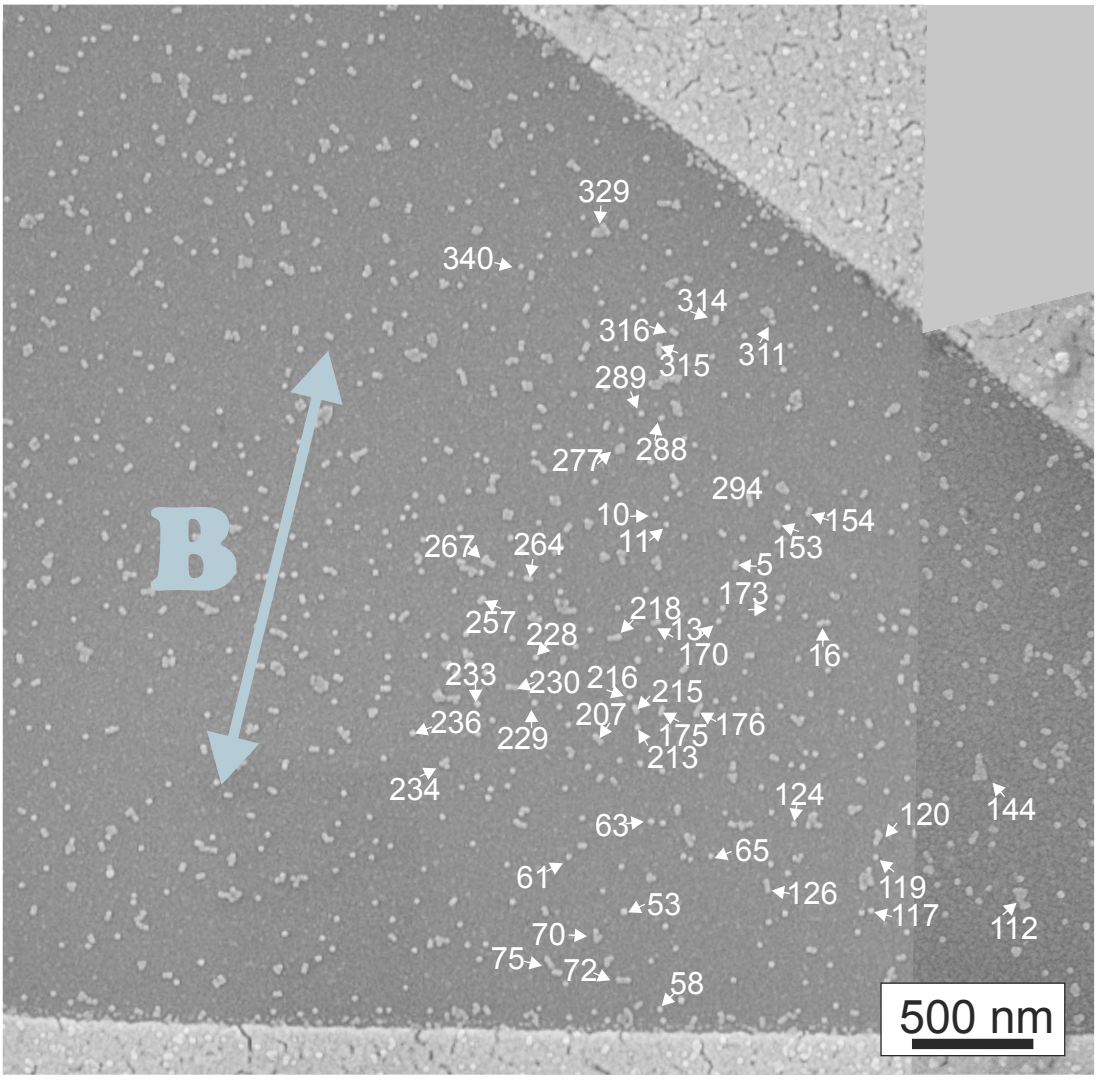

Figure 5.5.: Combined SEM image of the room temperature hysteresis sample (4B) showing the analyzed position. The diagonal gray bar in the top right corner and the horizontal one at the bottom are Au-markers. Since the reduced Fe-nanocubes are already covered with Al the image sharpness is reduced. The left part of the image was acquired prior to the synchrotron investigations whereas the right part was taken after the experiment and with a higher resolution.

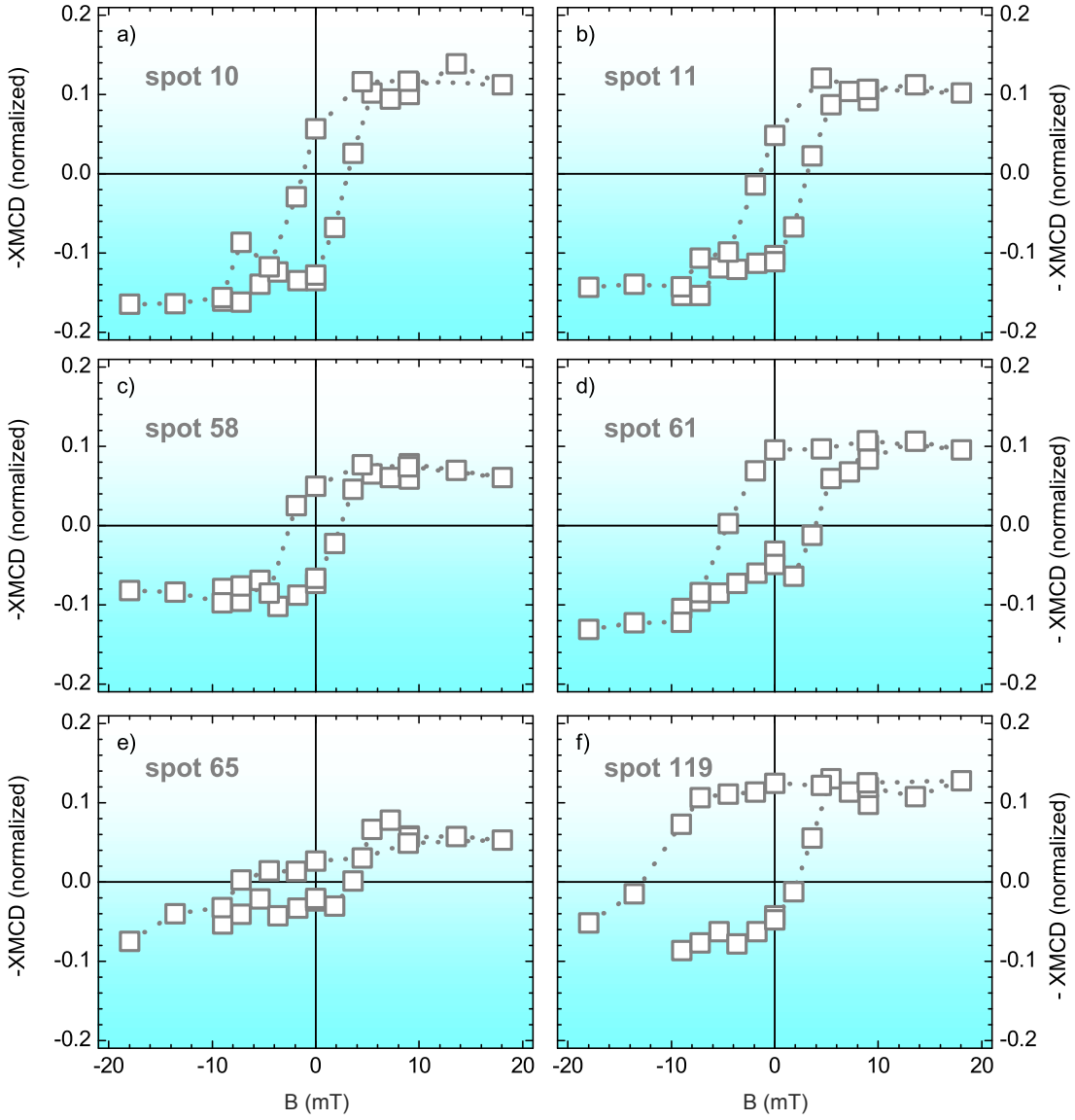

Figure 5.6.: **Single Nanocube Hysteresis I:** Room temperature hysteresis loops of individual nanocubes (measured between -18 mT and +18 mT). The dotted line serves as guide to the eye. Spot numbers are from the SEM overview image (Fig. 5.5). For an easier comparison to the simulations (also Chapters 5.3 and 6.3) or conventionally measured hysteresis loops with negative saturation magnetization in negative fields and consequently positive M_s in positive fields, the negative XMCD (asymmetry) is plotted as a function of the applied field B.

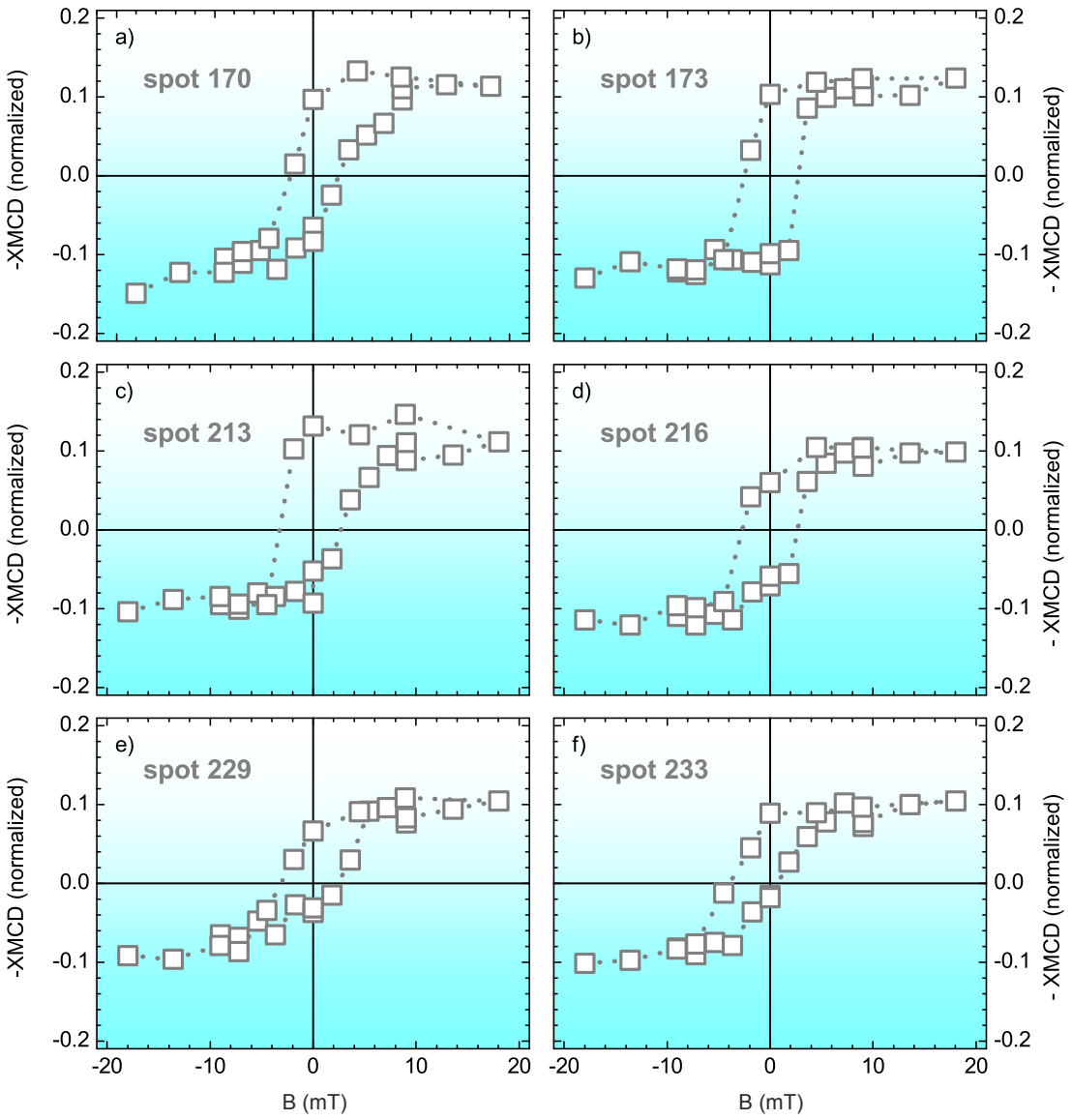

Figure 5.7.: **Single Nanocube Hysteresis II:** Room temperature hysteresis data of individual nanocubes. For details see figure caption of Fig. 5.6.

In the overview Figures I and II all particles show an open hysteresis with a coercivity in the range of several mT. Typical "noise" is in the range of 2 % of the normalized XMCD (i.e. asymmetry) signal. The mean saturation value for this sample is approximately 11 - 12%. For some particles, however, this can be very different, e.g. in spot 65 (Fig. 5.6 e)

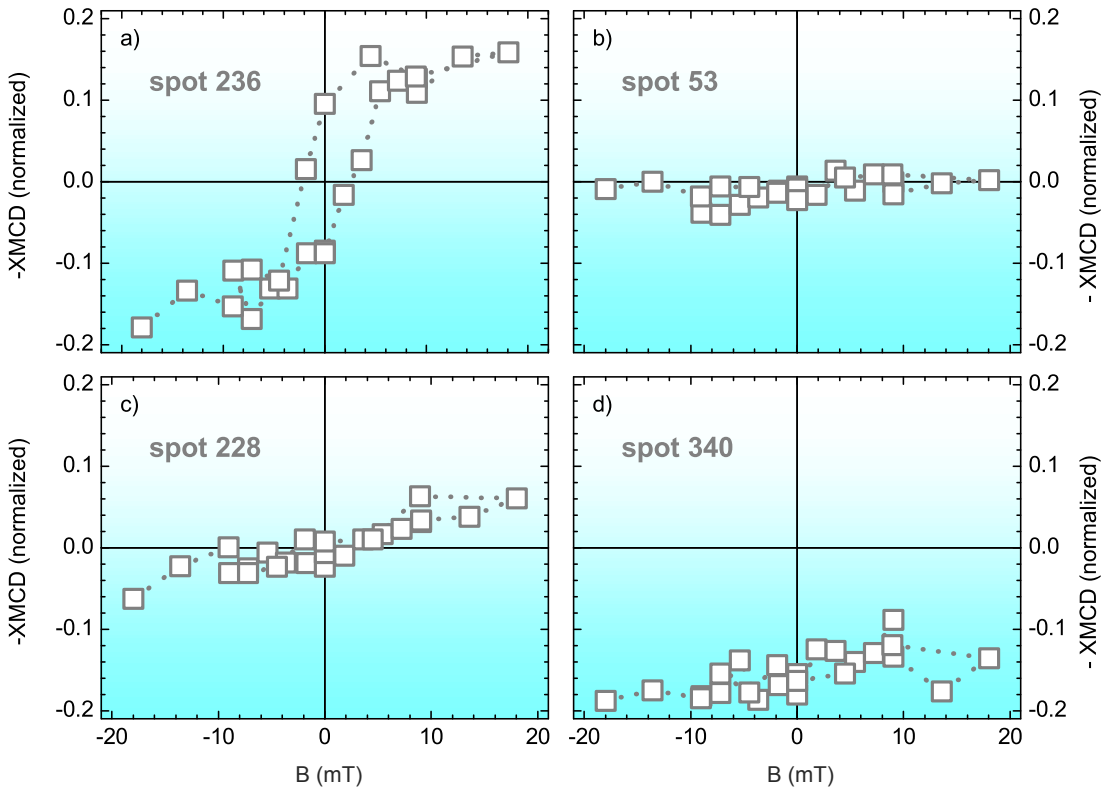

Figure 5.8.: **Single Nanocube Hysteresis III:** Room temperature hysteresis data of individual nanocubes. For details see figure caption of Fig. 5.6.

where M_s is only about 5 %. Furthermore, the coercivity is slightly enhanced and the hysteresis loop is apparently shifted into the negative field direction. Such an increased coercivity and shift also can be found for nanocubes 119 (Fig. 5.6 f) and 311 (Fig. 5.9 f). For the latter, a field of - 18 mT was not sufficient to reverse the magnetization into the initial negative field direction and the hysteresis loop is open.

The asymmetric shift is observed in very few hysteresis loops of individual nanocubes and can be attributed to the magnetic stray field from neighboring particles. For nanocube 119 (Fig. 5.6 f) there are two neighboring configurations below and above, which in addition are aligned approximately in the field direction. Their stray field consequently changes the effective field at the particle position. The nanocube in spot 311 (Fig. 5.9 f) lies next to a nanocube cluster. They are less than 5 nm apart and an apparent shift of the hysteresis loop can plausibly be due to the stray field of the cluster. For particle 65 (Fig. 5.6 e) neighboring particles are further (about three particle diameters)

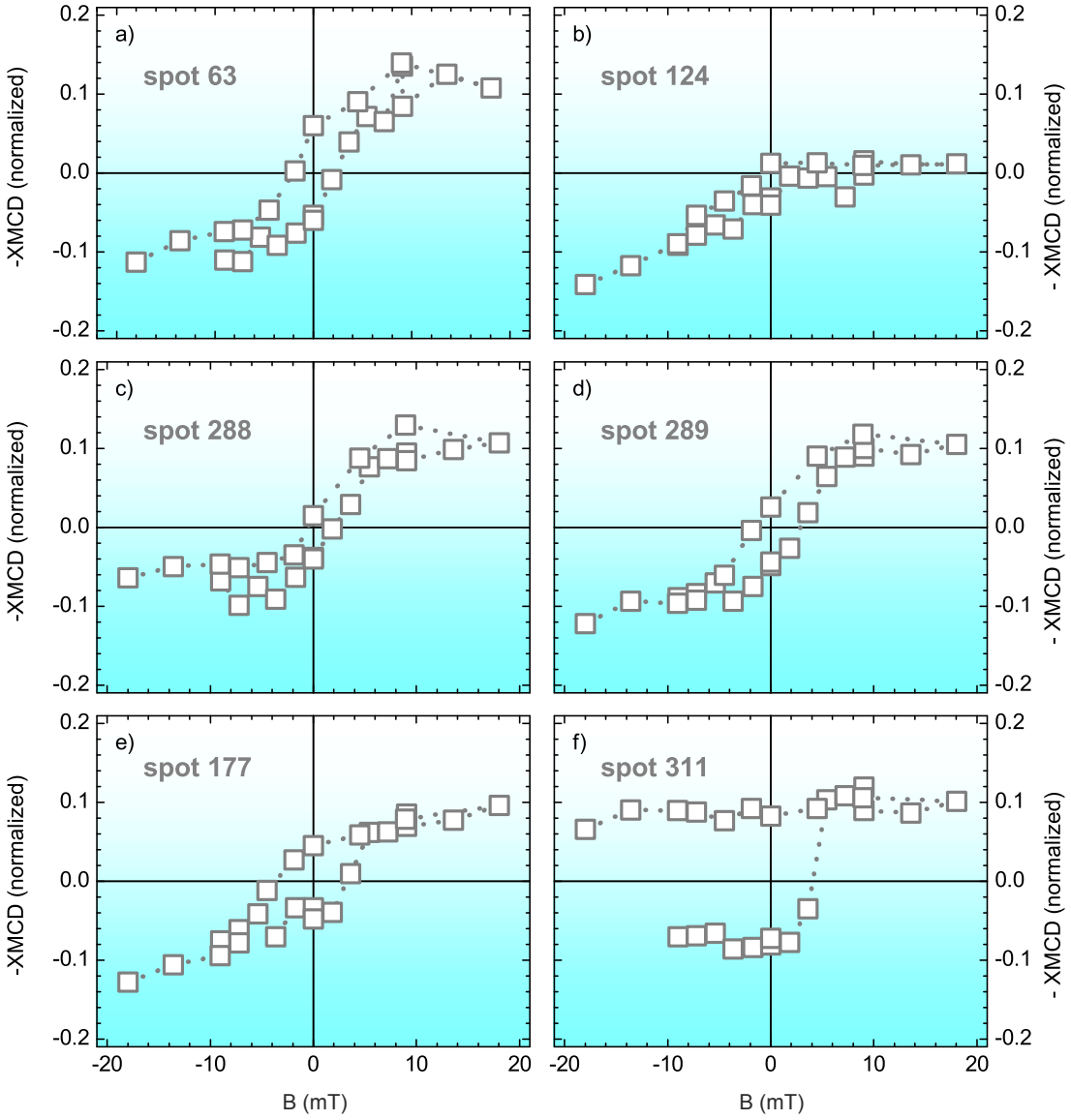

Figure 5.9.: **Single Nanocube Hysteresis IV:** Room temperature hysteresis data of individual nanocubes. For details see figure caption of Fig. 5.6.

away. At this distance, however, magnetic stray fields still have to be considered: a critical upper distance of approximately 60 nm was determined for individual nanocubes (Chapter 6.2.2, p. 106).

In Fig. 5.8 b - d (spots 53, 228, 340) three examples of linear reversal "loops" are shown: nanocube 53 (Fig. 5.8 b) shows zero magnetization, i.e. the magnetization vector is perpendicular to the incoming photon beam while the magnetic field was too small to align the magnetization parallel to the field. A superparamagnetic response can be excluded, since this would show up as an "S"-shape hysteresis with no coercivity.

For particle 228 (Fig. 5.8 c) a similar argumentation holds, in contrast to nanocube 53 the slope here is more dominant. The strength of the magnetic field, however, was too small to saturate the magnetization of this particle.

Spot 340 (Fig. 5.8 d) is an example for a nanocube, for which it was not possible to reverse the magnetization. The XMCD signal is about 19 % for negative fields and about 14 % for positive fields. This decrease in XMCD goes along with the switching of the dimer configuration (not shown here) placed at a distance of approximately 20 nm right below the nanocube (cf. Fig. 5.9). Since the hysteresis loop for the dimer is shifted to negative fields and its saturation magnetization is almost 20 %, it is plausible to believe that its stray field can stabilize the magnetization of the single cube even when a negative field is applied. However, the magnetization of the nanocube does not switch even when the dimer reverses its magnetization, indicating that the pinning of the magnetization is possibly rather attributable to a complex pinning, whose origin cannot be understood from the hysteresis data. Another example for complex switching behavior is found for spot 124 (Fig. 5.9 b). Starting at negative fields and decreasing the field strength leads to a decrease in magnetization and as soon as positive magnetic fields are reached, the magnetization is zero. Reversing the field confirms this switching behavior. On the right side of this nanocube there is a complex particle configuration at a distance of approximately two particle diameters. Its magnetization is stable at about 10 % XMCD asymmetry ($\propto M_s$) for this hysteresis measurement (not shown here) and thus its stray field may force the magnetization of the single cube in a direction perpendicular with respect to **k** in positive fields.

For the open hysteresis loops two kind of shapes can be distinguished: a) a rectangular type, as for example in spot 173 (Fig. 5.7 d) and b) a more "S"-shaped type as for spot 288 (Fig. 5.9 c). These forms resemble the different hysteresis shapes for easy and hard axis magnetization reversals in the ideal Stoner-Wohlfarth (SW) case of uniaxial anisotropy (Fig. 1.8 b, Chapter 1.2.3.1). As a consequence, the different shapes of the hysteresis loops can be attributed to different crystallographic orientations and thus to the intrinsic magnetocrystalline anisotropy of the particles. The latter should be cubic (not uniaxial as in the SW model) due to the shape of the particles.

The chemically synthesized Fe nanocubes have bcc structure with {100}-facets [170]. In Fe bulk materials, the <110>- and the <111>-directions correspond to intermediate and hard axes of magnetization, whereas the <100>-directions are the easy axes. Assuming an ideal Fe nanocube of 18 nm edge length with cubic anisotropy and the easy axes parallel to the facets, the hysteresis loops for easy and hard axis (the cube is aligned ei-

ther parallel or tilted by 45° with respect to the applied magnetic field) were simulated[4] (Fig. 5.10). In these simulations bcc Fe bulk parameters were used: $K_4 = 48\,kJ/m^3$, $M_s = 1700\,kA/m$ and the exchange constant $A = 21\,pJ/m$. In the diagram the reduced magnetization M/M_s is plotted as a function of reduced field ($H\mu_0 M_s/2K_4$). In contrast to the Stoner-Wohlfarth case, the coercive field for the hard axis reversal is non-zero but about one third of the value for the easy axis. The angular dependence of the azimuth, i.e. the angle between the applied field **B** and easy axis of magnetization, is discussed in Chapter 5.3.1.

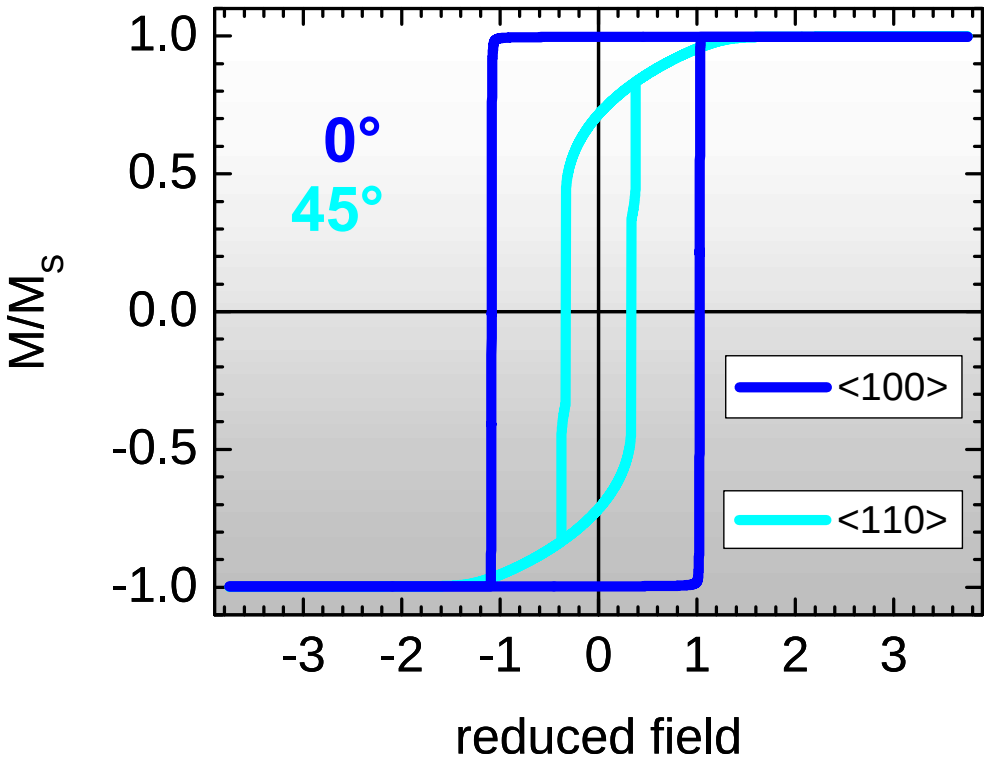

Figure 5.10.: Simulated hysteresis loops along easy and hard axes of an perfect $(18\,nm)^3$ Fe cube. According to the crystallographic structure, the easy axes are perpendicular to the cube facets and the hard axis perpendicular to the edges. The reduced magnetization M/M_s is plotted as a function of the reduced field ($H\mu_0 M_s/2K_4$).

[4] here: Micromagnetic Simulations by S. Gliga using the "Hertel"-code [162].

To confirm the orientation of the easy axis of magnetization in the nanocubes, the orientations of nearly 100 nanocubes were analyzed using the high resolution SEM images. About half of the hysteresis loops were obtained for particles with the edge axis parallel to the applied magnetic field, the other half for **B** applied at an angle of 45°±22°. In the averaged hysteresis loops shown in Fig. 5.11 blue squares represent the loop for cubes oriented with their <100>-axis along the magnetic field direction while circles represent the one for cubes oriented with the <110>-axis along the magnetic field direction[5].

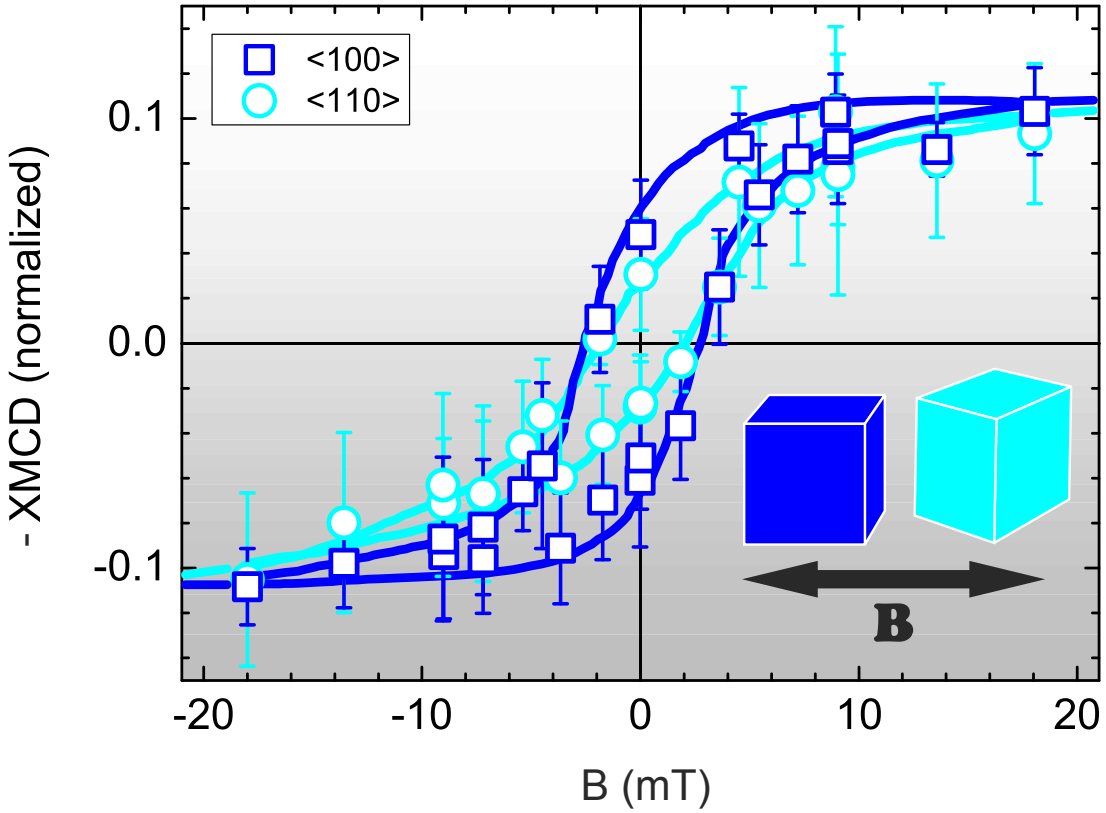

Figure 5.11.: Averaged room temperature hysteresis loops of single nanocubes showing distinct hysteresis behavior recorded with the magnetic field oriented parallel to the cube edge <100> (open squares) or at angle of 45° <110> (open circles). The rounding in comparison to Fig. 5.10 is due to the fact that loops of cubes which were oriented within ±22° with respect to the magnetic field direction were also averaged.

[5]Only those nanocubes showing distinct (open) hysteresis were included in these statistics.

The strongly enhanced remanence in the hysteresis and the shape of the loop recorded with the magnetic field along the <100> axis clearly evidences the presence of magnetocrystalline anisotropy with a preferred magnetization along the <100>-axis as confirmed by the micromagnetic simulations (Fig. 5.10). Furthermore, the coercive field for the <100>-axis is also slightly enhanced with respect to the <110>-axis (2.5 mT vs. 2 mT). The line is a guide to the eye within the error bars given by the standard deviation. These two average loops shown in Fig. 5.11 resemble the loops of a macroscopic measurement which masks the influence of small variations in particle size and orientation and averages over small changes of the magnetic anisotropy energy from particle to particle. As revealed by this plot the mean saturation magnetization (that is the normalized XMCD signal) for individual particles is about 11 %. For "calibration" XMCD measurements to determine orbital (μ_l) and spin (μ_s) magnetic moments per atom of the Fe nanocubes have to be performed in saturation. However, it can be concluded from the XMCD asymmetry, that the magnetization of the nanocubes is drastically reduced with respect to Fe bulk (XMCD asymmetry $\sim 30\,\%$). This reduction is also confirmed by XMCD-measurements on dimer nanocube configurations for a different sample (Chapter 6.1).

5.3. Simulations of the Magnetization Reversal in Individual Fe Nanocubes

The coercive field for coherent magnetization reversal is $H_c = \frac{2K}{M_s}$ (Chapter 1.2.3). Assuming bcc Fe bulk parameters (cubic magnetic anisotropy density $K_4 = 48\,kJ/m^3$ and $M_s = 1700\,kA/m$), one calculates [109, 193]:

$$H_c = \frac{2K_4}{M_s} = 56.5\,mT \tag{5.1}$$

The experimentally determined $H_c = 2.5\,mT$ at RT for the Fe nanocubes (Chapter 5.2), however, is only 4.5 % of that value. One origin of this discrepancy is that shape anisotropy has to be considered for cubic particles. The morphology of the "real" nanocubes, i.e. elongation and surface roughness (K_s) has to be taken into account (Chapter 5.3.3) which results in a K_{eff} different from the bulk K_4. Furthermore, the experimental value was determined at room temperature and therefore thermal fluctuations will also result in a smaller H_c. A smaller H_c may also be attributed to averaging over different relative orientations of the Fe nanocubes with respect to the external field.

To better understand this discrepancy in H_c a systematic study using the object oriented micromagnetic framework OOMMF-code (Chapter 2.4) was performed. Simulating the magnetization reversal along an easy axis of an ideal Fe cube of 18 nm side length and with bulk parameters yielded $H_c = 125\,mT$ (Fig. 5.12), which is larger than the coercivity according to eqn. 5.1. The influence of structural (truncated edges, core shell

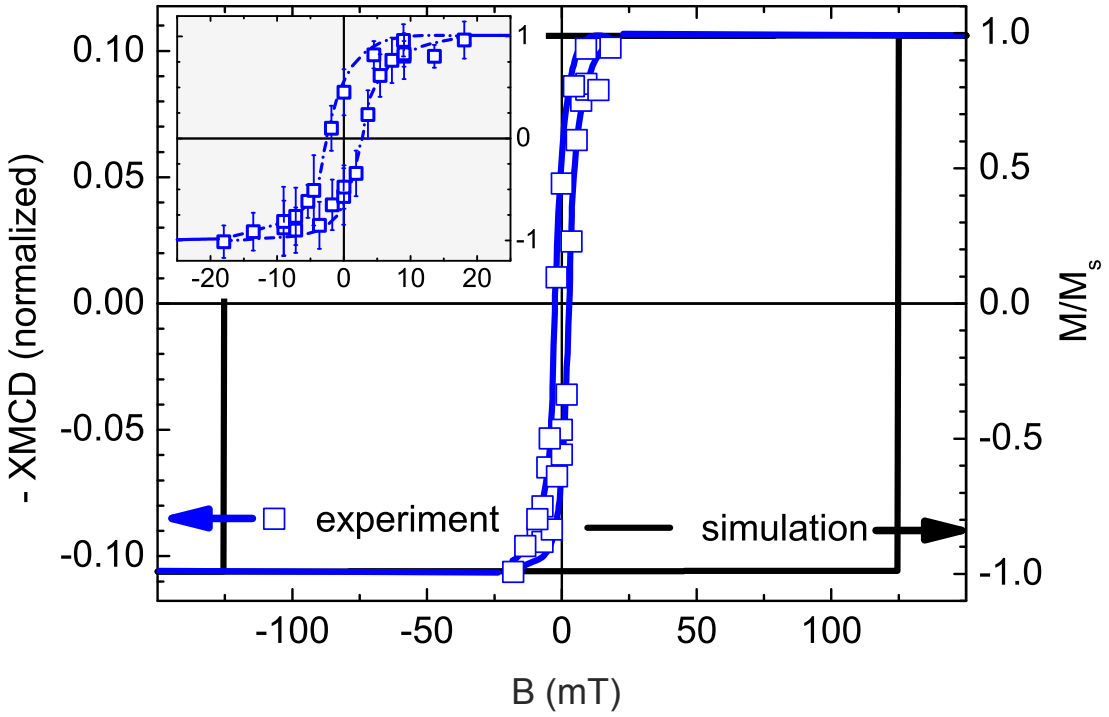

Figure 5.12.: Simulated hysteresis loop along an easy axis for a cubic particle of volume $(18\,\mathrm{nm})^3$ (black line). The blue squares are the experimental data. The inset shows the field range from $-25\,\mathrm{mT}$ - $+25\,\mathrm{mT}$. The line is a guide to the eye. For easier comparison, the experimental data is normalized.

structure) or magnetic modifications (K_4, M_s) on H_c is investigated in Chapter 5.3.2. The results when taking the morphology of the real nanocube into account are discussed in Chapter 5.3.3.

Besides the different coercive fields, the shape of the averaged experimental hysteresis loop measured along the easy axis is also different from theory, which predicts a square loop[6] (Fig. 5.12). The averaged hysteresis loop, however, is "rounded" and has a remanent magnetization of about $0.5\,M_s$ (inset Fig. 5.12). This effect can be attributed to averaging over the angular interval of about 22° when determining the relative orientation of cubes with respect to the external field (detailed discussion in Chapter 5.3.1).

[6] In the literature also the term squareness can be found, which is the ratio of remanent and saturation magnetization $\frac{M_r}{M_s}$. Consequently, the squareness is 1 for full saturation magnetization at remanence.

5.3.1. Angular Dependence of Coercivity

For the averaged hysteresis loops along the crystallographic easy and hard axes of magnetization (Fig. 5.11) cubes oriented within $\pm 22.5°$ with respect to the ideal alignment with respect to the field were also averaged. To estimate the influence on H_c, the angular-dependence of the coercive field was determined by micromagnetic simulations (Table 5.1 and Fig. 5.13). The particle in Fig. 5.15 b was used as input for the simulations and the magnetic field was applied in 0.5 mT steps for different azimuth values γ_a [7] from 0° to 45°.

An azimuth variation of only 1° with respect to the particle facet induces a reduction of the coercive field of about 40% (33.5 mT). H_c decreases fast and above 40° the coercivity is almost constant at 17 mT (Fig. 5.13). That means, there is a larger variation of coercivity (82.8 mT - 22 mT) for those nanocubes aligned parallel (0 ° - 22.5 °) with an easy crystallographic <100>-axis to the magnetic field than for those (22 mT - 16.75 mT) aligned with a hard <110>-axis (22.5 ° - 45 °) parallel to the field. Consequently, the average H_c in case of the easy axis alignment strongly depends on the azimuthal distribution whereas there is only a small influence for the hard axis. This is in good accordance to the experimental data, where averaging of about 100 hysteresis loops only revealed a small difference of H_c between easy (2.5 mT) and hard axis (2 mT).

Additionally, the reduced coercive field for a Stoner-Wohlfarth particle is also plotted in Fig. 5.13 (gray open squares, top and right axes). Whereas the coercivity of the cubic particle shows a continuos decrease with increasing γ_a, H_c decays non-uniformly with increasing γ, which is the angle between the magnetic field and the easy axis of magnetization, for the SW case.

In Fig. 5.14 the x-, y- and z- components of the magnetization[8] are shown for azimuth values of 0 ° (a), 2 ° (b), 20 ° (c) and 45 ° (d). For comparison to the experiment, the magnetization projection onto any azimuth direction - which is the experimentally measured quantity - has to be calculated (Chapter 5.3.3.2). For parallel orientation of magnetic field and easy axis ($\gamma_a = 0°$) the simulated data can be directly compared to the experimental data (Fig. 5.14 a).

[7] γ_a is the angle between the in-plane magnetic field component and the easy axis of magnetization. In the simulations **B** was applied in the x-y plane and the cube facets were oriented parallel to the x- and y- axes. γ_a is measured vs. the "easy" x-axis.

[8] $\frac{m_x}{M_s}$: x-component, $\frac{m_y}{M_s}$: y-component, $\frac{m_z}{M_s}$: z-component and

$$\frac{m_x^2}{M_s^2} + \frac{m_y^2}{M_s^2} + \frac{m_z^2}{M_s^2} = 1 \tag{5.2}$$

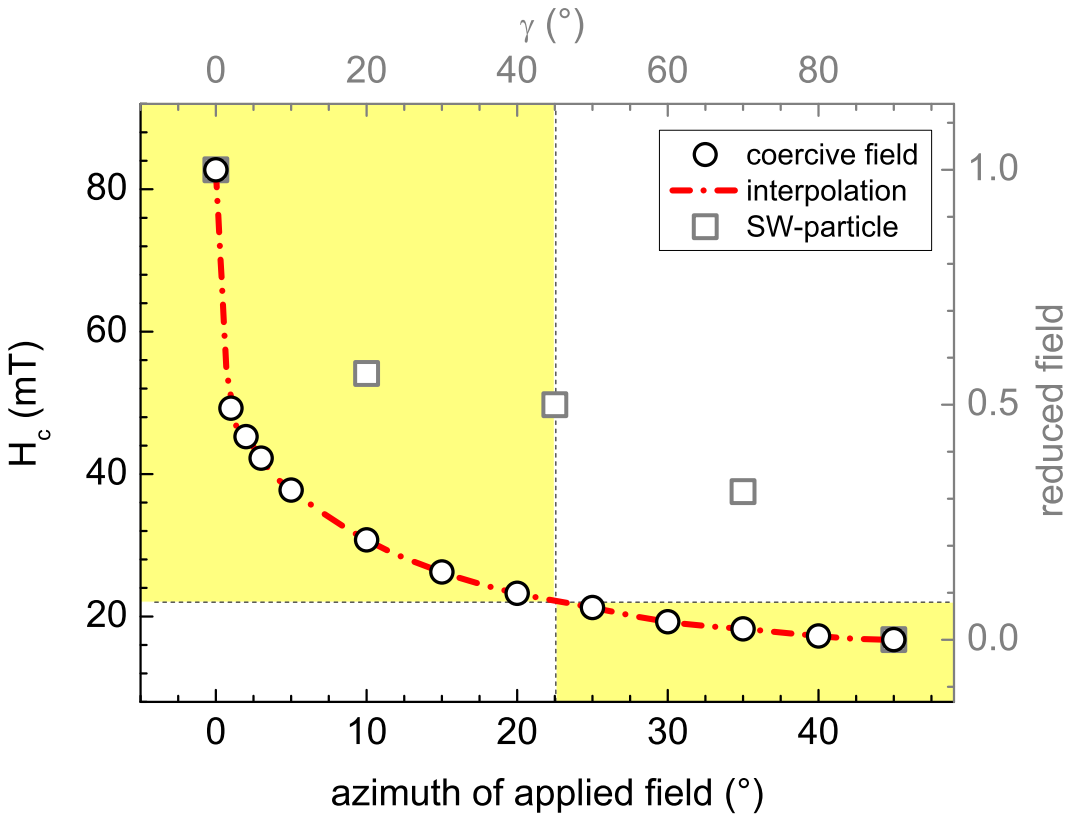

Figure 5.13.: Azimuthal dependence of the coercive field for the simulated particle with cubic magnetocrystalline anisotropy density according to Fig. 5.15 b. The yellow areas indicate the azimuthal error bar over which the relative orientations of nanocubes and magnetic field were averaged. The range in both cases is 22.5°. These data are compared with the Stoner-Wohlfarth model for uniaxial magnetocrystalline anisotropy density (gray squares, top and right axes), (cf. Fig. 1.8 b). γ is the angle between applied field and easy axis of magnetization.

γ_a (°)	0	1	2	3	5	10	15	20	25	30	35	40	45
H_c (mT)	84	49	45	42	38	30	26	23	21.5	19	18	17	17

Table 5.1.: Azimuthal dependence of H_c for an Fe nanocube with 18 nm side length and truncated edges (Fig. 5.15 b) as determined by micromagnetic simulations using bcc Fe bulk parameters. The error bar is 0.5 mT.

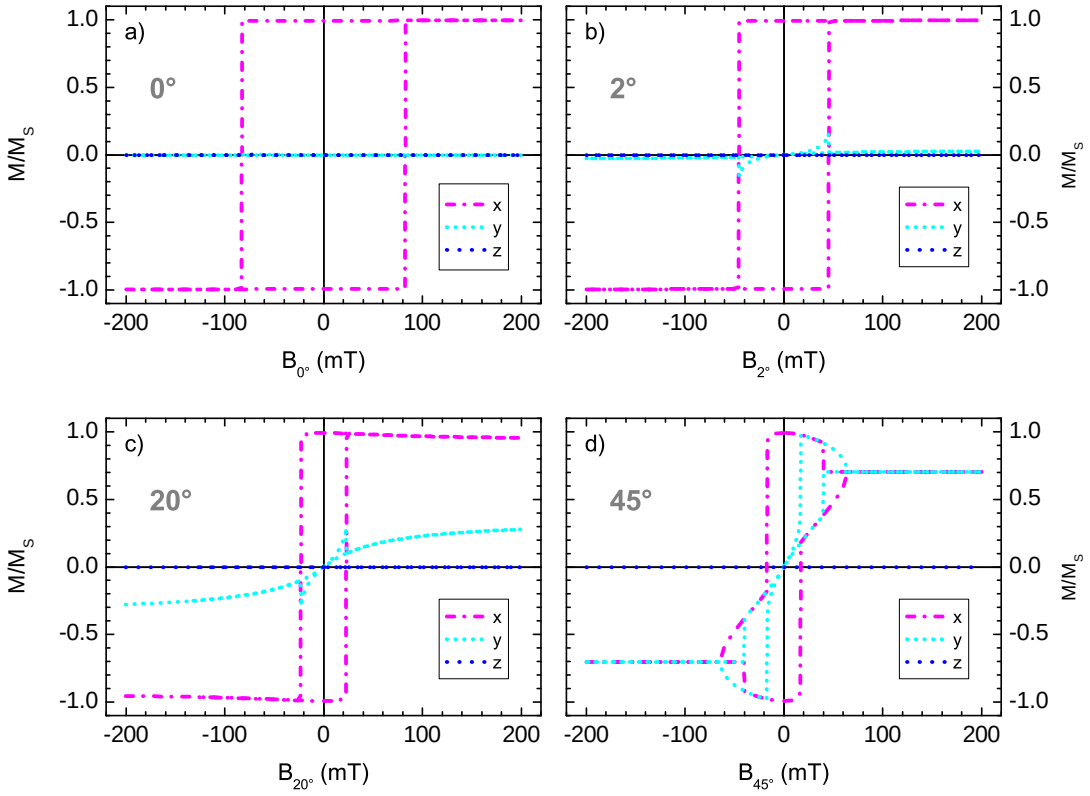

Figure 5.14.: Simulated $m_{x,y,z}$ hysteresis loops for four different azimuth values (0 °, 2 °, 20 ° and 45 °).

For $\gamma_a = 0\,°$ the cube is oriented with an easy <100>-axis parallel to the field. The resulting x-hysteresis has the typical rectangular form (Fig. 5.14 a). The y- and z-component are zero. For larger γ_a, the y-component increases (Fig. 5.14 b-d) and the z-component can be neglected. Since the magnetic field has x- and y-components there are always non-vanishing x- and y- components for the saturated magnetization.
For $\gamma_a = 2°$ (Fig. 5.14 b) y-decreases constantly with decreasing field, is zero at remanence, i.e. the magnetization is completely aligned parallel to an easy axis. For increasing field, the magnetization turns towards the positive field axis (x decreases, y increases) till it jumps almost into the opposite easy direction (+ 8°) when the external field equals the coercive field of 45.25 mT. From there on it rotates into the field direction.
For an $\gamma_a = 20°$ (Fig. 5.14 c) **M** switches similarly according to the same scheme, but with larger influence of the y-component. The coercive field here is 23.25 mT.
In panel (d) the hysteresis along an hard axis is plotted. At - 200 mT the particle is

completely saturated. The magnetization is parallel to the hard axis till the field reaches - 40.5 mT. Then M abruptly changes towards the negative x-axis and from there it rotates towards the easy direction (B = 0). From there it rotates continuously into the direction of the field axis. At the H_c =16.75 mT it jumps from 21° with respect to the negative x-axis to 89° with respect to the positive x-axis. Magnetocrystalline anisotropy would favor a perpendicular orientation to the axis (here, i.e. parallel to the y-axis) but the Zeeman energy is high enough to align the magnetization along the field direction. With further increasing field the magnetization rotates uniformly towards the field direction. At 65 mT full saturation is reached. The shape of the hysteresis loop for a perfect cube measured along a hard axis of magnetization is shown in Fig. 5.10 (45°).

5.3.2. Influence of Shape, Saturation Magnetization, Effective Anisotropy and Temperature

Simulations were used to probe the influence of small changes in the morphology of the nanocubes. In Fig. 5.15 a, a perfect cube is shown, as simulated using OOMMF. The structure is divided into discrete computational cells, each 1 nm^3 in volume, within which the effective field and thus the orientation of the magnetization is computed. The non-collinear (flower shaped) magnetization structure is sketched for zero field and strongly exaggerated for better visibility. In a second step, the edges of the cube were truncated (as defined in sketch on the right in Fig. 5.15) by 2 nm (b) and 3 nm (c) to investigate the influence of small morphological changes.
In addition, also the influence of a 2 nm (d) and 1 nm (e) oxide shell for 2 nm truncation was simulated. All hysteresis calculations were performed in ± 200 mT after saturation in negative field and the magnetic field **B** was applied parallel to the easy x-axis. If not noted otherwise, bcc Fe bulk parameters were used[9]. Fig. 5.16 shows the hysteresis loops and the corresponding coercive fields are listed in Table 5.2.

H_c of an ideal Fe cube is 125 mT (Figs. 5.12 and Fig. 5.16 a). Due to slight morphology modifications, i.e. truncations of the edges by 2 nm and 3 nm (Fig. 5.15 a - c), H_c decreases to 83.5 mT and 77 mT, respectively. Since the 2 nm truncation is a realistic approximation of the morphology according to TEM investigations, this structure was used for all subsequent changes of the magnetic parameters. The corresponding hysteresis is plotted in all panels of Fig. 5.16 as reference.
In Fig. 5.16 b hysteresis loops for Fe/Fe-oxide core-shell structures are displayed[10]. For the 1 nm Fe-oxide shell (Fig. 5.15 d) H_c is identical to the coercivity of the ideal cube (Fig. 5.16 b (c-s)). For the 2 nm Fe-oxide shell (Fig. 5.15 e) H_c is 102.5 mT (Fig. 5.16 b, $(c - s_{2nm})$).
The influence of either a 30 % smaller M_s or K_4 on the reversal behavior of a truncated

[9] $K_4 = 48\,kJ/m^3$, $M_s = 1700\,kA/m$ and the exchange constant $A = 21\,pJ/m$
[10] $M_s = 550\,kA/m$ was assumed for the Fe-oxide shell.

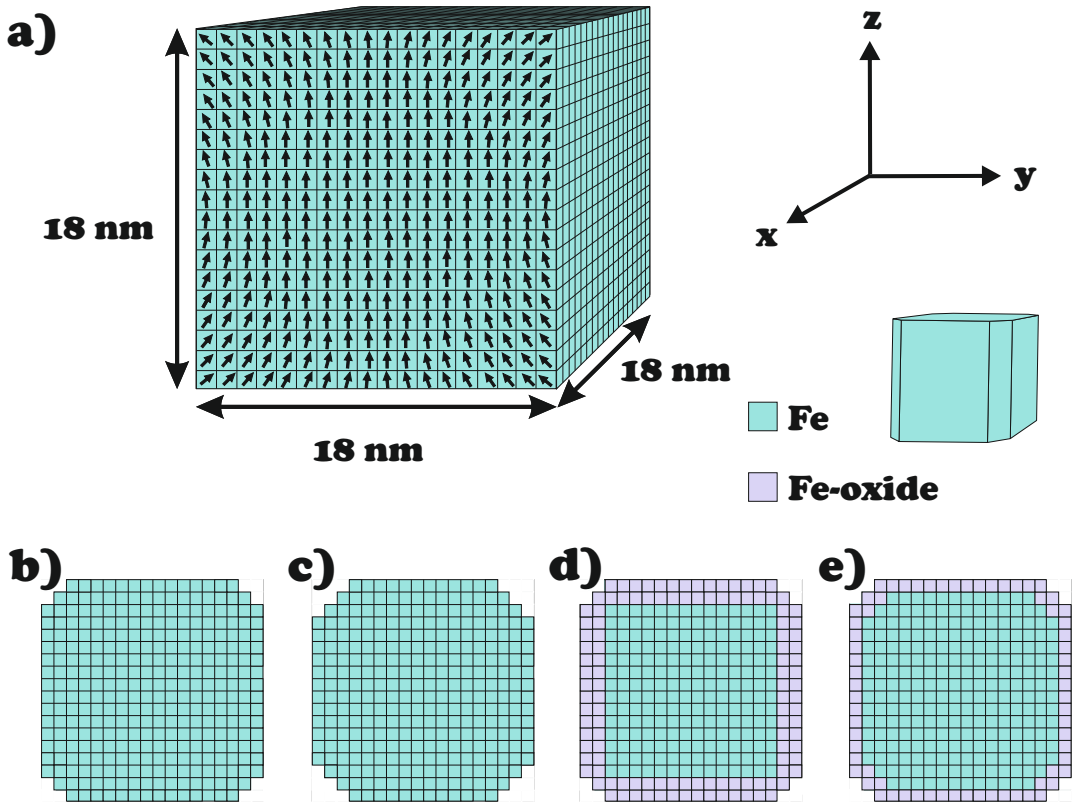

Figure 5.15.: Configurations for OOMMF simulations: a perfect cube with 18 nm edge length divided into 1 nm^3 cells, which represent an individual magnetic moment each (a), as indicated by the small arrows. In other simulations, the edges were truncated 2 nm (b) and 3 nm (c), respectively. Additionally, the influence of a Fe/Fe-oxide core-shell structure was simulated for 2 nm (d) and 1 nm (e) oxide shell thickness and 2 nm truncation.

Fe cube is presented in Fig. 5.16 c. Such a reduction of M_s (as determined in the experiment) leads to an enhanced coercive field. A smaller K_4 decreases H_c. In consequence, a smaller K_4 could be one explanation for the small experimental H_c. This explanation is in contrast to magnetic measurements of 13 nm Fe cubes by FMR revealing the Fe bulk MAE [194].

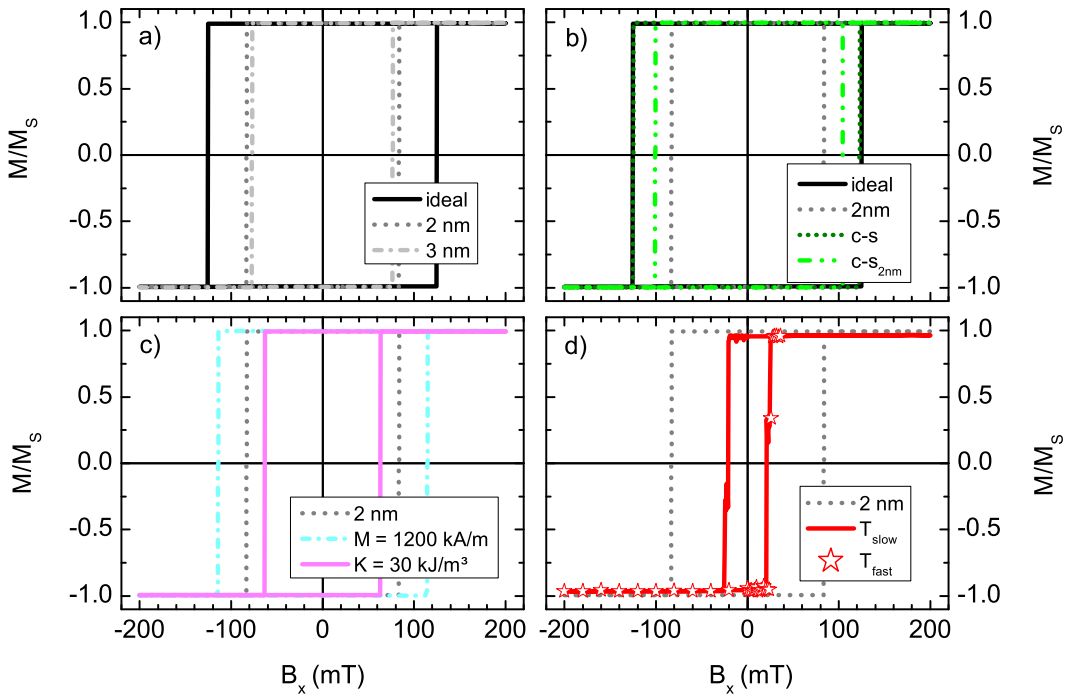

Figure 5.16.: Simulated hysteresis loops along an easy axis for a cubic particle of volume $(18\,\mathrm{nm})^3$ with different modifications as shown in Fig. 5.15. H_c-values are listed in Tab. 5.2.

configuration	H_c^{LT} (mT)	in Fig. 5.16	H_c^{RT} (mT)
ideal cube, Fig. 5.15 a	125	(a), (b)	31
truncation 2 nm, Fig. 5.15 b	83.5	(a), (b), (c), (d)	21
truncation 3 nm, Fig. 5.15 c	77	(a)	19
core-shell, Fig. 5.15 d	124.75	(b)	31
core-shell, Fig. 5.15 e	102.5	(b)	26
$M_s = 1200\,\mathrm{kA/m}$	114.5	(c)	29
$K_4 = 30\,\mathrm{kJ/m^3}$	63.25	(c)	16
$T = 300\,\mathrm{K}$	20.75	(d)	20.75

Table 5.2.: H_c (mT) for different magnetic parameters and shapes (Fig. 5.16) of a 18 nm cubic Fe or Fe/Fe-oxide particle. In the last column H_c^{LT} at 300 K is corrected by a factor of ≈ 0.25 as determined in the T-dependent simulation.

The hysteresis loops in Fig. 5.16 a - c were calculated for T = 0 K. The influence of room temperature (300 K) is simulated in panel (d): H_c decreased to 25 % of its low temperature value. Two different simulations with field steps of 4 mT (T_{fast}) and 0.5 mT (T_{slow}) have been performed[11]. Due to the large impact of temperature on H_c all simulations should take the temperature into account, which is however a huge drawback in terms of calculation time. Therefore, other simulations presented in this work were performed at 0 K and the correction of 0.25 needs to be considered for H_c when compared to RT data. In Tab. 5.2 the last column contains the RT-corrected H_c-values ($H_c^{RT} = 0.25\, H_c^{LT}$).
In summary, temperature effects and the truncation of the cube edges explain a smaller coercive field when compared to an ideal cube at $T = 0\,K$. Nevertheless, the simulated $H_c \approx 21$ mT still differs by one order of magnitude when compared to the experiment ($H_c \approx 2.5$ mT). If a distribution of relative orientations of the cubes with respect to the field is taken into account, the calculated H_c may decrease to ~ 10 mT (cf. Chapter 5.3.1).

5.3.3. Influence of Morphology

In previous chapters, only perfectly cubic particles were discussed. Although taking into account the geometry of the measurements and truncation of the edges yields a significant decrease in coercivity when compared to the ideal cube at T = 0 K, the discrepancy is still about one order of magnitude as compared to experiments. One aspect which has not been considered so far is the roughness of the particles. Three dimensional tomography by TEM on Fe/Fe_xO_y nanocubes was recorded by Christina Möller in our group [144]. Fig. 5.17 displays a bright field TEM (a) and a STEM (b) micrograph of the Fe/Fe_xO_y nanocubes. The reconstructed tomography data of the cubes is shown in (c).
The red particle in (c) is shown from three different viewing directions in Fig. 5.18. From comparison with 2D projection images the lateral resolution in the reconstruction is determined to 2 nm. For the "red" nanocube the dimensions:

$$\begin{aligned} x &= 19\,nm \pm 2\,nm \\ y &= 22\,nm \pm 2\,nm \\ z &= 20.5\,nm \pm 2\,nm \end{aligned} \tag{5.3}$$

are determined. The y-axis is elongated by about 16 % with respect to the x- and by about 7 % with respect to the z-axis. Because of the shape anisotropy the y-axis will be the easiest direction of magnetization. To estimate the effect of elongation and additional surface roughness on the magnetic properties of cubic Fe nanoparticles the tomography data were used as structural input for the OOMMF simulation. 17 cross sections of the x-y plane at a constant z-interval of 1.12 nm were taken and converted into black/white

[11] The nomenclature of T_{fast} and T_{slow} alludes to the total simulation time of two simulations with different field step sizes. The simulation of one branch of the "slow" hysteresis requires several weeks of computation time.

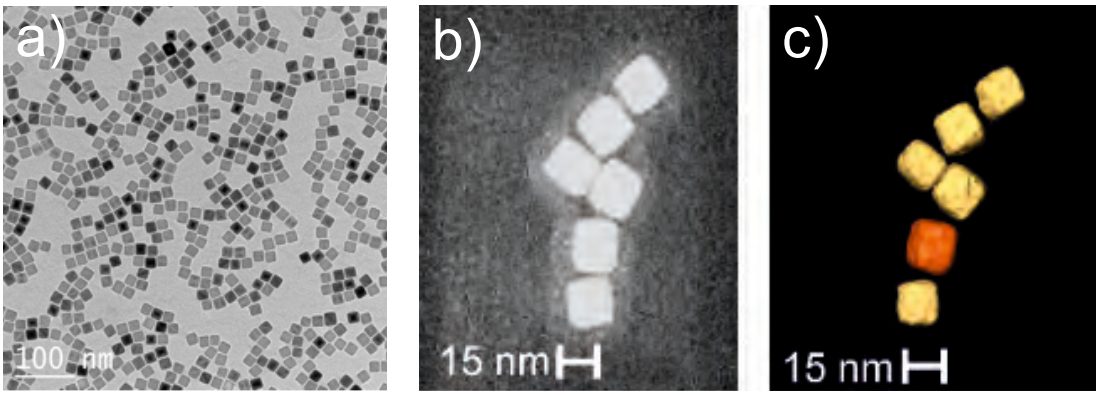

Figure 5.17.: (a) TEM overview image of as prepared Fe/Fe_xO_y-nanocube sample. (b) STEM (projection) image of six individual nanocubes which were three-dimensionally reconstructed from tomography data (c). The red colored particle is shown from different viewing directions in Fig. 5.18 (from [144]).

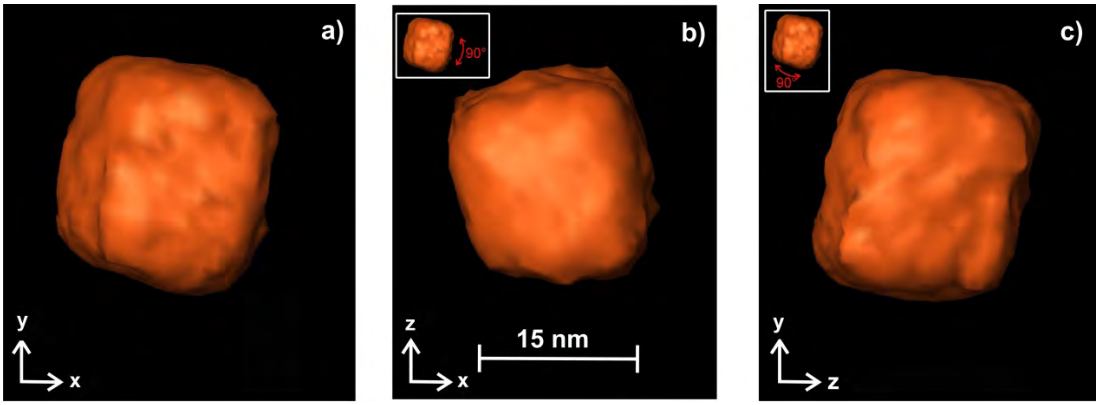

Figure 5.18.: Reconstructed tomography images from an as prepared oxidized Fe-nanocube [144]. Dimensions for this nanocube are given in eq. 5.3. Cross sections of the x-y planes at constant z-intervals were used as input for OOMMF simulations addressing the influence of surface roughness on the magnetic properties.

bitmap files (Fig. 5.19) which can be read into OOMMF - black pixels are defined as Fe and white as vacuum. The scale is 0.023 nm/pixel resulting in an outer image dimension of $x = 20.171\,nm$ and $y = 22.149\,nm$. The stacking height is $z = 19.04\,nm$. The input

"cuboid" was discretized into cell sizes with volume 0.403 nm × 0.443 nm × 1.12 nm with one magnetic moment per cell. Prior to the hysteresis simulations (T =0 K, bcc Fe bulk parameters) the particle was saturated in negative fields and the field step size was 1 mT.

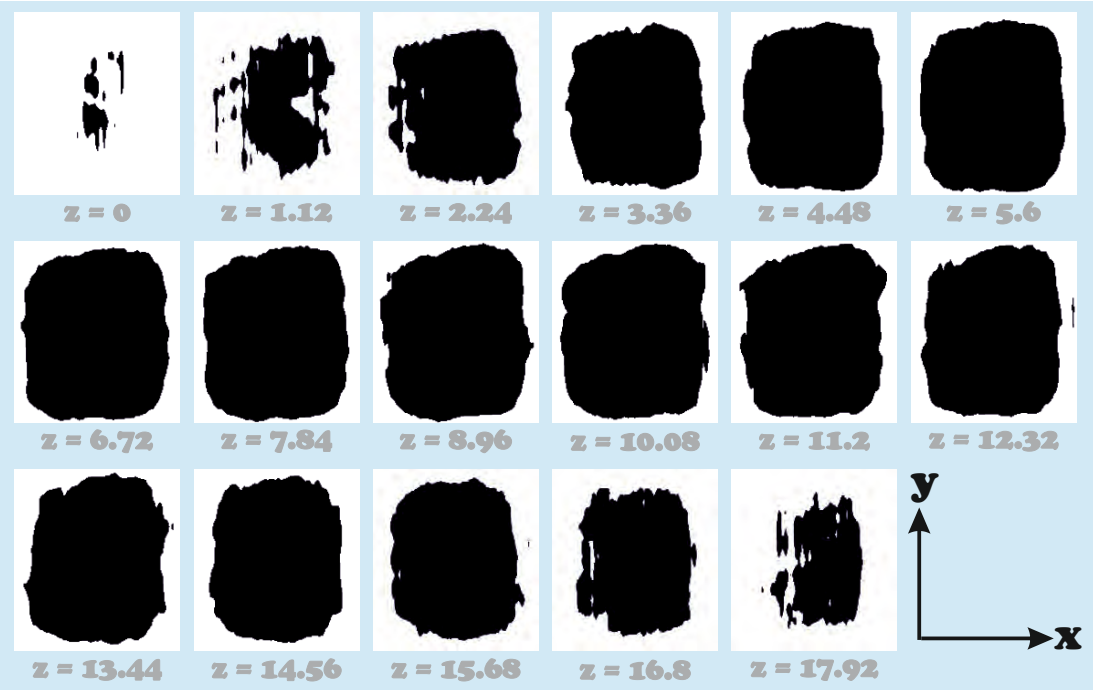

Figure 5.19.: Cross section images (parallel to the x-y plane) of a particle investigated by tomography used as input files for the OOMMF simulations. Dimensions of the images and the simulated system, respectively, are $x = 20.171\,nm$, $y = 22.149\,nm$, $z = 19.04\,nm$ and the z-interval between the cross sections is $1.12\,nm$. The corresponding z-interval position of the cross section is given in nm on the image. According to the geometry, the cell size in the simulations of the real particle structure was $0.403 \times 0.443 \times 1.12\,\mathrm{nm}^3$.

5.3.3.1. Easy Directions of Magnetization

In the first simulations the magnetic field was applied along the facets (x, y, z directions), i.e. the crystallographic easy <100>-axes of the "real morphology" particle. For an ideal cubic particle all 3 directions show the same switching behavior. For a real particle, this equivalence is destroyed resulting in very different shapes of the hysteresis loops (Fig. 5.20).

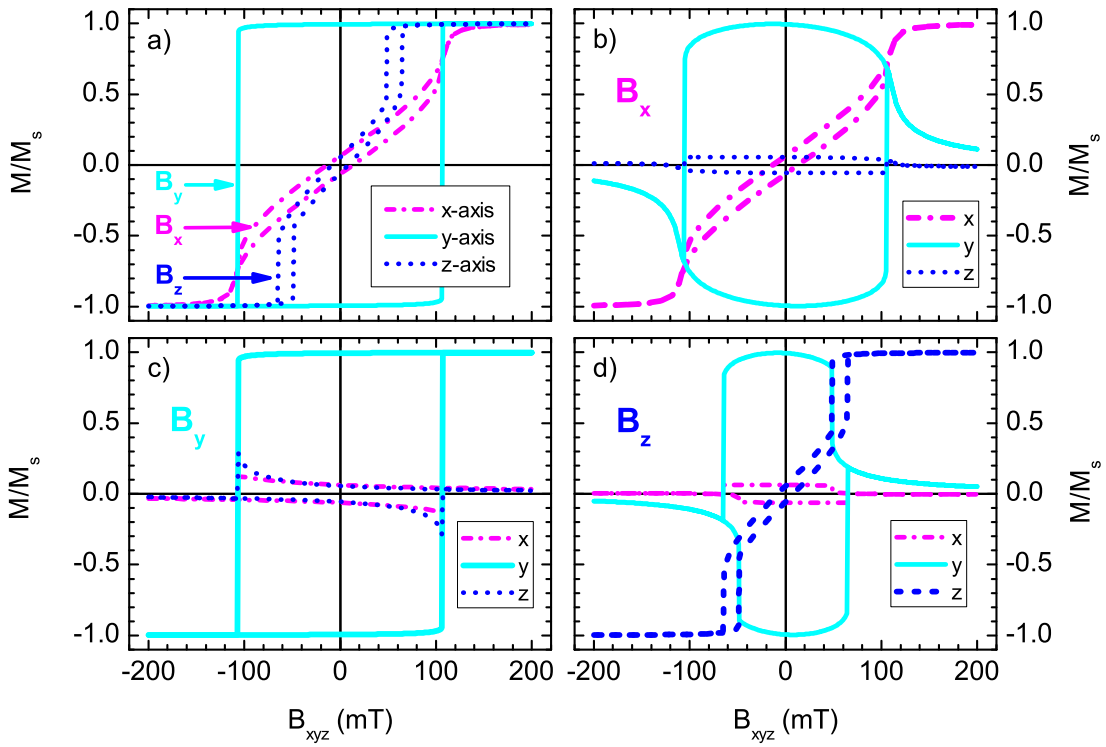

Figure 5.20.: Simulated hysteresis loops for the crystallographic "easy" axes of a real nanocube. (a): m_x, m_y and m_z components of the magnetization vector when the magnetic field **B** is applied in the x- (B_x), y- (B_y), or z- (B_z) direction. (b)-(d): x, y, z magnetization components for the cases when **B** is parallel to the x- (b), y- (c) and z-axis(z). For a detailed description see text.

The hysteresis along the elongated y- axis - which is the easiest axis - shows the expected easy axis rectangular shape with a coercive field of $\sim 100\,\mathrm{mT}$. The other two directions have much smaller coercive fields of $\sim 10\,\mathrm{mT}$. Considering the thermal fluctuations at RT ($H_c^{RT} = 0.25 H_c^{LT}$, Chapter 5.3.2) coercive fields of ~ 25 mT for the elongated axis and ~ 2.5 mT for the shorter axes are obtained. The latter fits the experimental data very well (Fig. 5.11). An elongation of the particle of $\sim 16\,\%$ in one direction is associated with an one order of magnitude increase in H_c!
The different shapes of the hysteresis loops for **B** applied in the x- and z- direction (Fig. 5.20 b, d) can be understood by considering the free energy landscape for cubic anisotropy (Fig. 5.21 e). Since the y-direction is the easiest direction of magnetization (favored by the crystal and shape anisotropies), the magnetization points along that

direction at remanence (Fig. 5.20 b - d). Small x- and z-contributions are still present, however. This is related to the morphology of the particle. Fig. 5.19 shows that the cross section is asymmetric. Shape anisotropy will favor a direction which is not exactly along the y-direction. When **B** is applied along the x-axis the hysteresis loop looks similar to a hard axis hysteresis loop (Fig. 5.10), and the magnetization reverses via coherent rotation in the x-y plane with a very small z-component. For **B** along the z-direction, the hysteresis loop shows steps, at which the magnetization jumps almost completely into the y-direction, followed by coherent reversal in the y-z-plane and jumps back again near the intermediate direction when $-\mathrm{B_z}$ is large enough to overcome the shape anisotropy.

These hysteresis loops demonstrate very clearly the influence of morphology. One may ask, if the different shapes of the hysteresis loops are really due to the complex morphology, or rather due to the cuboid dimensions of the particle. This was excluded by simulating a perfect cuboid with dimensions $x = 20.171\,nm$, $y = 22.149\,nm$, $z = 19.04\,nm$ and bcc Fe bulk parameters. Typical "easy axis" magnetization loops are found (Fig. 5.21 a - c). As expected $\mathrm{H_c}$ is largest if the external field **B** is applied parallel to the y-direction.
In summary, for an ideal cuboid an elongation of 16 % and 10 % increases $\mathrm{H_c}$ by almost 250 % and 190 %. Furthermore, if **B** is applied exactly along the facets, i.e. easy axes, the magnetization will directly switch along that direction as soon as the corresponding $\mathrm{H_c}$ is reached, and the resulting hysteresis loops are rectangular. This can be easily understood considering the free energy surface for cubic anisotropy:

$$F_{cubic} = K_4 \sin^2\theta + \frac{1}{8} K_4 (\cos 4\varphi + 7) \sin^4\theta \tag{5.4}$$

where θ is the polar angle and φ the azimuth of **M**. The corresponding energy surface is plotted in Fig. 5.21 e. The x-, y-, z-directions are energetically equivalent. If **B** is applied along one easy axis, the magnetization remains in that minimum as long as the Zeeman energy is smaller than the energy barrier. Elongation of the perfect cube in one direction can be expressed with an additional uniaxial term in the free energy:

$$F_{uni} = -K_{2||} \sin^2\theta \cos^2(\varphi - \varphi_u) \tag{5.5}$$

where $\mathrm{K_{2||}}$ is the component of $\mathrm{K_2}$ parallel to the film surface and φ_u the angle of the in plane axis. Assuming a real particle, an uniaxial anisotropy axis will certainly not be aligned parallel to the cubic easy axis and the minima of the free energy surface do not necessarily cross the easy axis of cubic anisotropy. Such a change in the energy landscape is shown in Fig. 5.21 f ($\varphi_\mathrm{u} = -0.1\pi$). Due to the real particle's morphology one has to consider higher order terms of anisotropy and maybe also additional unidirectional anisotropy. Therefore complex switching paths of the magnetization become possible. One example (Fig. 5.20 b) shows the simulated hysteresis along an easy axis of magnetization with respect to magnetocrystalline anisotropy. The shape of the loop, however,

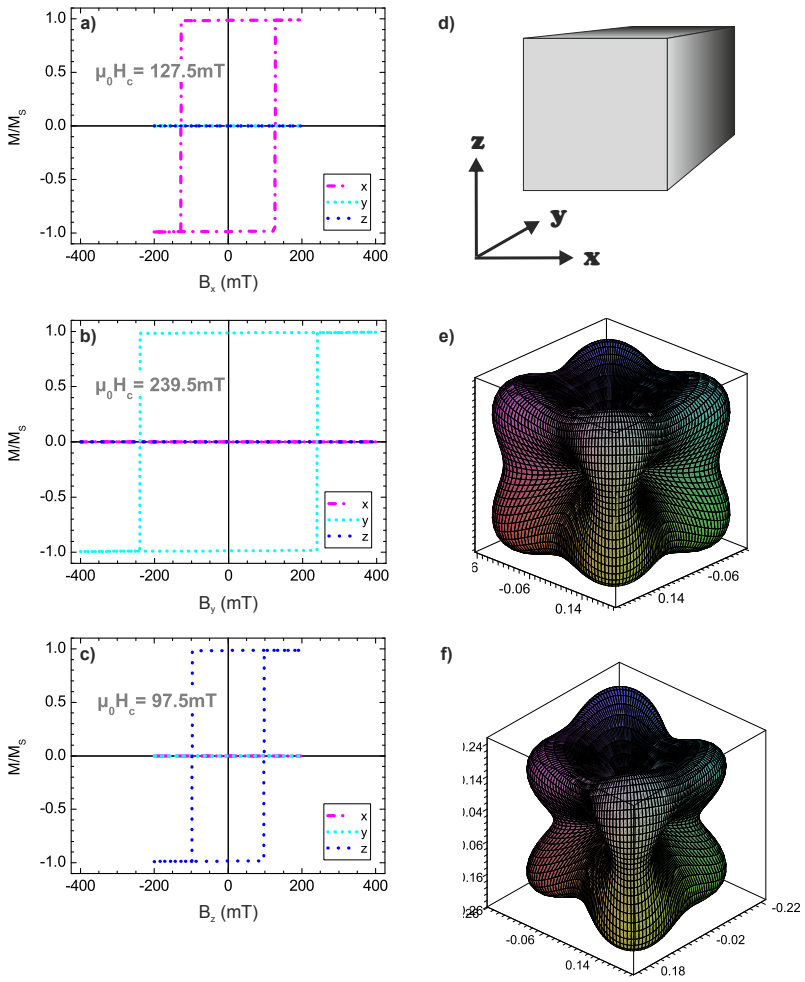

Figure 5.21.: (a)-(c):Simulated hysteresis loops for the crystallographic "easy" axes - parallel to the coordinate axes - of Fe cuboid (d) of the same dimensions as the tomography data input files for the OOMMF simulations, i.e. x = 20.171 nm, y = 22.149 nm, z = 19.04 nm. **B** is applied parallel to the x- (a), y- (b) and z-direction (c). Free energy density surface for cubic (e) and cubic + uniaxial anisotropy (f).

looks like a hard axis reversal with very low remanence. This is a further explanation for the rounded averaged experimental hysteresis loops (Fig. 5.11, p. 77). Furthermore, the larger coercivity for some individual particles as for example nanocube 61 (Fig. 5.6 d,

p. 71) can be understood in terms of an anisotropic elongation of the particle along the external field direction.

5.3.3.2. Hard Directions of Magnetization

Simulations were also performed for **B** along the hard or intermediate <110>-axes, that is under $\pm 45\,^{\circ}$ in the x-y, y-z and z-x planes. Due to the asymmetric particle shape the two possible field directions in a plane are energetically non-equivalent, requiring six additional simulations. Fig. 5.23 illustrates the nomenclature of these field directions with respect to the coordinate system. The two-dimensional projection m' of the magnetization vector onto the field direction is calculated by:

$$m' = m_{xy} \cos(\gamma - \varphi), \quad , \quad \text{x-y plane} \tag{5.6}$$

where γ is the angle between **B** and **M** and m is the length of the magnetization vector.

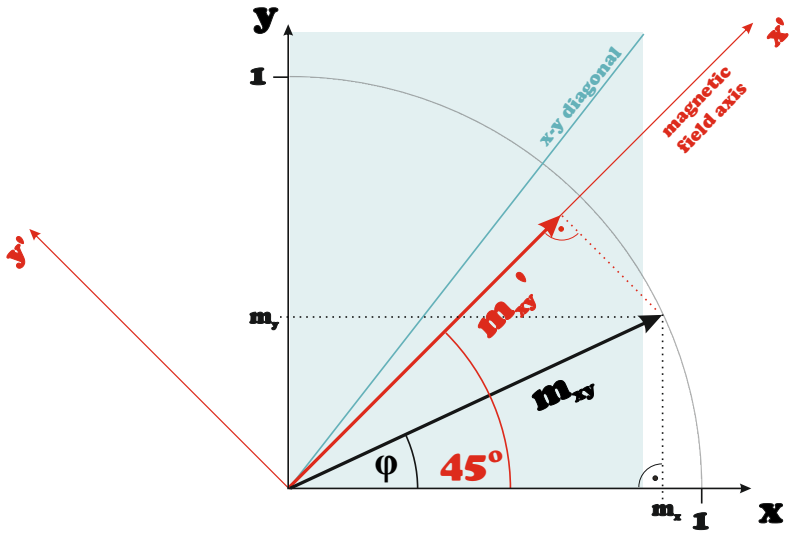

Figure 5.22.: Sketch for the calculation of the projection of the magnetization vector onto the magnetic field direction. The external magnetic field is applied along the <110>-axis of the crystal and according the nomenclature defined in Fig. 5.23 this is the "+"-direction in the x-y plane. In Fig. 5.24 the field direction is indicated by a "+" or a "-" of **B**. The apostrophe indicates that this direction is also the projection axis. A more detailed graphic can be found in the Appendix (Fig. C.1).

The projections onto the field direction for the hard axes of magnetization are given by:

$$\begin{aligned} m'_{xy} &= m_{xy}\cos(45° - \varphi) \quad , \quad \text{x-y plane} \\ m'_{yz} &= m_{yz}\cos(45° - \varphi) \quad , \quad \text{y-z plane} \\ m'_{zx} &= m_{zx}\cos(45° - \varphi) \quad , \quad \text{z-x plane} \end{aligned} \tag{5.7}$$

This is also sketched for the x-y plane in Fig. 5.22. A detailed description of the calculations can be found in the Appendix (Chapter C.1). For the case displayed in Fig. 5.22 the projection of the magnetization can be calculated according to eq. 5.7.
In Figure 5.24 the x-, y- and z-components of the magnetization and the projection of the magnetization vector onto the field axis (continuous gray line) are plotted as a function of **B**, which is applied along the hard axes. The indices of **B** indicate the plane and the direction along which it is applied (as defined in Fig. 5.23).
In (a)-(d) the shapes of the hysteresis loops correspond to the shape of a hard axis magnetization reversal for cubic anisotropy. H_c is about 90 mT and 80 mT in the x-y plane and 60 mT and 50 mT in the y-z-plane. In both cases the coercive field is $\sim$ 10 mT smaller when calculated along the negative direction. Larger coercivities along one direction can be attributed to an uniaxial anisotropy contribution, e.g. due to an elongation of the particle. This is confirmed for the positive x-y direction in the corresponding cross sections (Fig. 5.19) and can also be assumed for the positive y-z-axis from the tomography data (Fig. 5.18). In the x-z-planes, the shapes of the hysteresis loops are different.

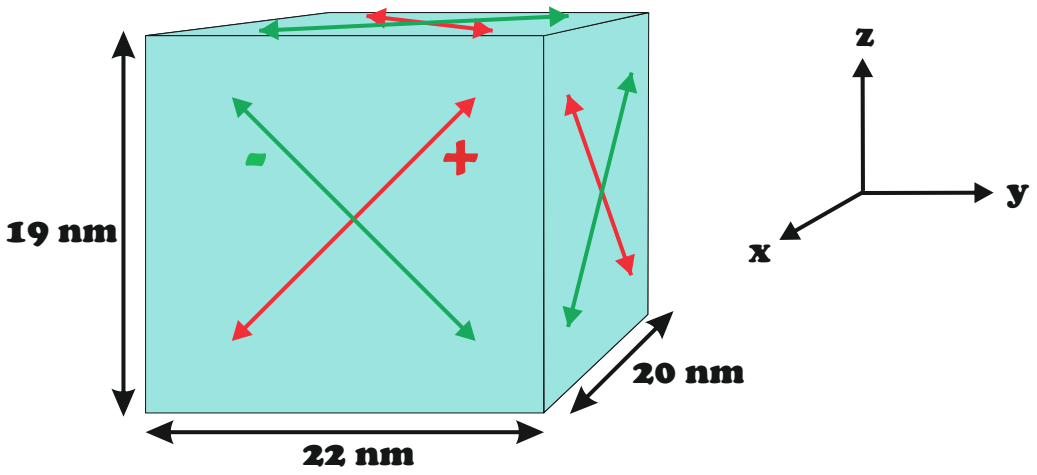

Figure 5.23.: Nomenclature of field directions for the hard axis simulations with respect to the coordinate system.

For the positive direction the hysteresis is open in the field range of about ± 90 mT, H_c is decrased to 20 mT, and the normalized magnetization at remanence is 10%. For the negative field direction, there is no remanent magnetization, H_c is also almost zero mT and the hysteresis is open in the field range of about $\pm (90 - 60)$ mT. For smaller field values the slope of the loop is linear. The small remanence value in both cases can be understood considering the y-component, which is almost one at remanence for all cases (a)-(f). Note, that the hysteresis loop along the positive z-x-axis in (e) looks almost identical to the loop along the x-axis in Fig. 5.20 a. That means that from the shape of the hysteresis loops the orientation of the particle cannot be uniquely determined.

In summary, ideal hard axis magnetization reversal is found along the <110>-axis in the planes parallel to the elongated y-axis of the nanocube. The differences in H_c can be attributed to different surface roughness and asymmetry of the particle correlated with an additional uniaxial contribution to the free energy density. In the planes perpendicular to the elongated y-axis the shapes of the hysteresis loops are more complex and smaller remanent magnetizations and coercive fields are determined.

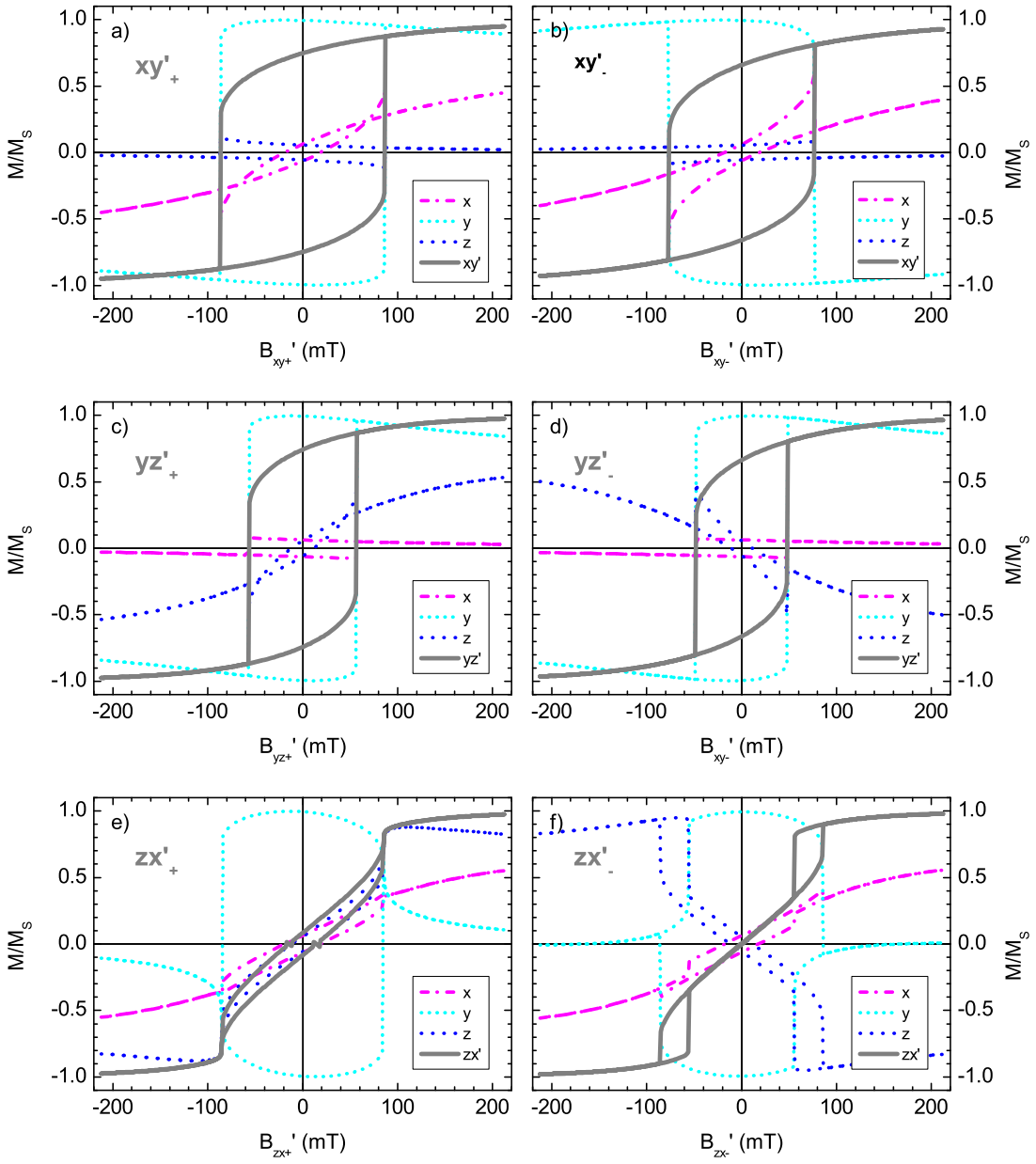

Figure 5.24.: Simulated hysteresis loops (x-, y-, z-magnetization components and projection of the magnetization vector onto the field direction) along the crystallographic "hard" axes of real nanocube morphology. The field direction is indicated by a "+" or a "-" suffix of **B**. The apostrophe indicates that this direction is also the projection axis.

5.4. Conclusion

In this chapter:

- Room temperature XPEEM hysteresis measurements of individual 18 nm Fe nanocubes were performed. These revealed:
  1. the existence of cubic anisotropy in the Fe nanocubes by analysis of about one hundred particles.
  2. a coercivity of about 2.5 mT.
  3. a reduced magnetization of the Fe nanocubes by about 50% with respect to the bulk.
  4. shifted loops which may be attributed to the stray fields of neighboring particle clusters.
- To understand these deviations from the expected behavior of the nanoparticles (Stoner-Wohlfarth behavior), micromagnetic simulations were used. Simulated ideal 18 nm cubes revealed that slight changes in morphology and reduced K_{eff} resulted in a decreased coercivity. Furthermore, H_c at RT is reduced by a factor of 0.25 with respect to H_c at 0 K.
- Introducing the experimentally measured morphology of the nanoparticles into the simulations allowed to fully explain the measured hysteresis loops:
  1. a 16% anisotropic elongation of an cuboid results in an increase of up to 250 % in H_c and a 6 % elongation to 30 % increase.
  2. differences in coercivity of up to one order of magnitude can be attributed to differences in surface roughness of about 2 nm.
  3. very different shapes of hysteresis loops are recorded and simulated along energetically equivalent crystallographic directions due to the morphology of the particle.
  4. the orientation of a real particle with respect to the external field cannot be concluded from the shape of the hysteresis. Identical shapes of hysteresis loops are simulated along an easy <100>- and a hard <110>-direction of magnetization.
  5. when taking into account the real morphology of the particles, higher order terms of magnetic anisotropy and additional uniaxial/directional contributions have to be considered to understand the magnetization reversal.

6. Magnetism of Nanoparticle Ensembles

In this chapter, hysteresis loops and XAS data of monomer, dimer, trimer and many-particle configurations are presented. For an easier comparison the diagrams containing experimental data are color coded: Light blue background indicates single nanoparticle measurements (also chapter 5.2 p. 68), light pink and yellow background correspond to dimer and trimer configurations, and green background to many-particle configurations or large clusters.

6.1. XAS and XMCD Studies on Individual and Many-Particle Configurations

The element-specific orbital (μ_l) and spin magnetic moment (μ_s) can be derived from normalized XMCD spectra and the application of sum rules [134, 135][1].

configuration	μ_s^{eff}	μ_l	$\frac{\mu_l}{\mu_s^{eff}}$
dimer 28	1.17(0.25)	0.08(0.02)	0.072(0.04)
dimer 55	1.05(0.2)	0.04(0.01)	0.04(0.02)
literature [136]	1.98	0.086	0.043

Table 6.1.: Orbital and effective spin magnetic moment (μ_B/atom) for two dimer configurations (spots 28 and 55 in Fig. 6.1). Saturation or self absorption effects are not corrected. Literature values for bcc Fe are also given for comparison.

μ_l and the effective spin moment μ_s^{eff}[2] were determined for two different dimer configurations (spots 55 and 28) in Fig. 6.1 (p. 98). Fig. 6.2 (p. 99) shows the corresponding room temperature XMCD spectra which were obtained in remanence after saturation[3]

[1] See Appendix C.2, p. 166 and [e.g. 106, 195, 196, and references therein] for details of the XMCD analysis.
[2] μ_s^{eff} includes the dipolar matrix element, which considers asphericities in spin density
[3] The magnetic field was applied along the direction of the Au markers.

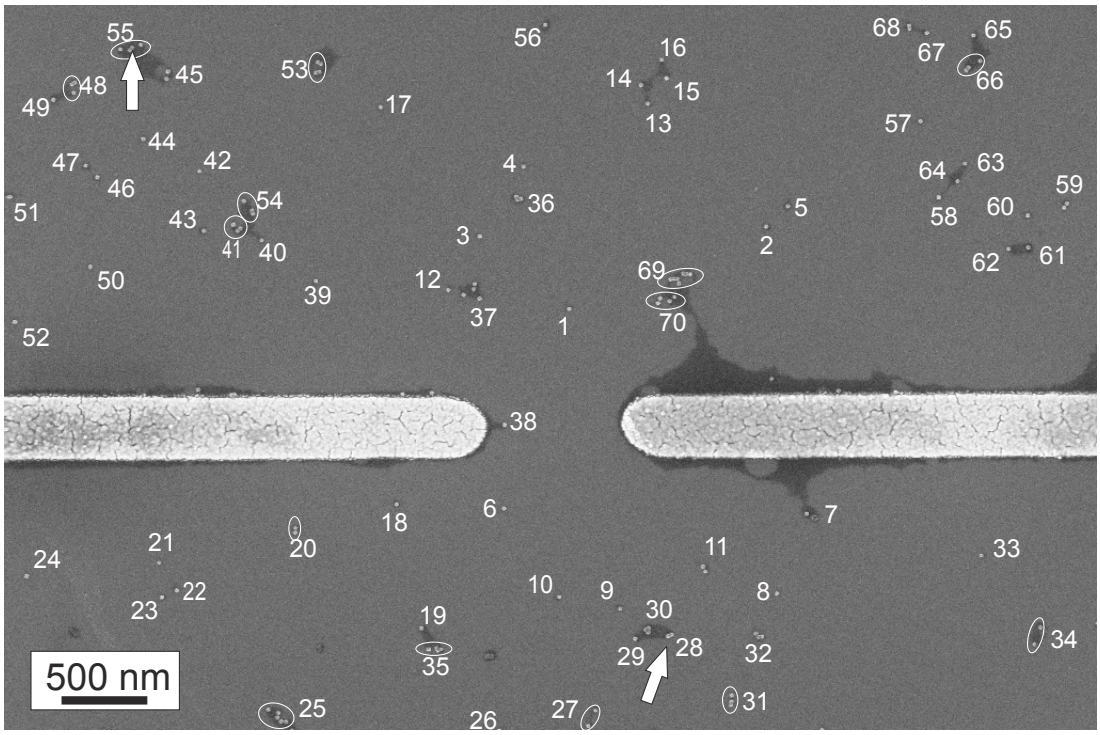

Figure 6.1.: SEM overview image of sample L3 acquired prior to the plasma treatment and Al-capping. XMCD spectra of the dimers (spots 28 and 55) recorded at B = 0 (remanence) are shown in Fig. 6.1.

in - 20 mT. The calculated moments are given in Table 6.1. The error bars are 20% for μ_s^{eff} and up to 50% for μ_l/μ_s^{eff} for the sum rule evaluation of my measurements covering a total energy range of 40 eV[4].

Magnetic moments of individual nanocubes could not be determined due to the low blocking temperature ($T_b < 290$ K) of this sample (p. 102 ff.). Figure 6.3 shows the σ^+ and σ^- absorption spectra for two nanoparticles (Spots 3 (a) and 4 (c) in Fig. 6.1). In comparison to the dimers, the signal-to-noise ratio is lower, and no XMCD contrast is detectable in (b), (d).

For the two dimers $\mu_s^{\text{eff}} = 1.1 \pm 0.25\mu_B$ is reduced by almost 50 % with respect to bcc Fe bulk. This reduction can be due to several factors:

[4]Typical error bars for sum rule evaluations are 10%-15% for Fe [197, 198], if a range of 100 eV around the Fe $L_{2/3}$-absorption thresholds can be evaluated.

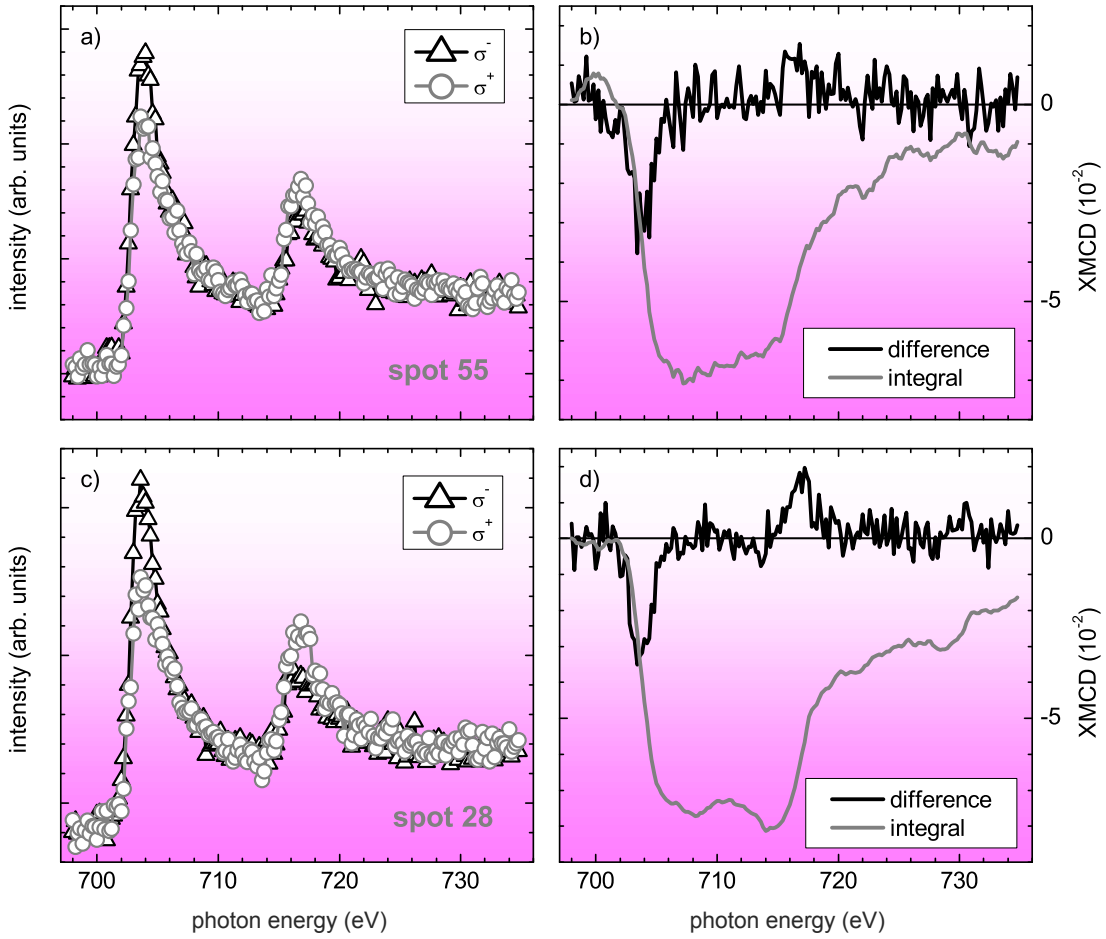

Figure 6.2.: RT XAS and XMCD spectra of dimer nanocube configurations recorded at remanence after saturating the sample with a field B = - 20 mT. Spot numbers refer to Fig. 6.1 on page 98.

1. Non-collinear spin alignment at the surface
2. Presence of magnetic domains
3. Formation of Al-Fe alloys
4. Presence of Fe-oxide
5. Impurities due to chemical synthesis

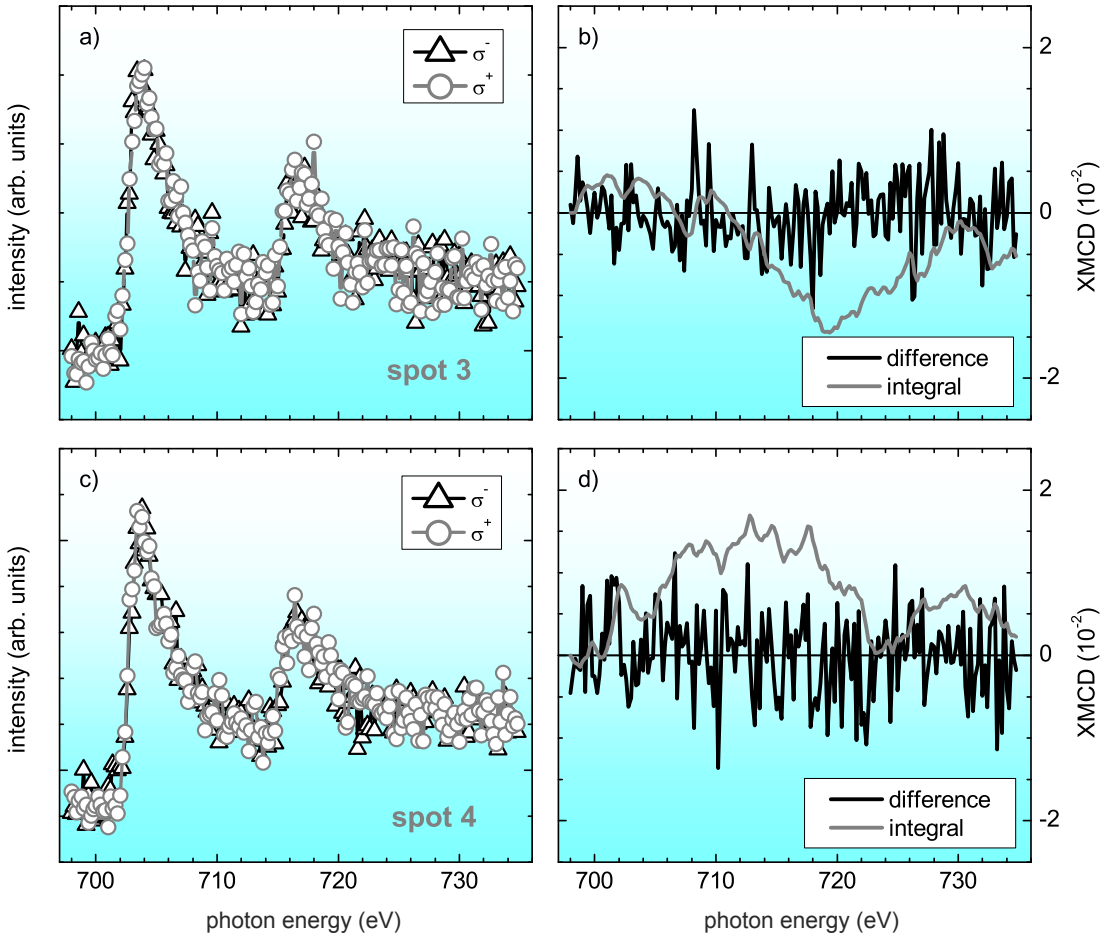

Figure 6.3.: (a, c) Room temperature XAS data of individual nanocubes (spots 3 and 4, Fig. 6.1) acquired at remanence after applying a saturating field of - 20 mT. No dichroism is observed (b, d).

6. Amorphous Fe with possibly strongly reduced magnetic moment on the surface due to plasma treatment

7. Thermal fluctuations of M over the time of spectra acquisition (~ 200 min)

The possibilities 1 and 2, i.e. non-collinear spin alignments or the presence of magnetic domains can be excluded. Indeed, micromagnetic simulations confirmed that no domains are formed and a spin canting would be in the range of a few degrees only, leading at most to a decrease of the magnetization of less than 1 %.

3.: The Al capping and the resulting alloy formation of Al and Fe at the interface is not likely to explain the reduction of the Fe magnetic moment μ_{Fe}. Indeed, in chemically disordered $Fe_{1-x}Al_x$ alloys μ_{Fe} is reduced to $\sim 0.9\,\mu_B$ and to less than $0.2\,\mu_B$ for FeAl and $FeAl_3$ [199]. Taking into account the XPEEM probing depth of 5 - 7 nm, an approximate 4 nm thick intermixed interface would be necessary to explain the reduction. This thickness is substantially larger than the 0.6 nm Fe/Al interlayer thickness found for thin films [200].
4.: No explicit signature of Fe-oxide is seen in the XAS spectra. i.e. if any oxide was present, it could only be at the bottom interface to the substrate. A 30 % reduced saturation magnetization had also been reported for an ensemble of similar 14 nm Fe nanocubes [194]. Even assuming that each Fe cube contains 10% of an antiferromagetic Fe oxide at the surface and/or the interface of particle and substrate could not explain this reduction. Consequently, the reduced magnetic moment cannot be completely explained by a partial oxidation of the nanocubes.
5.: Impurities due to the chemical synthesis are excluded as well: HRTEM investigations revealed single crystals. If any organic impurities were present, the particles would exhibit amorphous features, which were not observed. Furthermore, during the synthesis the mixture of precursor, sodium oleate, oleic acid and squalene was heated to the boiling temperature (310 °C − 320 °C) [170], i.e. the chemical bonds of the precursors are broken and only the "naked" Fe atoms coalesce forming the particle. The ligands, which attach to the surfaces, are still stable at these temperatures. Consequently, no precursor material should be inside of the particle.
6.: Since the Fe-oxide shell of the as prepared nanocubes has been reduced by a reactive hydrogen plasma, it can also be assumed that the Fe atoms did not perfectly recrystallize in the bcc-lattice but form an amorphous surface layer. Such a structural modification goes along with an immense decrease in magnetic anisotropy which was not found and Fe bulk values of K_{eff} have been reported [194]. Therefore, an amorphous surface layer as origin of the large magnetization reduction is excluded as well. Nevertheless, in-situ investigations of the particle crystallinity after the plasma treatment could not be carried out and will be the task of further studies.

A side effect of the plasma treatment, which reduces the Fe-oxide to Fe, is the resulting volume reduction of the nanoparticles. If the initial configuration is a perfect Fe/Fe-oxide cube with 3 nm oxide-shell thickness and $(18\,\mathrm{nm})^3$ volume, the dimension of the resulting pure Fe-cube is reduced to about 15.5 nm side length. This reduction is correlated with a decrease of the blocking temperature, i.e. the thermal fluctuation frequency increases. (7.:) In Table 6.2 the fluctuation time τ is exemplarily calculated for Fe nanoparticles assuming bulk anisotropy (K_{eff}[5] $= 48\,\mathrm{kJ/m^3}$), $T = 300\,\mathrm{K}$ and particle volumes of $(18\,\mathrm{nm})^3$ and $(15.5\,\mathrm{nm})^3$, and $\tau_0 = 10^{-12}\mathrm{s}$. For the larger particle the

[5]Note that in this example only the magnetocrystalline anisotropy is considered. Due to surface roughness of the particle K_{eff} may be different

magnetization is stable for billions of years whereas the fluctuation time is about one week for the smaller one. In consequence, for the smaller volume the magnetization fluctuates over the time scale of the hysteresis measurement (2 - 3 days), leading to a measured reduced magnetization.

K_{eff} (kJ/m^3)	18 nm	15.5 nm
48	2×10^{17} s	5×10^{6} s
44	8×10^{14} s	2×10^{5} s
40	3×10^{12} s	4×10^{3} s
30	2×10^{6} s	5×10^{-1} s
20	2×10^{0} s	7×10^{-5} s
10	1×10^{-6} s	8×10^{-9} s

Table 6.2.: Volume and anisotropy (K_{eff}) dependence of thermal magnetization fluctuations τ in a nanocube of 18 nm (15.5 nm) side length. τ calculated according to eqn. 1.17 with $\tau_0 = 10^{-12}$s and T = 300 K.

In conclusion, the reduced magnetization can be explained by thermal fluctuations over the timescale of the measurements, i.e. T_b of the reduced nanocubes is close to room temperature. This is also confirmed by SQUID measurements of an equivalent sample (not shown here [179]). Other possible explanations for the low T_b could be the decrease of the magnetic volume of the nanocubes, and a decrease of the effective anisotropy, due to the presence of amorphous layers at the surface.

The absence of a distinct XMCD signal for the individual cubes (Fig. 6.3) also indicates a T_b close to room temperature. In the dimers, strong dipolar coupling between the particles stabilizes the magnetization and increases T_b.
However, the nanocubes in sample 4B, which was used for the room temperature hysteresis measurements, must have a higher T_b than those investigated here (sample L3), since most particles showed an open hysteresis. The origin of this discrepancy in T_b in both samples is not clear but may be attributed to aging. Since the XAS spectra do not reveal oxide features, oxidation of the particles is excluded. As previously discussed, a decrease in size or in K_{eff} also results in a decrease of T_b. So the nanocubes of sample L3 could either be smaller than those of sample 4B or they could have a smaller effective anisotropy. Both samples were prepared using the same initial particle solution with the only difference that L3 was prepared several months later. When longer in solution the particles are likely to undergo small changes in morphology, e.g. become more spherical [201] due to different reactivities and surface energies of the different facets. As a consequence, shape and surface contributions to the effective anisotropy will change and in

case of a sphere a smaller K_{eff} is obtained[6]. However, such aging-induced morphology changes could not be confirmed by SEM within the resolution (2 nm) of the instrument.

Blocking and Magnetic Dipolar Interactions

Different blocking temperatures in the two samples (4B and L3) can be attributed to different magnitudes of magnetic dipolar interactions due to the different particle distributions on the two substrates. Sample L3 is more dispersed than sample 4B: The mean interparticle distances are $\sim 500\,nm$ (cf. Fig. 6.1) and $\sim 100\,nm$ (cf. Fig. 5.5).
For magnetically interacting particles Shrikman and Wohlfarth proposed a Vogel-Fulcher law considering the effective dipolar interaction energy (k_bT_0) in a nanoparticle ensemble. For $T_b >> T_0$ [202–204] the following formula quantifies the influence of magnetic dipolar coupling with the thermal fluctuation time τ:

$$\tau = \tau_0 \exp\left[\frac{K_{eff}V}{k_B(T_b - T_0)}\right] \tag{6.1}$$

For two point dipoles with magnetic moment μ at distance D the maximum dipolar interaction energy is given by $E_{dip} = (\mu_0/4\pi)(\mu^2/D^3)$ [104]. Assuming $T_0 = 30\,K$ and considering two Fe nanoparticles with $(15.5\,nm)^3$ and $(18\,nm)^3$ volume ($\mu_{15.5nm} = 350\,000\mu_B$, $\mu_{18nm} = 550\,000\mu_B$) each yields $D_{15.5nm} = 136$ nm and $D_{18nm} = 184$ nm. These distances are larger than the average inter-particle distance in sample 4B, and the influence of E_{dip} can be estimated by the Vogel-Fulcher law: Assuming $T_b = 300\,K$ and $\tau_0 = 10^{-12}$s, $\tau = 6.8 \times 10^8\,s$ for 15.5 nm Fe cubes with bulk anisotropy[7], which is two orders of magnitude higher than for non-interacting particles at RT ($\tau = 5 \times 10^6\,s$, cf. Table 6.2). This simple example clearly demonstrates the large influence of magnetic dipolar interactions on the particle's blocking behavior.

In this context the question arises: what is the criterion for non-interacting particles? Generally, dipolar interactions can be neglected if $E_{dip} << K_{eff}V$. However, the definition of the critical ratio of E_{dip} to $K_{eff}V$ is defined according to the experiment. Yang et al. proposed a critical ratio of $E_{dip}/(K_{eff}V) = 10^{-5}$ based on ac-susceptibility measurements [205]. In this reference, the authors suggest a simple general equation to

[6] An estimation of the influence of small variations in K_{eff} towards the thermal stability of the magnetization is listed in Table 6.2: For 18 nm cubes the magnetization does not fluctuate over the time scale of the hysteresis measurements unless K_{eff} is reduced to less than two third of the bulk value ($K_{eff} = 30\,kJ/m^3$). The reduced K_{eff} pushes the fluctuation time below one second for $(15.5\,nm)^3$ volume. Moreover, a slight K_{eff}-reduction of 9 % (from 48 to 44 kJ/m^3) for the cubes of 15.5 nm edge length decreases τ by more than one order of magnitude, that is from $5 \times 10^6\,s$ (58 days) to $2 \times 10^5\,s$ (~ 2 days).

[7] $\tau = 4.3 \times 10^{20}\,s$ for 18 nm Fe cubes

determine the critical spacing D for monodisperse non-interacting particles with particle diameter d and saturation magnetization M_s:

$$D = (20/3)\sqrt[3]{(30\mu_0 M_s^2/K_{eff})} \times d \tag{6.2}$$

Using Fe bulk values for M_s and K_{eff} and the sphere diameter of 19.2 nm - so that the volume of the sphere is identical to the volume of a $(15.5\,\mathrm{nm})^3$ cube - D is 780 nm. A reduction of the magnetization of 50 % as determined by our measurements still yields a critical interaction distance of about 492 nm. According to this, dipolar interactions need to be considered in sample 4B and may be neglected in case of L3. These examples confirm the correlation of different blocking temperatures and particle dispersions in our samples.

The critical radius of about 500 nm, which is on the order of 30 particle diameters, may hold for slight shifts of T_b due to dipolar interactions. Nevertheless, it appears rather large. As a rule of thumb it is typically assumed, that particles are non-interacting if the inter-particle distance is ten times the particle diameter. For our cubes, that would define a critical distance of about 170 nm. Consequently, what is the critical distance, at which a measured hysteresis loop is not influenced by the magnetic stray field of the surrounding particles? In this context, it is reasonable to assume that dipolar interactions are negligible when the stray field amplitude is smaller than the coercive field of the particle. For a single Fe nanocube $H_c \approx 2\,\mathrm{mT} - 2.5\,\mathrm{mT}$ as presented in Chapter 5.2 defining a critical stray field magnitude of 2 mT. The Zeeman energy of a 15.5 nm (18 nm) Fe nanocube in this field is 40 meV (62 meV) which is larger than the thermal energy at RT (~ 25 meV). The corresponding anisotropy energies are 1.1 eV and 1.7 eV, assuming Fe bulk K_{eff}. Consequently, the critical distance according to this criterion is smaller than 100 nm, as will be shown in the next section (cf. Fig. 6.6, p. 109).

Additional Aspects

In a cluster configuration of several hundreds of dense-packed nanoparticles, anisotropic dipolar interactions have a large impact on the blocking behavior. Either, they stabilize the magnetization, i.e. increase the energy barrier for low anisotropy particles, or they decrease the energy barrier in case of relatively high single particle anisotropy [32].

Helicity-dependent x-ray absorption spectra were recorded for a large nanoparticle configuration (marked by a green circle, top left of Fig. 6.22, p. 130). However, correcting the raw data necessary for sum rule evaluation was not possible[8], magnetic moments were not determined and no information on the influence of dipolar interaction could be obtained.

[8] The raw data is shown Fig. D.4, p. 170.

Nevertheless, the cluster XAS data show, that saturation effects have to be considered (Fig. 6.4). The lower intensity of the cluster spectrum with reference to a 40 nm Fe film [196, 206] strongly hints that saturation effects are present. Their correction, however, is non-trivial for nanoparticles.

Saturation effects were calculated for spherical Co-nanoparticles by means of Monte Carlo simulations [207]. For grazing incidence of 80° with respect to the surface normal μ_s was found to be reduced to 93 % (86 %) for particles with 10 nm (30 nm) diameter. For orbital moments (μ_l) saturation effects lead to a reduction to 56 % (24 %). Due to the larger number of d-holes in Fe, the absorption in Fe is stronger than in Co, and saturation effects gain more influence.

In our XMCD evaluation, this was neglected. Nevertheless, even if an underestimation of about 20 % of the spin magnetic momentis assumed, it does not provide an explanation for the measured reduced magnetic moments.

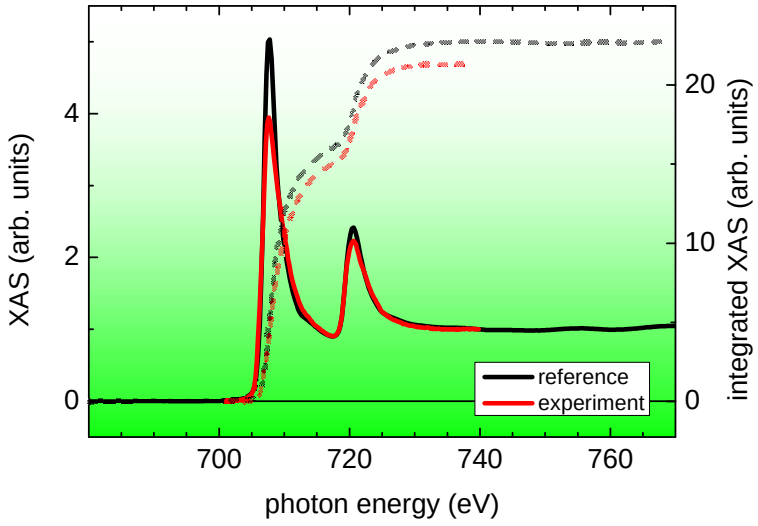

Figure 6.4.: Normalized Fe $L_{2/3}$ − edge XAS and integrated white line intensity for cube assembly (red) and for a Fe reference film (black)[196, 206].

In conclusion, the reduced magnetization determined in the Fe nanocubes can most likely be attributed to thermal fluctuations over the time scale of the measurement, i.e. at room temperature the nanocubes are close to their blocking temperature. T_b depends on the strength of the magnetic dipolar coupling of the particles and thus the inter-particle distance.

6.2. Remanent Magnetization and Strength of Dipolar Interactions

One experiment is described, which allows to address dipolar magnetic coupling effects in nanoparticle systems. The magnetic interactions between the nanocubes and the correlated complex stray fields may offer another explanation for the reduced average magnetization discussed in the previous chapter. To determine the strength of the dipolar interactions one needs to know the orientation of the remanent magnetization within the individual particles. How this information can be derived by XPEEM measurements is described in this section. Three results for the very diluted sample L3 are given as examples.

6.2.1. Measurement and Data Treatment

If the magnetization is in-plane, the remanent orientation and magnitude of the magnetization can also be determined directly by angular dependent measurements, i.e., by azimuthal rotation of the sample. If an out-of-plane component of the magnetization is also present, only the projection onto the photon incidence direction (k-vector) is determined. Evaluating the XMCD contrast for XPEEM data as a function of the azimuthal angle yields maximum and minimum contrast for parallel and anti-parallel orientations of the magnetization with respect to the photon k-vector ($y(\phi) = \mathbf{M}\cdot\mathbf{k}$). Accordingly, the XMCD contrast is given by:

$$y(\phi) = A + B\cos(\phi + C) \tag{6.3}$$

where ϕ is the azimuth, A, B and C are fitting parameters. A is an offset in the XMCD contrast and vanishes in an ideal experiment. B gives the strength of magnetization (maximum XMCD value) and C is the angular offset (tilt of the magnetization) with respect to the photon incidence direction. The photon incidence direction in Figure 6.1 is approximately parallel (from right to left) to the Au-marker for the reference measurement (0°). The sample was rotated clockwise and additional measurements were performed at 47.5°, 93.5°, 137° and 160° azimuthal rotation. Due to technical limitations measurements at larger angles were not possible.

6.2.2. Results

In Figure 6.5 the XMCD contrast as a function of azimuthal angle for three different particle configurations, one monomer (a), and two dimers (b), (c) is displayed. The corresponding configuration is sketched on the right and the fitting parameter B, i.e. the magnetization strength (M), is given. The relative orientation of the magnetization and its strength is represented by the orientation and length of the black arrows.

The magnetization of the monomer (spot 65) and the dimer (spot 20) are significantly smaller, than that of the dimer at spot 28. The latter exhibits a maximum XMCD of about 19 % which is of about the same range as the maximum values determined by the room temperature hysteresis measurements of sample 4B. Therefore, the total magnetization of the dimer is mostly in plane and dipolar coupling aligns the individual particle's magnetization along the elongated axis. Small deviations can be attributed to the morphology of the cubes and their imperfect alignment. For the monomer at spot 65 the small magnetic signal can be explained by an out of plane orientation. Assuming that the maximum XMCD value is 19 % for perfect in plane orientation of the magnetization, an out of plane orientation would reduce the XMCD to 5.4 %. This is in good agreement with the measured value of 4.1 %.

The magnetization determined for the dimer in spot 20 is even smaller. With 1.6 % it is also too small to be explained by an out-of-plane orientation of the magnetization. Furthermore, due to the magnetic interactions within the dimer cubes, an in plane orientation of the magnetization is expected. Thus, the magnetization vectors of both cubes must have opposite orientations favored by the dipolar coupling, so that the net magnetization is almost zero. Unfortunately, the lateral resolution of the instrument does not allow for individual magnetic imaging of each nanocube in the dimer.

To estimate the interaction radius of the Fe nanocubes, the magnetic stray field of an ideal 18 nm Fe nanocube with bulk M_s has also been calculated by micromagnetic simulations (performed by S. Gliga). The results are displayed in Fig. 6.6. The upper illustration shows the calculated stray field lines (small arrows) and the color map indicates the field strength of both, the outer stray field and the inner demagnetizing field. The white frame around the cube indicates its position. The maximum field value is about $H_{stray} = 1.2\,T$ at the edges of the cubes and H_{stray} quickly decays. In the two graphs below, the stray field decay is plotted as function of the distance from the cube edges along the easy axis, line A, (black solid line) and the hard axis, line B (red solid line). For the easy (hard) axis $\mu_0 H_{stray}$ is smaller than 5 mT at a distance of about 60 nm (50 nm). Additionally, the stray field decay has also been simulated for M_s reduced by 30 % (dashed lines). Here, $\mu_0 H_{stray}$ is smaller than 5 mT at a distance of 52 nm (< 45 nm) from the cube edge.

The magnetic stray field is smaller than 2 mT at 87 nm distance. Note also, that the simulations were performed at 0 K and for a perfect cubic shape. For a real Fe nanocube thermal fluctuations and morphology will influence the magnitude of the stray field and a smaller critical distance is expected. Therefore magnetic interactions most likely have to be considered only within an interaction radius $r < \sim 60$ nm. In this sample therefore only few configurations like those in spot 69 and spot 70 will "see" each other.

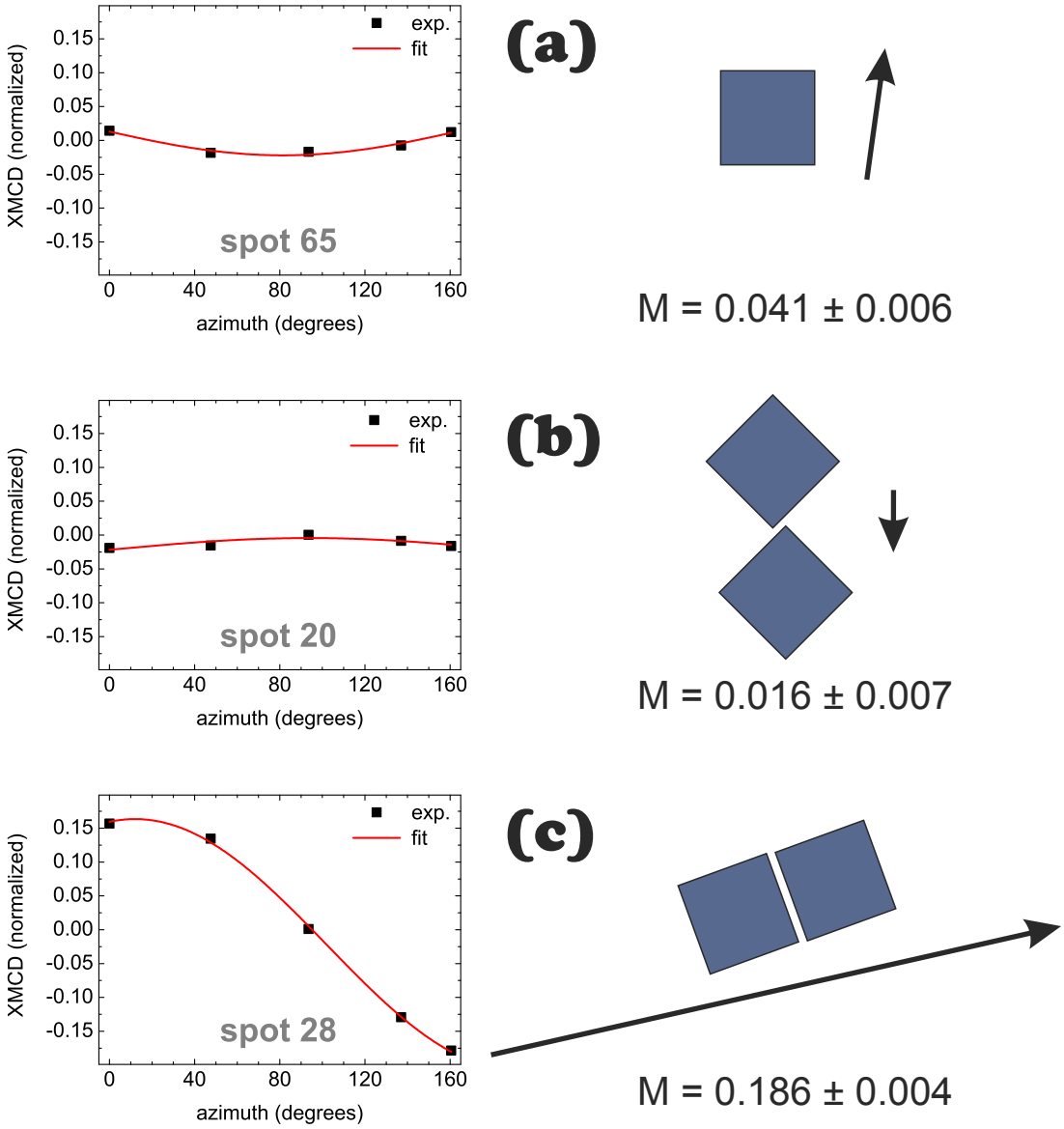

Figure 6.5.: Magnitude and relative orientation of remanent net magnetization of one monomer (a) and two dimers (b), (c). The length and orientation of the black arrow on the right respectively represent the magnitude and orientation of the magnetization (M) - dimensionless XMCD contrast - data obtained from fits in the plots on the left. The spot numbers refer to the numbering in Fig. 6.1. For details see text.

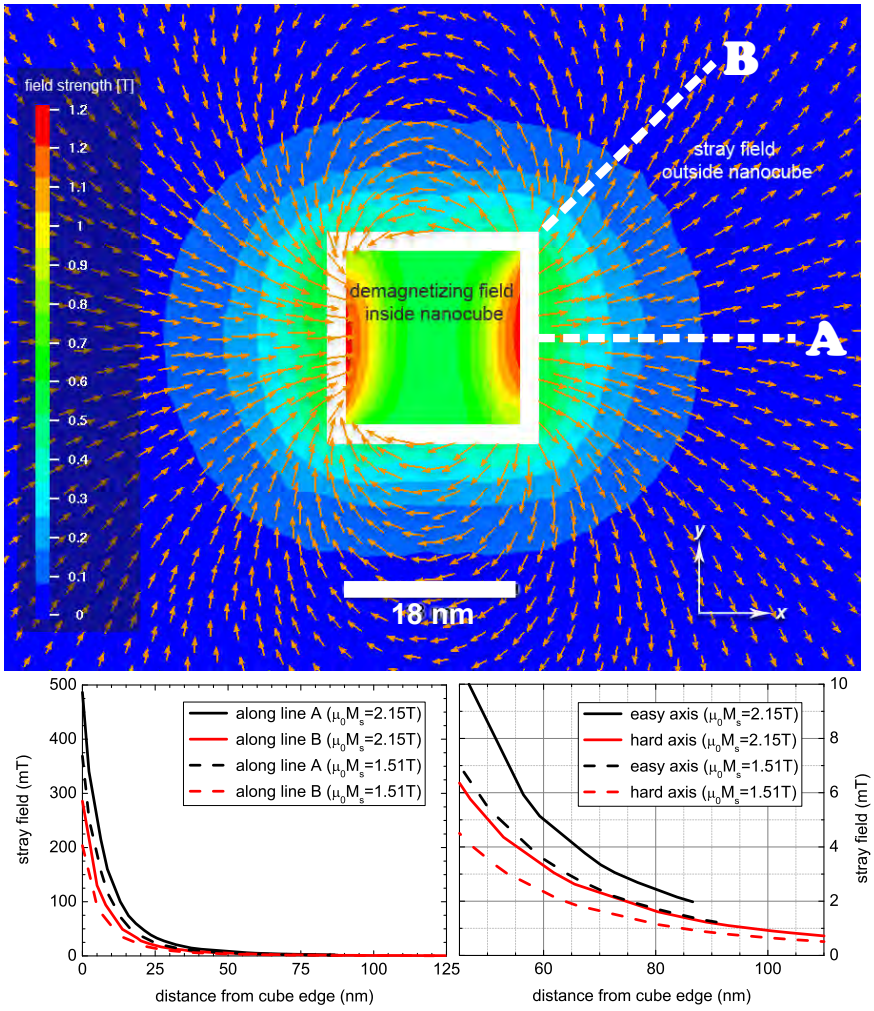

Figure 6.6.: Simulated demagnetizing and stray fields of an ideal 18 nm Fe cube with $\mu_0 M_s = 2.15T$ along a cutplane of the cube. The color scale represents the field strength and the arrows represent the direction of the stray field generated by the cube. Below (left), the decay of the stray field with increasing distance from the cube edge is plotted along its easy (A) and hard (B) axis. In addition, the corresponding data for a 30 % reduction in magnetization, i.e. $\mu_0 M_s = 1.51T$, is plotted. On the right hand side an enlargement of the area 45 nm - 110 nm is displayed. [Courtesy of S. Gliga]

6.3. Hysteresis of Dimers, Trimers and Other Particle Ensembles

6.3.1. Room Temperature Hysteresis of Dimers

Figs. 6.7 and 6.8 show hysteresis loops for two-particle (dimer) configurations. The results were obtained from the same image set of sample 4 B as the individual particle loops discussed in Chapter 5.2. The starting point of the hysteresis loops is - 9 mT. The corresponding SEM overview is shown on p. 70 (Fig. 5.5). An open hysteresis is found for all configurations, except for spot 13 in Fig. 6.7 b showing a linear response with no magnetization reversal.

First, I discuss the three dimers that show a closed hysteresis loop, i.e. spots 5 and 215 in Fig. 6.7 a, f and dimer 257 in Fig. 6.8 a. Dimer 215 shows a symmetric, nearly rectangular hysteresis with a coercive field $H_c \approx 3$ mT and a saturation magnetization of about 12 %, indicating an easy axis reversal. H_c[9] is only slightly enhanced with respect to the $H_c = 2.5$ mT of individual particles. A possible explanation is the existence of relative orientations of magnetic moments for which the dipolar interaction energy is zero, and the particle does not sense the stray field of the neighboring particle. In consequence, the coercivity could be that of individual particles.

For dimer 5 (Fig. 6.7 a) the saturation is 14 % and the coercive field is strongly enhanced ($H_c \approx 8\,mT$) with respect to dimer 215. For dimer 257 (Fig. 6.8 a) H_c is about the same as for dimer 5, whereas the magnetization is reduced by app. 30 %. Both loops are shifted to the negative field by about - 4 mT. Such a shift was also found for individual particles due to the magnetic stray field of neighboring particles. Here, no particles within a radius of 100 nm are found. A discussion of the horizontal shift of the hysteresis loops is presented Chapter 6.4.

Micromagnetic simulations (section 6.2.2) show that for an individual 18 nm cube the magnetic stray field decays rapidly and is smaller than 2 mT at a distance of four cube-diameters (> 60 nm). This excludes the stray field as the origin of the negative shift, which, except for spots 215 (Fig. 6.7 f) and spot 13 (Fig. 6.7 b), is present in all dimer hysteresis loops presented here.

One should note, that most hysteresis loops are still open at - 18 mT (c, d, e in Fig.6.7 and b, c, d in Fig. 6.8), indicating the recording of minor loops due to larger coercive fields when e.g. compared to the closed loop of dimer 5 (Fig.6.7 a).
The saturation magnetizations are typically in the range 10 % - 14 % (XMCD asymmetry of bulk Fe: ≈ 30 %). A significant reduction is only found for dimer 264 (Fig. 6.8 b). Here, however, the magnetization curve has still a slope, indicating that this configuration was not saturated within the applied field range, and the magnetization is perpendicular to the applied field. This is also confirmed by the SEM (Fig. 5.5), which shows that the

[9] For simplicity H_c is always given in mT as in the last chapter. (SI): $[\mu_0 H_C] = \mathrm{mT}$.

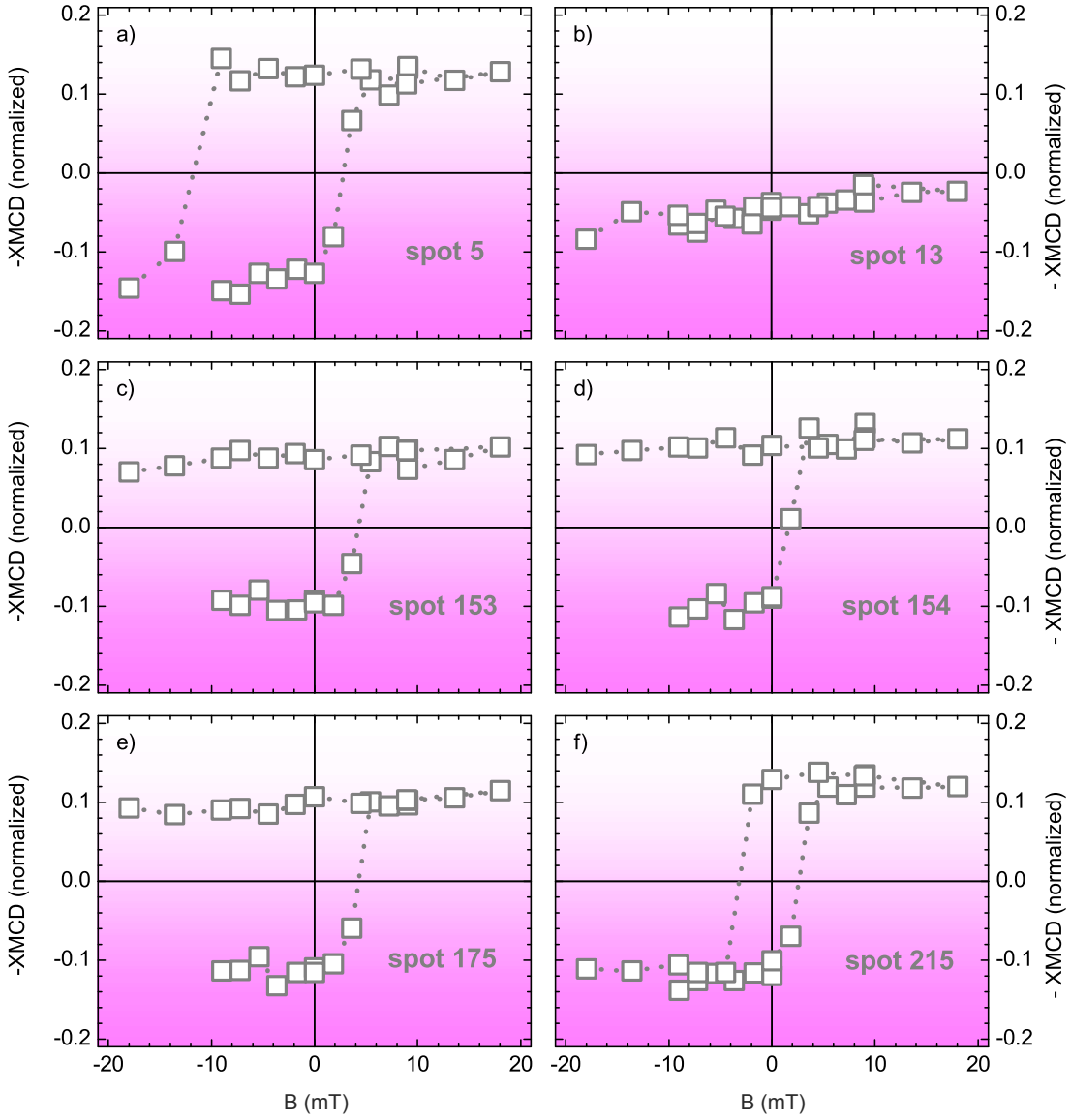

Figure 6.7.: **Dimer Nanocube Hysteresis I:** Experimental room temperature hysteresis data of different dimer configurations. Spot numbers refer to numbering in Fig. 5.5, p. 70.

dimer axis and its easy axis of magnetization is perpendicular oriented to the applied field.

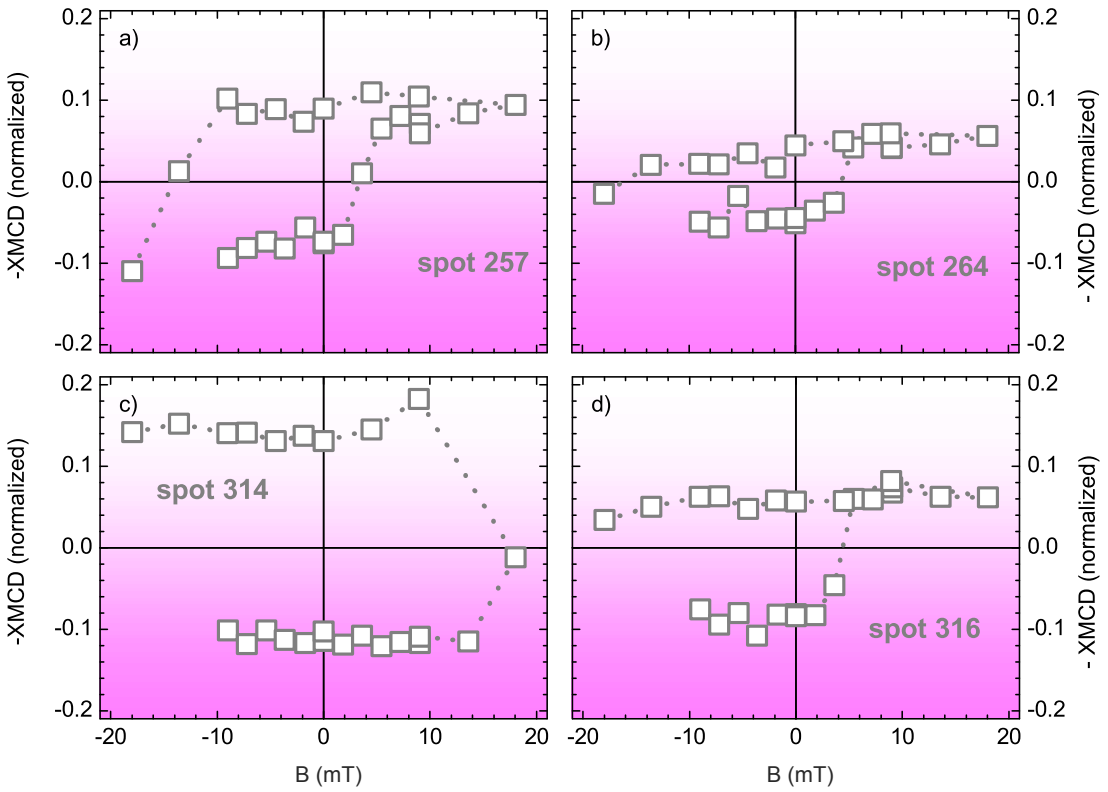

Figure 6.8.: **Dimer Nanocube Hysteresis II:** Experimental room temperature hysteresis data of different dimer configurations. Spot numbers refer to numbering in Fig. 5.5, p. 70.

For some configurations nearly zero magnetization was measured at 18 mT. This can be explained by an antiparallel magnetization orientation in the two cubes which is not possible to resolve experimentally. An example is shown in Fig. 6.8 d (spot 314). At + 18 mT the magnetization is slightly below zero. And at lower fields the magnetization jumps to high positive values. This indicates a slow continuous magnetization reversal: At + 18 mT the total magnetization was not completely reversed on the time scale of the measurement. Exposition to + 18 mT over several hours before the field was decreased to + 9 mT again, however, leads to a complete reversal.

Dimer: Simulation and Experiment

The hysteresis of an ideal dimer (18 nm side length perfect cubes with 2 nm distance) aligned parallel to the magnetic field, as e.g. the dimer in spot 5, was computed using micromagnetic simulations. Fig. 6.9 b shows the simulated loop which is in good accordance to the magnetization reversal measured for dimer 5 (a): H_c is more than doubled with respect to the individual cube and almost full saturation magnetization is obtained at remanence. No horizontal shift is found in the simulation. Three-dimensional sketches of the surface spin-structure at positions A - D are shown in Fig. 6.10. It is obvious, that the magnetization is still canted at the edges of the cubes even at the maximum applied fields. At remanence this canting is stronger, that is why the remanent magnetization is slightly smaller ($< 2\,\%$) than M_s.

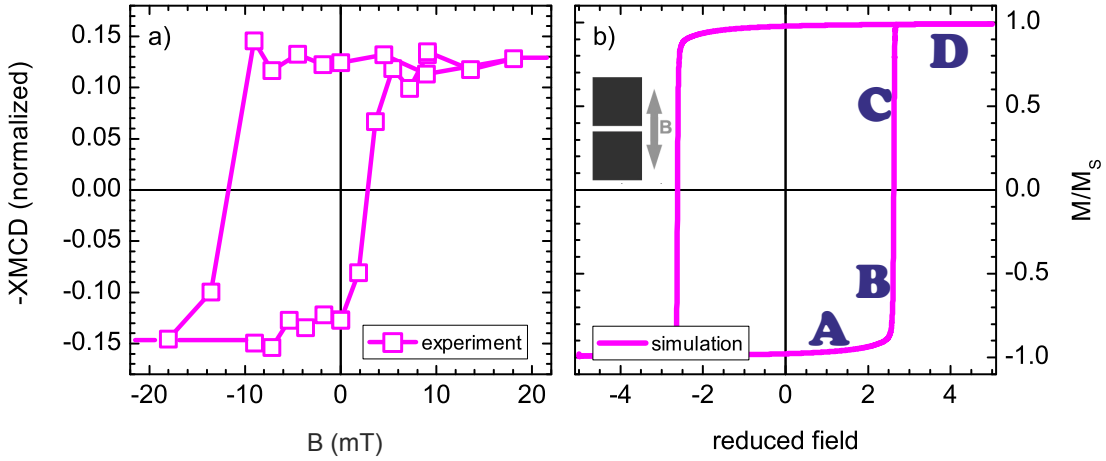

Figure 6.9.: Simulated hysteresis loops for a dimer configuration of perfect $(18\,\mathrm{nm})^3$ Fe cubes as sketched in (b). The normalized magnetization is plotted as a function of reduced field ($H\mu_0 M_s/2K_4$, bcc Fe bulk parameters). A - D correspond to snap shots of the orientations of "magnetic moments" as shown in Fig. 6.10.

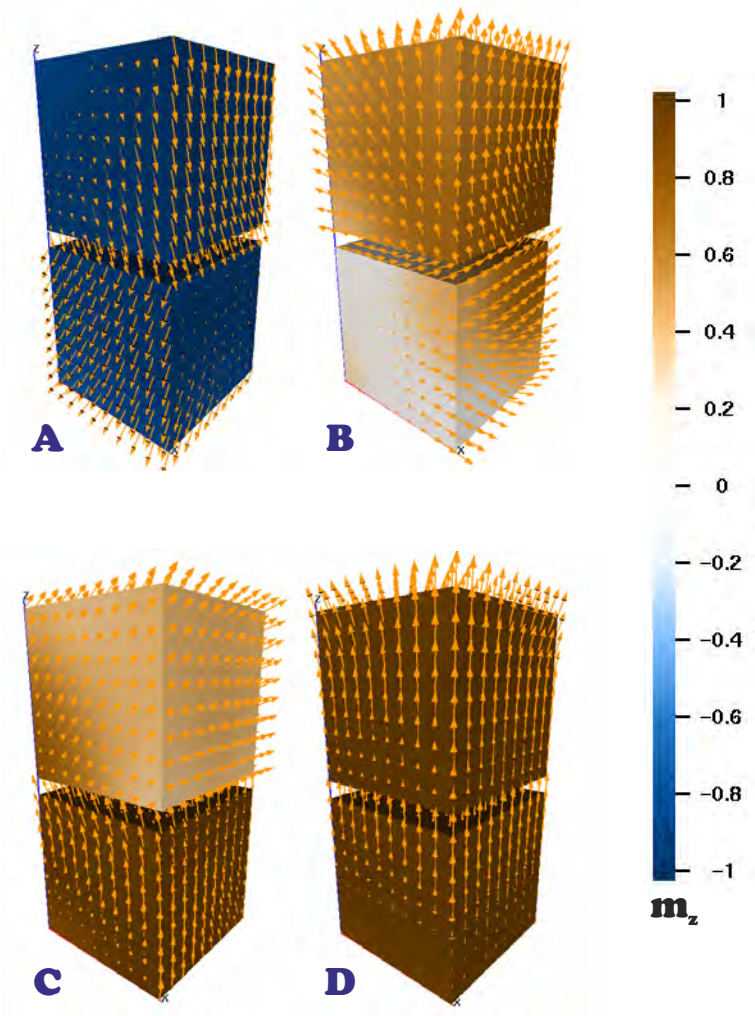

Figure 6.10.: Snapshots of the magnetization of a dimer at different locations (A-D) of the hysteresis loop (Fig. 6.9). The magnetic field is applied parallel to the z axis, i.e. the easy axis of the cubes. The z-component of the magnetization is given by the color code on the right.

6.3.2. Room Temperature Hysteresis of Trimers

In Fig. 6.11 the magnetic response of six trimer configurations is shown. Within error bars (a)-(e) show a linear response with no detectable slope, i.e., the magnetic field was too small to change the orientation of the total magnetization. M for the trimers in spots 16(a), 72(b) and 230(e) is almost zero, i.e. the easy axis for those cube alignments is perpendicular to the field direction, whereas trimers 126 (c) and 207 (d) have higher magnetization, about 15 % for spot 126, and therefore the easy axis must be more parallel to the field direction.

The trimer in spot 234 (d) shows an open hysteresis loop, with a small $H_c \approx 3$ mT, i.e. about the value of H_c of the individual cubes. In analogy to the discussion of the magnetic response for dimer 215, the relative alignment of the three cubes here, which is triangular, must favor a magnetic decoupling during the magnetization reversal. Additional magnetization curves for nanocube trimers are shown in Fig. D.3 in the Appendix, p. 169.

6.3.3. Room Temperature Hysteresis of Many-Particle Configurations

The shapes of many-particle magnetization curves are exemplarily shown for seven different configurations in Fig. 6.12. Open hysteresis loops were measured for spots 70 (a), 112 (b), 144 (c) and 329 (f). In (d) two linear responses are shown, spot 277 with magnetization reversal and spot 120 where there is no reversal. Interestingly, the magnetization in the latter configuration stays constant in the opposite direction of the starting field which can only be explained by a complex magnetic stray field due to dipolar coupling to the surrounding particle configurations.

The linear slope and small magnetization measured for spot 277 also indicate a hard axis reversal and no saturation within the applied field. As found for some dimer configurations the hysteresis loops in (b) and (c) are still open after the complete field cycle and exhibit a shift to negative field values. In case of spot 112 the estimated coercivity $H_c \approx 16\,mT$ and the shift is of the same order as found for the closed dimer loops, i.e. - 4 mT. For spot 134 H_c could not be determined, since the loop was still open at - 18 mT. It must be larger than 11 mT, and therefore the bias is larger than - 4 mT. Spot 70 (a) shows a minor magnetization loop. Another minor loop can be assumed for spot 267 (e). The magnetic field range, however, was not large enough to saturate that configuration.

Spot 329 shows an interesting two-step magnetization reversal, indicating a complex non-coherent magnetization reversal within that cluster. This specific configuration could not be resolved in the SEM image but the reversal behavior is similar to that simulated for a trimer configuration as shown in the following section.

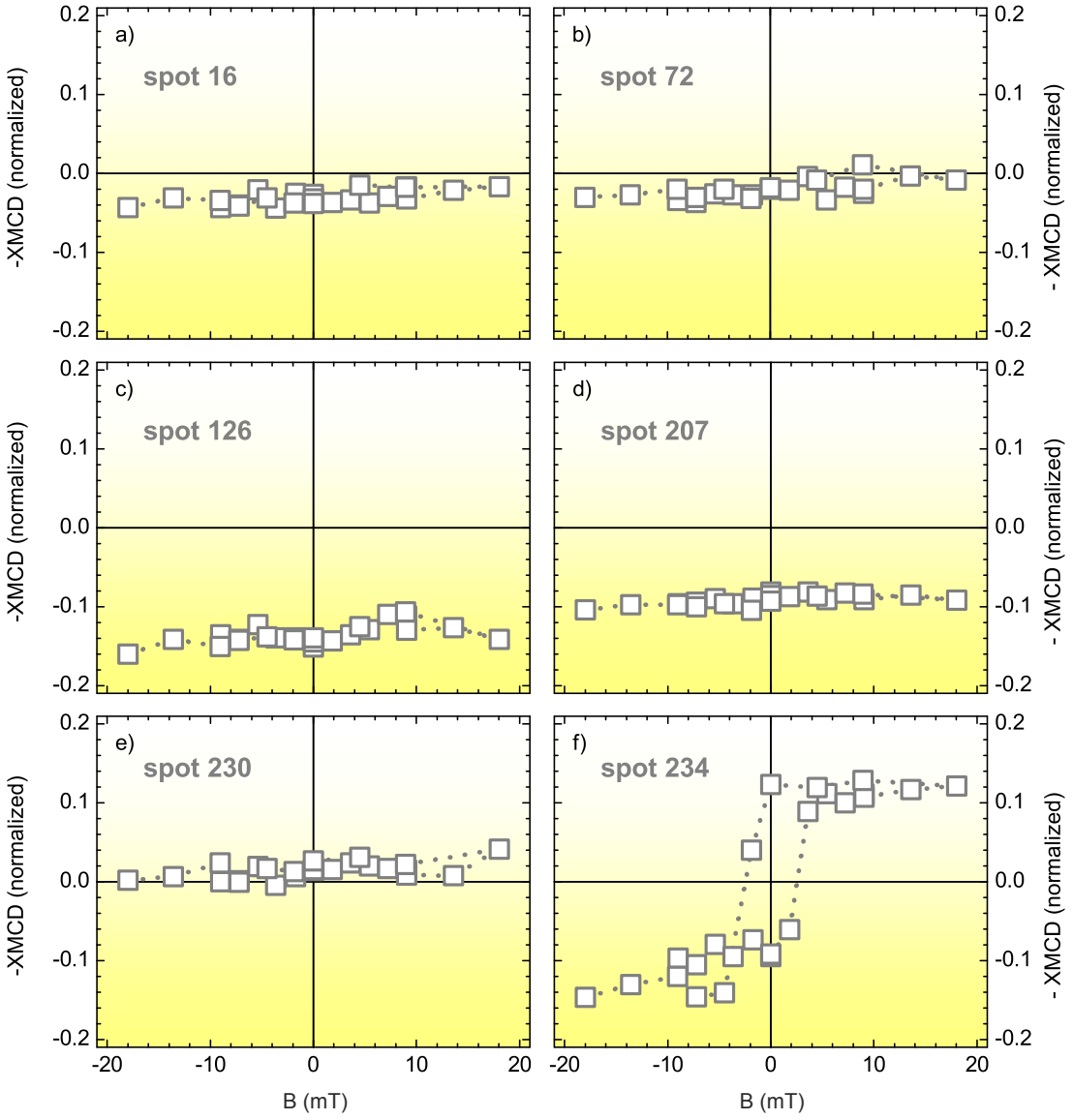

Figure 6.11.: **Trimer Nanocube Hysteresis I:** Experimental room temperature hysteresis data for trimer nanocube configurations (Sample 4B). Spot numbers refer to numbering in Fig. 5.5, p. 70. More trimer hysteresis data can be found in the Appendix D, p. 169 (Fig. D.3).

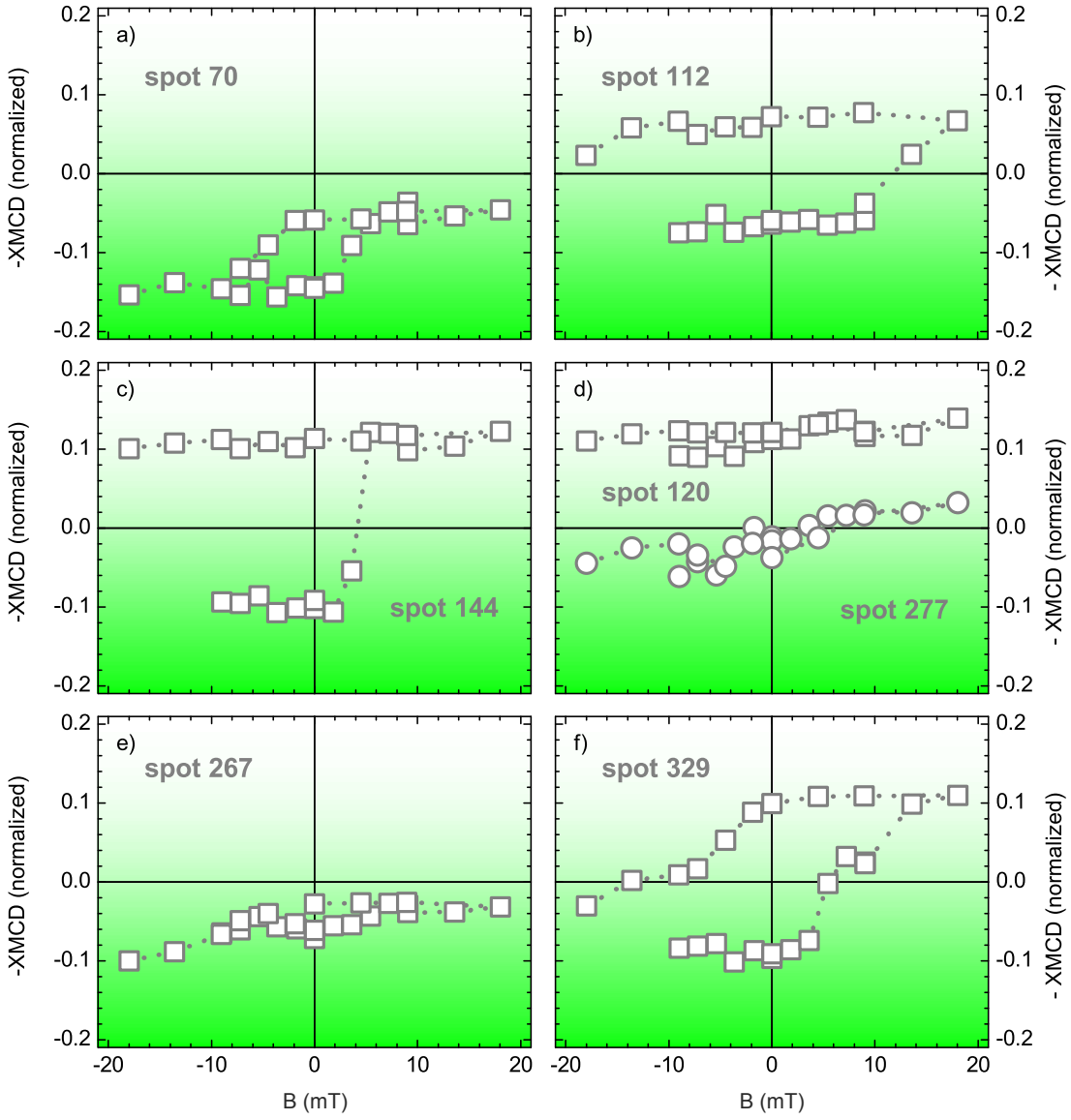

Figure 6.12.: **Many-Nanocube Hysteresis:** Room temperature experimental hysteresis loops for different many-nanocube configurations (Sample 4B). Spot numbers refer to numbering in Fig. 5.5, p. 70.

Trimer: Simulation and Experiment

In micromagnetic simulations of a trimer in which one nanocube is not aligned face-to-face but includes some angle with the other two nanocubes (inset Fig. 6.13 b) a similar behavior of the magnetization reversal as for spot 329 is found. When compared to the dimer in Fig. 6.9 b, this configuration has a significantly reduced saturation magnetization indicating the presence of magnetic fluctuations or frustration, caused by the larger distance between the Fe nanocubes or by their non-collinear alignment, respectively. Spin-resolved sketches of positions A - D of the first hysteresis branch are shown in Fig. 6.14.

The first step of the magnetization reversal (B) can be attributed to a switching of the middle cube whereas the outer cubes rather have a perpendicular magnetization alignment with respect to the applied field, and H_c has about the value of an ideal single cube. At the second step (C), the magnetization in the other cubes also rotates in the field direction.

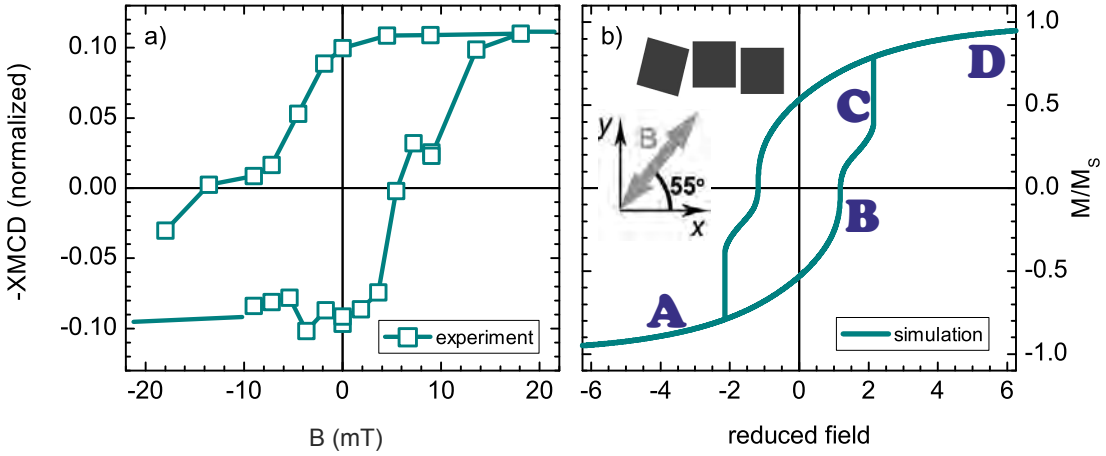

Figure 6.13.: Measured (a) and simulated (b) hysteresis loops for a trimer configuration configuration (sketched in the inset of figure b) of perfect $(18\,\mathrm{nm})^3$ Fe cubes. The magnetization is plotted as a function of reduced field ($H\mu_0 M_s/2K_4$, bcc Fe bulk parameters). A - D correspond to snapshots of the spin configurations shown in Fig. 6.14.

In summary, complex RT magnetization reversals were measured for dimer, trimer and many particle configurations. The origin of the complex reversal behavior can be attributed to the different anisotropic dipolar coupling of the specific configurations due to different relative orientations of the nanocubes with respect to each other. Furthermore, since at RT the particles are close to their blocking temperature, different sizes and

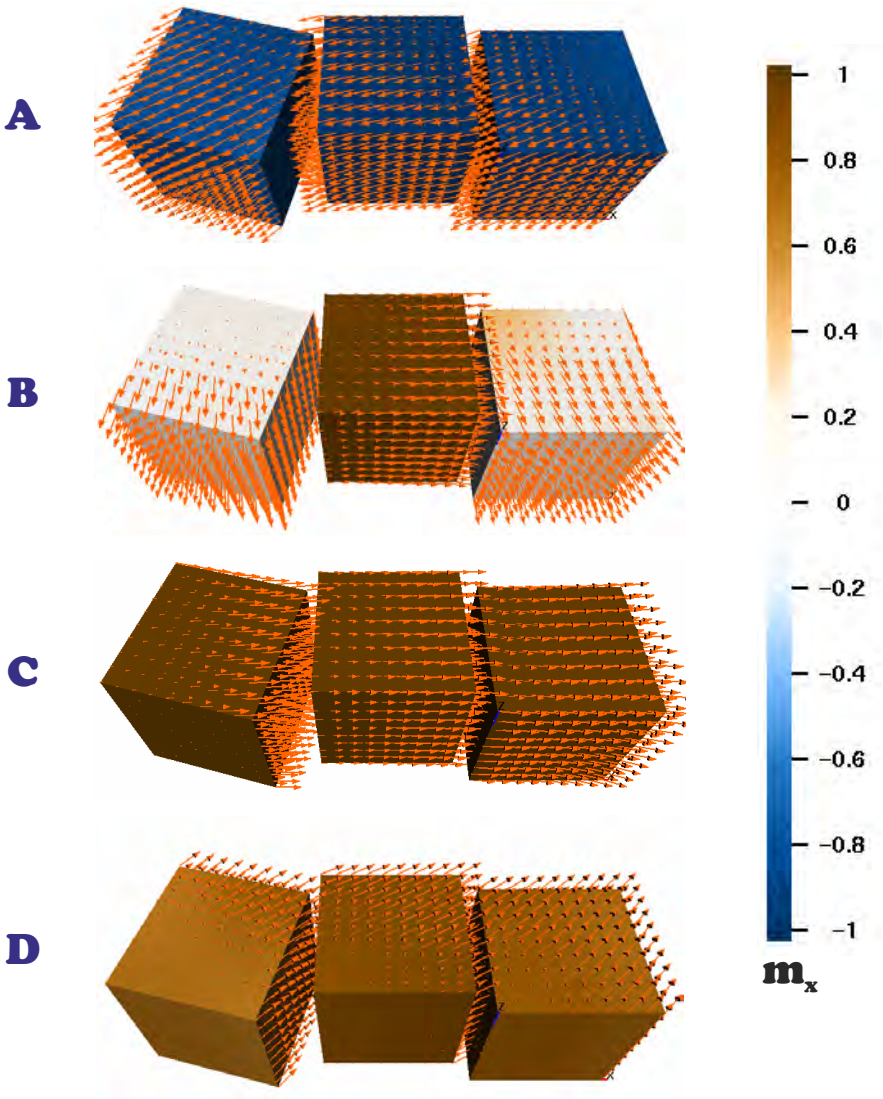

Figure 6.14.: Snapshots of the evolution of the magnetization along the first branch of the hysteresis loop (positions A-D in Fig. 6.13) of a trimer configuration. The cubes in the trimer are aligned along the x-axis and the external magnetic field was applied in the x-y plane at 55° inclination angle with respect to the x-axis. The x-component of the magnetization is given by the color code (right).

morphologies influence H_c and the measured saturation magnetization. H_c is enhanced due to the dipolar coupling and the field range of ± 18 mT is too small to reverse the magnetization in most particle configurations larger than or equal to two nanoparticles.

Additionally, an unexpected horizontal shift of the hysteresis loops to negative field values is found for many configurations. Such a shift is reminiscent of the exchange bias effect [115, 116, 118] commonly due to unidirectional coupling between a ferro- and an antiferromagnet after cooling the sample in an applied magnetic field. In consequence, an antiferromagnetic Fe-oxide layer in the cubes should be present, although it was not not observed by XAS measurements. The discussion of possible origins of this peculiar "exchange bias" will be addressed in Chapter 6.4, p. 130 ff.

6.3.4. Micromagnetic Simulations of Many-Particle Configurations

All micromagnetic simulations presented in this chapter (thanks to C. Hassel and S. Stienen) were performed at 0 K using the OOMMF code with bcc Fe bulk parameters. After saturation in negative fields, the hystereses were simulated in ± 200 mT and ± 400 mT, respectively.

6.3.4.1. Coercivity of Linear Chains

The coercive fields for linear chains consisting of up to 8 nanocubes have been simulated. All particles had truncated edges (radius 2 nm), Fig. 5.16 b. A three dimensional view is also sketched in (a) of the same figure. The cubic particles were packed facet-to-facet along the magnetic field (x-)axis with a distance of 2 nm. In Figure 6.15 the simulated hysteresis loops are displayed and in the inset the respective coercive fields (Table 6.15) are plotted as a function of number of particles in a chain. The error is ± 0.25 mT according to the field step size in the simulations. The coercive field increases by nearly a factor of two from the single particle to the dimer configuration. This increase is non-linear as a function of the number of particles in a row, and H_c seems to approach a saturation value for longer chains (more than 8 particles).

This can be understood as follows: The more particles in a row, the closer is the dimension of the chain to infinity. For an infinitely long rod parallel to x with the magnetization parallel to the cylinder axis the demagnetization factor $N_x = 0$. N_x for not infinitely long chains will also become zero when the magnetic poles created at the ends will be too far away to matter [87]. Therefore, H_c will saturate at some number of particles.

For an infinitely long rod H_c is half the saturation magnetization, i.e. about 1 T for Fe bulk, which is significantly larger than 271.5 mT found for the 8 nanocube chain here.

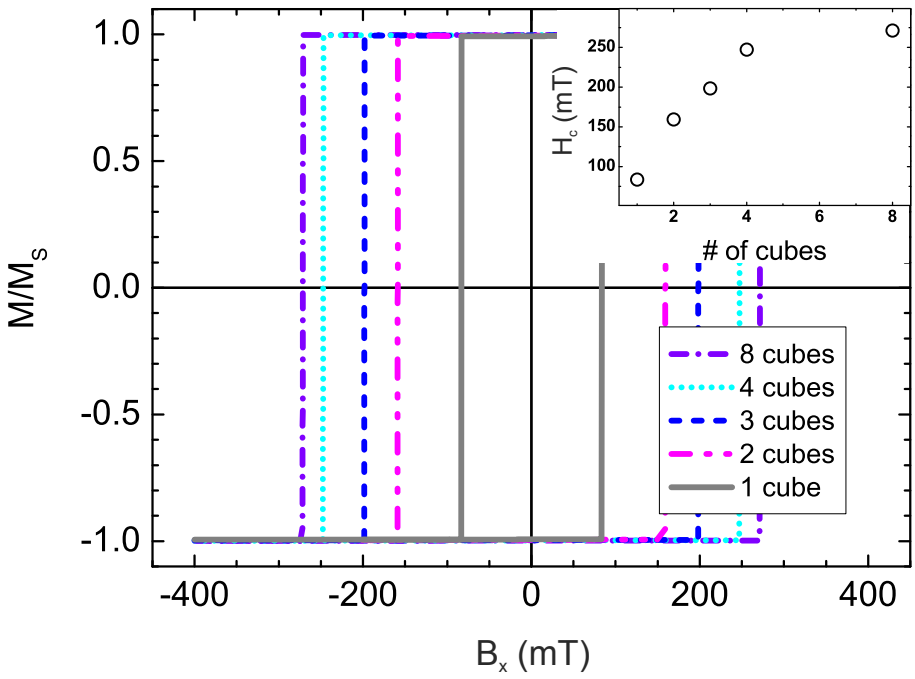

Figure 6.15.: Simulated hysteresis loops for linear chains consisting of 1, 2, 3, 4 and 8 particles aligned along the field axis with a distance of 2 nm in between. The inset shows the coercive fields as a function the number of particles in the chain.

# of particles in chain	1	2	3	4	8
H_c (mT)	83.75	159.25	198.25	247.38	271.5

Table 6.3.: Coercive fields for linear chains of 18 nm truncated Fe nanocubes as calculated by OOMMF (Fig. 6.15).

6.3.4.2. Hysteresis of Many-Cube Configurations

As revealed by the measurements, there is no identical hysteresis for single nanoparticles (Chapter 5.3.3, p. 86). Consequently, any configuration of individual particles exhibits (slightly) different magnetic responses. Complete understanding would require the full tomography data of all particles in the configuration. The influence of morphology on the magnetization reversal of an individual particle was discussed in detail in Chapter 5.3.3. Here, without further discussion, the simulated hysteresis of four different idealized configurations (two dimers (a, b), one trimer (c) and a four particle cluster (d)) are exem-

plarily displayed in Fig. 6.16 to demonstrate the variety in their magnetization reversals and the resulting hysteresis loops. The corresponding nanocube configurations are shown as top view of the x-y plane as insets in the panels and the magnetic field B was applied along the x-axis, which is parallel to the x-axis of the diagrams. It is noteworthy, that H_c in cases (b) - (d) is smaller than for the ideal dimer configuration in (a). Interestingly, the 45 ° tilt of one particle with respect to the other also reduces the coercivity to a value smaller than 84 mT which was determined for an individual nanocube.

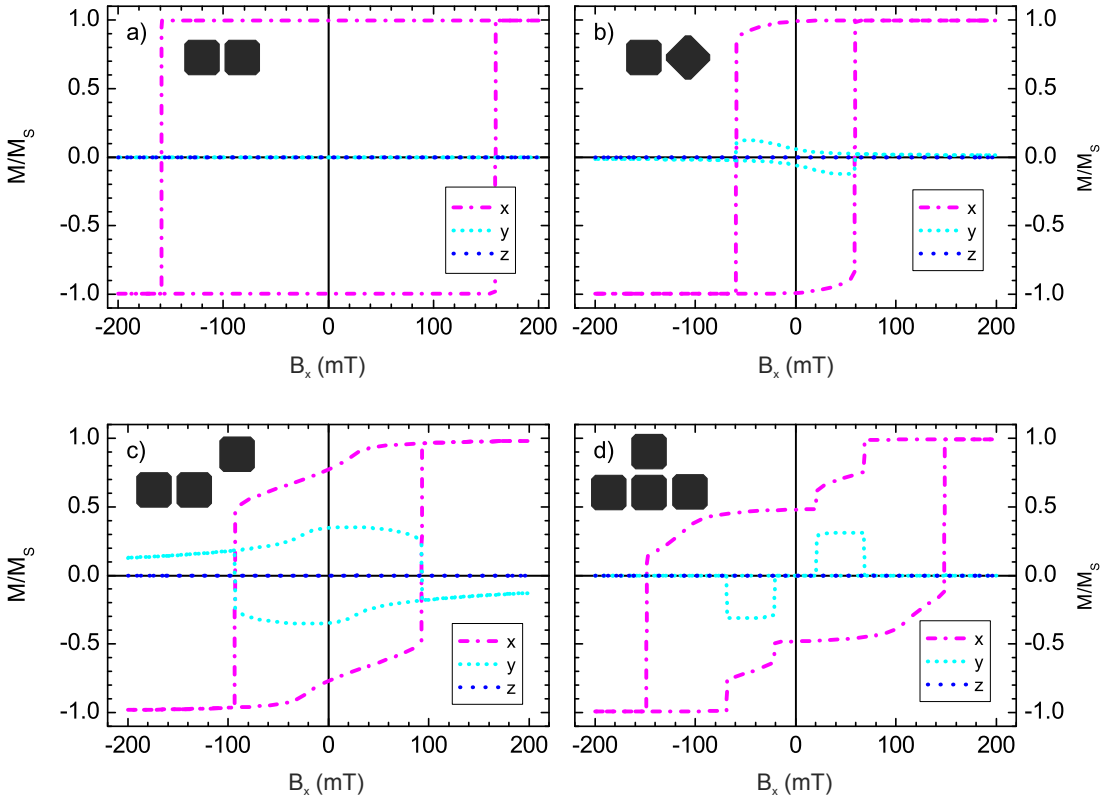

Figure 6.16.: Simulated $m_{x,y,z}$ hysteresis loops for truncated nanocube configurations as sketched in the corresponding panels. The magnetic field B_x is applied along the x-axis. The configuration sketches show the top view of the x-y plane, and the x-direction is parallel to the x-axis of the diagrams.

6.3.4.3. Influence of Morphology

As discussed in Chapter 5.3.3 the hysteresis behavior is dramatically influenced by the morphology of the nanoparticles. To understand this influence three exemplary simulations A, B, C for a dimer configuration were performed. The dimer consists of two identical nanoparticles with the morphology determined by tomography measurements (Chapter 5.3.3). In simulation A the real morphology of the particle was copied along the x-direction with about 2 nm spacing in between (Fig. 6.17). The nanocube was copied along the elongated y-axis in B (Fig. 6.19) and in C (Fig. 6.20) along the x-axis again and the right cube is tilted by 45° clockwise with respect to the left one. In all three cases the corresponding x-y plane top views are sketched in the figures and the x- and y-axes of the diagrams are parallel to the x- and y- directions of the sketches. For A and C also spin resolved cross sections from the middle of the particles are shown in Fig. 6.18 and Fig. 6.21.

A: Real Morphology Dimer Packed Along X-Axis

Figure 6.17 shows the simulated hysteresis loop for two particles packed along a short axis and parallel to the external field direction. The z-component of the overall magnetization is approximately zero. That means, the magnetization rotation of the dimer particles either takes place almost completely in the x-y plane, or the z-components of both particles exactly compensate each other. Due to their elongation along the y-direction, the shape anisotropy of an individual particle favors the magnetization alignment parallel to the elongated axis which is perpendicular to the dimer axis.

The particles were initially saturated in the negative x-direction, and therefore the magnetic dipolar interaction energy initially favors the parallel coupling (1). When approaching remanence a significant re-orientation of the individual magnetizations occurs at -15 mT (2), i.e., the Zeeman energy is too small to exceed the individual shape anisotropy and the dipole-dipole interaction stabilizes the antiparallel alignment. Figure 6.18 shows calculated spin resolved images directly before (2a) and after this re-orientation (2b). It is visible, that the magnetic moments are non-collinear within the particles with spin canting at the edges. There are some areas at the top of the particles which have positive x-magnetization components, although the field was not reversed yet. From there on, the magnetization reverses uniformly and in zero-field, apart from a very small x-component (-0.015), there is no remanent net magnetization. Complete compensation of the x-component is obtained at $H_c = 3\,\mathrm{mT}$. Both magnetizations further rotate uniformly into the field direction when B is increased to positive values. The slope is linear like the one of an hard axis reversal in the Stoner-Wohlfarth model.

At $+52\,\mathrm{mT}$ the magnetic energy is strong enough to overcome the individual shape anisotropy and the magnetizations turn instantaneously into the field direction (Figure 6.18, 4a and 4b). Due to the asymmetric shape of the particle, there is some pref-

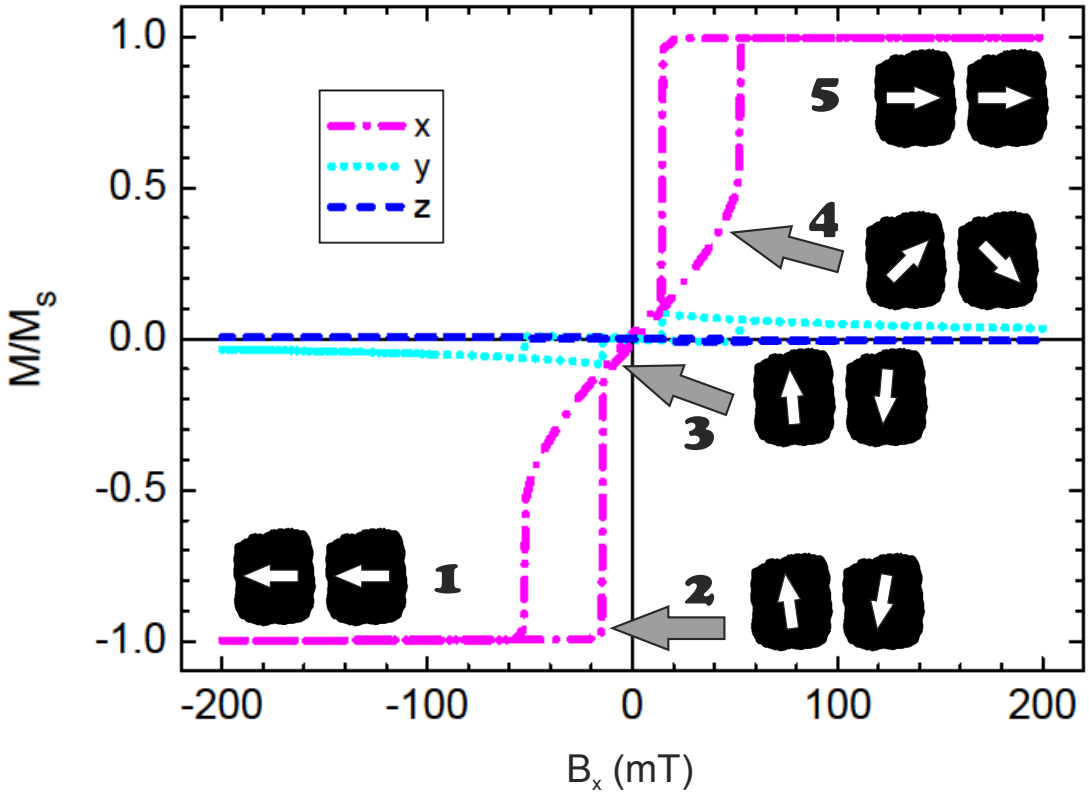

Figure 6.17.: Simulated net $m_{x,y,z}$ hysteresis loop of a dimer configuration consisting of two identical nanocubes with real morphology. **B** was applied along the packing (x-) axis. At positions 1 - 5 the orientation of the individual nanocube magnetization is sketched. More detailed cross section images showing the magnetic moment alignment in the vicinity of 2 and 4 are displayed in Fig. 6.18.

erence for a diagonal (x-y) magnetization alignment. This gives a positive contribution to the y-magnetization component, which decreases with increasing field. Nevertheless, $\pm 200\,\mathrm{mT}$ is obviously not sufficient to saturate this dimer along the x-direction. In panels 2a and 4b of Figure 6.18 it becomes obvious that the strong canting at the top right corner of the right particle is responsible for this y magnetization contribution.

The magnetization reversal of this dimer is very different when compared to the simulation result for an idealized dimer configuration (section 6.3.1, Fig. 6.10 b). For the latter, a rectangular hysteresis with a coercive field of about twice the magnitude of H_c of an idealized single particle was found.

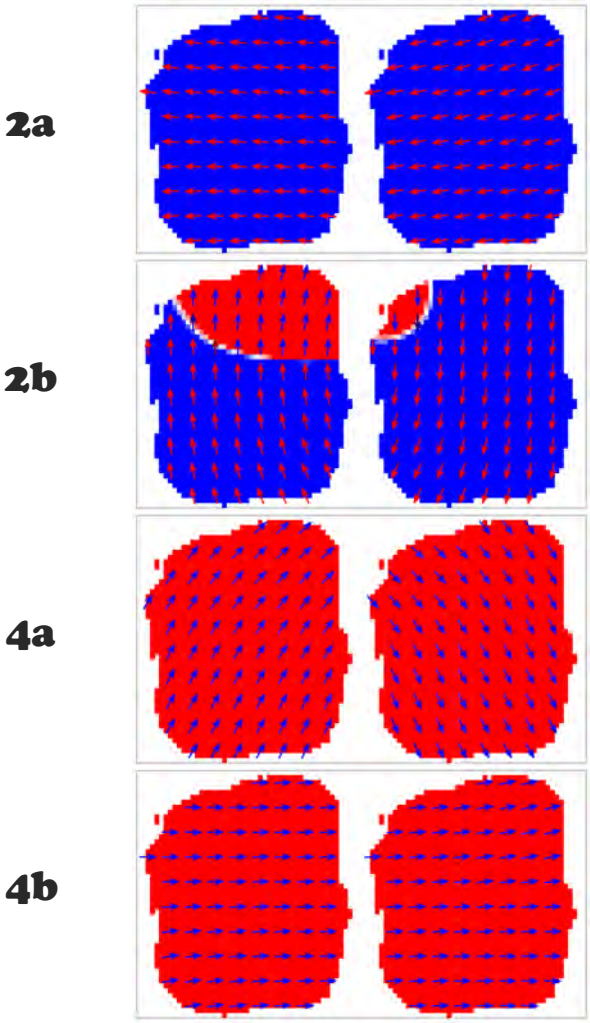

Figure 6.18.: Cross section snapshots of the orientation of the magnetization within an inner plane of a "real morphology" dimer configuration. The corresponding hysteresis loop is displayed in Fig. 6.17 and the numbers refer to the marked positions: 2/4a immediately before the jump in the hysteresis loop at positions 2/4, and b refers to the magnetization orientation after that jump. The color code represents the sign of the x-component, blue means negative, red means positive and white means no x-component. In 2a/b, the resulting x-component is negative, whereas it is positive in 4a/b.

Obviously, in that ideal case there is one easy axis along the packing direction due to shape anisotropy. Accordingly, the hysteresis loop for real particles stacked along their individually elongated axes should be rectangular, since both, magnetic dipolar interaction and shape anisotropy of the individual particle favor the same direction, and the overall system is expected to behave uniaxial.

B: Real Morphology Dimer Packed Along Y-Axis

If the real morphology particles are packed along their elongated axis, the hysteresis is of rectangular type with a large coercivity, i.e., the magnetization reverses via coherent rotation along an easy axis, as confirmed by the simulation (Fig. 6.19, with a $H_c = 202.5\,mT$, which is about twice the magnitude as for a single cube with real morphology (106.5 mT). The net $m_{x,z}$-components are equally involved at the switching point. In case of the individual nanocube, m_z has a stronger contribution at that point.

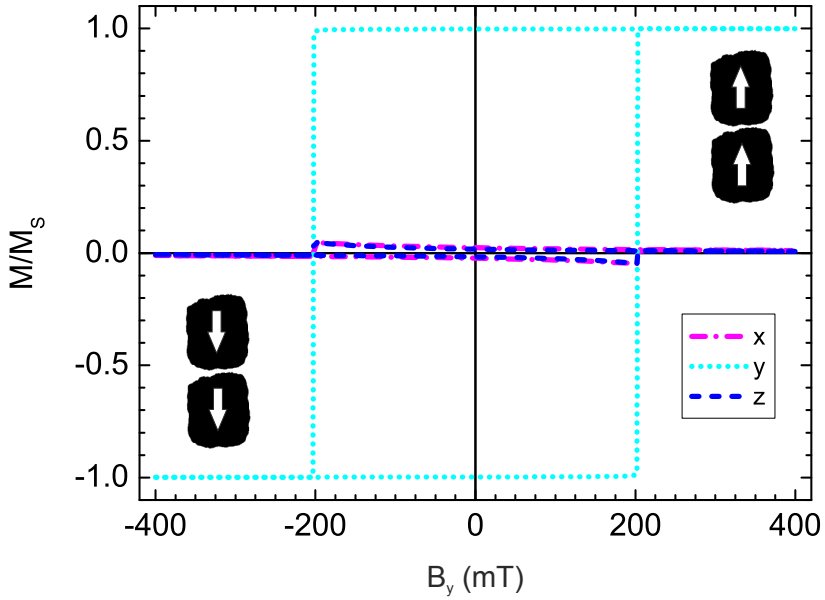

Figure 6.19.: Simulated $m_{x,y,z}$ hysteresis loops for a dimer configuration of two identical nanocubes with real morphology. **B** was applied along the packing (y-) axis.

C: Real Morphology Dimer Packed Along X-Axis: 1 Cube Tilted

As in example A, two identical nanocubes with real morphology are packed along the x-axis, but here the right particle is clockwise tilted by 45 ° with respect to the left one. The

simulated $m_{x,y,z}$ hysteresis loops are shown in Figure 6.20. For better understanding, also magnetization-component-resolved-cross-section images at positions 2 - 6 are displayed in Fig. 6.21.

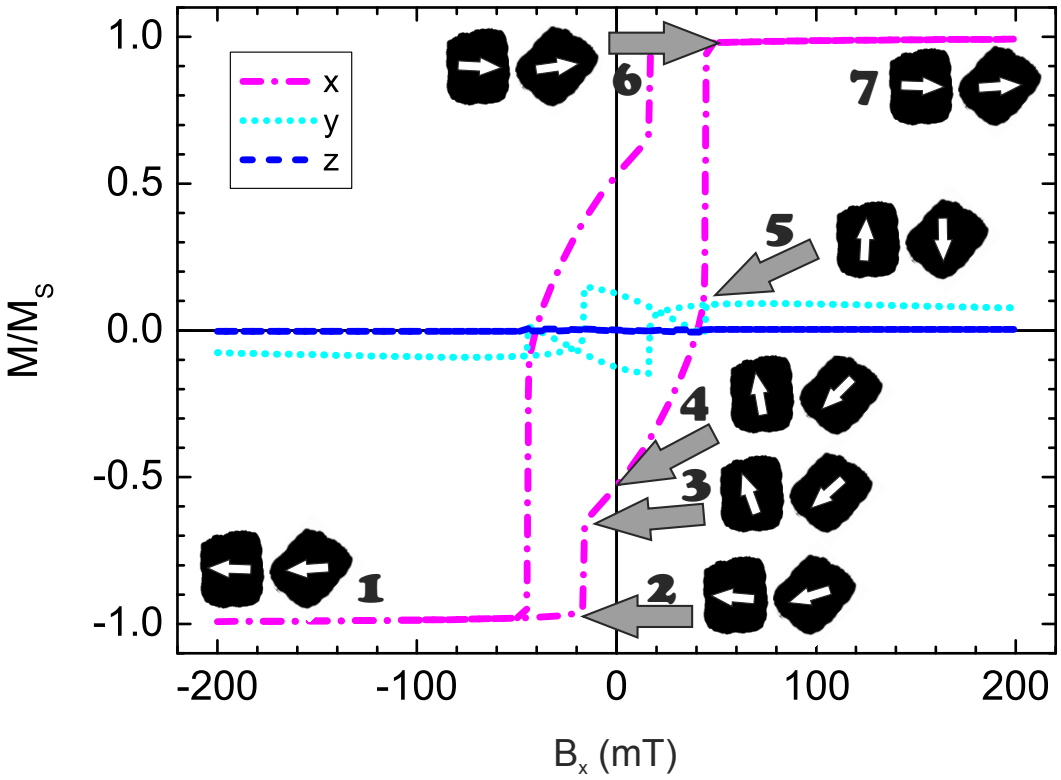

Figure 6.20.: Simulated $m_{x,y,z}$ hysteresis loops for a dimer configuration of two identical nanocubes with real morphology. The right nanocube is tilted by 45 ° with respect to the left one. **B** was applied along the packing (x-) axis. At positions 1 - 7 the orientations of the individual nanocube magnetization is sketched. More detailed cross section images showing the magnetic moment alignment within one inner plane in the vicinity of positions 2 - 6 are displayed in Fig. 6.21.

In analogy to example A, the z-component is zero for the whole hysteresis cycle. The y-component is non-negligible, though. The reversal will be discussed for the first hysteresis branch. At $\pm 200\,\mathrm{mT}$ the dimer was not saturated along the x-axis due to a non-vanishing y-component (1). For decreasing negative field values, the individual

magnetizations tend to rotate towards the elongated diagonal directions of the particles (2), which are the easy axes due to shape anisotropy. In between - 17 mT and - 16 mT there is a small jump in the x-component, and the individual magnetizations now point along the diagonal directions (3). Approaching remanence, there are only small changes, the individual magnetization is almost parallel to the elongated y-axis of the individual particles (4). Increasing **B** in the positive direction leads to a continuous rotation of the magnetizations to a perpendicular alignment with respect to the external field, and an opposite alignment with respect to each other. $H_c = 40.5$ mT. At slightly larger fields, i.e., + 45 mT the Zeeman energy exceeds the individual particles' shape anisotropy and both particle magnetizations are oriented almost parallel to the field direction (6). Nevertheless, the individual shape anisotropy induces still a non-vanishing y-component at + 200 mT (7) which can be attributed to the particle on the right side which exhibits larger spin canting than the left one (Fig. 6.21 (6)).

Summing up the results for the three different dimer configurations a huge influence of morphology and relative orientations of the particles is found. For the three different dimer configurations, the external field was applied along the stacking direction, only the relative orientation of the particles is different. The coercive fields, however, vary from almost 0 mT to more than 200 mT. Consequently, the magnetic response is dramatically influenced by the energy balance of magnetic dipolar interaction, individual shape anisotropy and magnetocrystalline anisotropy, which favors the magnetization alignment along the cube facets, which are the easy <100>-directions.

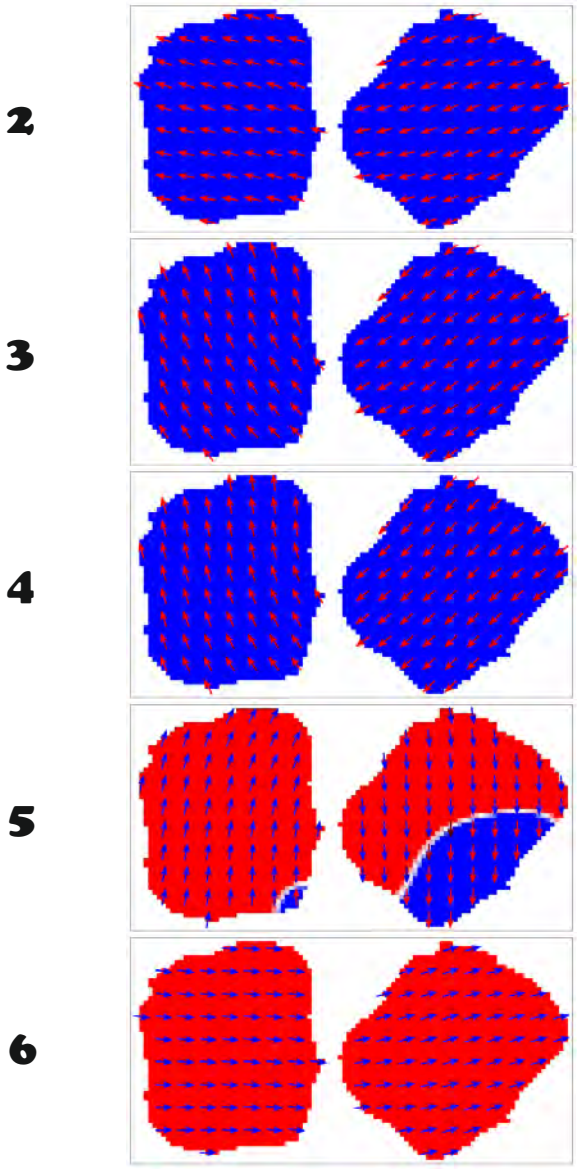

Figure 6.21.: Cross section snapshots of the orientation of the magnetization within an inner plane of a dimer configuration of two "real morphology" particles. The right nanocube is tilted by 45 ° with respect to the left one. The corresponding hysteresis loop is displayed in Fig. 6.20 and the numbers refer to the marked positions. As in example A, the color code represents the sign of the x-component (blue: negative, red: positive and white: no x-component).

6.4. Temperature Dependent Hysteresis

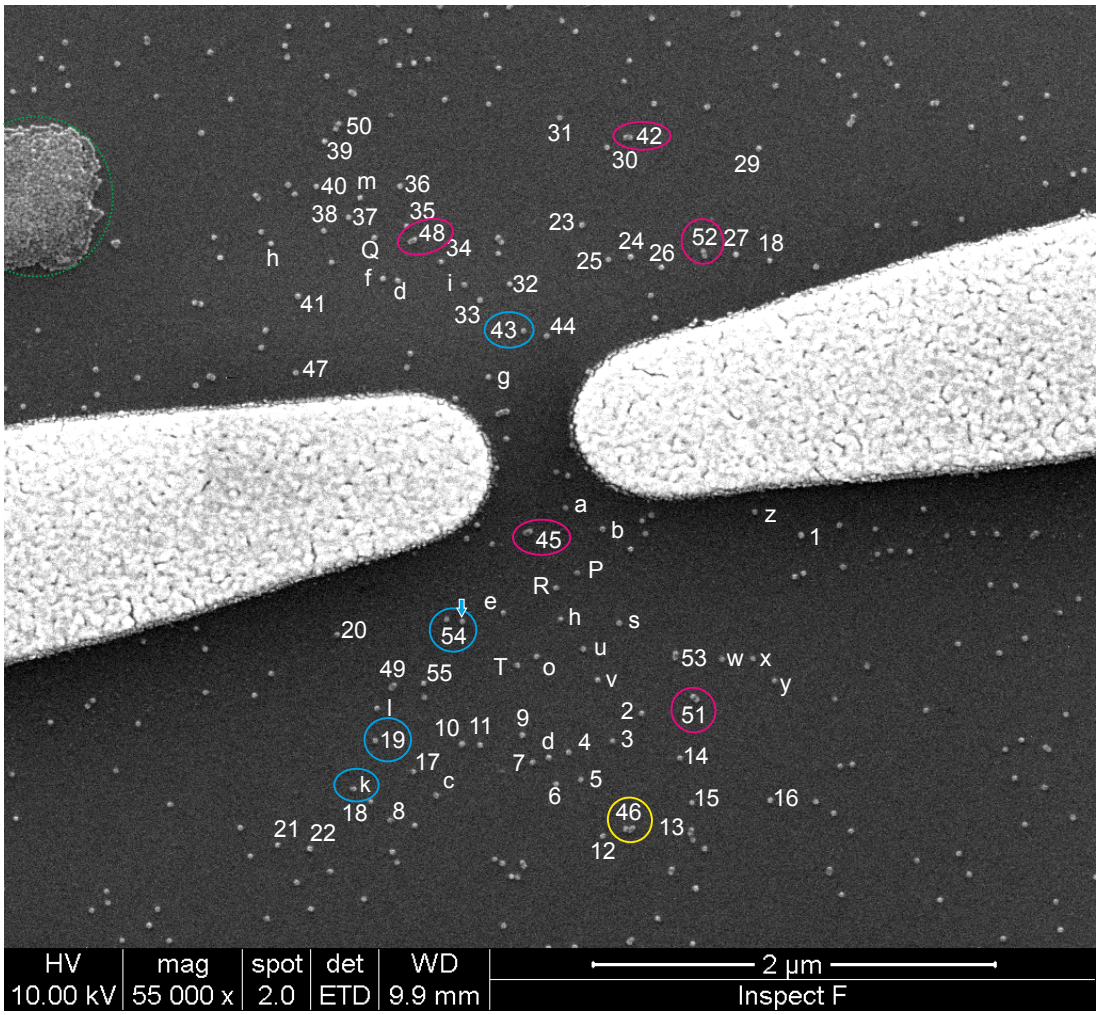

Figure 6.22.: SEM image of sample L5. The corresponding XPEEM image is shown in Fig. 6.23. Fig. 6.24 and Fig. 6.25 show the hysteresis data of color-marked particle configurations according to the color code for monomers (blue), dimers (pink), trimers (yellow) and many particles (green).

Temperature dependent hysteresis loops were recorded of sample L5. An SEM image acquired prior to the reduction and Al capping is shown in Fig. 6.22 and an XPEEM image of the same sample position acquired at the Fe L_3-edge is displayed in Fig. 6.23.

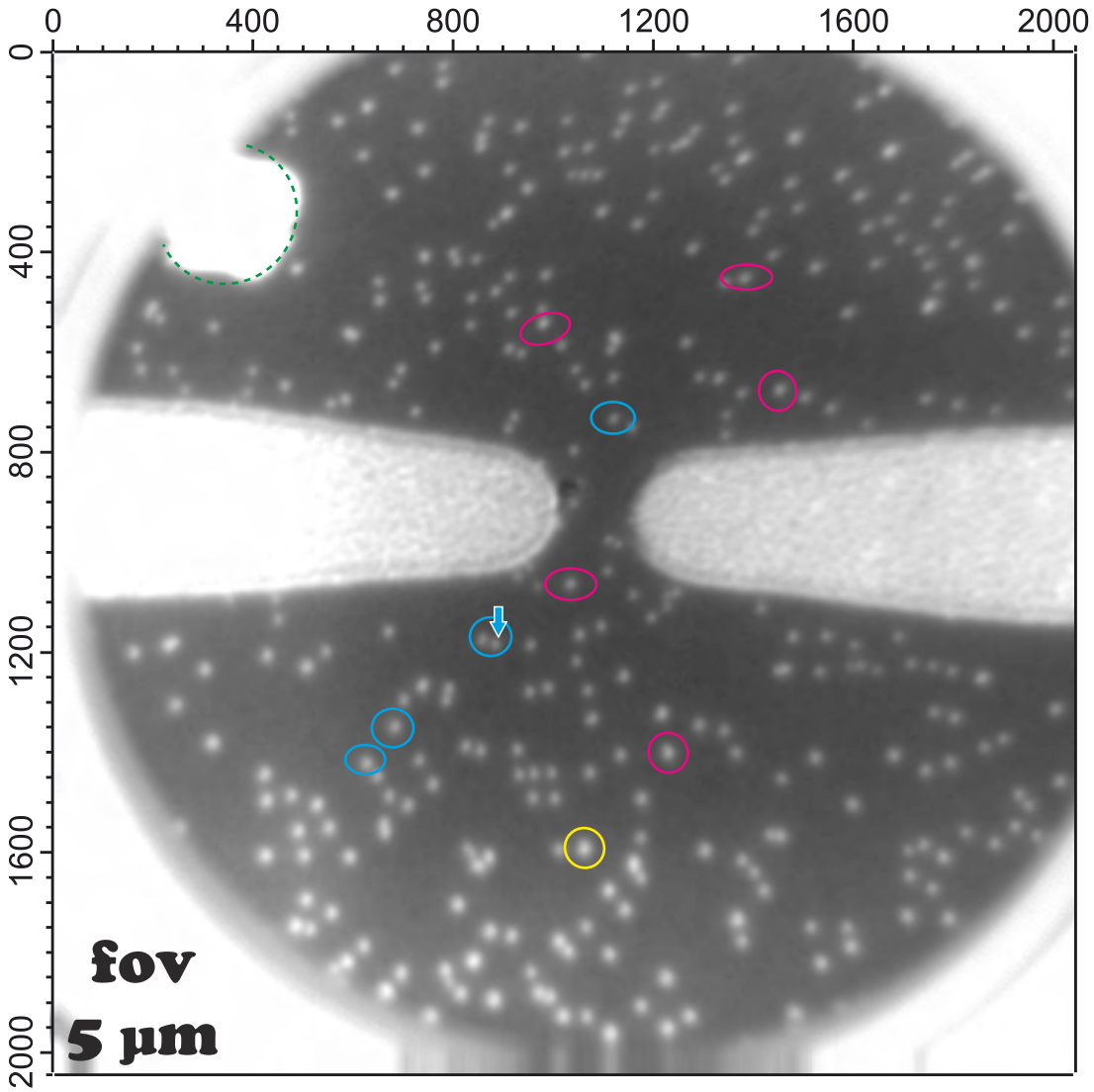

Figure 6.23.: XPEEM image (Fe L_3-edge) of sample L5 at the sample position of the SEM image in Fig. 6.22. The x- and y-axis scales refer to the number of pixels in the image. This image is a sum image of about 200 individual images. The outer circle is defined by the aperture. The blurry "edges" are due to the drift correction before averaging the individual images. The color markers are the same as in the SEM image (Fig. 6.22).

After the RT hysteresis measurement in $\pm 50\,mT$ the sample was cooled down to 110 ± 10 K in a magnetic field of - 50 mT and another hysteresis (image stack) recorded (Fig. 6.24 and Fig. 6.25). Figure 6.24 shows 4 hysteresis loops of individual particles from this image stack ("scan"). The signal-to-noise ratio is smaller than for the RT hysteresis of

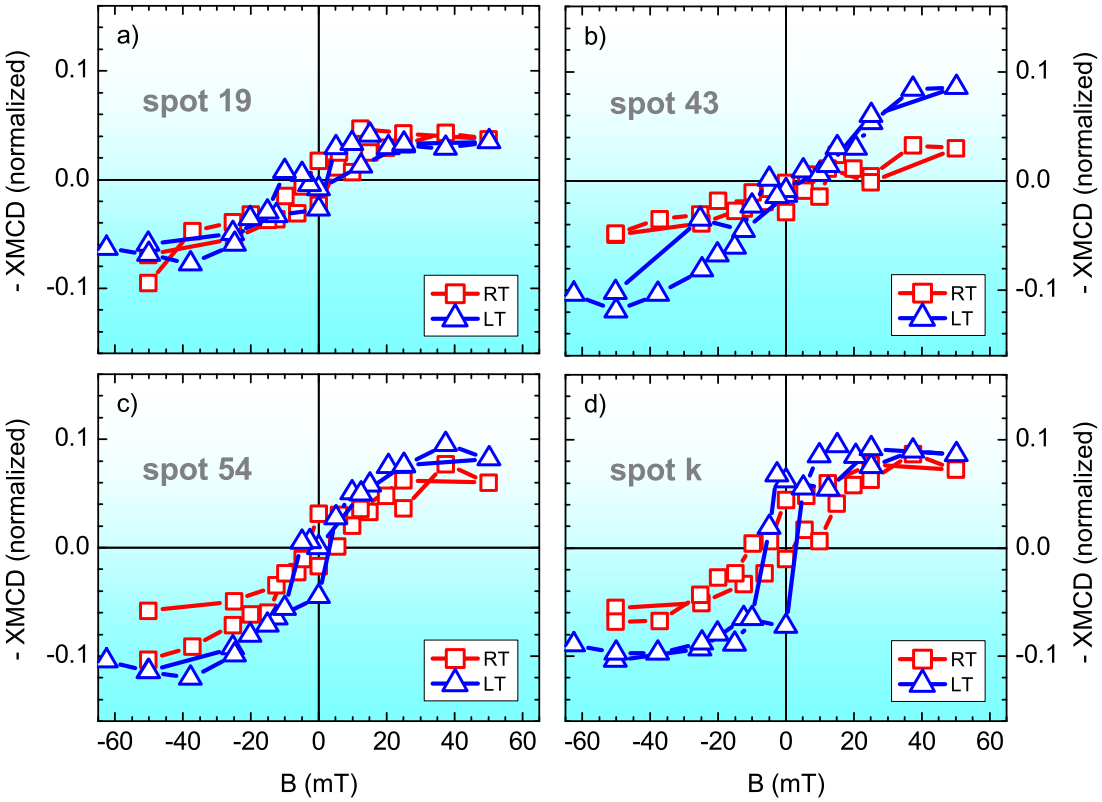

Figure 6.24.: Single nanocube hysteresis loops acquired at room temperature (open red squares) and at 110 ± 10 K after field cooling in - 50 mT (blue open triangles). Spot numbers are the ones in the SEM overview image (Fig. 6.22).

sample 4B (p. 71 ff.), and the magnetization saturates at a larger field. In Fig. 6.24 the RT loops are either linear, as for spot 43 (b) or have an S-shape like the monomers 19 (a), 54 (c), k (d) indicating superparamagnetic behavior. H_c is smaller than the field steps of about 5 mT, i.e., within errors the RT value of $H_c \approx 2.5$ mT for individual nanocubes (section 5.2) is confirmed. The LT loops in (b) - (d) show the expected increase of magnetization with respect to the RT loops. For spot 19 (a) there is no significant difference in both loop shapes. Spot 43 shows a large increase in magnetization and the loop has an S-shape. No opening of the hysteresis is observed. The particle is still in the SPM

state. The particle in spot 54 shows a distinct opening of the hysteresis with an S-shaped loop.
The most considerable difference between room and low temperature response is found for spot k. Here, the loop shape changed from pure S-shape to the square-like form, which looks like an easy axis reversal in the Stoner-Wohlfarth model. That means, cube k was very close to its blocking temperature at RT and its magnetization was blocked at LT. These four examples demonstrate very clearly, that the individual magnetic response is quite different from particle to particle. Most nanocubes in this sample show an SPM behavior and M_s is about 10 %. For cube 19, M_s is only about half this value.

As a consequence, T_b in this sample (L5) is expected to be lower than for the particles of sample 4B. Since this T_b-reduction can not be attributed to differences in the preparation[10], the origin must be related either to the different particle density on the substrate, which is about the same as in sample L3 and thus smaller than in sample 4B (see chapter 6.1) and/or to the presence of an antiferromagnetic oxide layer at the interface of substrate and particles. A XAS spectrum acquired from the large particle cluster (marked by the green circle in the SEM image) prior to the hysteresis measurement, however, revealed no oxide. In Figure 6.25 temperature-dependent hysteresis loops for five dimer (a) - (e) and one trimer (f) configuration on the same sample are displayed. All configurations have an open hysteresis, also at room temperature. Consequently, the dipolar interactions in between the nanocubes stabilize the magnetization. Larger M_s and H_c with decreasing temperature are also observed. The increase of the magnetization is largest in the dimer configuration in spot 45 (b).

Most significant is the horizontal shift of the hysteresis loops for all configurations, at both RT and at LT. Except for the RT hysteresis loops of dimer 51 (d) and the trimer 46 (f), which are shifted towards the positive field direction, all other loop shifts are towards the negative field direction, i.e., in the cooling field direction. Note also, that at LT within the field range of $\pm 50\,mT$ the magnetization of most configurations did not reverse into the direction of the initial cooling field again and to reverse the magnetization an increase of the magnetic field to more than - 60 mT was necessary. In spite of the complex behavior, H_c and the horizontal shift, which will be referred to as H_s in the following, are very similar for all configurations within errors[11]. H_c at RT is in the range of 14 - 18 mT and in the range of 31 -37 mT at LT. Dimer 48 (c) has the same magnitude of H_c at both temperatures. H_s at RT is in the range - (5 - 9) mT and

[10] The differences in the preparation are (a) the use of different plasma setups (capacitive in case of 4B, inductive in case of L3) and (b) the Al capping, performed in two different chambers. For sample L5 plasma and subsequent capping were performed in situ. Sample 4B was transferred to another chamber for Al-capping. Therefore, a possible reduction of magnetization due to oxidation during the transfer could have been expected here. Nevertheless, this sample shows higher blocking than sample L5.

[11] The error bars are defined by the field step sizes, which vary from $\pm 5mT$ for smaller field values to $\pm 12.5mT$ for fields larger than 50 mT

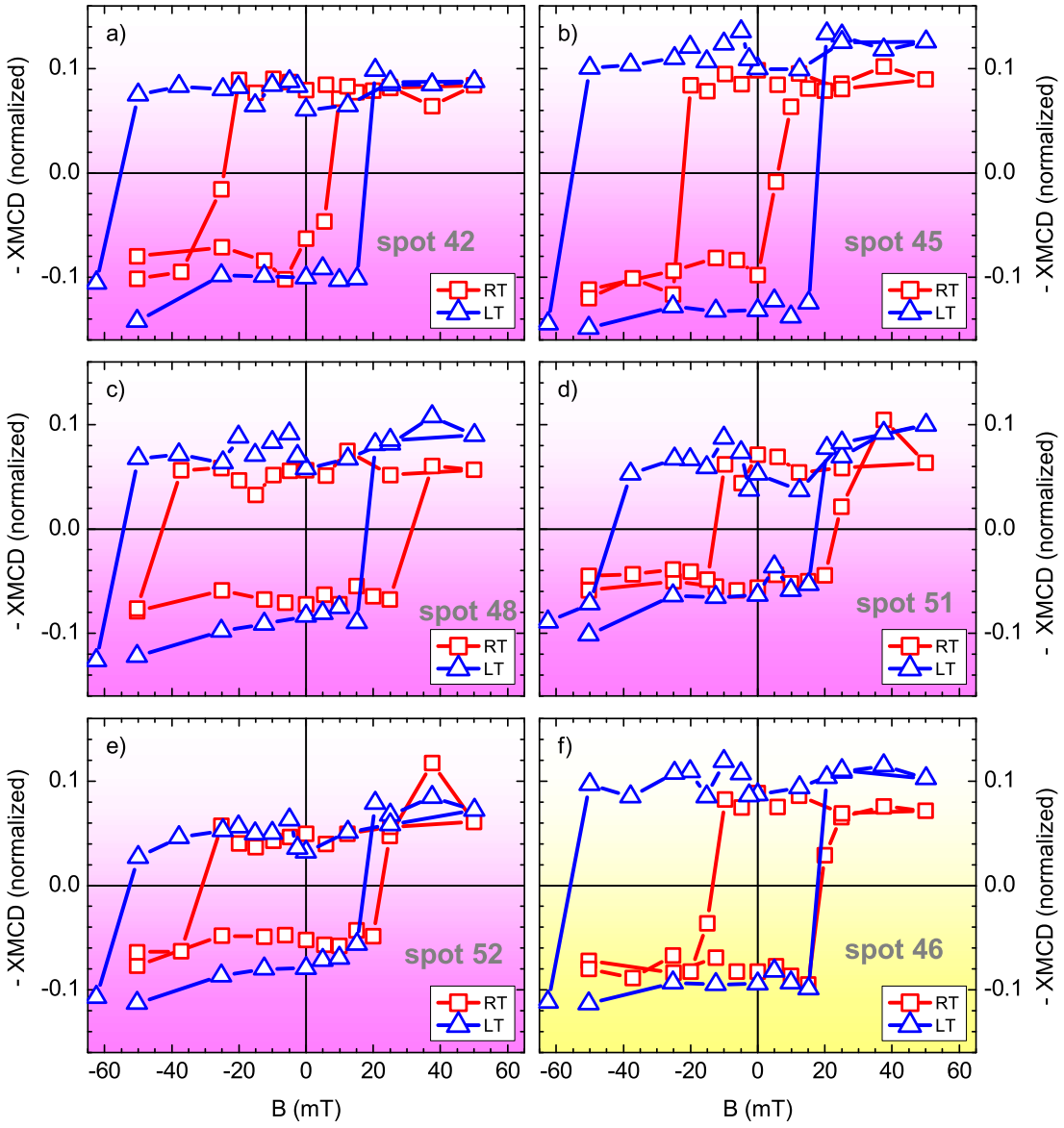

Figure 6.25.: Dimer (a)-(e) and trimer (f) nanocube hysteresis loops acquired at room temperature (open red squares) and after field cooling in about $110 \pm 10\,\mathrm{K}$ (blue open triangles). Spot numbers are the ones in the SEM overview image (Fig. 6.22).

- (13 - 19) mT at LT. Horizontal shifts of $H_s = +7$ mT and $H_s = +3.5$ mT are found for dimer 51 (d) and for trimer 46 (f).

Since H_c and H_s are in the same range, the shift seems not to be a stray field (of neighboring configurations) related effect. Furthermore, a negative H_s was also observed for some dimer configurations in sample 4B (Chapter 6.3). In these measurements with an available field of $\pm 18\,mT$ no complete hysteresis loops could be recorded yielding no comparable values for H_c and H_s. For the dimer in spot 5 $H_c \approx 8$ mT, and $H_s \approx -4$ mT at RT (Fig. 6.7 a). The variation in H_c in comparison to other particles (Fig. 6.25) is due to small changes in morphology and relative tilts with respect to each other (Chapter 6.3.4). The possible physical reasons for the shift of the hysteresis loops to the negative field are discussed as below:

6.4.1. Horizontal Shift of Hysteresis Loops

A horizontal shift of the hysteresis loop is observed for a ferromagnetic/antiferromagnetic bi- or multilayer systems after field-cooling the sample through T_N of the AFM inducing uni-directional coupling, i.e., the magnetically hard layer pins the magnetically softer layer. This exchange bias effect [115, 116, 118] leads in most cases to a shift of the hysteresis loop in the opposite direction of the cooling field (normal/negative EB) but in some cases shifts into the cooling field direction have been reported as well [123] (Chapter 1.2.4).

Consequently, the observed H_s in our samples could be due the the presence of an antiferromagnetic (or also ferrimagnetic) oxide. Such a material, however, is not detectable in our XAS measurements[12]. A possible oxidation during the acquisition of hysteresis loops is excluded due to the Al capping. XAS measurements on a reduced, non-capped nanocube cluster also revealed no significant changes in the spectra before and after a hysteresis measurement (next section). Furthermore, the loop shifts are also observed at RT. This is not explained by the common EB models in which the pinning occurs via a field-cooling process through T_N.

The horizontal hysteresis shift is only observed for particle configurations as dimers, trimers, but not for individual particles and larger clusters.

That means, the shift is a) related to coupling effects within small nanoparticle configurations, b) just too small to be detected for individual particles or c) due to the limited field range.

Apart from the presence of oxide, other possible explanations for an apparent shift of the hysteresis are: a) minor loops and complex domain configurations, b) an influence of the Al-capping layer, c) magnetic stray field effects, d) complex magnetic dipolar coupling and surface pinning.

[12] XMCD measurements performed on the same sample half a year later, however, showed a meanwhile oxidation of the individual nanocubes and small clusters (Figs. D.1 and D.2), whereas the big cluster agglomeration revealed no oxide indication in the spectra (Fig. D.4).

For an uni-directional coupling a symmetry break must be present. In this context, a complex magnetic domain pattern in each cube with many local energy minima could be assumed. Due to their small size, however, the nanocubes are in the single domain state as also confirmed by micromagnetic simulations. Minor loops can also be excluded since all hysteresis loops (of monomers, dimers and trimers) show a similar saturation magnetization and the technique provides an absolute scale of the magnetic moment per atom. Consequently, minor loops would be detectable via vertical shifts (cf. Fig. 6.12 a, p. 117).

Fe_xAl_{1-x} alloys are typically ferro- or paramagnetic but are also known to show spin-glass behavior (similar to antiferromagnetic correlations) below a critical $T \approx 100\,K$ [199]. An intermixed "antiferromagnetic" FeAl interface layer, however, cannot be the explanation, since then the "exchange bias" should a) also be observed for single particles and b) vanish at RT. On the other hand, Fe/Al multilayer systems are well known to show antiferromagnetic exchange coupling [208, 209]. For epitaxial Fe/Al/Fe [209] and Fe/Ag/Fe [210] layers, a non-vanishing exchange-coupling is found at 2.6 nm and 1.8 nm thickness of the Al(Ag) layer. Since this distance matches the typical spacing of the nanocubes in the as-prepared state on the substrate exchange coupling mediated by the Al-capping layer in between the Fe nanocubes may be another explanation for H_s in some particle geometries (e.g. a dimer with perpendicular alignment with respect to **B**). This coupling, however, is expected to be very weak since the Al films are non-epitaxial and in addition, the spacing of the nanocubes after the plasma treatment is estimated to be two to three times larger than the initial 2 nm due to the volume reduction when the oxide is reduced. As a consequence, antiferromagnetic exchange coupling does not explain the large shifts observed in our hysteresis measurements. The trivial effect of an apparent shift due to the contributions of magnetic stray fields from other nanocubes can be ruled out for the dimers and trimer discussed here as well. Indeed, the micromagnetic simulations presented in Chapter 6.2.2 show that the stray field of the Fe nanocubes (assuming full bulk-like magnetization) is smaller than 2 mT at a distance of app. 60 nm. Furthermore, if the shifts were related to the stray field of the surrounding particle configurations, a statistical distribution of shifts in both directions would be expected.

As a result, we have to consider either a complex uni-directional coupling due to diverging stray fields at the cube edges (as sketched in Figure 6.26) or the presence of an antiferromagnetic (oxidic) bottom layer (e.g. $\alpha - Fe_2O_3$). While the latter should also be present in monomers and vanish at RT, the complex stray field coupling could be present only in specially ordered dimers or polymers and is expected to be compensated in large particle clusters. Additionally, a small exchange coupling contribution may also be present. However, at the current status of our zero Kelvin micromagnetic simulations this complex situation involving a large surface anisotropy contribution and strongly inhomogeneous magnetization per cube cannot be interpreted at present and requires further investigations.

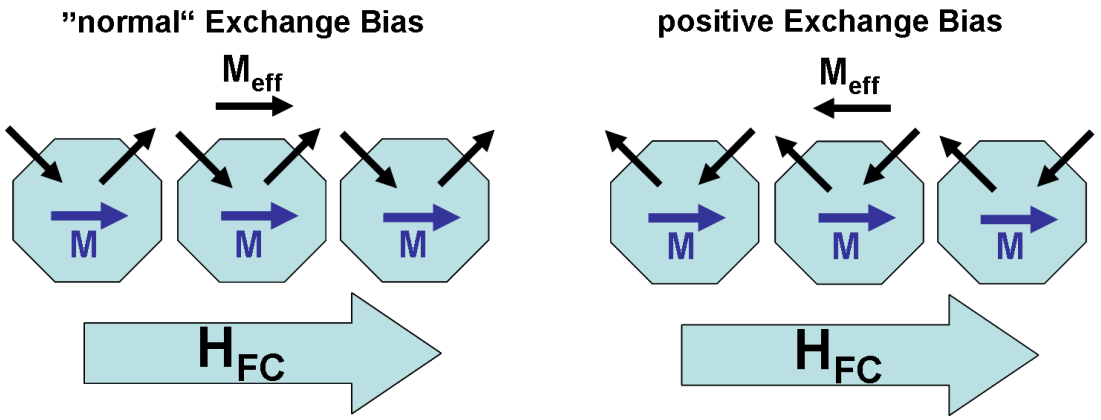

Figure 6.26.: "Normal" and "positive" exchange bias scenarios. In the "normal" case, the effective magnetization pinning is parallel to the field cooling direction while it is in the opposite direction in the "positive" case.

6.4.2. Studies of Different Oxidation States

In Fig. 6.27 helicity dependent XAS data and their corresponding XMCD spectra acquired at different oxidation/preparation states of the sample are shown. The x-ray absorption (XMCD) spectra of the as prepared sample are displayed in (a) and (d). The spectra show distinct oxide features, and the structure of the XMCD signal supports the presence of magnetite [211] found by Shavel et al. [170]. After the first plasma treatment (oxygen and hydrogen) the oxide is significantly reduced, as revealed by the reduced XAS-intensity (b) and the XMCD features (e), but not completely reduced, and a second hydrogen plasma treatment was performed. Afterwards, the sample was kept for two hours in the load lock of the SPEEM preparation chamber while pumping down to a pressure of 10^{-6} mbar. The overall time between the second plasma and the acquisition of the XAS spectra is approximately 12 hours in a pressure better than 10^{-6} mbar. Within errors the oxidation state of the sample did not change between the first and the second plasma (c). After about 48 hours in $\sim 10^{-9}$mbar and x-ray exposition another XAS spectrum was acquired with linear polarized light. This data is given as reference -(*), dotted red line - in (c). Obviously, the sample did not significantly oxidize during the measurement.

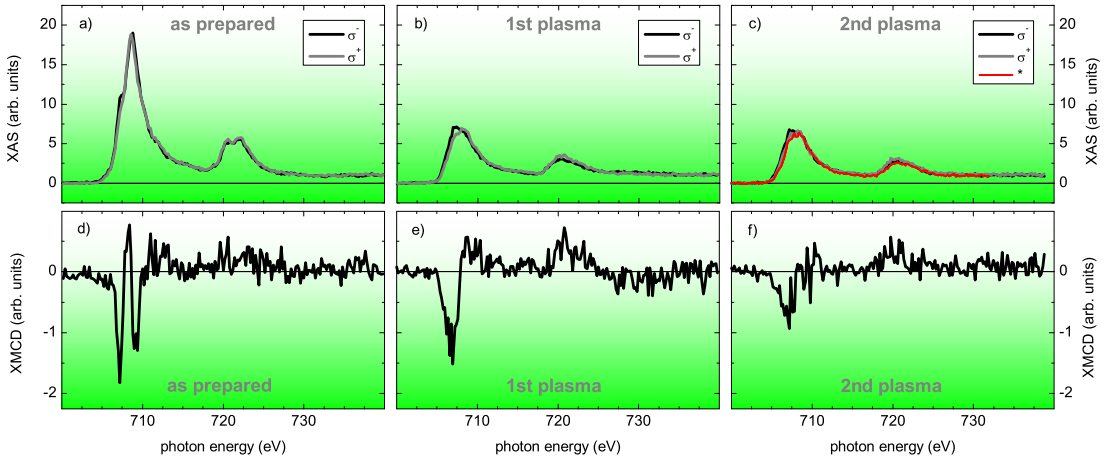

Figure 6.27.: Polarization dependent XAS and XMCD of three different sample oxidation states. (a), (d) As prepared oxidized nanocubes; (b), (e) after 1st plasma treatment; (c), (f) after second plasma. In (c) also a linear polarized absorption scan acquired after one hysteresis measurement(*) is sketched. For further details see text.

6.5. MTXM Studies

In this section preliminary results obtained by magnetic transmission x-ray microscopy (MTXM) are presented.

6.5.1. Fe Octahedra

Fe Octahedra (Fig. 3.2 c, d) were deposited either on a Si_3N_4-membrane (Sample M3) or on a Si_3N_4-membrane with a heating device (Sample H2), see Chapter 3.4. The results of the measurements in a magnetic field range of $\pm 100\,\mathrm{mT}$ are shown in Figs. 6.28, 6.30 (M3) and Figs. 6.32, 6.33 (H2). The magnetic field is applied along the film/membrane plane and the membrane is tilted by 60° with respect to the photon axis. This results in a larger field of view along the horizontal direction by a factor of $1/\cos 30°$ with respect to the vertical scaling.

In the first experiment it is demonstrated, that the magnetization of several nanoparticles clusters (Fig. 6.29) could be switched between range of $\pm 100\,\mathrm{mT}$ (Fig. 6.28). (a) and (b) are averaged images acquired at the Fe L_3-edge in negative and positive magnetic field, respectively[13]. (c) and (d) show the magnetic contrast. Due to technical

[13]Number of images in average: 4. CCD parameters for 1 image: 20 accumulations, 0.8 s exposure time.

problems only one photon helicity was available during the beam time, therefore the magnetic contrast is calculated by dividing the image taken at positive maximum field by the image taken at zero field after the application of the maximum negative field (Fig. 6.28 b) and vice versa (Fig. 6.28 a).

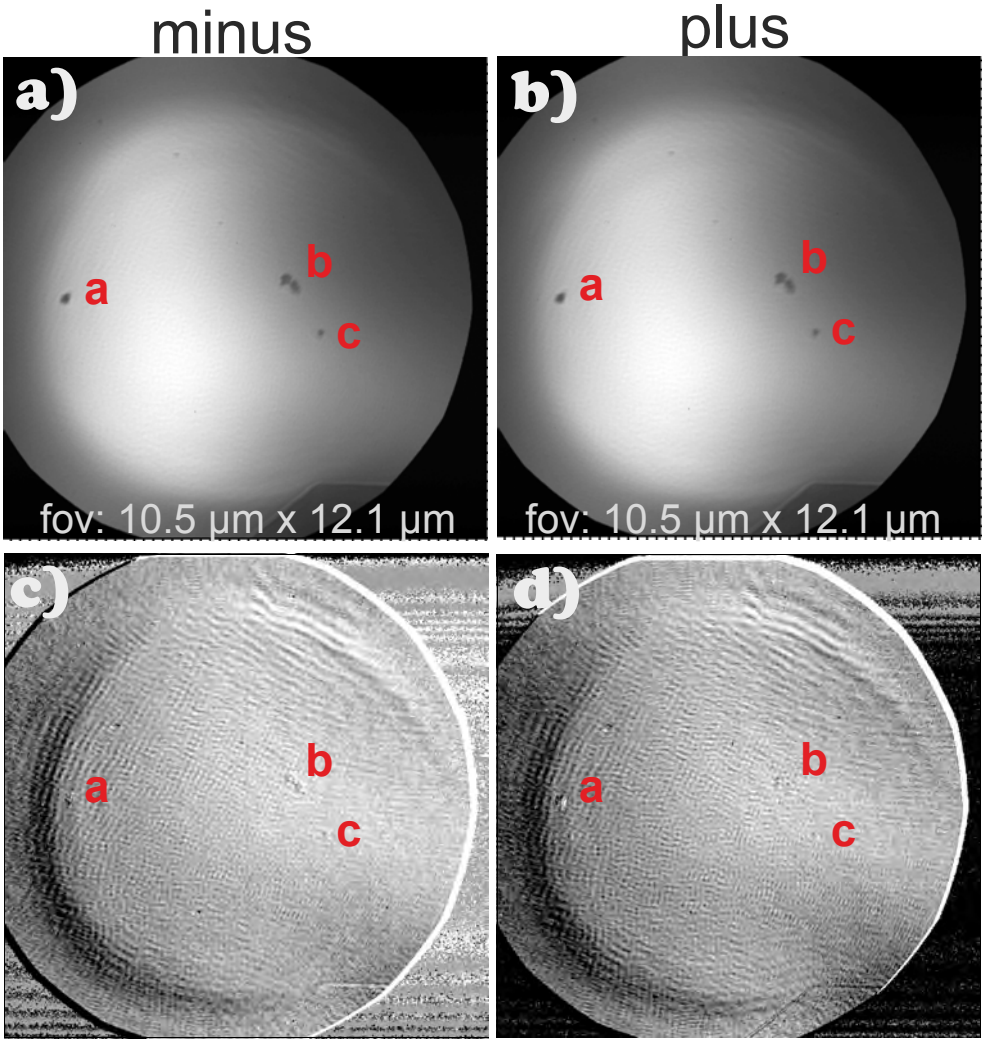

Figure 6.28.: TXM (a),(b) and corresponding XMCD (c), (d) images of Fe polyhedra particle clusters (Fig. 6.29). The magnetic field is applied parallel to the vertical of the images. Left: negative field direction. Right: positive field direction. a, b, c mark three different cluster configurations shown in the SEM images in Fig. 6.29.

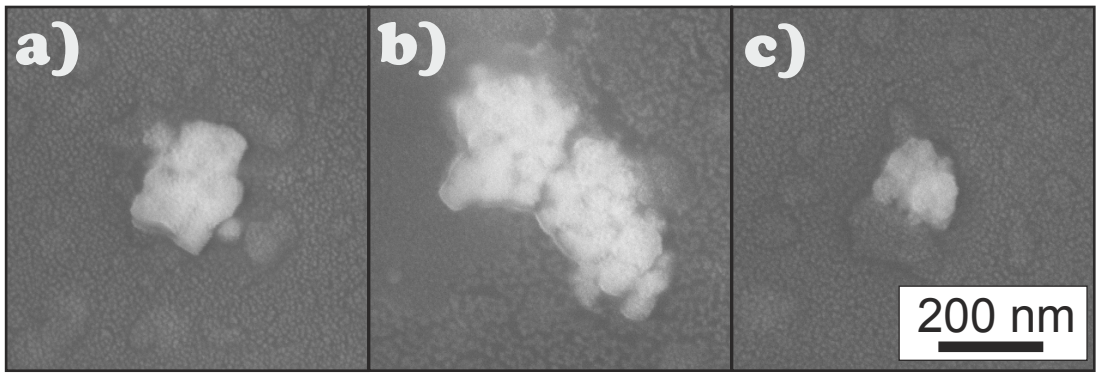

Figure 6.29.: High Resolution SEM images of Fe/Fe-oxide polyhedral nanoparticles (sample M3). The scale bar is the same for all panels. (a), (b) and (c) refer to the alphabetical numbering of the clusters in the TXM-images (Fig. 6.28, Fig. 6.30).

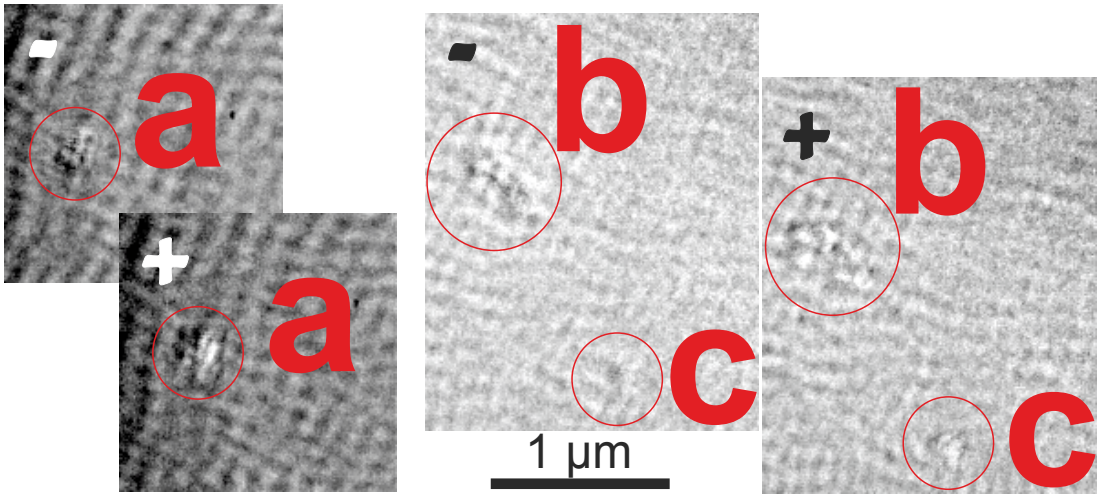

Figure 6.30.: XMCD images of Fe octahedra clusters a - c (Fig. 6.29) obtained in negative (-) and positive (+) magnetic fields.

A contrast inversion can be observed confirming magnetic switching of the particle configurations (Fig. 6.28 c, d). These inversions are better visible in Figure 6.30, which shows enlarged XMCD images of the clusters marked by circles. High resolution SEM images of the particle clusters a - c are displayed in Fig. 6.29. According to other SEM and TEM investigations, octahedra clusters of this size are mainly of 1 - 2 particle layer (one parti-

cle "diameter" $\approx$ 50 nm) thickness. The diffuse gray contrast around them indicates that a large amount of organic material is present which quickly degrades under illumination, thus preventing a full hysteresis analysis. The images in Fig. 6.30 were recorded at the maximum and zero magnetic fields. Changes in the magnetic contrast are detectable. The most distinct contrast change is observed for cluster a. Here, large black, white and smaller gray areas are seen in the cluster. The two clusters in (b) exhibit many black and white areas in the XMCD image and thus a complex domain structure can be assumed. Magnetic switching or magnetic re-orientation is observed in all three clusters, however, the magnetic field of $\pm$ 100 mT is too small to saturate any configuration.

In a second experiment, the Fe/Fe-oxide octahedra were measured between 296 K and $\sim$313 K. During the measurements, the temperature was not monitored. Exemplary infrared (IR) camera images of two different samples are shown in Fig. 6.31. Heating currents in the range of several mA were applied. For our measurements the indicated

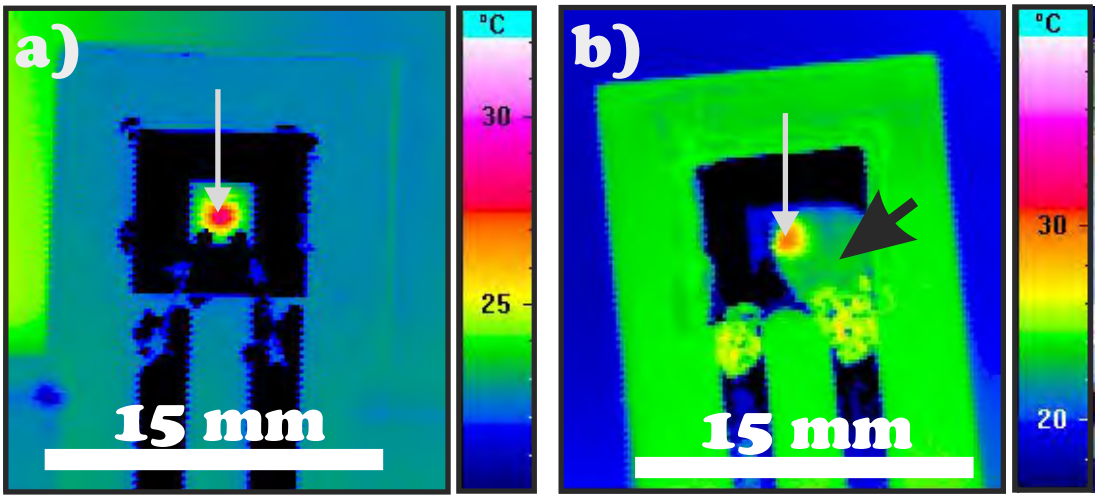

Figure 6.31.: Infrared Camera images of two different heater samples. The temperature scale is given on the right. White arrows show the "warmest" areas on the membranes. In (b) the black arrow shows an area where an excess of organic material is present. For details see text.

temperature has to be corrected by + 10 K [212]. The maximum real temperature of the two heaters in Fig. 6.31 is about 40° C (313 K). The heater device shown in (b) is the same shown in the sample preparation part (Fig. 3.4, p. 49). It is noteworthy, that the heating efficiency is higher in areas containing organic material seen in (b) where some organic residual drop was placed on the bottom right part of the membrane (indicated

by the black arrow). Therefore, it can be assumed that the local temperature in particle clusters surrounded by organic material is higher, than measured by the IR camera.

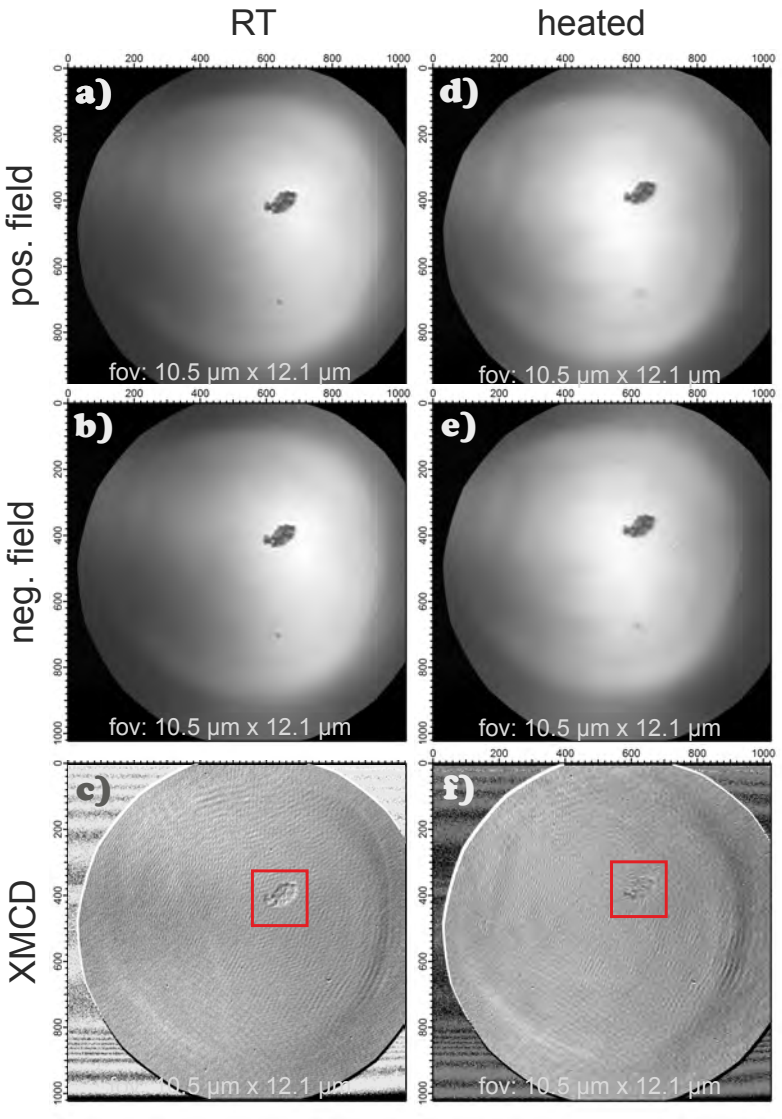

Figure 6.32.: MTXM data of Fe octahedra sample on a heating device. The images were acquired at the Fe L_3-edge and at 296 K (RT) - 313 K (heated). Enlarged XMCD images of the particle cluster (marked by the red frame in (c) and (d)) are shown in Fig. 6.33. For details see text.

Figure 6.32 shows the MTXM results of the heated experiment. The average images in the left column were taken at RT and the images on the right during heating[14]. In the first and second row, the data obtained in positive (a, d) and negative (b, e) fields are displayed. The last row contains the corresponding XMCD images (c, f). Enlarged XMCD images of the cluster marked by the red boxes are displayed in Fig. 6.33 [(a): RT, (b): heating]. The dimension of the particle cluster is about 1 micron and as revealed by the inhomogeneous chemical contrast in Fig. 6.32 has a non-uniform thickness, i.e., within the cluster areas thicker than 1 particle layer exist. Due to charging problems the corresponding HR SEM image could not be acquired.

The magnetic contrast at RT and HT (during heating) is different and appears to be lower at HT. To verify that the loss of XMCD contrast is real, intensity linescans along line 1 (maximum contrast change in RT image) and along line 2 (maximum contrast change in HT image) are shown in Fig. 6.33 c, d. At RT (a) a stripe-like domain configuration along the positive diagonal can be assumed due to the black and white stripe-like areas along that direction. The linescan was acquired perpendicular to the "stripes" with an integration width of 49 pixels and a dominant magnetic signal is detected (c). At HT the same linescan yields an intensity profile where no distinct magnetic signal is detectable. Consequently, the XMCD contrast has disappeared possibly due to thermal fluctuations of M. Or it averages out over the integration area which could be due to a break up of the domain configuration into smaller domains.

The linescan data obtained along line 2 reveals no significant difference in the magnitude of the RT and HT XMCD contrast with respect to the noise level (Fig. 6.33 d). The noise level is much higher here than for line 1 (a) due to the smaller integration width of the linescan. The different peak positions, however, confirm that the magnetic domain configuration of the cluster is different at both temperatures. The heating efficiency of our device is obviously sufficient to bring some particles closer to T_b (Fig. 3.2 e) and thermal fluctuations lead to a break-up of the large domains.

A technical artifact as the origin of the different XMCD contrast is excluded via thorough analysis[15] and therefore the functionality of our heating device is confirmed.

6.5.2. Fe Nanocubes

Figure 6.34 shows an TXM image acquired at the Fe L_3 – edge (a) of an Al-capped Fe nanocube membrane sample and the corresponding SEM image (b). In the chemical contrast image (a) no individual cubes, but small nanoparticle configurations of 2 to 3 cubes can be identified. However, no magnetic contrast was detectable within the noise level and no comparison to the room temperature XPEEM hysteresis measurements of an equivalent Fe nanocube sample is possible.

[14] Number of images in average: 8. CCD parameters for 1 image: 20 accumulations, 0.8 s exposure time.
[15] by two independent scientists

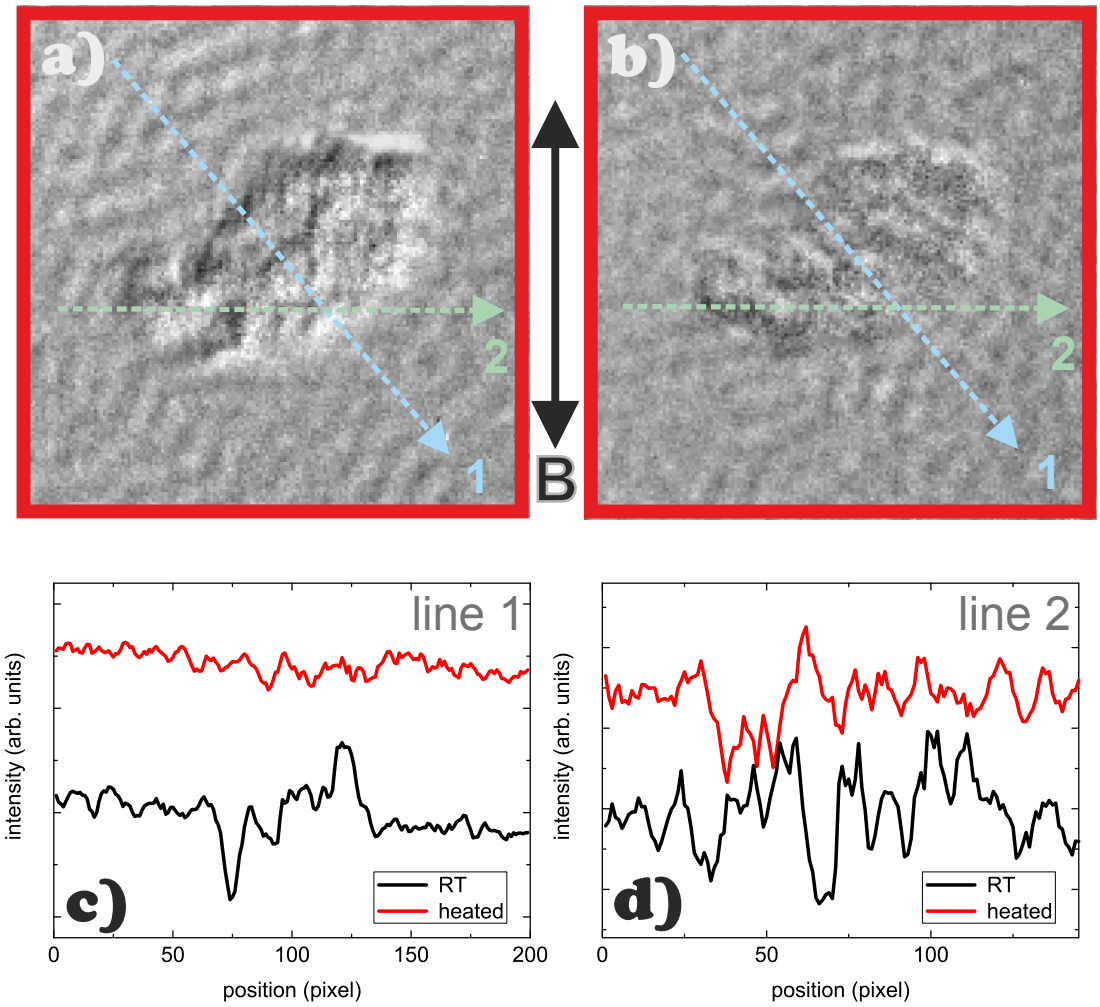

Figure 6.33.: Magnetic contrast (XMCD) images of Fe octahedra cluster obtained at RT (a) and ∼313 K (b). (c) and (d) show intensity linescans obtained along line 1 (c - 49 pixels integration width) and line 2 (d - 5 pixels integration width). The arrows also point in the scan direction.

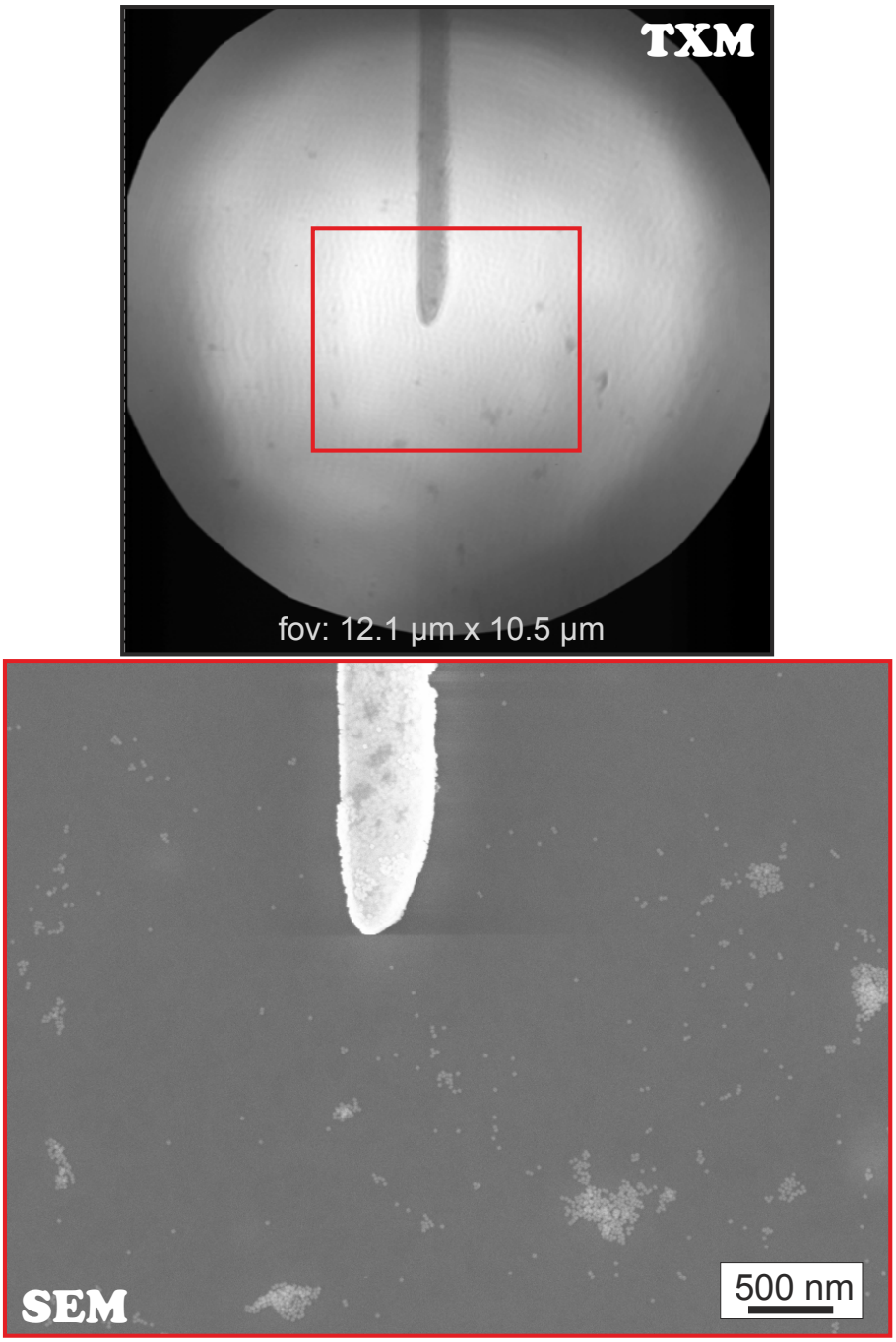

Figure 6.34.: TXM image of Al capped Fe Nanocube sample acquired at the Fe L_3 − edge (a). The red square refers to the dimension of the corresponding SEM image (b).

6.6. Conclusion

In this chapter:

- Hysteresis and XMCD measurements were performed on small ensembles of nanocubes, such as dimers and trimers. These constitute the first measurements of the magnetic structure of individual nanoparticles of only a few tens of nanometers in lateral dimension. In particular, these measurements have allowed to determine:
  1. $\mu_s^{eff} = 1.11\,\mu_B$ for Fe nanocube dimers is determined by XMCD measurements. The reduction of the magnetization can be explained by thermal fluctuations of the magnetization over the timescale of the XPEEM measurements (2 days).
  2. Different blocking behavior for different particle densities is observed: T_b increases with particle density, confirming that dipolar coupling within nanocube ensembles stabilizes the magnetization.
  3. In addition to the dipolar coupling between neighboring nanocubes within a configuration, the dipolar interaction can equally influence the behavior of nanocube clusters located at a certain distance from each other. The cut-off distance for the influence of the stray field, i.e. at which $H_{stray} < H_c$, was determined to be of about 60 nm for individual Fe nanocubes at RT ($H_c = 2 - 2.5\,mT$).
  4. Room temperature hysteresis loops measured for dimer, trimer and many-nanocube configurations are compared to micromagnetic simulations. Different H_c from 3 mT to 203 mT are attributed to differences in morphology and different relative orientations of the nanoparticles. For some arrangements H_c is of the same size as for individual particles, indicating a complex dipolar coupling mechanism.
  5. A horizontal shift of the hysteresis loop is observed for dimers and trimers, but not for individual nanocubes. Since the exchange bias models do not explain such a shift, a complex stray field coupling due to strongly inhomogeneous cube magnetizations is proposed.
- The first MTXM studies on Fe nanocubes and Fe/Fe-oxide octahedra in a temperature range 297 K - 313 K are presented. For the latter, a complex T-dependent magnetization reversal is observed in small ensembles.
- The successful fabrication of a Si_3N_4-membrane heating devices is demonstrated (heating capability up to 20 K above RT).

7. X-ray Imaging of Individual Co Nanorods

In this chapter, room temperature XPEEM and MTXM measurements of Co nanorods are presented. The rods have diameters of about 4 nm and 7 nm, and a length from several hundreds of nanometers to about one micron (Chapter 3.2). This chapter describes preliminary results obtained towards the end of the PhD thesis. A complete discussion is beyond the scope of the current thesis.

Chemical synthesis of the nanorods had been performed in Toulouse by Dumestre et al. [213] who found ferromagnetic behavior at room temperature and a saturation magnetization identical to Co bulk at 2 K by SQUID-magnetization measurements on Co nanorod powder kept in a gelatin capsule. Additional time-dependent SQUID magnetization studies at 2 K on the same sample showed a large reduction in M_s (- 12 %) and H_c (- 44 %) after one week. After 5 months, a further reduction in M_s (- 47 %) was found while the coercivity increased by 6 % [214]. HRTEM measurements of these Co nanorods also revealed hcp structure with <0001>-growth direction. The formation of oxides was investigated by holography. It starts at the (0001)-oriented end facet of the wires [172, and references therein][1]. Based on this result, only slight oxidation and ferromagnetism at room temperature was expected for the Co nanorods.

7.1. XPEEM measurements

In Fig. 7.1 a, an XPEEM sum image (positive polarization, Co L_3-edge 778 eV) and in (c) an SEM image of the red frame enclosed area in (a) are shown. The investigated Co rods with lengths between $\sim$ 100 nm and 300 nm are very well separated on the substrate. The corresponding XMCD image is displayed in (b). The Co nanorods are clearly visible in the chemical contrast image (a), however no magnetic contrast is detectable within the background noise (b). Consequently, the Co nanorods are either superparamagnetic at room temperature or antiferromagnetic due to oxidation between sample preparation and XPEEM measurement. During this period of about ten days, the sample was stored under ambient conditions.

[1] The holography samples were prepared in the glove box and stored under Ar atmosphere. Just before introducing them into the microscope they were exposed to air.

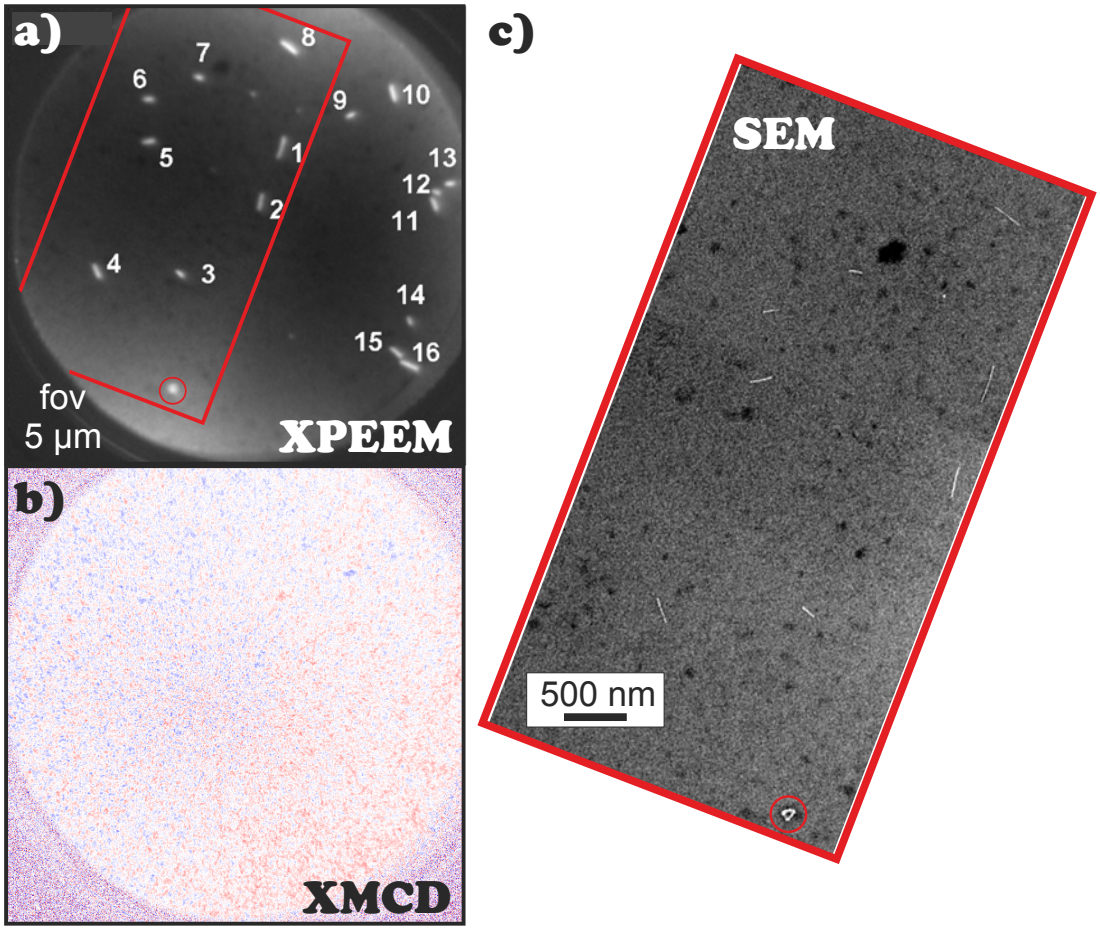

Figure 7.1.: (a) XPEEM chemical contrast image (positive photon polarization) of Co nanorod sample. The area enclosed by the red frame is also shown in the SEM image (c). The corresponding XMCD image is shown in (b). For the XPEEM and XMCD images the circular field of view is 5 μm.

Spatially resolved x-ray absorption spectra were acquired using linearly polarized light with a spectral resolution of 0.2 eV. In Fig. 7.2, the spatially resolved XAS data of two nanorods are depicted. Further explanation is given in the figure caption. In Fig. 7.3, the corresponding x-ray absorption spectra - obtained from the end, center and from the entire particle - for these two single rods (spot 1, Fig. 7.3 a, and spot 7, Fig. 7.3 b) and the average of all 16 nanorods (Fig. 7.3 c) are shown. In all cases, the Co L_3-peak exhibits a fine structure similar to the reference spectra of Co oxides (Fig. 7.4). The nanorod in spot 1 is approximately three times longer than the one in spot 7.

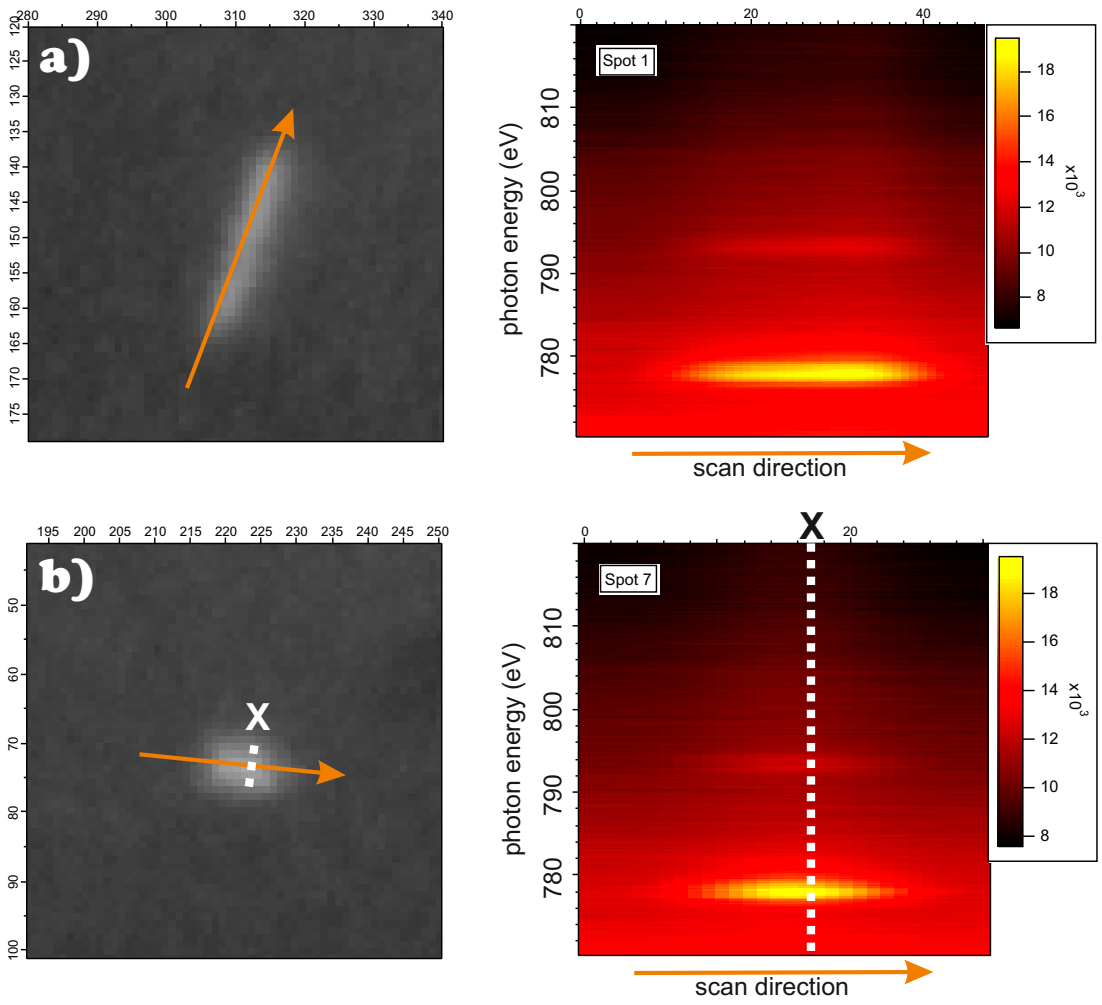

Figure 7.2.: Left panels show XPEEM images of (a) 300 nm Co nanorod, spot 1, in Fig. 7.1 a and (b) 100 nm Co nanorod, spot 7 in Fig. 7.1 a. X- and y-axis are scaled in pixels (1 pixel corresponds to ∼10 nm). Right panels show corresponding spatially resolved XAS data of the nanorods. To obtain these data the intensity was read out (with an integration width of 6 pixels) as function of photon energy along the arrows. An x-ray absorption spectrum as shown in Fig. 7.3 b by the red line is obtained by monitoring of the XAS intensity along the X-marked white dashed line.

Considering that oxidation starts at the ends of the nanorods, a different oxidation state in the center was expected but was not found. The spectra show identical oxide features,

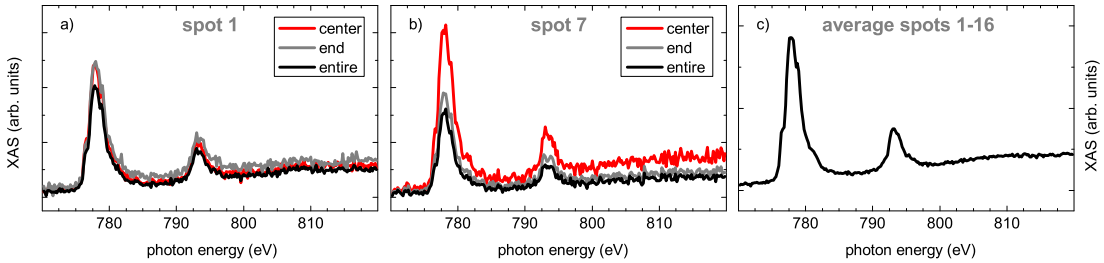

Figure 7.3.: X-ray absorption spectroscopy data of individual Co nanorods [spot 1 and spot 7, (a, b)] and the average signal of all 16 particles (c) as marked in Fig. 7.1 a. All scans are normalized to the neighboring background. The absorption was measured spatially resolved at the edges, the center and of the entire particle.

and a metallic Co-contribution from a non-oxidized core cannot be resolved.
Note that the pixel resolution is about 10 nm. The lateral resolution of the instrument is ~ 25 nm which is greater than the particle diameter. This also explains the larger intensity of the spectrum (red) in Fig. 7.3 b. The nanorod is only 100 nm long and therefore the spectrum contains information on almost the entire particle[2]. In case of nanorod '1' this effect smears out, and almost the same normalized intensities are detected. Since the Co nanorods have a diameter of 4 nm and the effective sampling depth is in the order of 5 nm, the complete nanorod is probed.

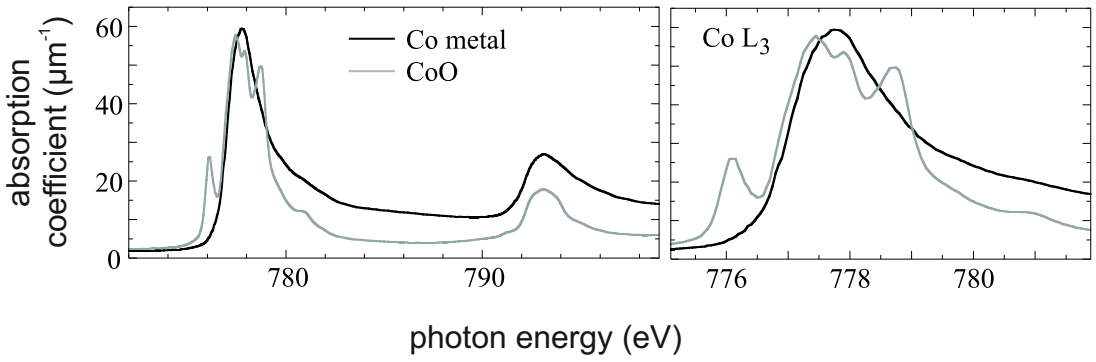

Figure 7.4.: Co and CoO reference spectra [131].

[2]In the scans the intensity in the region of interest is normalized to the number of pixels in the region of interest and an averaged background signal

In consequence, we find a complete oxidation of the nanorods. The observed distribution of the nanorods on the substrate is in agreement with the presence of antiferromagnetic Co oxide. If the particles were already oxidized prior or during the deposition onto the substrate, they could not form bundles due to magnetic dipolar forces (see also p. 45) as described in Chapter 3.2.

The strong oxidation (in comparison to Dumestre's results) can be understood as follows: In order to prevent aggregation and prepare very dispersed samples, our Co nanorod solution was purified and a big excess of ligands removed before deposited onto the substrate. Therefore the diffusion of oxygen is faster, and oxidation of the particles starts with smaller delay time. Oxidation of the samples can also be hindered by storing them under Ar atmosphere as is revealed by an additional XPEEM measurement on a different Co nanorod sample (synthesis as for MTXM measurements). Although the sample was exposed to air for mounting it onto the PEEM sample holder for about half an hour, the x-ray absorption spectra showed metallic spectra and magnetic contrast (Fig. 7.5). For applications, the time-dependent progress of oxidation is of importance, and experiments with controlled oxidations are desired. This requires that sample preparation and XPEEM measurement can be performed in situ, i.e., without exposure to air - a challenging task for further XPEEM studies on colloidal nanoparticles.

7.2. MTXM Measurements

Fig. 7.6 shows an MTXM image in zero field (a), the corresponding magnetic contrast image ($\pm 100\,\mathrm{mT}$)(b) and an SEM overview image (c) in which the ellipsoidal[3] field of view $\sim 11 \times 13\,\mu\mathrm{m}^2$ for the x-ray imaging is marked by the red circle. No background normalization of the individual x-ray images was performed. Statistics was improved by adding 8(16) images[4]. In (a), the Au-marker on the Si_3N_4-membrane and organic clusters can be identified, but only one individual rod or agglomeration of few parallel rods (marked by the red arrow) is weakly visible (compare to SEM overview image (c)). No magnetic contrast is detectable (b). The black/white spots are artifacts occurring in the processing of the XMCD image and can be related to contamination of the imaging optics and "dead" pixels. The absence of magnetic contrast either means that the lateral resolution of the instrument was not sufficient, and the magnetic signal is lost in the noise level; or the rods are oxidized. The latter is also supported by XPEEM studies on a similar Co nanorod sample presented in the previous section. Obviously, separated nanorods completely oxidize within several days when stored under ambient conditions.

Magnetic contrast is still detectable when the sample is stored under Ar atmosphere (p. 152, Fig. 7.5). Here, the sample was stored and investigated under ambient conditions.

[3] sample is mounted in in-plane geometry

[4] Number of images in sum image: 16 for zero field, 8 for each magnetic field direction. CCD parameters: 20 accumulations, 0.7 s exposure time.

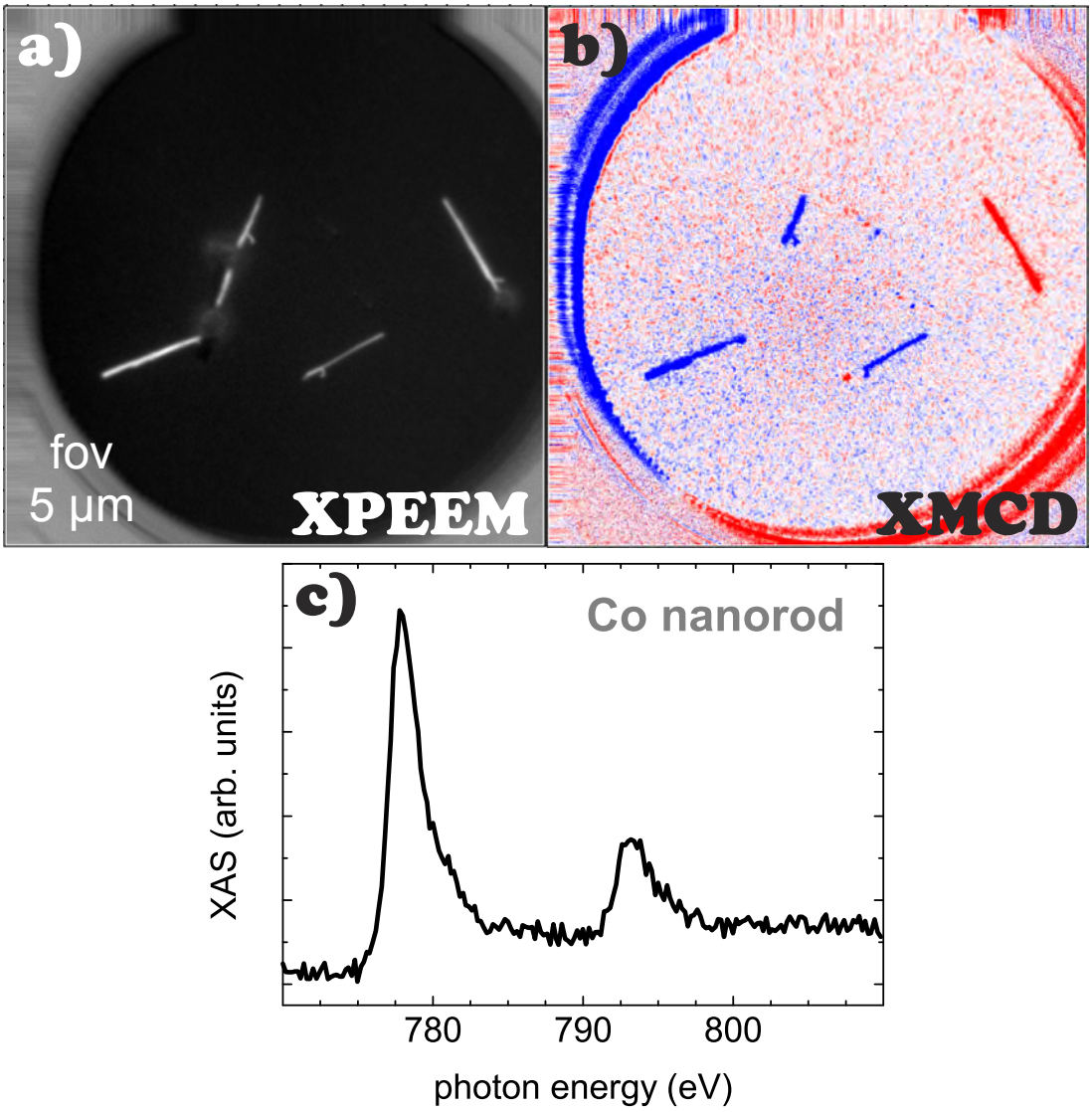

Figure 7.5.: (a) XPEEM chemical contrast image of Co nanorod sample. The corresponding XMCD image is shown in (b). The magnetic contrast is represented by the color scale, blue and red refer to opposite magnetization directions. The circular field of view in (a, b) is 5 μm. (c) Exemplary XAS spectrum (normalized to background) of a single Co nanorod.

To finally address the oxidation question, complementary time-dependent spectroscopic oxidation studies with high lateral resolution would be necessary.

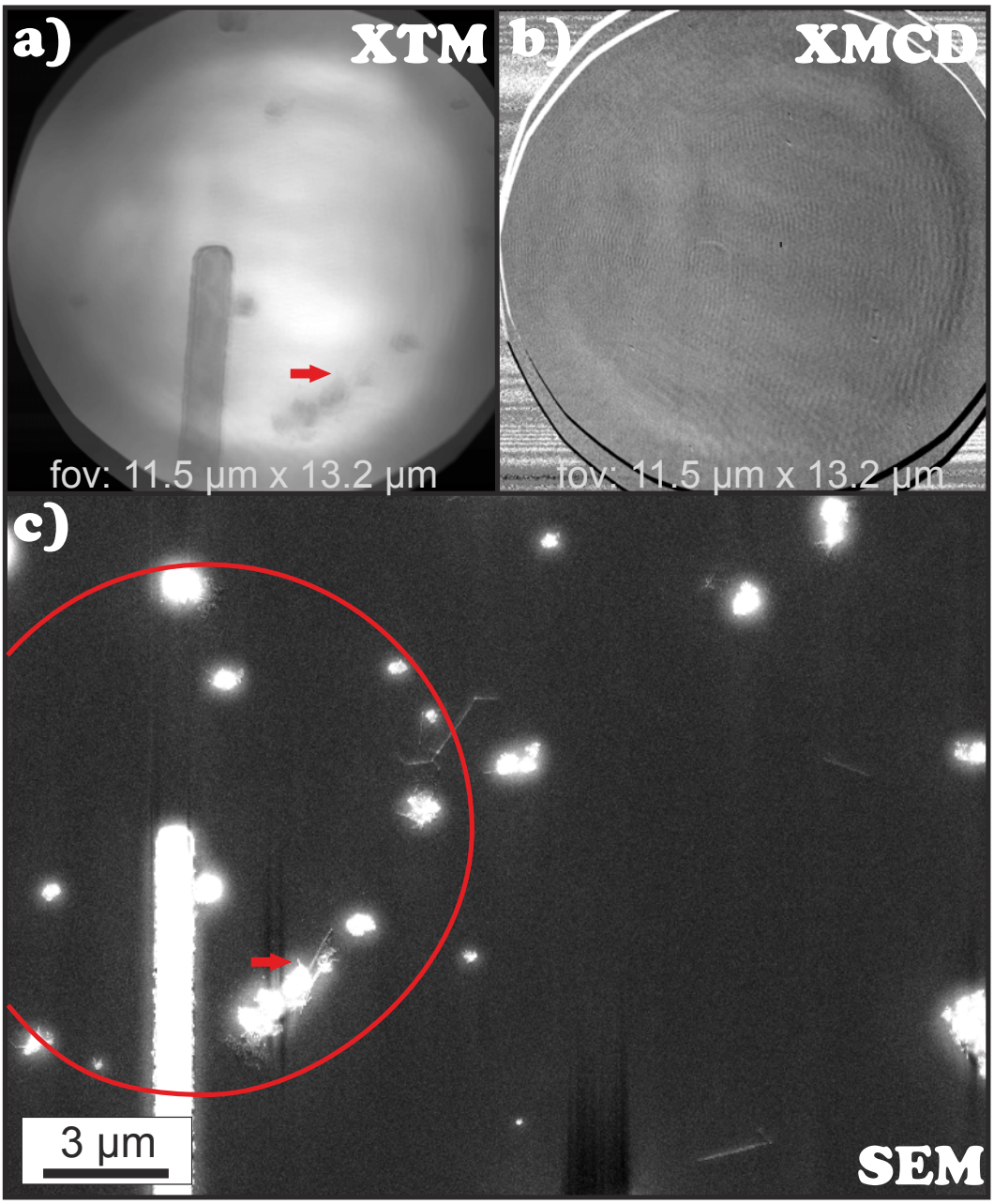

Figure 7.6.: X-ray transmission image acquired in zero magnetic field of a sample with Co nanorods (a). The field of view (here: total image dimension) is about 11.5 μm x 13.2 μm. (b) Corresponding XMCD and (c) SEM image in which the field of view in the MTXM-experiments is marked by the red circle. The 'single' nanorods as e.g. marked by the red arrow in the SEM image in panel (c) typically consist of several agglomerated rods, which cannot be resolved by the SEM instrument due to charging effects.

7.3. Conclusion

X-ray magnetic imaging experiments on Co nanorods of different lengths from 100 nm up to 2 - 3 μm and diameters of 4 nm and 7 nm were performed. XPEEM allowed magnetic imaging and spectroscopic analysis of the individual nanorods with a lateral resolution of about 25 nm and an energy resolution of 0.2 eV. A complete oxidation of the purified, dispersed nanorods was found when stored under ambient conditions for more than a week. Dumestre et al. reported relative slow oxidation for samples with a huge excess of ligands on the other hand. These findings are important for applications of Co nanorods in which they need to be purified and separated.

The MTXM instrument did not offer sufficient resolution for (magnetic) imaging of the 7 nm diameter wires (a 25 nm zone plate was installed). The implementation of a new 10 nm zone plate should allow for magnetic imaging of nanostructures below 10 nm in magnetic fields > 100 mT.

8. Conclusion

The main motivation of this thesis was to investigate the correlation between the crystallographic structure and morphology of individual nanoparticles and their magnetic properties.
This task was accomplished in two parts: first, the structural surface layer relaxation in Fe_xPt_{1-x} nanoparticles was analyzed by HRTEM and in the second part, the magnetic hysteresis loops of individual 18 nm Fe nanocubes were measured by XPEEM. These results constitute the first measurement of the magnetic properties of individual nanoparticles with a lateral size below 20 nm. Additionally, magnetic hysteresis loops of different nanocube configurations were measured. These were found to be strongly influenced by the dipolar coupling between adjacent nanoparticles and neighboring clusters of particles, as well as by the morphology of the particles themselves. Furthermore, pioneering work on the temperature-dependent magnetic analysis of different nanoparticle systems using MTXM is shown.
Whereas the possibility to study structural properties on the atomic scale by means of HRTEM is well established, only few techniques exist which have the sensitivity required to perform hysteresis measurements on individual (few) nanoparticles. In fact, none offers sufficient statistics, a broad temperature range and and sensitivity to different directions of the external field. Here, element-specific x-ray microscopy with a spatial resolution comparable to the size of the measured particles (~ 25 nm) was introduced. This technique allows to simultaneously access the chemical state and element-specific magnetic properties. Surface-sensitive XPEEM was mainly used, complemented by volume-sensitive MTXM in magnetic fields of up to 100 mT. About one thousand different nanoparticles and nanoparticle configurations were analyzed. The best ones are presented in this thesis.
Typically, standard magnetic characterization techniques (e.g. SQUID, FMR, XMCD) require large ensembles (millions) of monodisperse nanoparticles. Here, it is shown that the results obtained for ensembles are not necessarily representative of the individual particles. Coercive fields can indeed vary by one order of magnitude owing to small changes in morphology. Understanding these variations is crucial for applications where equivalent magnetic responses of the nanoparticles are required, such as for example in high density storage media.

In the following, the main conclusions of this work are summarized.

Oscillatory surface layer relaxation: Strong evidence for the existence of oscillatory surface layer relaxation in the range of several percent in Fe_xPt_{1-x} nanoparticles is found and can be related to the "openness" of the surface, i.e., the effect *depends on the crystallographic orientation at the surface.* The more open the surface, the more pronounced is the oscillation amplitude. Since oscillatory surface layer relaxation was found in colloidal and gas phase synthesized particles, the effect seems to be an *intrinsic property* of the particles and not related to the preparation method. It was found, however, to be more irregular for colloidal particles with organic ligands attached to their surfaces. As a result, the existence of irregular lattice layer spacings within magnetic nanoparticles should be considered in theoretical calculations.
Furthermore, large outward relaxations of the outermost surface layer could be attributed to the presence of carbon traces within or around the nanoparticles. This result is of fundamental importance for the interpretation of HRTEM nanoparticle images.

Magnetic characterization of individual nanoparticles and small nanoparticle ensembles: The challenge to *simultaneously record magnetic hysteresis loops of individual nanomagnets as well as of small ensembles was successfully met by using x-ray photoemission electron microscopy.* Hysteresis loops of ~ 18 nm Fe nanocubes were measured at room temperature, at ~ 110 K and with different in-plane orientations of the magnetic field of up to 100 mT. For *individual nanoparticles, room temperature coercivities in the range 2 to 2.5 mT were determined and could be attributed to different easy axes of magnetization.* Statistics of about 100 nanocubes revealed that for cubes aligned with their facets along the field direction, i.e., along the easy <100>-direction, H_c is larger than for cubes with their hard <110>-directions aligned along the field direction, which is in good agreement with theory (bulk bcc Fe, cubic anisotropy). Nevertheless, this value is more than one order of magnitude smaller than calculated by micromagnetic simulations for an ideal Fe nanocube. In micromagnetic simulations, the magnetization was found to reverse by *uniform rotation* (Stoner-Wohlfarth case) rather than by fanning or curling which would normally explain a smaller H_c. This discrepancy between simulated and experimentally determined H_c was in part attributed to the fact that the calculations were performed for $T = 0$ K. In OOMMF simulations, the coercive field of the nanoparticles was reduced by 75 % when a temperature of 300 K was taken into account. In addition, it was shown that the *morphology of the particles*, i.e., surface roughness and elongation *strongly affects the shape of the hysteresis loop and therefore* H_c. For example, a 2 nm surface roughness in a particle may change H_c by one order of magnitude. As a consequence, spin non-collinearities due to surface roughness and different surface anisotropy can be crucial in determining the magnetic charateristics of nanoparticles. Accordingly, the results of simulations of idealized "computer generated" structures can differ dramatically from the experimental results.

When the true morphology of the particles was used as input for the micromagnetic simulations, good agreement with experimental data was obtained. It was also shown

that *in a real particle, the shape of the hysteresis loop may be identical for the crystallographic easy <100>- and hard <110>- directions of magnetization.* As a consequence, the relative orientation of nanocube and magnetic field direction cannot be determined from the hysteresis.

For Fe nanocube dimers $\mu_s^{eff} = 1.11\,\mu_B$ *was found* via RT XMCD measurements at remanence. *Magnetic moments of individual Fe nanocubes could not be determined.* Indeed, compared to the Fe bulk magnetization, this value was found to be reduced by 50 % which can be explained by thermal fluctuations over the timescale of the XMCD and hysteresis measurements (~ 2 days). This means that T_b *of the Fe nanocubes, which have an effective side length smaller than 18 nm, is close to room temperature.* This is also confirmed by my experiments, which reveal a different blocking behavior: in samples with higher particle density, i.e., when the average next neighbor distance is ~ 100 nm, open RT hysteresis for individual particles were recorded, whereas a superparamagnetic response was found in samples with next neighbor distances of ~ 500 nm. Consequently, *dipolar coupling within nanoparticle ensembles stabilizes the magnetization* which also explains that magnetic moments could only be determined in dimer configurations.

The *influence of dipolar coupling on the coercivity can be very complex* especially if the morphology of the particles is considered. This was confirmed by the comparison of experimental room temperature hysteresis measurements of *dimers, trimers and many-nanocube configurations which sometimes have the same coercive field as a single particle* to micromagnetic simulations. For example, the calculated H_c ($T = 0$ K) for a dimer configuration of two "real" nanocubes was found to vary between 3 mT - 203 mT depending on their relative orientation.

It was also observed that *the magnetic stray field of neighboring particles may lead to an apparent horizontal shift of the hysteresis loop* since the effective field at the particle position is different from the external magnetic field. From the data, it was suggested that *the stray field's influence extends up to a distance of* ~ 60 *nm for single Fe nanocubes at RT. Above this distance,* $H_{stray} < H_c$. Apart from this hysteresis shift related to the stray field, a horizontal shift of the hysteresis loop is also observed for nanocube dimers and trimers, but not for individual cubes. Typically, such shifts are due to an exchange bias in the presence of an antiferromagnetic oxide. The presence of an oxide, however, could not be confirmed. Also because the effect is observed at both low temperature and room temperature it cannot be explained by the presence of an exchange bias. Strongly inhomogeneous magnetizations of the cubes (large influence of surface anisotropy) and a related complex stray field coupling between the nanocubes are proposed as a possible explanation.

In addition to the XPEEM experiments, first MTXM experiments on different nanoparticle systems as Fe/Fe-oxide octahedra and Co nanorods were performed. At the time of the experiments, the optics of the MTXM-instrument did not allow for the magnetic imaging of the individual particles.

Finally, the successful fabrication of Si_3N_4-membrane heating devices with a heating capability up to 20 K above RT for MTXM imaging was demonstrated, and a complex T-dependent magnetization reversal was observed in small Fe/Fe-oxide octahedra ensembles ($\sim$ 48 nm particle size).

These results further the understanding of the interplay between surface, bulk and morphology effects in self-assembled magnetic nanoparticles and open the door to reliably characterizing and controlling the magnetization down to a scale of a few nanometers.

A. Experimental Parameters

A.1. Microscope Parameters

microscope	CM300	TecnaiF20 ST
voltage (kV)	300	200
electron wavelength (pm)	1.97	2.51
C_S (mm)	0.6	1.2
semiconvergence angle α (mrad)	0.2	0.1
defocus spread (nm)	1.5	10
information limit (nm)	0.08	0.15
sampling rate (Å/pixel)	0.202	0.216

Table A.1.: Microscope Parameters

A.2. E-Beam Lithography (EBL)

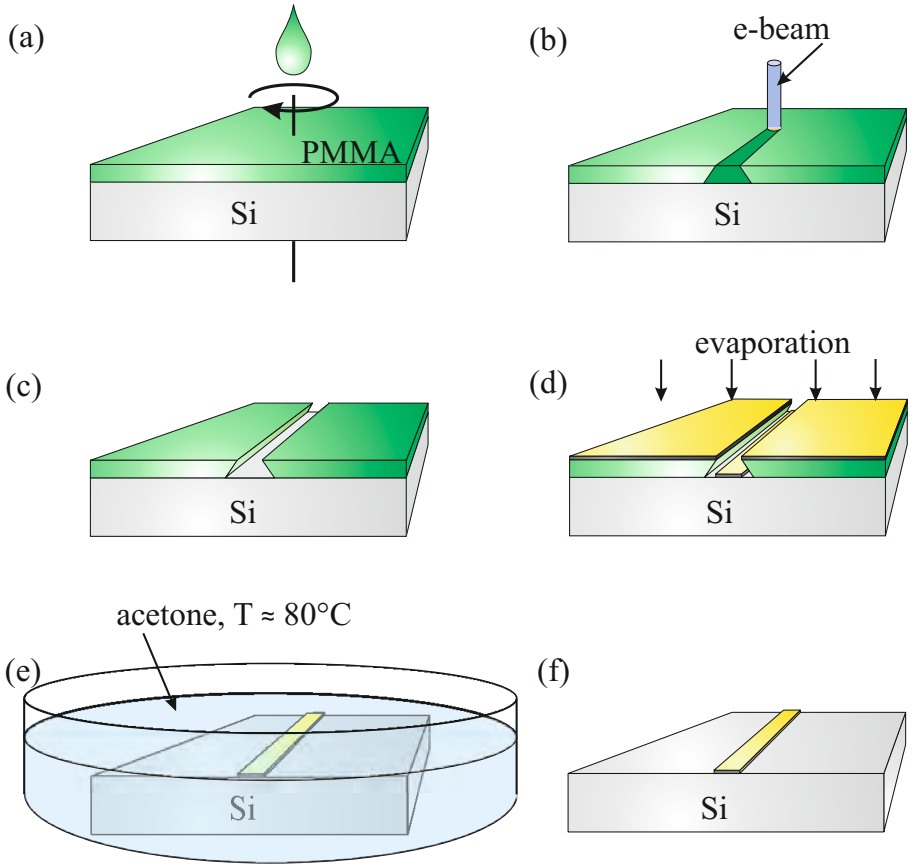

Figure A.1.: Schematic drawing of a standard e-beam lithography (EBL) process. Adapted from [215]. First, the resist (polymethyl methacrylate - PMMA) is spin coated onto the (Si-)substrate (a). In a second step, the resist is dried for 10 min at $\sim 150°C$ - not shown here. (b) The desired structure is written into the resist by the e-beam . (c) After exposition to the developer and a subsequent stopping bath, the resist is removed at the e-beam exposed areas in case of positive resist (vice versa for negative resist). The metal (here Au) is evaporated (d). (e) Complete removal of resistant by an acetone bath at about 80°C. (f) Only the desired (metallic) structure remains on the substrate.

B. Beamline Specifications

B.1. UE49-PGM-a-SPEEM

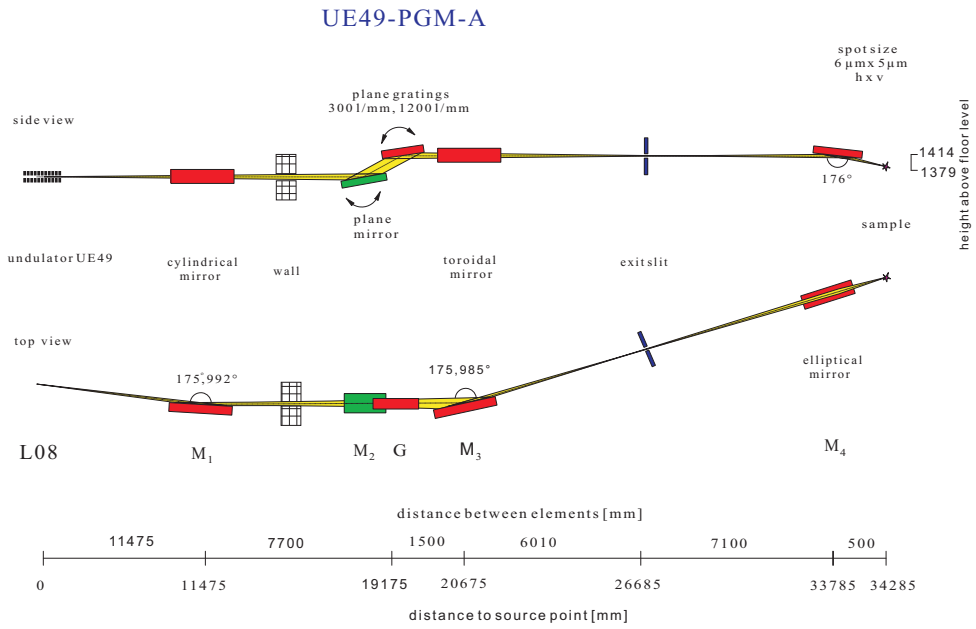

Figure B.1.: Schematical setup of beamline UE49-PGM-a at BESSYII.

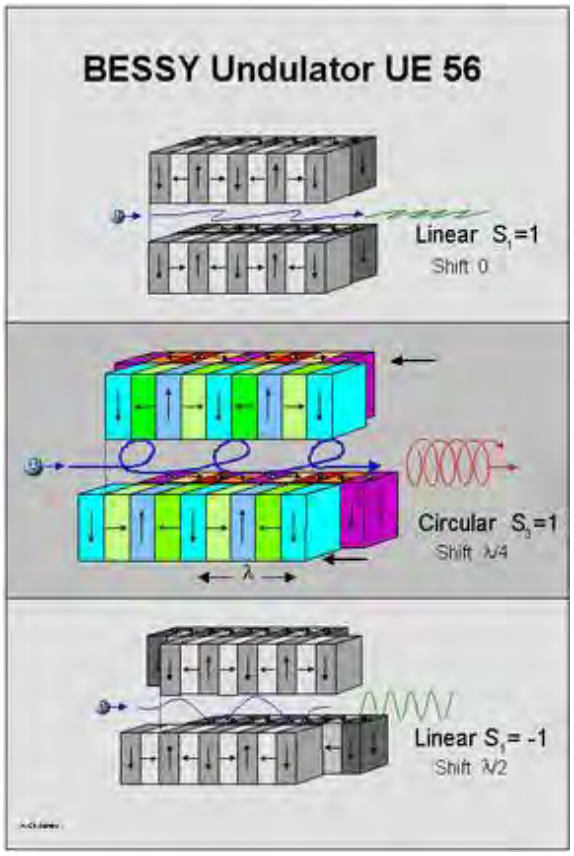

Figure B.2.: Schematic drawing of the functional principle of an APPLEII undulator as used at beamline UE49 at BESSYII. **Top: horizontally polarized light** (linear mode without shift). **Middle: circular polarized light** (The shift is set to the position with equal amplitudes of the horizontal and vertical magnetic fields, i.e., nearly a quarter period ($\lambda/4$) of the magnetic structure). **Bottom: parallel or elliptical mode** (linear mode with shift set to half period ($\lambda/2$) of the magnetic structure. Moving the two rows parallel the horizontal and vertical magnetic fields are out of phase by 90°). In the so called antiparallel or inclined mode the two rows move in opposite directions. As a result there is no phase difference between the horizontal and the vertical magnetic fields and the emitted light remains linearly polarized but with a variable angle. This additional mode is realized in the angular range - 90° - + 90° at UE49. $\lambda = 49mm$. Adapted from [216].

C. Data Treatment

C.1. Projection Calculation for Hysteresis Simulation Data of Hard Axes of Magnetization

For the calculation of the projection of the magnetization towards the applied field axis the problem is treated 2-dimensionally (Chapter 5.3.3.2). Here, the projection calculation is exemplarily described for the x-y plane. Indices have to be permuted for the two other planes.
The Cartesian coordinate system is divided in the standard sectors 1-4 (counterclockwise) but additionally a subdivision into subsectors a) and b) each covering 45° was necessary. The formulas used for the calculation of the corresponding projection depend on the projection axis, either x' or y' (Fig. C.1). The angle φ_i is measured vs. the x-axis and is given by:

$$\varphi_i = \arctan \frac{|m_y|}{|m_x|} \tag{C.1}$$

Projection Calculations - Positive Field Direction

1st sector:

a), b) $0° < \varphi_i < 90°$

$$m'_{xy} = m_{xy} \cos(45° - \varphi_i) \tag{C.2}$$

2nd sector:

a) $45° < \varphi_i < 90°$

$$m'_{xy} = m_{xy} \cos(135° - \varphi_i) \tag{C.3}$$

b) $0° < \varphi_i < 45°$

$$m'_{xy} = m_{xy} \cos(45° + \varphi_i) \tag{C.4}$$

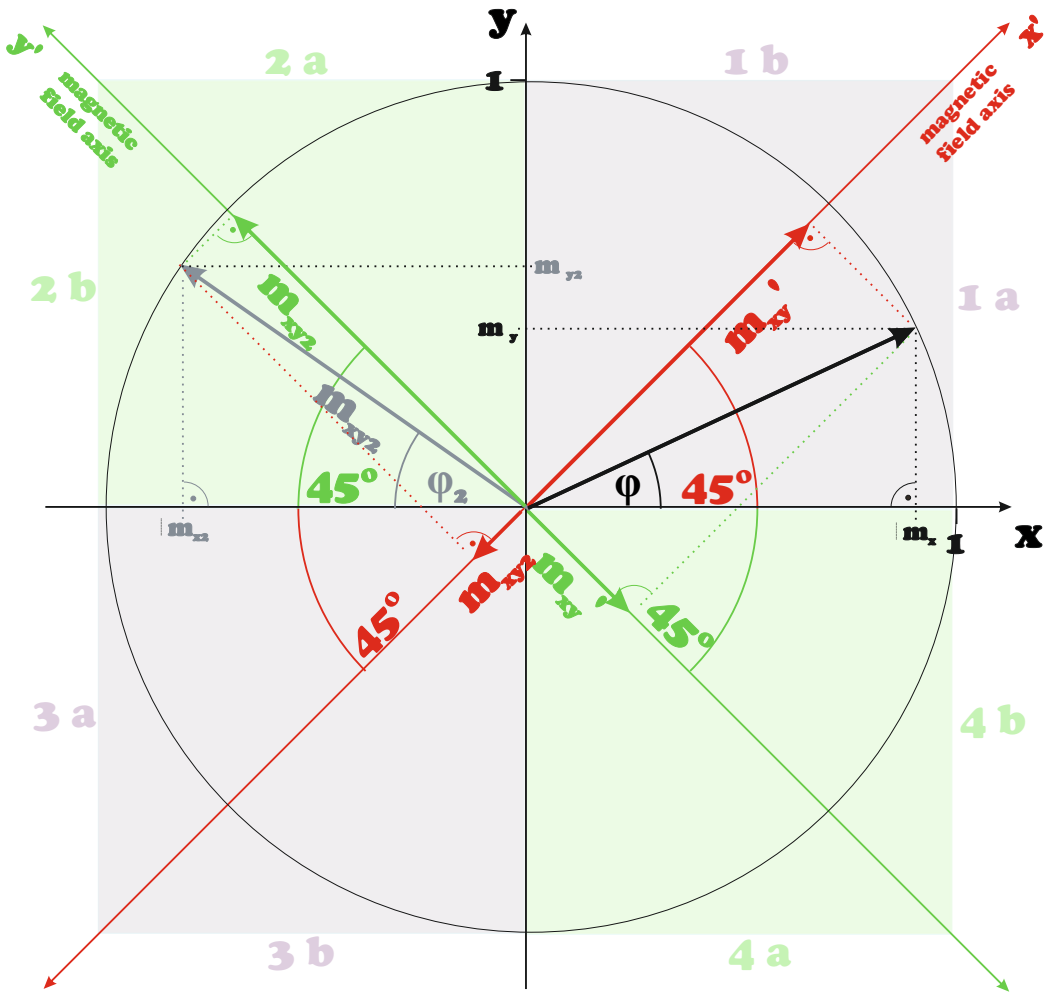

Figure C.1.: In the hysteresis simulations for the hard axis of magnetization the magnetic field is applied along the <110>-axes of the crystal, i.e. rotated by 45° with respect to the easy <100>-axes and to the coordinate axes. The convention for the positive x' (red) field direction with respect to the coordinate system is displayed. The negative y' (green) direction is consequently rotated by 90° with respect to the positive one. For details see text.

3rd sector:

a), b) $0° < \varphi_i < 90°$

$$m'_{xy} = m_{xy} \cos(45° - \varphi_i) \tag{C.5}$$

4th sector:

$a)$ $45^\circ < \varphi_i < 90^\circ$

$$m'_{xy} = m_{xy} \cos(135^\circ - \varphi_i) \tag{C.6}$$

$b)$ $0^\circ < \varphi_i < 45^\circ$

$$m'_{xy} = m_{xy} \cos(45^\circ + \varphi_i) \tag{C.7}$$

Projection Calculations - Negative Field Direction

1st sector:

$a)$ $0^\circ < \varphi_i < 45^\circ$

$$m'_{xy} = m_{xy} \cos(45^\circ + \varphi_i) \tag{C.8}$$

$b)$ $\frac{\pi}{4} < \varphi_i < \frac{\pi}{2}$

$$m'_{xy} = m_{xy} \cos(135^\circ - \varphi_i) \tag{C.9}$$

2nd sector:

a), b) $0^\circ < \varphi_i < 90^\circ$

$$m'_{xy} = m_{xy} \cos(45^\circ - \varphi_i) \tag{C.10}$$

3rd sector:

$a)$ $0^\circ < \varphi_i < 45^\circ$

$$m'_{xy} = m_{xy} \cos(45^\circ + \varphi_i) \tag{C.11}$$

$b)$ $\frac{\pi}{4} < \varphi_i < \frac{\pi}{2}$

$$m'_{xy} = m_{xy} \cos(135^\circ - \varphi_i) \tag{C.12}$$

4th sector:

a), b) $0^\circ < \varphi_i < 90^\circ$

$$m'_{xy} = m_{xy} \cos(45^\circ - \varphi_i) \tag{C.13}$$

C.2. XMCD Evaluation

μ_-: XAS intensity for anti parallel orientation of sample magnetization and photon spin
μ_+: XAS intensity for parallel orientation of sample magnetization parallel and photon

$$\mu = \frac{1}{2}(\mu_+ + \mu_-) \tag{C.14}$$

$$r = \int_{L_3+L_2} \mu \mathrm{d}E \tag{C.15}$$

$$q = \int_{L_3+L_2} (\mu_+ - \mu_-)\mathrm{d}E \tag{C.16}$$

$$p = \int_{L_3} (\mu_+ - \mu_-)\mathrm{d}E \tag{C.17}$$

Orbital (μ_l) and spin (μ_s) magnetic moments are calculated as [136]:

$$\mu_l = -\frac{2}{3}\frac{q}{r} \cdot n_h \cdot \mu_B \tag{C.18}$$

$$\mu_s = -\frac{3p - 2q}{r} \cdot n_h \cdot \left(1 + \frac{7\langle T_z \rangle}{2\langle S_z \rangle}\right)^{-1} \cdot \mu_B \tag{C.19}$$

n_h is the number of unoccupied d-states (3.39 for Fe bulk [136]), T_z is the expectation value of the magnetic dipole operator and is often neglected for bulk material and is 0 for cubic systems. Note that the effective spin moment

$$\mu_s^{eff} = \mu_s - 7m_T$$

which includes the dipolar term ($\mathrm{m_t}$) is usually determined:

$$\mu_s^{eff} = -\frac{3p - 2q}{r} \cdot n_h \cdot \mu_B \tag{C.20}$$

D. Additional Data

D.1. Experimental Data

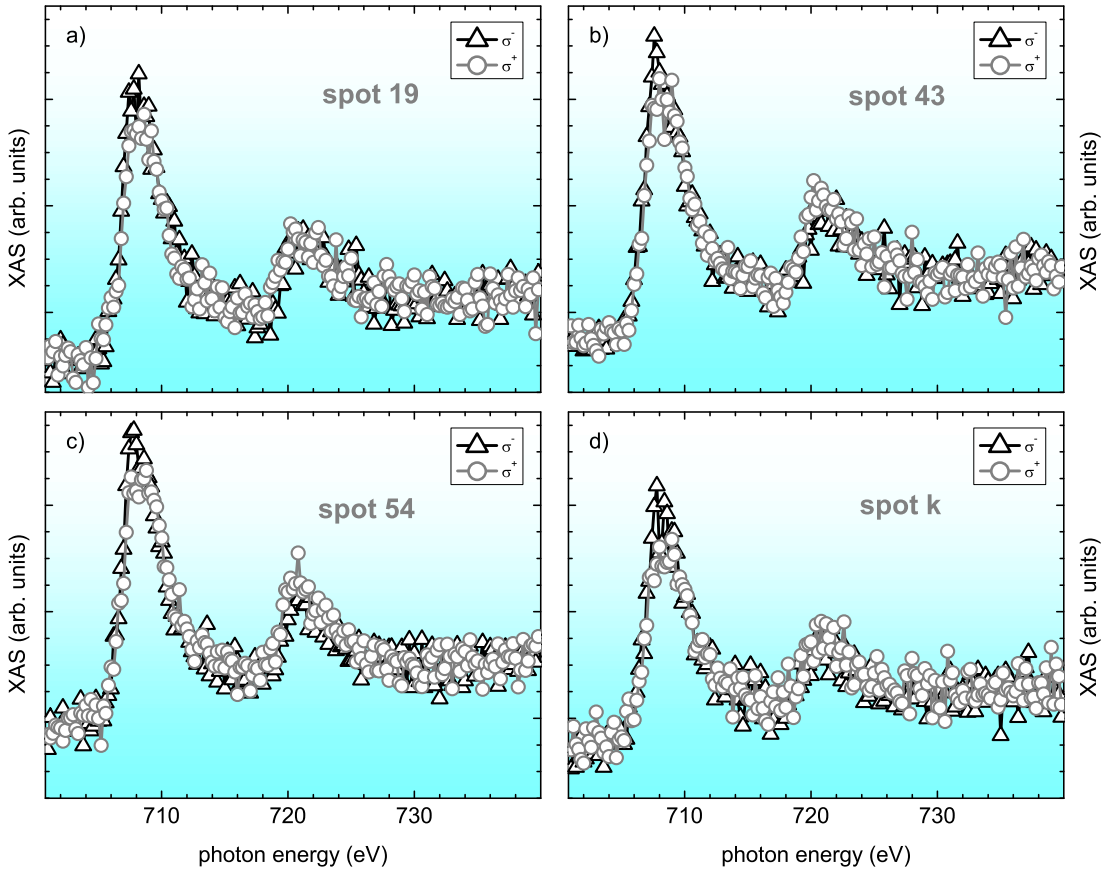

Figure D.1.: RT σ^+ and σ^- XAS spectra of individual nanocubes [XAS spectra were recorded half a year later than the temperature dependent hysteresis loops (Chapter 6.4)]. Spot numbers refer to numbering in the SEM overview image (Sample L5, Fig. 6.22).

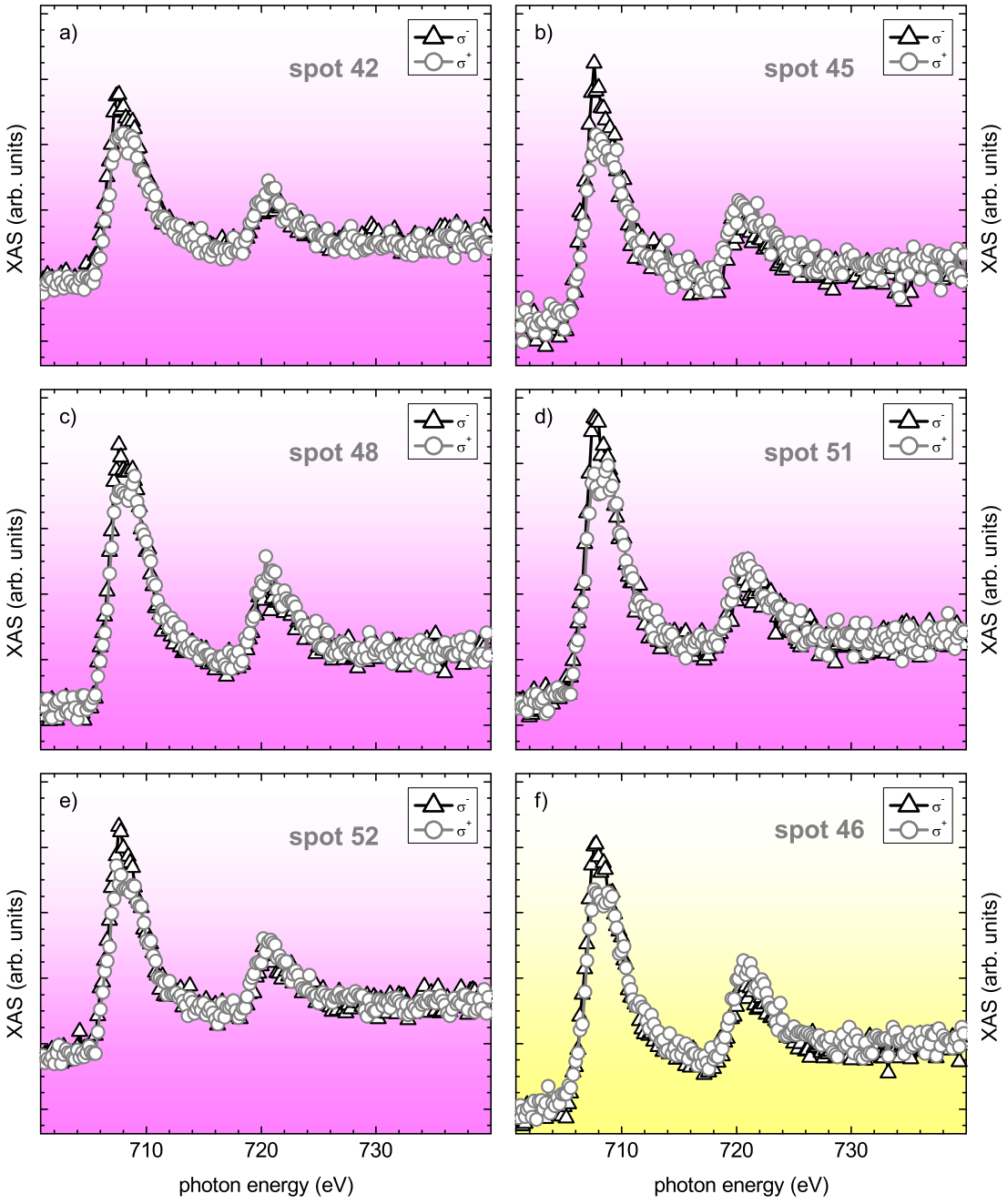

Figure D.2.: RT σ^+ and σ^- XAS spectra of dimer and trimer nanocube configurations [XAS spectra were recorded half a year later than the temperature dependent hysteresis loops (Chapter 6.4)]. Spot numbers refer to numbering in the SEM overview image (Sample L5 Fig. 6.22).

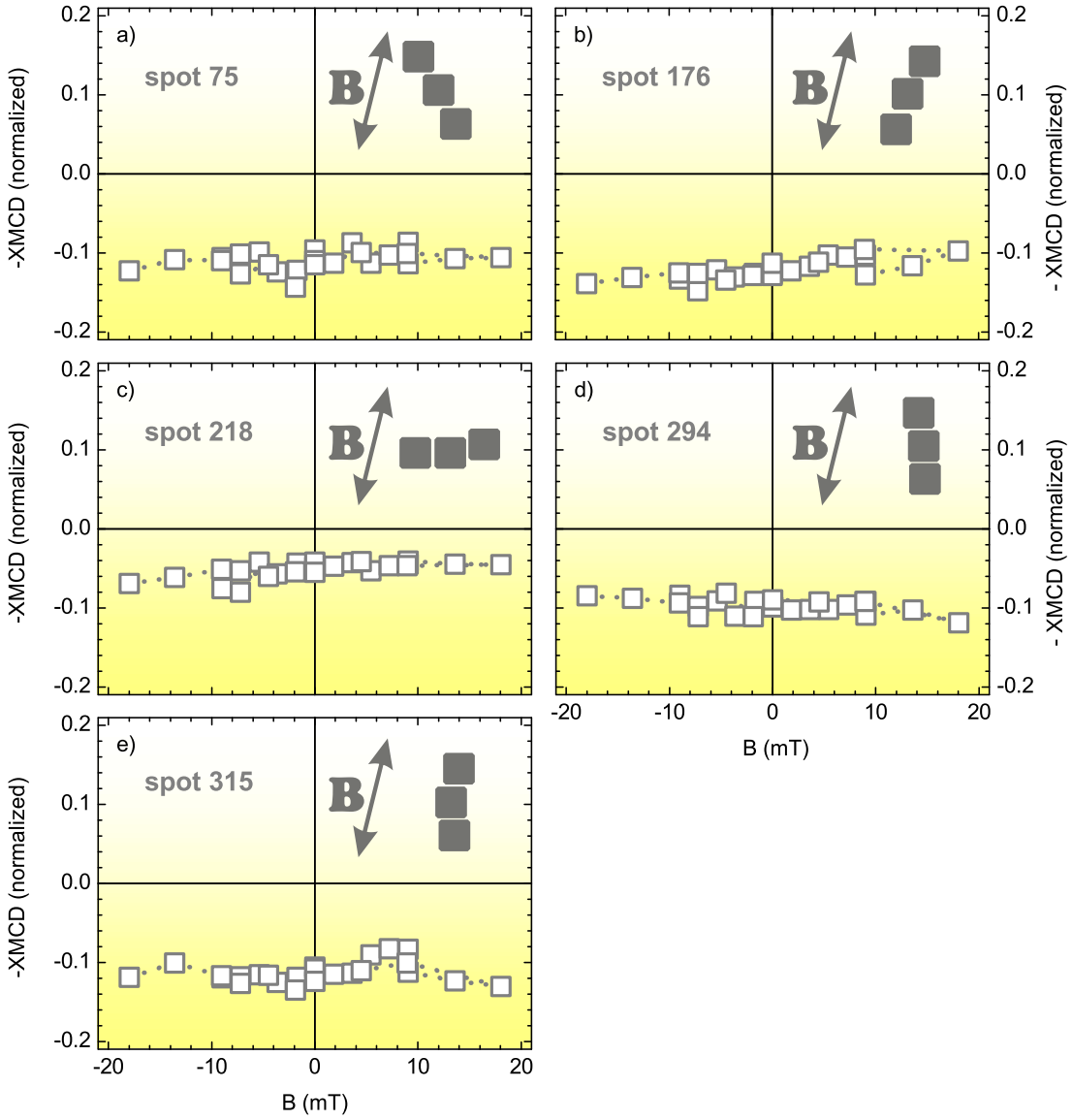

Figure D.3.: **Trimer Nanocube Hysteresis II:** Experimental room temperature hysteresis loops for trimer nanocube configurations (Sample 4B). The corresponding configurations and their relative orientations with respect to the applied field are sketched.

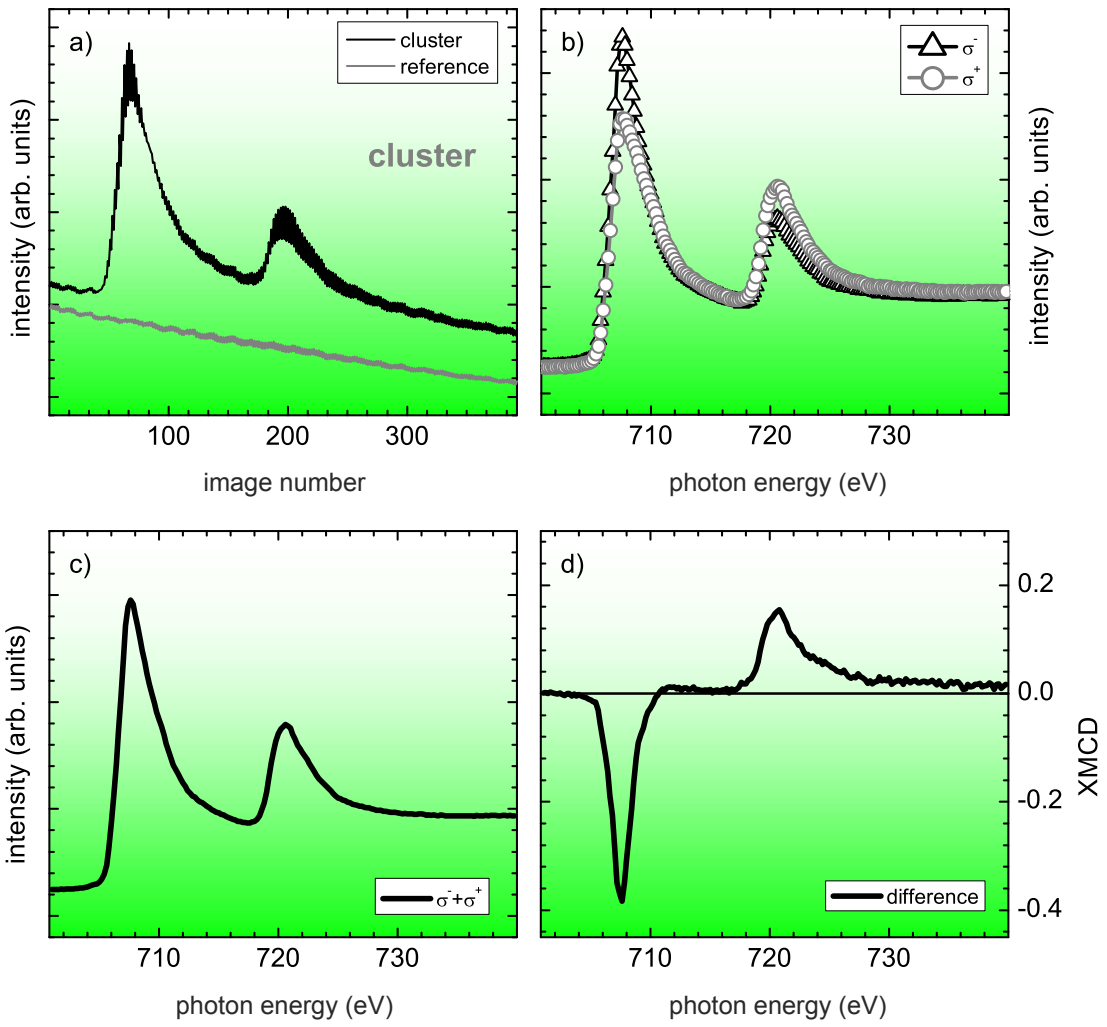

Figure D.4.: XAS and XMCD data (Fe L_3 – edge) of a cluster of several hundreds of Fe nanocubes (Fig. 6.22). XAS raw spectra for alternating circular polarization and the corresponding background signal are shown in (a). The x-axis represents the image number from which the XAS-signal is extracted (Chapter 5.1). Images are numbered consecutively, i.e., the first image and the second image were acquired using σ^- and σ^+ photon polarization at the first energy value. The third and the forth image correspond to σ^- and σ^+ photon polarization images acquired at the next energy value and so on. The oscillations in the spectra are due to intensities variations between both circular polarizations. In (b) the corresponding background normalized σ^- and σ^+ XAS spectra are shown. In panels (c) and (d) the sum and the difference (XMCD) spectra are displayed. Note that (a) - (d) are raw spectra. Prior to the application of sum rules to determine μ_l and μ_s the spectra in (b) are typically corrected for artifacts and normalized.

D.2. Simulation Data

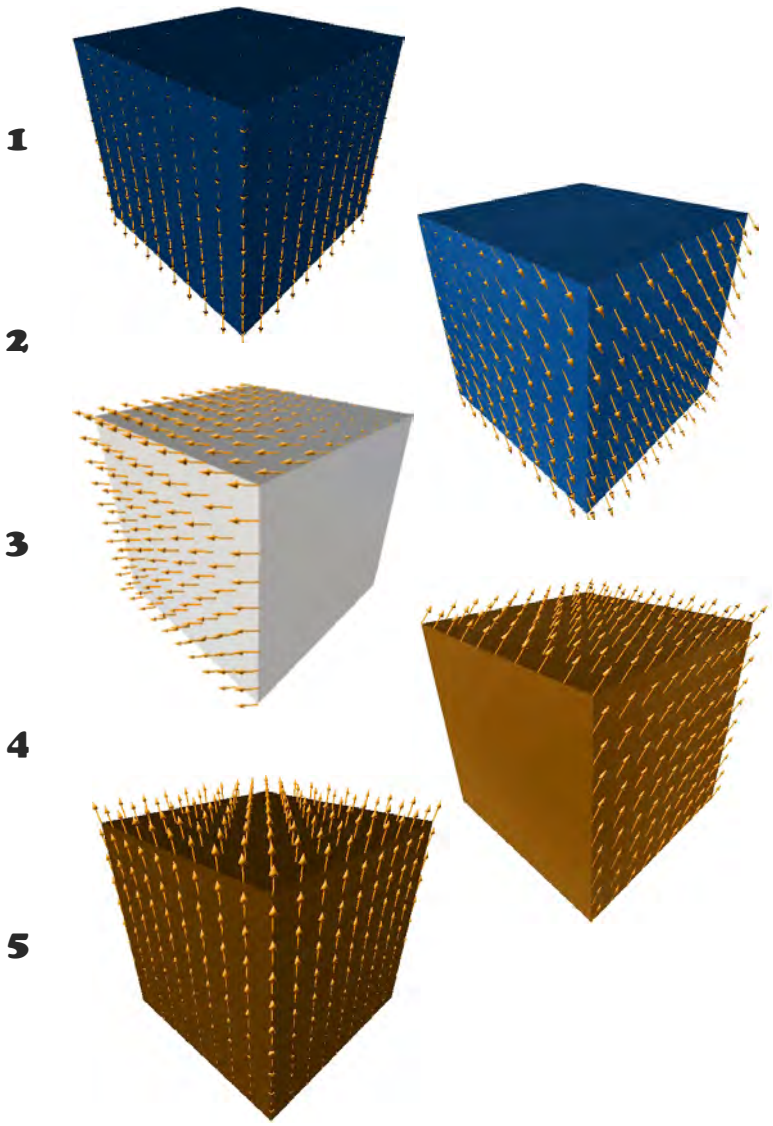

Figure D.5.: Snapshots of the evolution of the magnetization during the magnetization reversal of an ideal Fe cube with 18 nm side length and the magnetic field applied along an easy axis. The numbers correspond to positions 1 - 5 along the hysteresis loop in Fig. D.6. [Courtesy of S. Gliga]

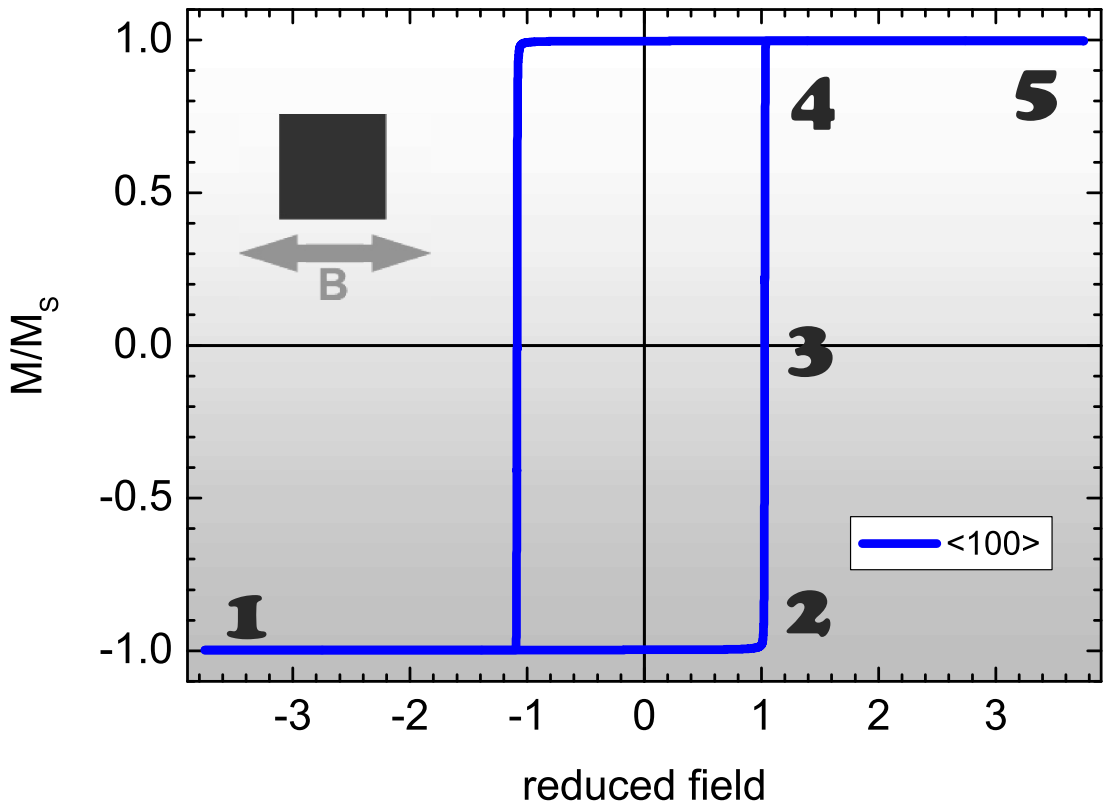

Figure D.6.: Simulated hysteresis loop of an ideal 18 nm Fe cube. **B** was applied along an easy axis. Snapshots of the orientation of "magnetic moments" for the numbered positions are displayed in Fig. D.5.

D.3. Tables

Oxide	Magnetite (Fe_3O_4)	Maghemite (γ-Fe_2O_3)	Haematite (α-Fe_2O_3)	Wuestite(FeO)
Crystal System	cubic	cubic or tetragonal	trigonal	cubic
Cell dimensions (nm)	$a = 0.839$	$a = 0.834$	$a = 0.503c = 1.375$	$a = 0.430$
Density (g/cm^3)	5.18	4.87	5.26	5.99
Type of Magnetism	ferri	ferri	weakly ferro or antiferro	antiferro
T_C $(K)T_N$ (K)	$T_C = 850$, 120^*	$T_C = 820 - 986$	$T_C = 956$, $T_M = 260$	$T_N = 203 - 211$
M_s (Am^2/kg)	$92 - 100$	$60 - 80$	0.3	–
M_s (A/m)	$(477 - 518) \times 10^3$	$(292 - 390) \times 10^3$	1.58×10^3	–
K_{eff} (erg/cm^3)	10^5-10^6	10^6	6×10^5	–
K_{eff} (J/m^3)	10^4-10^5	10^5	6×10^4	–

* Verwey transition

Table D.1.: Tabulated values of Fe-oxides [217].

Bibliography

[1] R. H. Kodama, *Magnetic nanoparticles*, Journal of Magnetism and Magnetic Materials, **200**, 359–372 (1999). xv

[2] Q. A. Pankhurst, J. Connolly, S. K. Jones and J. Dobson, *Applications of magnetic nanoparticles in biomedicine*, Journal of Physics D: Applied Physics **36**, R167 (2003). xv

[3] K. O'Grady, *Progress in applications of magnetic nanoparticles in biomedicine*, Journal of Physics D: Applied Physics **42**, 220301 (2009). xv

[4] P. Tartaj, M. del Puerto Morales, S. Veintemillas-Verdaguer, T. González-Carreño and C. J. Serna, *The preparation of magnetic nanoparticles for applications in biomedicine*, Journal of Physics D: Applied Physics **36**, R182 (2003). xv

[5] C. C. Berry and A. S. G. Curtis, *Functionalisation of magnetic nanoparticles for applications in biomedicine*, Journal of Physics D: Applied Physics **36**, R198 (2003). xv

[6] Q. A. Pankhurst, N. K. H. Thanh, S. K. Jones and J. Dobson, *Progress in applications of magnetic nanoparticles in biomedicine*, Journal of Physics D: Applied Physics **42**, 224001 (2009). xv

[7] A. G. Roca, R. Costo, A. F. Rebolledo, S. Veintemillas-Verdaguer, P. Tartaj, T. González-Carreño, M. P. Morales and C. J. Serna, *Progress in the preparation of magnetic nanoparticles for applications in biomedicine*, Journal of Physics D: Applied Physics **42**, 224002 (2009). xv

[8] C. C. Berry, *Progress in functionalization of magnetic nanoparticles for applications in biomedicine*, Journal of Physics D: Applied Physics **42**, 224003 (2009). xv

[9] D. E. Nikles and J. W. Harrell, *Dekker Encyclopedia of Nanoscience and Nanotechnology, Second Edition*, chap. Magnetic Nanoparticles for Granular Recording Media, p. 2001, Taylor & Francis (2009). xv

[10] G. Reiss and A. Hütten, *Magnetic nanoparticles: Applications beyond data storage*, Nature Materials **4**, 725–726 (2005). xv

[11] S. Sun, C. B. Murray, D. Weller, L. Folks and A. Moser, *Monodisperse FePt Nanoparticles and Ferromagnetic FePt Nanocrystal Superlattices*, Science **287**, 1989–1992 (2000). xv, 43

[12] S. Stappert, B. Rellinghaus, M. Acet and E. F. Wassermann, *Gas-phase preparation of L10 ordered FePt nanoparticles*, Journal of Crystal Growth **252**, 440–450 (2003). xv

[13] S. Sun, S. Anders, T. Thomson, J. E. E. Baglin, M. F. Toney, H. F. Hamann, C. B. Murray and B. D. Terris, *Controlled synthesis and assembly of FePt nanoparticles*, Journal of Physical Chemistry B **107**, 5419–5425 (2003). xv

[14] M. S. Seehra, V. Singh, P. Dutta, S. Neeleshwar, Y. Y. Chen, C. L. Chen, S. W. Chou and C. C. Chen, *Size-dependent magnetic parameters of fcc FePt nanoparticles: applications to magnetic hyperthermia*, Journal of Physics D: Applied Physics **43**, 145002 (2010). xv

[15] C. Antoniak and M. Farle, *Magnetism at the nanoscale: The case of FePt*, Modern Physics Letters B **21**, 1111–1131 (2007). xvi

[16] N. Friedenberger, *Layer resolved Lattice Relaxation in Magnetic* Fe_xPt_{1-x} *Nanoparticles*, Master's thesis, Universität Duisburg-Essen 2006. xvi, 6, 34, 43, 53, 55, 60

[17] C. Antoniak, M. Spasova, A. Trunova, K. Fauth, M. Farle and H. Wende, *Correlation of magnetic moments and local structure of FePt nanoparticles*, Journal of Physics: Conference Series **190**, 012118 (2009). xvi

[18] M. Jamet, W. Wernsdorfer, C. Thirion, D. Mailly, V. Dupuis, P. Mlinon and A. Prez, *Magnetic Anisotropy of a Single Cobalt Nanocluster*, Physical Review Letters **86**, 4676–4679 (2001). xvii

[19] J.-P. Cleuziou, W. Wernsdorfer, V. Bouchiat, T. Ondarcuhu and M. Monthioux, *Carbon nanotube superconducting quantum interference device*, Nature Nanotechnology **1**, 53–59 (2006). xvii

[20] L. Theil Kuhn, A. K. Geim, J. G. S. Lok, P. Hedegård, K. Ylänen, J. B. Jensen, E. Johnson and P. E. Lindelof, *Magnetisation of isolated single crystalline Fe-nanoparticles measured by a ballistic Hall micro-magnetometer*, The European Physical Journal D **10**, 259–263 (2000). xvii

[21] T. Uhlig and J. Zweck, *Recording of single-particle hysteresis loops with differential phase contrast microscopy*, Ultramicroscopy **99**, 137–142 (2004). xvii

[22] E. Snoeck, C. Gatel, L. M. Lacroix, T. Blon, S. Lachaize, J. Carrey, M. Respaud and B. Chaudret, *Magnetic Configurations of 30 nm Iron Nanocubes Studied by Electron Holography*, Nano Letters **8**, 4293–4298 (2008). xvii

[23] P. Schattschneider, S. Rubino, C. Hébért, J. Rusz, J. Kuneš, P. Novák, E. Carlino, M. Fabrizioli, G. Panaccione and G. Rossi, *Detection of magnetic circular dichroism using a transmission electron microscope*, Nature **441**, 486–488 (2006). xvii

[24] P. Schattschneider, M. Stöger-Pollach, S. Rubino, M. Sperl, C. Hurm, J. Zweck and J. Rusz, *Detection of magnetic circular dichroism on the two-nanometer scale*, Physical Review B (Condensed Matter and Materials Physics) **78**, 104413 (2008). xvii

[25] J. Stöhr and H. C. Siegmann, *Magnetism From Fundamentals to Nanoscale Dynamics*, Springer 2006. xviii, 30, 32, 35, 36, 39, 40

[26] H. A. Dürr, T. Eimüller, H. J. Elmers, S. Eisebitt, M. Farle, W. Kuch, F. Matthes, M. Martins, H. C. Mertins, P. M. Oppeneer, L. Plucinski, C. M. Schneider, H. Wende, W. Wurth and H. Zabel, *A Closer Look Into Magnetism: Opportunities With Synchrotron Radiation*, IEEE Transactions on Magnetics **45**, 15–57 (2009). xviii, 35

[27] S. Eisebitt, J. Lüning, W. F. Schlotter, M. Lörgen, O. Hellwig, W. Eberhardt and J. Stöhr, *Lensless imaging of magnetic nanostructures by X-ray spectro-holography*, Nature **432**, 885–888 (2004). xviii

[28] P. Fischer, T. Eimüller, G. Schütz, G. Denbeaux, A. Pearson, L. Johnson, D. Attwood, S. Tsunashima, M. Kumazawa, N. Takagi, M. Kohler and G. Bayreuther, *Element-specific imaging of magnetic domains at 25 nm spatial resolution using soft x-ray microscopy*, Review of Scientific Instruments **72**, 2322–2324 (2001). xviii, 40

[29] A. Fraile Rodríguez, F. Nolting, J. Bansmann, A. Kleibert and L. J. Heyderman, *X-ray imaging and spectroscopy of individual cobalt nanoparticles using photoemission electron microscopy*, Journal of Magnetism and Magnetic Materials **316**, 426–428 (9 2007). xviii

[30] F. Kronast, J. Schlichting, F. Radu, S. K. Mishra, T. Noll and H. A. Dürr, *Spin-resolved photoemission microscopy and magnetic imaging in applied magnetic fields*, Surface and Interface Analysis **42**, 1532–1536 (2010). xviii, 37, 38, 39

[31] C. Frandsen, C. W. Ostenfeld, M. Xu, C. S. Jacobsen, L. Keller, K. Lefmann and S. Mørup, *Interparticle interactions in composites of nanoparticles of ferrimagnetic*

($\gamma - Fe_2O_3$) *and antiferromagnetic* (CoO, NiO) *materials*, Physical Review B **70**, 134416 (2004). xviii, 18

[32] D. V. Berkov, *Density of energy barriers in fine magnetic particle systems*, IEEE Transactions on Magnetics **38**, 2637–2639 (2002). xviii, 18, 104

[33] C. Xu and D. J. O'Connor, *Surface Relaxation Trend Study with Iron Surfaces*, Nuclear Instruments & Methods in Physics Research Section B-Beam Interactions with Materials and Atoms **53**, 315–325 (1991). 1

[34] R. N. Barnett, U. Landman and C. L. Cleveland, *Multilayer lattice relaxation at metal surfaces: A total-energy minimization*, Physical Review B **28**, 1685–1695 (1983). 1, 5, 60

[35] P. Jiang, P. M. Marcus and F. Jona, *Relaxation at Clean Metal-Surfaces*, Solid State Communications **59**, 275–280 (1986). 1, 4, 5, 60, 63

[36] J. Sokolov, F. Jona and P. M. Marcus, *Trends in metal surface relaxation*, Solid State Communications **49**, 307–312 (1984). 1, 4, 5, 56, 60, 63

[37] M. Methfessel, D. Hennig and M. Scheffler, *Trends of the surface relaxations, surface energies, and work functions of the 4d transition metals*, Physical Review B **46**, 4816–4829 (1992). 1, 2

[38] A. Zangwill, *Physics At Surfaces*, Cambridge University Press 1989. 1

[39] J. Friedel, *Electronic Structure of Primary Solid Solutions in Metals*, Advances in Physics **3**, 446–507 (1954). 1

[40] P. Fulde, *Perspectives and interpretations in the study of surface magnetism*, Physica B+C **91**, 251–257 (1977). 1

[41] P. J. Feibelman, *First-principles calculation of the geometric and electronic structure of the Be(0001) surface*, Physical Review B **46**, 2532–2539 (1992). 2

[42] M. W. Finnis and V. Heine, *Theory of lattice contraction at aluminium surfaces*, Journal of Physics F: Metal Physics **4**, L37 (1974). 2

[43] R. Smoluchowski, *Anisotropy of the electronic work function of metals*, Physical Review **60**, 661–674 (1941). 2

[44] J. K. Nørskov and N. D. Lang, *Effective-medium theory of chemical binding: Application to chemisorption*, Physical Review B **21**, 2131–2136 (1980). 2

[45] M. J. Stott and E. Zaremba, *Quasiatoms: An approach to atoms in nonuniform electronic systems*, Physical Review B **22**, 1564–1583 (1980). 2

[46] L. Pauling, *The nature of the chemical bond and the structure of molecules and crystals; an introduction to modern structural chemistry*, Cornell University Press 1960. 2

[47] V. Heine and L. D. Marks, *Competition between pairwise and multi-atom forces at noble metal surfaces*, Surface Science **165**, 65–82 (1986). 2

[48] D. G. Pettifor, *Theory of energy bands and related properties of 4d transition metals. III. S and D contributions to the equation of state*, Journal of Physics F: Metal Physics **8**, 219–230 (1978). 2

[49] G. Allan and M. Lannoo, *Asymptotic behavior of relaxation and reconstruction near crystalline surfaces*, Physical Review B **37**, 2678–2681 (1988). 2

[50] K. Kádas, Z. Nabi, S. K. Kwon, L. Vitos, R. Ahuja, B. Johansson and J. Kollár, *Surface relaxation and surface stress of 4d transition metals*, Surface Science, **600**, 395–402 (2006). 2

[51] I. M. Tidswell, N. M. Marković and P. N. Ross, *Potential dependent surface relaxation of the Pt(001)/electrolyte interface*, Physical Review Letters **71**, 1601–1604 (1993). 3

[52] J. A. Davies, T. E. Jackman, D. P. Jackson and P. R. Norton, *Surface Relaxation of the Platinum (100)-(1x1) Surface at 175-K*, Surface Science **109**, 20–28 (1981). 3, 61

[53] J. F. Van Der Veen, R. G. Smeenk, R. M. Tromp and F. W. Saris, *Relaxation effects and thermal vibrations in a Pt(111) surface measured by medium energy ion scattering*, Surface Science **79**, 219–230 (1979). 3

[54] D. L. Adams, H. B. Nielsen and M. A. V. Hove, *Quantitative analysis of low-energy-electron diffraction: Application to Pt(111)*, Physical Review B **20**, 4789–4806 (1979). 3, 61

[55] R. Hirschl, F. Delbecq, P. Sautet and J. Hafner, *$Pt_{80}Fe_{20}$ surface from first principles: Electronic structure and adsorption of CO and atomic H*, Physical Review B **66**, 155438 (2002). 3, 6, 57, 63

[56] E. Holub-Krappe, K. Horn, J. W. M. Frenken, R. L. Krans and J. F. Van Der Veen, *Multilayer relaxation at the Ag(110) surface*, Surface Science **188**, 335–349 (1987). 3

[57] Y. Kuk and L. C. Feldman, *Oscillatory relaxation of the Ag(110) surface*, Physical Review B **30**, 5811–5816 (1984). 3

[58] L. E. Gonzalez and D. J. Gonzalez, *Temperature dependent surface relaxation for Al(110) and Mg(10-10) studied by orbital free ab initio molecular dynamics* (2006), arXiv:cond-mat/0606130v1 [cond-mat.mtrl-sci]. 3

[59] S. Walter, H. Baier, M. Weinelt, K. Heinz and T. Fauster, *Quantitative determination of Cu(117) multilayer surface relaxations by LEED*, Physical Review B **63**, 155407 (2001). 3

[60] H. D. Shih, F. Jona, D. W. Jepsen and P. M. Marcus, *Atomic-Structure of Fe(111)*, Surface Science **104**, 39–46 (1981). 4

[61] H. D. Shih, F. Jona, U. Bardi and P. M. Marcus, *The Atomic-Structure of Fe[110]*, Journal of Physics C-Solid State Physics **13**, 3801–3808 (1980). 4

[62] K. O. Legg, F. Jona, D. W. Jepsen and P. M. Marcus, *Low-Energy Electron-Diffraction Analysis of Clean Fe(001)*, Journal of Physics C-Solid State Physics **10**, 937–946 (1977). 4

[63] W. T. Geng, M. Kim and A. J. Freeman, *Multilayer relaxation and magnetism of a high-index transition metal surface: Fe(310)*, Physical Review B **63**, 245401 (2001). 4

[64] J. Sokolov, H. D. Shih, U. Bardi and F. Jona, *New Relaxation Phenomena in the Outer Atomic Layers of Fe(211)*, Solid State Communications **48**, 739–741 (1983). 4

[65] J. Sokolov, H. D. Shih, U. Bardi, F. Jona and P. M. Marcus, *Multilayer Relaxation of Body-Centered-Cubic Fe(211)*, Journal of Physics C-Solid State Physics **17**, 371–383 (1984). 4

[66] J. Sokolov, F. Jona and P. M. Marcus, *Parallel and Perpendicular Multilayer Relaxation of Fe(310)*, Physical Review B **29**, 5402–5409 (1984). 4

[67] J. Sokolov, F. Jona and P. M. Marcus, *Multilayer Relaxation of the Fe(210) Surface*, Physical Review B **31**, 1929–1935 (1985). 4

[68] J. Sokolov, F. Jona and P. M. Marcus, *Multilayer Relaxation of a Clean Bcc Fe(111) Surface*, Physical Review B **33**, 1397–1400 (1986). 4

[69] B. J. Lee, M. I. Baskes, H. Kim and Y. K. Cho, *Second nearest-neighbor modified embedded atom method potentials for bcc transition metals*, Physical Review B **64**, 184102 (2001). 4

[70] P. Błoński and A. Kiejna, *Structural, electronic, and magnetic properties of bcc iron surfaces*, Surface Science **601**, 123–133 (2007). 4

[71] J. R. Smith and A. Banerjea, *Equivalent-crystal theory of oscillatory surface relaxation*, Physical Review B **37**, 10411–10414 (1988). 5

[72] M. E. Gruner, G. Rollmann, P. Entel and M. Farle, *Multiply Twinned Morphologies of FePt and CoPt Nanoparticles*, Physical Review Letters **100**, 087203 (2008). 6

[73] H. G. Boyen, A. Ethirajan, G. Kästle, F. Weigl, P. Ziemann, G. Schmid, M. G. Garnier, M. Büttner and P. Oelhafen, *Alloy Formation of Supported Gold Nanoparticles at Their Transition from Clusters to Solids: Does Size Matter?*, Physical Review Letters **94**, 016804 (2005). 6

[74] R. M. Wang, O. Dmitrieva, M. Farle, G. Dumpich, H. Q. Ye, H. Poppa, R. Kilaas and C. Kisielowski, *Layer Resolved Structural Relaxation at the Surface of Magnetic FePt Icosahedral Nanoparticles*, Physical Review Letters **100**, 017205 (2008). 6, 56, 60, 61

[75] R. Wang, O. Dmitrieva, M. Farle, G. Dumpich, M. Acet, S. Mejia-Rosales, E. Perez-Tijerina, M. J. Yacaman and C. Kisielowski, *FePt Icosahedra with Magnetic Cores and Catalytic Shells*, The Journal of Physical Chemistry C **113**, 4395–4400 (2009). 6, 56, 61

[76] C. Antoniak, A. Trunova, M. Spasova, M. Farle, H. Wende, F. Wilhelm and A. Rogalev, *Lattice expansion in nonoxidized FePt nanoparticles: X-ray absorption measurements*, Physical Review B (Condensed Matter and Materials Physics) **78**, 041406 (2008). 6, 55, 60

[77] K. Du, F. Ernst, M. C. Pelsozy, J. Barthel and K. Tillmann, *Expansion of interatomic distances in platinum catalyst nanoparticles*, Acta Materialia **58**, 836–845 (2010). 6, 61

[78] L.-L. Wang and D. D. Johnson, *Predicted Trends of Core-Shell Preferences for 132 Late Transition-Metal Binary-Alloy Nanoparticles*, Journal of the American Chemical Society **131**, 14023–14029 (2009). 6

[79] A. Dannenberg, M. E. Gruner, A. Hucht and P. Entel, *Surface energies of stoichiometric FePt and CoPt alloys and their implications for nanoparticle morphologies*, Physical Review B **80**, 245438 (2009). 6

[80] C. Antoniak, M. Spasova, A. Trunova, K. Fauth, F. Wilhelm, A. Rogalev, J. Minar, H. Ebert, M. Farle and H. Wende, *Inhomogeneous alloying in FePt nanoparticles as a reason for reduced magnetic moments*, Journal of Physics: Condensed Matter **21**, 336002 (2009). 6

[81] C. Antoniak, J. Lindner, M. Spasova, D. Sudfeld, M. Acet, M. Farle, K. Fauth, U. Wiedwald, H. G. Boyen, P. Ziemann, F. Wilhelm, A. Rogalev and S. Sun, *Enhanced Orbital Magnetism in Fe50Pt50 Nanoparticles*, Physical Review Letters **97**, 117201 (2006). 6, 50

[82] R. C. O'Handley, *Modern Magnetic Materials: Principles and Applications*, Wiley 2000. 7, 8, 15, 16

[83] M. Farle, *Ferromagnetic resonance of ultrathin metallic layers*, Reports on Progress in Physics **61**, 755–826 (1998). 7, 8, 10, 11

[84] A. E. Berkowitz and K. Takano, *Exchange anisotropy - a review*, Journal of Magnetism and Magnetic Materials **200**, 552–570 (1999). 7, 26

[85] J. Lindner and M. Farle, *Magnetic Anisotropy of Heterostructures*, in *Advances and Perspectives in Spinstructures and Spintransport*, edited by H. Zabel and S. D. Bader, vol. 227 of *Series: Springer Tracts in Modern Physics*, Springer 2008. 8

[86] P. Bruno, *Tight-binding approach to the orbital magnetic moment and magnetocrystalline anisotropy of transition-metal monolayers*, Physical Review B **39**, 865–868 (1989). 8

[87] B. D. Cullity and C. D. Graham, *Introduction to Magnetic Materials*, John Wiley & Sons, Inc., Hoboken, NJ, USA. 2009. 10, 12, 18, 19, 22, 23, 24, 120

[88] M. Spasova, U. Wiedwald, R. Ramchal, M. Farle, M. Hilgendorff and M. Giersig, *Magnetic properties of arrays of interacting Co nanocrystals*, Journal of Magnetism and Magnetic Materials, **240**, 40–43 (2002). 10

[89] M. Jamet, W. Wernsdorfer, C. Thirion, V. Dupuis, P. Mlinon, A. Prez and D. Mailly, *Magnetic anisotropy in single clusters*, Physical Review B **69**, 024401 (2004). 11, 12

[90] L. Néel, *Anisotropie magnétique superficielle et surstructures d'orientation*, Journal de Physique et le Radium **15**, 225–239 (1954). 12

[91] W. Wernsdorfer, *Surface Effects in Magnetic Nanoparticles*, chap. Magnetic Anisotropy and Magnetization Reversal Studied in Individual Particles, pp. 263–298, Springer (2005). 12

[92] F. Bødker, S. Mørup and S. Linderoth, *Surface effects in metallic iron nanoparticles*, Physical Review Letters **72**, 282–285 (1994). 12

[93] L. Néel, *Théorie du traînage magnétique des ferromagnétiques en grains fins avec applications aux terres cuites*, Annales de Géophysique **5**, 99 (1949). 13

[94] W. F. Brown, *Thermal Fluctuations of a Single-Domain Particle*, Physical Review **130**, 1677–1686 (1963). 14

[95] J. L. Dormann, D. Fiorani and E. Tronc, *Magnetic relaxation in fine-particle systems*, Advances in Chemical Physics **98**, 283–494 (1997). 14, 17

[96] C. P. Bean, *Hysteresis Loops of Mixtures of Ferromagnetic Micropowders*, Journal of Applied Physics **26**, 1381–1383 (1955). 14

[97] C. Antoniak, J. Lindner, V. Salgueiriño-Maceira and M. Farle, *Multifrequency magnetic resonance and blocking behavior of Fe_xPt_{1-x} nanoparticles*, physica status solidi (a) **203**, 2968–2973 (2006). 15

[98] S. Blundell, *Magnetism in Condensed Matter*, Oxford University Press 2001. 15

[99] C. Kittel, *Theory of the Structure of Ferromagnetic Domains in Films and Small Particles*, Physical Review **70**, 965–971 (1946). 15, 16

[100] J. Weissmüller, R. D. McMichael, A. Michels and R. D. Shull, *Small Angle Neutron Scattering by the Magnetic Microstructure of Nanocrystalline Ferromagnets Near Saturation*, J. Res. Natl. Inst. Stand. Technol. **104**, 261 (1999). 16

[101] C. Kittel, *On the Gyromagnetic Ratio and Spectroscopic Splitting Factor of Ferromagnetic Substances*, Physical Review **76**, 743–748 (1949). 17

[102] C. M. Srivastava and R. Aiyar, *Spin wave stiffness constants in some ferrimagnetics*, Journal of Physics C: Solid State Physics **20**, 1119–1128 (1987). 17

[103] A. Hubert and R. Schäfer, *Magnetic Domains The Analysis of Magnetic Microstructures*, Springer Berlin Heidelberg 1998. 18, 24

[104] S. Bedanta and W. Kleemann, *Supermagnetism*, Journal of Physics D: Applied Physics **42**, 13001–13028(28) (2009). 18, 103

[105] J. Lindner, *Ferromagnetische Resonanz an ultradünnen magnetischen Einfach- und Mehrfachlagen der 3d-Übergangsmetalle - Struktur und Dynamik*, Ph.D. thesis, Freie Universität Berlin 2002. 19

[106] C. Antoniak, *Magnetische Eigenschaften des Legierungssystems Fe-Pt - Volumenmaterialien und Nanopartikel*, Ph.D. thesis, Universität Duisburg-Essen 2007. 19, 35, 97

[107] A. Trunova, *Ferromagnetische Resonanz an oxidfreien magnetischen Fe und FeRh Nanopartikeln*, Ph.D. thesis, Universität Duisburg-Essen 2009. 19, 50, 51

[108] W. Wernsdorfer, *Advances in Chemical Physics*, chap. Classical and Quantum Magnetization Reversal Studied in Nanometer-Sized Particles and Clusters, pp. 99–190, Advances in Chemical Physics, John Wiley & Sons, Inc., Hoboken, NJ, USA. (2007). 19, 20, 21, 22, 24

[109] E. C. Stoner and E. P. Wohlfarth, *A Mechanism of Magnetic Hysteresis in Heterogeneous Alloys*, Philosophical Transactions of the Royal Society of London. Series A, Mathematical and Physical Sciences **240**, 599–642 (1948). 19, 78

[110] L. Néel, **Magnetisme - Le Champ Coercitif Dune Poudre Ferromagnetique Cubique a Grains Anisotropes*, Comptes Rendus Hebdomadaires Des Seances De L Academie Des Sciences **224**, 1550–1551 (1947). 19

[111] A. Thiaville, *Extensions of the geometric solution of the two dimensional coherent magnetization rotation model*, Journal of Magnetism and Magnetic Materials **182**, 5–18 (1998). 20, 21

[112] A. Thiaville, *Coherent rotation of magnetization in three dimensions: A geometrical approach*, Physical Review B **61**, 12221–12232 (2000). 20, 21

[113] F. E. Luborsky and P. E. Lawrence, *Saturation Magnetization and Size of Iron Particles Less than 100 Å in Diameter*, Journal of Applied Physics **32**, S231–S232 (1961). 22

[114] I. S. Jacobs and C. P. Bean, *An Approach to Elongated Fine-Particle Magnets*, Physical Review **100**, 1060–1067 (1955). 22, 23

[115] W. H. Meiklejohn and C. P. Bean, *New magnetic anisotropy*, Physical Review **105**, 904–913 (1957). 25, 28, 120, 135

[116] W. H. Meiklejohn and C. P. Bean, *New magnetic anisotropy [1]*, Physical Review **102**, 1413–1414 (1956). 25, 120, 135

[117] M. Kiwi, *Exchange bias theory*, Journal of Magnetism and Magnetic Materials **234**, 584–595 (2001). 25, 26, 29

[118] W. H. Meiklejohn, *Exchange anisotropy - A review*, Journal of Applied Physics **33**, 1328–1335 (1962). 26, 28, 120, 135

[119] J. Nogués and I. K. Schuller, *Exchange bias*, Journal of Magnetism and Magnetic Materials **192**, 203–232 (1999). 26, 28, 29

[120] J. Nogués, J. Sort, V. Langlais, V. Skumryev, S. Suriñach, J. S. Muñoz and M. D. Baró, *Exchange bias in nanostructures*, Physics Reports **422**, 65–117 (2005). 26, 27, 28

[121] O. Iglesias, A. Labarta and X. Batlle, *Exchange Bias Phenomenology and Models of Core/Shell Nanoparticles*, Journal of Nanoscience and Nanotechnology **8**, 2761–2780(20) (2008). 26

[122] S. Demirtas and A. R. Koymen, *Thickness dependence of oscillatory exchange bias*, Journal of Magnetism and Magnetic Materials **286**, 238–242 (2005). 27, 28

[123] J. Nogués, D. Lederman, T. J. Moran and I. K. Schuller, *Positive exchange bias in FeF_2-Fe bilayers*, Physical Review Letters **76**, 4624–4627 (1996). 27, 135

[124] S. K. Mishra, F. Radu, H. A. Dürr and W. Eberhardt, *Training-induced positive exchange bias in NiFe/IrMn bilayers*, Physical Review Letters **102**, 177208 (2009). 28

[125] F. Canet, S. Mangin, C. Bellouard and M. Piecuch, *Positive exchange bias in ferromagnetic-ferrimagnetic bilayers: FeSn/FeGd*, Europhysics Letters **52**, 594–600 (2000). 28

[126] A. L. Kobrinskii, A. M. Goldman, M. Varela and S. J. Pennycook, *Thickness dependence of the exchange bias in epitaxial manganite bilayers*, Physical Review B - Condensed Matter and Materials Physics **79**, 094405 (2009). 29

[127] C. Binek, A. Hochstrat and W. Kleemann, *Exchange bias in a generalized Meiklejohn-Bean approach*, Journal of Magnetism and Magnetic Materials **234**, 353–358 (2001). 29

[128] A. P. Malozemoff, *Random-field model of exchange anisotropy at rough ferromagnetic- antiferromagnetic interfaces*, Physical Review B **35**, 3679–3682 (1987). 29

[129] H. Wende, *Recent advances in x-ray absorption spectroscopy*, Reports on Progress in Physics **67**, 2105–2181 (2004). 30

[130] J. Stöhr, *NEXAFS Spectroscopy*, Springer, Berlin 1992. 31

[131] T. J. Regan, H. Ohldag, C. Stamm, F. Nolting, J. Lüning, J. Stöhr and R. L. White, *Chemical effects at metal/oxide interfaces studied by x-ray-absorption spectroscopy*, Physical Review B - Condensed Matter and Materials Physics **64**, 2144221–21442211 (2001). 31, 150

[132] J. L. Erskine and E. A. Stern, *Calculation of the M_{23} magneto-optical absorption spectrum of ferromagnetic nickel*, Physical Review B **12**, 5016–5024 (1975). 31

[133] G. Schütz, W. Wagner, W. Wilhelm, P. Kienle, R. Zeller, R. Frahm and G. Materlik, *Absorption of circularly polarized x rays in iron*, Physical Review Letters **58**, 737–740 (1987). 31

[134] B. T. Thole, P. Carra, F. Sette and G. van der Laan, *X-ray circular dichroism as a probe of orbital magnetization*, Physical Review Letters **68**, 1943–1946 (1992). 32, 97

[135] P. Carra, B. T. Thole, M. Altarelli and X. Wang, *X-ray circular dichroism and local magnetic fields*, Physical Review Letters **70**, 694–697 (1993). 32, 97

[136] C. T. Chen, Y. U. Idzerda, H. J. Lin, N. V. Smith, G. Meigs, E. Chaban, G. H. Ho, E. Pellegrin and F. Sette, *Experimental confirmation of the x-ray magnetic circular dichroism sum rules for iron and cobalt*, Physical Review Letters **75**, 152–155 (1995). 32, 97, 166

[137] D. B. Williams and C. B. Carter, *Transmission Electron Microscopy*, Springer New York 1996. 33, 34

[138] L. Reimer, *Transmission Electron Microscopy*, Springer Berlin Heidelberg 1984. 33

[139] E. J. Kirkland, *Improved High resolution Image Processing Of Bright Field Electron Micrographs*, Ultramicroscopy **15**, 151–172 (1984). 33

[140] W. M. J. Coene, A. Thust, M. Op de Beeck and D. V. Dyck, *Maximum-likehood method for focus-variation image reconstruction in high resolution transmission electron microscopy*, Ultramicroscopy **64**, 109–135 (1996). 33, 34

[141] A. Thust, W. Coene, M. Op de Beeck and D. V. Dyck, *Focal-series reconstruction in HRTEM: simulation studies on non-periodic objects*, Ultramicroscopy **64**, 211–230 (1996). 33, 34

[142] H. Lichte, *Optimum focus for taking electron holograms*, Ultramicroscopy **38**, 13–22 (1991). 34

[143] O. Dmitrieva, *Hochauflösende Elektronenmikroskopie und Kontrastsimulation zur Strukturaufklärung an gesinterten FePt-Nanopartikeln*, Master's thesis, Universität Duisburg-Essen 2003. 34

[144] C. Möller, *Dreidimensionale Tomographie an Nanostrukturen mittels Transmissionselektronenmikroskopie*, Master's thesis, Universität Duisburg-Essen 2010. 34, 86, 87

[145] E. Beaurepaire, H. Bulou, F. Scheurer and J.-P. Kappler, *Magnetism: A Synchrotron Radiation Approach*, in *Lect. Notes Phys. 697*, Springer 2006. 35

[146] E. Beaurepaire, H. Bulou, F. Scheurer and J.-P. Kappler, *Magnetism and Synchrotron Radiation*, in *Springer Proceedings in Physics 133*, Springer 2010. 35, 40

[147] J. Schlichting, *Magnetische Schaltprozesse in Exchange Bias Systemen: eine Photoelektronen-Mikroskopie-Studie*, Master's thesis, Freie Universität Berlin 2007. 35, 38, 39

[148] F. Nolting, A. Scholl, J. Stöhr, J. W. Seo, J. Fompeyrine, H. Siegwart, J. P. Locquet, S. Anders, J. Lüning, E. E. Fullerton, M. F. Toney, M. R. Scheinfein and H. A. Padmore, *Direct observation of the alignment of ferromagnetic spins by antiferromagnetic spins*, Nature **405**, 767–769 (2000), 15. 35

[149] H. Ohldag, T. J. Regan, J. Stöhr, A. Scholl, F. Nolting, J. Lüning, C. Stamm, S. Anders and R. L. White, *Spectroscopic Identification and Direct Imaging of Interfacial Magnetic Spins*, Physical Review Letters **87**, 247201 (2001). 35

[150] W. Kuch, *X-ray magnetic circular dichroism for quantitative element-resolved magnetic microscopy*, Physica Scripta T **T109**, 89–95 (2004). 35

[151] J. Stöhr, H. A. Padmore, S. Anders, T. Stammler and M. R. Scheinfein, *Principles of x-ray magnetic dichroism spectromicroscopy*, Surface Review and Letters **5**, 1297–1308 (1998). 35, 36

[152] C. M. Schneider and G. Schönhense, *Investigating surface magnetism by means of photoexcitation electron emission microscopy*, Reports on Progress in Physics **65**, 1785–1839 (2002). 35, 37

[153] A. Locatelli and E. Bauer, *Recent advances in chemical and magnetic imaging of surfaces and interfaces by XPEEM*, Journal of Physics: Condensed Matter **20**, 093002 (2008). 35, 37

[154] R. Fink, M. R. Weiss, E. Umbach, D. Preikszas, H. Rose, R. Spehr, P. Hartel, W. Engel, R. Degenhardt, R. Wichtendahl, H. Kuhlenbeck, W. Erlebach, K. Ihmann, R. Schlögl, H. J. Freund, A. M. Bradshaw, G. Lilienkamp, T. Schmidt, E. Bauer and G. Benner, *SMART: a planned ultrahigh-resolution spectromicroscope for BESSY II*, Journal of Electron Spectroscopy and Related Phenomena **84**, 231–250 (1997). 37

[155] A. Scholl, H. Ohldag, F. Nolting, J. Stöhr and H. A. Padmore, *X-ray photoemission electron microscopy, a tool for the investigation of complex magnetic structures (invited)*, Review of Scientific Instruments **73**, 1362–1366 (2002). 37

[156] G. Schönhense, *Imaging of magnetic structures by photoemission electron microscopy*, Journal of Physics: Condensed Matter **11**, 9517–9547 (1999). 37

[157] P. Fischer, *Studying nanoscale magnetism and its dynamics with soft X-ray microscopy*, IEEE Transactions on Magnetics **44**, 1900–1904 (2008). 39, 40, 41

[158] W. Chao, B. D. Harteneck, J. A. Liddle, E. H. Anderson and D. T. Attwood, *Soft X-ray microscopy at a spatial resolution better than 15 nm*, Nature **435**, 1210–1213 (2005). 39, 40

[159] P. Fischer, *private communication* (2009). 39, 48

[160] http://www.cxro.lbl.gov/XM1. 40

[161] http://www.cxro.lbl.gov/BL612/index.php?content=facilities.html. 41

[162] R. Hertel, O. Fruchart, S. Cherifi, P. O. Jubert, S. Heun, A. Locatelli and J. Kirschner, *Three-dimensional magnetic-flux-closure patterns in mesoscopic Fe islands*, Phys.Rev.B **72**, 214409 (2005). 42, 76

[163] http://math.nist.gov/oommf/. 42

[164] F. Kronast, N. Friedenberger, K. Ollefs, S. Gliga, L. Tati-Bismaths, R. Thies, A. Ney, R. Weber, C. Hassel, F. M. Römer, A. V. Trunova, C. Wirtz, R. Hertel, H. A. Dürr and M. Farle, *Element-Specific Magnetic Hysteresis of Individual 18 nm Fe Nanocubes*, Nano Letters **11**, 1710–1715 (2011). 42

[165] http://math.nist.gov/oommf/doc/userguide12a3/userguide/. 42

[166] http://www.nanoscience.de/group_r/stm-spstm/projects/temperature/download.shtml. 42

[167] http://www.nanoscience.de/group_r/stm-spstm/projects/temperature/theory.shtml. 42

[168] O. Dmitrieva, *Strukturelle und magnetische Eigenschaften von FePt-Nanopartikeln aus der Gasphase*, Ph.D. thesis, Universität Duisburg-Essen 2007. 43

[169] O. Margeat, M. Tran, M. Spasova and M. Farle, *Magnetism and structure of chemically disordered $FePt_3$ nanocubes*, Phys. Rev. B **75**, 134410 (2007). 43

[170] A. Shavel, B. Rodríguez-González, M. Spasova, M. Farle and L. M. Liz-Marzán, *Synthesis and Characterization of Iron/Iron Oxide Core/Shell Nanocubes*, Advanced Functional Materials **17**, 3870–3876 (2007). 43, 46, 47, 75, 101, 137

[171] A. Shavel, B. Rodríguez-González, J. Pacifico, M. Spasova, M. Farle and L. M. Liz-Marzán, *Shape Control in Iron Oxide Nanocrystal Synthesis, Induced by Trioctylammonium Ions*, Chemistry of Materials **21**, 1326–1332 (2009). 43, 46, 47

[172] M. Comesaña-Hermo, *Synthesis of cobalt-based nanohybrids and study of their magnetic and optical properties. Carbon coating and functionalization with luminescent dyes.*, Ph.D. thesis, Universität Duisburg-Essen 2010. 43, 44, 45, 147

[173] S. Stappert, B. Rellinghaus, M. Acet and E. F. Wassermann, *Gas-Phase Preparation of L10 ordered FePt Nanoparticles*, Journal of Crystal Growth **252**, 440 (2003). 43

[174] B. Rellinghaus, S. Stappert, M. Acet and E. F. Wassermann, *Magnetic properties of FePt nanoparticles*, Journal of Magnetism and Magnetic Materials **266**, 142 (2003). 43

[175] S. Stappert, *FePt-Nanopartikel aus der Gasphase: Herstellung, Struktur und Magnetismus*, Ph.D. thesis, Universität Duisburg-Essen 2003. 43

[176] O. Dmitrieva, M. Acet, J. Kästner, G. Dumpich and W. Wunderlich, *Nitrogenation of FePt nanoparticles*, Journal of Nanoparticle Research **9**, 507–511 (2007). 43

[177] O. Dmitrieva, M. Acet, J. Kästner, G. Dumpich, C. Antoniak and M. Farle, *Enhancement of L10 phase formation in FePt nanoparticles by nitrogenization*, Journal of Physics D: Applied Physics **39**, 4741 (2006). 43

[178] D. Zhu, M. Guizar-Sicairos, B. Wu, A. Scherz, Y. Acremann, T. Tyliszczak, P. Fischer, N. Friedenberger, K. Ollefs, M. Farle, J. R. Fienup and J. Stöhr, *High-Resolution X-Ray Lensless Imaging by Differential Holographic Encoding*, Physical Review Letters **105**, 043901 (2010). 46

[179] K. J. Ollefs, *Structure and Magnetic Correlations in Nanoengineered Systems*, Master's thesis, Universität Duisburg-Essen 2008. 46, 102

[180] D. R. Queen and F. Hellman, *Thin film nanocalorimeter for heat capacity measurements of 30 nm films*, Review of Scientific Instruments **80**, 063901 (2009). 48

[181] H. G. Boyen, K. Fauth, B. Stahl, P. Ziemann, G. Kästle, F. Weigl, F. Banhart, M. Hessler, G. Schütz, N. Gajbhiye, J. Ellrich, H. Hahn, M. Büttner, M. Garnier and P. Oelhafen, *Electronic and Magnetic Properties of Ligand-Free FePt Nanoparticles*, Advanced Materials **17**, 574–578 (2005). 50

[182] U. Wiedwald, K. Fauth, M. Heßler, H. G. Boyen, F. Weigl, M. Hilgendorff, M. Giersig, G. Schütz, P. Ziemann and M. Farle, *From colloidal Co/CoO core/shell nanoparticles to arrays of metallic nanomagnets: Surface modification and magnetic properties*, ChemPhysChem **6**, 2522–2526 (2005). 50

[183] http://www.uni-due.de/agfarle/labore/fmr. 51

[184] X. Xu, S. P. Beckman, P. Specht, E. Weber, D. Chrzan, R. P. Erni, I. Arslan, N. Browning, A. Bleloch and C. Kisielowski, *Distortion and Segregation in a Dislocation Core Region at Atomic Resolution*, Physical Review Letters **95**, 145501 (2005). 53

[185] A. Trunova, *Elektronenmikroskiopie zur Strukturcharakterisierung von chemisch synthetisierten Fe_xPt_{1-x}-Nanopartikeln*, Master's thesis, Universität Duisburg-Essen 2004. 55, 60

[186] R. Hirschl, F. Delbecq, P. Sautet and J. Hafner, *Adsorption of unsaturated aldehydes on the (111) surface of a Pt-Fe alloy catalyst from first principles*, Journal of Catalysis **217**, 354–366 (2003). 57, 61

[187] L. A. Ivanovskii, *Platinum group metal nitrides and carbides: synthesis, properties and simulation*, Russian Chemical Reviews **78**, 303 (2009). 57, 61

[188] J.-H. Cho, Ismail, Z. Zhang and E. W. Plummer, *Oscillatory lattice relaxation at metal surfaces*, Physical Review B **59**, 1677–1680 (1999). 60

[189] S. P. Chen, A. F. Voter and D. J. Srolovitz, *Oscillatory Surface Relaxations in Ni, Al, and Their Ordered Alloys*, Physical Review Letters **57**, 1308–1311 (1986). 60

[190] F. Weigend, F. Evers and J. Weissmüller, *Structural Relaxation in Charged Metal Surfaces and Cluster Ions*, Small **2**, 1497–1503 (2006). 62

[191] T. Kakeshita, T. Takeuchi, T. Fukuda, M. Tsujiguchi, T. Saburi, R. Oshima and S. Muto, *Giant magnetostriction in an ordered Fe_3Pt single crystal exhibiting a martensitic transformation*, Applied Physics Letters **77**, 1502–1504 (2000). 62

[192] F. Kronast (continuosly developing). 65

[193] E. C. Stoner and E. P. Wohlfarth, *A mechanism of magnetic hysteresis in heterogeneous alloys*, IEEE Transactions on Magnetics **27**, 3475–3518 (1991). 78

[194] A. V. Trunova, R. Meckenstock, I. Barsukov, C. Hassel, O. Margeat, M. Spasova, J. Lindner and M. Farle, *Magnetic characterization of iron nanocubes*, Journal of Applied Physics **104**, 093904 (2008). 84, 101

[195] F. Wilhelm, *Magnetic Properties of Ultrathin Films, Coupled Trilayers and 3d/5d Multilayers studied by X-ray Magnetic Circular Dichroism*, Ph.D. thesis, Freie Universität Berlin 2000. 97

[196] A. Scherz, *Spin-dependent X-ray Absorption Spectroscopy of 3d Transition Metals: Systematics and Applications*, Ph.D. thesis, Freie Universität Berlin 2003. 97, 105

[197] R. Wu, D. Wang and A. J. Freeman, *First principles investigation of the validity and range of applicability of the x-ray magnetic circular dichroism sum rule*, Physical Review Letters **71**, 3581–3584 (1993). 98

[198] R. Wu and A. J. Freeman, *Limitation of the Magnetic-Circular-Dichroism Spin Sum Rule for Transition Metals and Importance of the Magnetic Dipole Term*, Physical Review Letters **73**, 1994–1997 (1994). 98

[199] J. G. Booth, *Springer Materials - The Landolt Börnstein Database*, vol. 32B: Alloys and Compounds of d-Elements with Main Group Elements. Part 1 of *Landolt-Börnstein - Group III Condensed Matter Numerical Data and Funktional Relationships in Science and Technology*, chap. 1.5.3.3.3. Figures, pp. Figs. A103 – A137, Springer (). 101, 136

[200] W. Egelhoff, P. J. Chen, R. D. McMichael, C. J. Powell, R. D. Deslattes, F. G. Serpa and R. D. Gomez, *Surface oxidation as a diffusion barrier for Al deposited on ferromagnetic metals*, Journal of Applied Physics **89**, 5209–5214 (2001). 101

[201] V. F. Puntes, D. Zanchet, C. K. Erdonmez and A. P. Alivisatos, *Synthesis of hcp-Co Nanodisks*, Journal of the American Chemical Society **124**, 12874–12880 (2002). 102

[202] S. Shtrikman and E. P. Wohlfarth, *The theory of the Vogel-Fulcher law of spin glasses*, Physics Letters A **85**, 467–470 (1981). 103

[203] J. Dormann, L. Bessais and D. Fiorani, *A dynamic study of small interacting particles - superparamagnetic model and spin-glass laws*, Jounal of Physics C - Solid State Physics **21**, 2015–2034 (1988). 103

[204] J. L. Dormann and D. Fiorani, *Nanophase magnetic materials: size and interaction effects on static and dynamical properties of fine particles*, Journal of Magnetism and Magnetic Materials **140-144**, 415–418 (1995). 103

[205] H. T. Yang, H. L. Liu, N. N. Song, H. F. Du, X. Q. Zhang, Z. H. Cheng, J. Shen and L. F. Li, *Determination of the critical interspacing for the noninteracting magnetic nanoparticle system*, Applied Physics Letters **98**, 153112 (2011). 103

[206] A. Scherz, H. Wende and K. Baberschke, *Fine structure of X-ray magnetic circular dichroism for early 3d transition metals*, Applied Physics A: Materials Science & Processing **78**, 843–846 (2004). 105

[207] K. Fauth, *How well does total electron yield measure x-ray absorption in nanoparticles?*, Applied Physics Letters **85**, 3271–3273 (2004). 105

[208] Z. Wu, V. Suresh Babu, M. S. Seehra and W. Abdul-Razzaq, *Two magnetic-ordering temperatures in Fe/Al multilayered films*, Physical Review B **45**, 2285–2289 (1992). 136

[209] A. Fuß, S. Demokritov, P. Grünberg and W. Zinn, *Short- and long period oscillations in the exchange coupling of Fe across epitaxially grown Al- and Au-interlayers*, Journal of Magnetism and Magnetic Materials **103**, L221 – L227 (1992). 136

[210] R. Meckenstock, *Untersuchung der magnetischen Eigenschaften von Fe/Al Schichtsystemen mit der konventionellen und der ortsaufgelösten ferromagnetischen Resonanz*, Ph.D. thesis, Ruhr-Universität-Bochum 1997. 136

[211] E. Pellegrain, M. Hagelstein, S. Doyle, H. O. Moser, J. Fuchs, D. Vollath, S. Schuppler, M. A. James, S. S. Saxena, L. Niesen, O. Rogojanu, G. A. Sawatzky, C. Ferrero, M. Borowski, O. Tjernberg and N. B. Brookes, *Characterization of nanocrystalline $\gamma - Fe_2O_3$ with synchrotron radiation techniques*, physica status solidi (b) **215**, 797–801 (1999). 137

[212] D. Spoddig and R. Meckenstock. private communication. 141

[213] F. Dumestre, B. Chaudret, C. Amiens, M.-C. Fromen, M.-J. Casanove, P. Renaud and P. Zurcher, *Shape Control of Thermodynamically Stable Cobalt Nanorods through Organometallic Chemistry*, Angewandte Chemie **114**, 4462–4465 (2002). 147

[214] M. Comesaña-Hermo. private communication. 147

[215] O. Posth, *Spin-Transfer-Torque in ferro/nichtferromagnetischen Säulenstrukturen*, Ph.D. thesis, Universität Duisburg-Essen 2010. 160

[216] http://www.helmholtz-berlin.de/forschung/grossgeraete/undulatoren/. 162

[217] R. M. Cornell and U. Schwertmann, *The iron oxides*, VCH 1996. 173

List of Figures

List of Tables

Publications

Articles

6) N. Friedenberger, Z.-A. Li, O. Dmitrieva, O. Margeat, M. E. Gruner, C.Y. Song, C. Kisielowski, and M. Farle, *Oscillatory Surface Relaxation in* $Fe_xPt_{1-x} - Nanoparticles$, in preparation

5) N. Friedenberger, S. Stienen, C. Möller, Z.-A. Li, M. Spasova, F. Kronast, H. Dürr, and M. Farle, *Single nanoparticle hysteresis: influence of morphology*, "Nanostructures: Physics and Technology", 19th Int. Symp., Ekaterinburg, Russia, June 20-25, 2011, Proceedings, 38 (2011)

4) F. Kronast, N. Friedenberger, K. Ollefs, S. Gliga, L. Tati-Bismaths, R. Thies, A. Ney, R. Weber, C. Hassel, F. M. Römer, A. V. Trunova, C. Wirtz, R. Hertel, H. A. Dürr, and M. Farle, *Element-Specific Magnetic Hysteresis of Individual 18 nm Fe Nanocubes*, Nano Lett. 11, 1710 (2011)

3) D. Zhu, M. Guizar- Sicairos, B. Wu, A. Scherz, Y. Acremann, T. Tyliszczak, P. Fischer, N. Friedenberger, K. Ollefs, M. Farle, J. R. Fienup, and J. Stöhr, *High-Resolution X-Ray Lensless Imaging by Differential Holographic Encoding*, Phys. Rev. Lett. 105, 043901 (2010)

2) M. Ali, N. Friedenberger, M. Spasova, and M. Winterer, *A Novel Approach for Chemical Vapor Synthesis of ZnO Nanocrystals: Optimization of Yield, Crystallinity*, Chem. Vap. Deposition 15, 192 (2009)

1) D. Sudfeld, O. Dmitrieva, N. Friedenberger, G. Dumpich, M. Farle, C.Y. Song, C. Kisielowski, M. E. Gruner, and P. Entel, *HR-TEM Studies of FePt Nanoparticles by Exit Wave Reconstruction*, Mater. Res. Soc. Symp. Proc. Volume 998E, 0998-J01-06 (2007)

Invited Talks

4) N. Friedenberger and M. Farle: *Individual Magnetic Responses of Nanoparticles - Results and Challenges*, "XM-3 A next generation full-field soft X-ray microscope for materials sciences at LBNL" - Workshop, Berkeley, CA, USA (2010)

3) N. Friedenberger, F. Kronast, H. Dürr, and M. Farle: *Individual Magnetic Responses of Fe-Nanocubes*, King Abdullah University of Science and Technology (KAUST), Thuwal, Saudi-Arabia (2010)

2) N. Friedenberger, K. Ollefs, F. Kronast, H. Dürr, and M. Farle: *Imaging Magnetic Responses of Individual Fe-Nanocubes*, First Joint BER II and BESSY II Users' Meeting, Berlin (2009)

1) N. Friedenberger, O. Dmitrieva, C. Kisielowski, and M. Farle: *Surface Relaxation in FePt-Nanoparticles*, 19. Edgar Lüscher Seminar 2008, Klosters, Switzerland (2008)

Contributed Talks

9) N. Friedenberger: *Magnetic Properties of Individual Nanoparticles Studied by XPEEM*, SFB 445 and CeNIDE Symposium, Venice, Italy (2010)

8) N. Friedenberger, K. Ollefs, and M. Farle: *Towards Single Nanoparticle Magnetic Hysteresis: Second Results*, SFB 445 Klausurtagung und Workshop, Papenburg (2009)

7) N. Friedenberger, K. Ollefs, F. Kronast, H. Dürr, and M. Farle: *Individual Magnetic Responses of Self-Assembled Fe-Nanocubes in Different Configurations*, International Conference on Magnetism, Karlsruhe (2009)

6) N. Friedenberger, K. Ollefs, F. Kronast, H. Dürr, and M. Farle: *Imaging Magnetic Responses of Different Fe-Nanocube Configurations*, DPG-Frühjahrstagung, Dresden (2009)

5) F. Kronast, F. Radu, H. A. Dürr, W. Eberhardt, N. Friedenberger, K. Ollefs, and M. Farle: *Imaging Magnetic Responses of Fe-Nanocube Monomers, Dimers and Trimers*, MRS fall meeting, Boston, MA, USA (2008)

4) N. Friedenberger, K. Ollefs, and M. Farle: *Towards Single Nanoparticle Magnetic Hysteresis: First Results*, SFB 445 Klausurtagung und Workshop, Duisburg (2008)

3) N. Friedenberger, O. Dmitrieva, D. Sudfeld, C. Kisielowski, and M. Farle: *Layer-*

Resolved Crystal Structure of FePt Nanoparticles with sub-Angstrom Resolution, Mitarbeiterworkshop SFB 445, Nordwalde (2007)

2) N. Friedenberger, O. Dmitrieva, D. Sudfeld, C. Kisielowski, and M. Farle: *Layer-Resolved Crystal Structure of FePt Nanoparticles with sub-Angstrom Resolution*, DPG-Frühjahrstagung, Regensburg (2007)

1) N. Friedenberger: *Lattice Expansion in 3 nm FePt Colloidal Nanoparticles*, International Summer School and 4th Workshop on "Synthesis and Orbital Magnetism of core-shell nanoparticles", Thessaloniki, Greece (2006)

Posters

7) N. Friedenberger, K. Ollefs, F. Kronast, H. Dürr, and M. Farle: *Magnetic Properties of Individual Fe-Nanocubes*, "Frontiers in Modern Nano-Magnetism" - Swedish-German Summer School, Härjarö, Sweden (2010)

6) N. Friedenberger, K. Ollefs, F. Kronast, H. Dürr, and M. Farle: *Magnetic Properties of Individual Fe-Nanocubes*, SNI 2010, Berlin (2010)

5) N. Friedenberger, K. Ollefs, F. Kronast, H. Dürr, and M. Farle: *Imaging Magnetic Responses of Different Fe-Nanocube Configurations with XPEEM*, 20. Edgar Lüscher Seminar, Klosters, Switzerland (2009)

4) N. Friedenberger, K. Ollefs, F. Kronast, H. Dürr, and M. Farle: *Imaging Magnetic Responses of Different Fe-Nanocube Configurations with XPEEM*, Vth International School on Magnetism and Synchrotron Radiation, Mittelwihr, France (2008)

3) N. Friedenberger, O. Dmitrieva , C. Kisielowski, D. Sudfeld, O. Margeat, M. Acet, G. Dumpich, M. Spasova, M. Tran, and M. Farle: *Crystal Structure of Magnetic FePt-Nanocrystals with Different Shapes*, 3rd CHIRALTEM workshop, Triest, Italy (2007)

2) N. Friedenberger, O. Dmitrieva , C. Kisielowski, D. Sudfeld, O. Margeat, M. Acet, G. Dumpich, M. Spasova, M. Tran, and M. Farle: *Crystal Structure of Magnetic FePt-Nanocrystals with Different Shapes*, 18. Edgar Lüscher Seminar, Klosters, Switzerland (2007)

1) N. Friedenberger, O. Dmitrieva , C. Kisielowski, D. Sudfeld, O. Margeat, M. Acet, G. Dumpich, M. Spasova, M. Tran, and M. Farle: *Crystal Structure of Magnetic FePt-Nanocrystals with Different Shapes*, Biomaterials 2006, Essen (2006)

Curriculum Vitae

Due to data protection reasons the curriculum vitae is not included in the online-version of this thesis.

Aus Datenschutzgründen ist der Lebenslauf in der Online-Version dieser Dissertation nicht enthalten.

Acknowledgement/Danksagung

Mein Dank gilt allen, die mich in der Zeit der Anfertigung dieser Arbeit auf diese oder jene Weise unterstützt und begleitet haben. Einigen Personen möchte ich jedoch noch einmal persönlich danken.

Hier gilt mein ganz besonderer Dank meinem Doktorvater Prof. Dr. Michael Farle für die Möglichkeit, diese Arbeit in seiner Arbeitsgruppe anzufertigen und während dieser Zeit sehr interessante Kollaborationsprojekte weltweit bearbeiten zu können. Auch möchte ich nicht vergessen, mich dafür zu bedanken, dass er immer ein offenes Ohr für mich hatte - nicht nur die physikalischen Fragestellungen betreffend - und dass ich mich stets auf seine Unterstützung verlassen konnte.

Ein ganz großes Danke geht an Dr. Florian Kronast für die vielen spannenden Kollaborationsprojekte am PEEM und seine prima Unterstützung und Hilfsbereitschaft - und natürlich auch für die willkommenen Mittwochs-Ausflüge in den Sand.

Für Ihre tolle Unterstützung bei den Messzeiten und der Datenauswertung gilt mein Dank: Dr. Julia Herrero-Albillos, Dr. Logane Tati-Bismaths, Dr. Ramona Weber, Olga Mesheriakova, Marina Radulaški, Oliver Sandig und Ronja Thies. Sie alle haben dazu beigetragen, dass mir die XPEEM-Messzeiten in sehr angenehmer Erinnerung bleiben.

Dr. Hermann Dürr für die Initiative zur Kollaboration für das Projekt “Nanocubes”.

Dr. Riccardo Hertel und Dr. Sebastian Gliga für die gute Zusammenarbeit und die Bereitschaft mikromagnetische Simulationen der “Nanocubes” durchzuführen.

Dr. Peter Fischer und Dr. Mi-Young Im für die wertvolle Unterstützung bei den MTXM-Experimenten.

Dr. Christian Kisielowski und ChengYu Song für die angenehme und erfolgreiche Zeit bei NCEM.

Dr. Andreas Scherz für die Realisierung des gemeinsamen Projekts an der SSRL. Hier sei auch noch einmal der gesamten “Stöhr Group” gedankt.

Dr. Alexey Shavel für die Bereitstellung der “Nanocubes”, ohne die diese Arbeit gar nicht erst möglich gewesen wäre.

Dr. Miguel Comesaña-Hermo für sehr angenehme BESSY-Messzeiten und seine super Hilfsbereitschaft und viele, viele Co Nanorods.

Bei Frau Dr. Marina Spasova bedanke ich mich für die schöne Bürogemeinschaft, Ihre Hilfsbereitschaft und für die vielen interessanten Diskussionen und Gespräche - auch über die nicht so physikalischen Dinge.

Horst Zähres, einfach für alles. Egal mit welchem Problem man auf ihn zukam, es blieb nicht ungelöst.

Dieter Schädel, für zahlreiche Probenhalter, bei denen auch durchaus der eine oder der andere Bohrer einmal “dran glauben” musste.

Michael Vennemann für den guten PC-Support. In diesem Zusammenhang möchte ich auch noch einmal Dr. Detlef Spoddig erwähnen. Dank seiner schnellen Unterstützung habe ich den Festplattencrash während des Zusammenschreibens doch ohne zu großen Schaden überstanden. Auch sage ich danke für seine große Hilfs- und Diskussionsbereitschaft. Dieser Dank gilt auch Dr. Ralf Meckenstock, Dr. Jürgen Lindner, Dr. Marc Möller und Prof. Dr. Mehmet Acet.

Besonders möchte ich mich auch beim ehemaligen “MAGLOMAT”-Team für SQUID-Messungen und auch die eine oder andere Probenherstellung bedanken. Ein großes Danke geht hier speziell an Dr. Andreas Ney und Dr. Verena Ney für die super Kalifornien-Tipps und die ALS-Messzeit-Unterstützung.

Im Folgenden möchte ich den anderen Doktoranden, Studenten und auch ehemaligen Kommilitonen, die mich teilweise schon mein ganzes Studium begleitet haben, ganz besonders danken. Neben der Unterstützung im Labor und bei den Experimenten, habe ich auch das freundschaftliche Verhältnis immer sehr geschätzt. Ohne die Hilfe von Nathalie Reckers, Dr. Oliver Posth, Anja Banholzer, Christian Wirtz, Florian Römer, Dr. Anastasia Trunova und Dr. Christoph Hassel wäre die Probenherstellung nicht möglich gewesen. Zusammen mit Sven Stienen wurde ich von Dr. Christoph Hassel mit der Durchführung von OOMMF Simulationen unterstützt. Bei Christina Möller bedanke ich mich für die Tomografie-Daten und die Unterstützung bei BESSY. Mit Katharina Ollefs verbinde ich viele gemeinsame Messzeitaufenthalte, sowohl bei BESSY, als auch bei der SSRL und der ALS in Kalifornien. Bei der Probenkonzeptionierung, Präparation und auch bei den Experimenten habe ich unsere angenehme Zusammenarbeit sehr geschätzt. Auch die gemeinsamen Exkursionen in die Weiten Kaliforniens als Kontrast-

programm zu den Synchrotron-Experimenten werden mir in guter Erinnerung bleiben. Danke auch für die seelische Unterstützung.

Dr. Markus Gruner danke ich für die Bereitstellung der Simulationsdaten und seine Hilfs- und Diskussionsbereitschaft.

Dr. Carolin Antoniak, Dr. Claudia Weis, Bernhard Krumme, Anne Warland und auch Prof. Dr. Kai Fauth für doch die eine oder andere "gemeinsame" Messzeit bei BESSY und Ihre Hilfsbereitschaft beim Kampf mit den XMCD-Daten.

Katrin Neureiter für Ihre Hilfe und den Mut sich durch diverse Messzeit-Datenberge zu kämpfen.

Helga Mundt und Sabina Grubba, die einfach einen super Job machen und auch immer ein offenes Ohr für mich hatten.

Während der vielen Jahre in der Experimentalphysik-AG Farle habe ich mich stets sehr wohl gefühlt und dafür bedanke ich mich noch einmal ganz herzlich bei allen Mitarbeitern und Ehemaligen.

Ganz besonders liegt es mir jedoch noch am Herzen, meinen Eltern zu danken, die wirklich immer für mich da waren. Insbesondere gilt mein Dank und vor allem meine Bewunderung meiner Mutter, die trotz Ihrer schweren Erkrankung immer wieder noch die Kraft gefunden hatte, mich zu ermutigen, meinen Weg weiterzugehen und nach vorne zu schauen.

Zu guter Letzt möchte ich noch allen Personen danken, die hier nicht namentlich erwähnt wurden, die mir jedoch in den letzten Jahren wichtige Begleiter waren und auf die ich mich immer verlassen konnte: Danke für Eure Unterstützung und Euer Vertrauen.